Topographic controls on gravity flow behaviour, and microplastic transfer in the deep sea

Edward Keavney
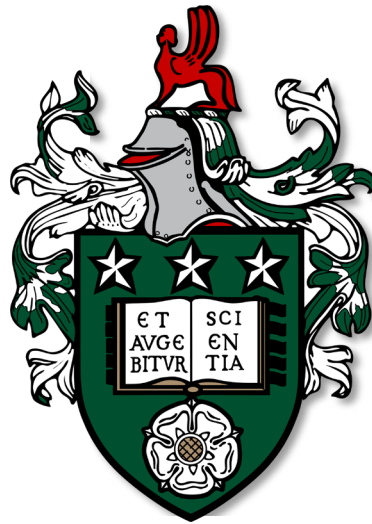
Submitted in accordance with the requirements for the degree of

Doctor of Philosophy (PhD)

The University of Leeds

School of Earth and Environment

September 2024

This page is intentionally left blank.

Declaration

The candidate confirms that the work submitted is their own, except where work which has formed part of jointly authored publications has been included. The contribution of the candidate and the other authors to this work has been explicitly indicated below. The candidate confirms that appropriate credit has been given within the thesis where reference has been made to the work of others.

Chapter 3 – Published in Sedimentology

Keavney, E., Peakall, J., Wang, R., Hodgson, D.M., Kane, I.A., Keevil, G.M., Brown, H.C., Clare, M.A. and Hughes, M. 2024. Unconfined gravity interactions with orthogonal topography: Implications for combined-flow processes and the depositional record. *Sedimentology*. https://doi.org/10.1111/sed.13227

Author contributions:

Keavney, E. – Experimental design, data collection and analysis, and figure and manuscript preparation.

Peakall, J. – Conceptualisation and detailed manuscript review.

Wang, R. – Detailed manuscript review.

Hodgson, D.M – Conceptualisation and detailed manuscript review.

Kane, I.A. – Conceptualisation and detailed manuscript review.

Keevil, G.M – Experimental design, laboratory assistance, and conceptualisation.

Brown, H.C. – Experimental design and laboratory assistance.

Clare, M.A. – Detailed manuscript review.

Hughes, M – Detailed manuscript review.

Submitted: 31st January 2024

Decisioned: 14th June 2024

Revisions submitted: 5th July 2024

Accepted: 16th July 2024

Chapter 4 – Submitted October 2024

Keavney, E., Taylor, W.J., Hodgson, D.M., Kane, I.A. and Peakall, J. 2024. Abrupt downstream changes in submarine canyon-margin architecture.

Author contributions:

Keavney, E. – Conceptualisation, led data collection and analysis, figure and manuscript preparation.

Taylor, W.J. – Fieldwork assistance, conceptualisation, and detailed manuscript review.

Hodgson, D.M. – Conceptualisation and detailed manuscript review.

Kane, I.A. – Conceptualisation and detailed manuscript review.

Peakall, J. – Conceptualisation and detailed manuscript review.

Target Journal: The Depositional Record

The fieldwork in relation to Chapter 4 was conducted in April-May 2022 in Baja California, Mexico. In addition to leading the fieldwork and constructing the photogrammetric drone model for Chapter 4, E Keavney was also a field assistant for a joint industry programme (JIP). For this reason, the photogrammetric drone model used in Chapter 4 cannot be made publicly accessible due to confidentiality agreements with the JIP sponsors.

Chapter 5 – Submitted October 2024

Keavney, E., Kane, I.A., Clare, M.A., Hodgson, D.M., Huvenne, V.A.I., Sumner, E.J., Peakall, J., Mienis, F. and Kranenburg, J**.** 2024. Pervasive microplastic pollution in a land-detached submarine canyon.

Author contributions:

Keavney, E. – Conceptualisation, led laboratory methodology, data analysis, and figure and manuscript preparation.

Kane, I.A. – Conceptualisation, laboratory assistance, and detailed manuscript review.

Clare, M.A. – Organised and led data collection, conceptualisation, and detailed manuscript review.

Hodgson D. M. – Conceptualisation and detailed manuscript review.

Huvenne, V.A.I – Organised and led data collection, onboard scientist, and manuscript review.

Sumner, E.J. – Organised and led data collection, onboard scientist, and manuscript review.

Peakall, J. – Conceptualisation and detailed manuscript review.

Mienis, F. – Data collection and analysis.

Kranenburg, J. – Data analysis.

Target Journal: The Journal of the Geological Society London

The data made available for this Chapter were obtained from three research cruises to the Whittard Canyon, UK. The details for each cruise are included in Chapter 5. E Keavney led the sediment/microplastic extraction at the University of Manchester and the sediment grain-size analysis at the University of Leeds. J Kranenburg (Vrije Universiteit Amsterdam) performed the initial ^{210}Pb sediment accumulation rate analysis.

Acknowledgements

I would like to thank my supervisors in Leeds, Dave Hodgson and Jeff Peakall, for their support, mentorship, and the beers throughout this project. Furthermore, a huge thank you to Ian Kane and Mike Clare for their continued supervision over the last four years, and to Ian and Helen for their hospitality whilst working in the lab in Manchester. To Gareth and Helena in the Sorby Lab, your support and friendliness brought a sense of normality to the start of my time in Leeds during Covid lockdowns, thank you.

I would also like to thank the members of the research groups in Leeds and Manchester: Will, Max, Euan, Adam, Ander, Ash, Rhodri, Rufus, Miquel, Steve, Mo, Grace, Meg, Carys, Yan, Ru, Mia, Steven, Josh, Daniel and Jewel, for all the memories (highs and lows) associated with field seasons in Spain, Mexico, South Africa and Greenland, office chat, and conferences.

To my family, thank you for your continuous love and support. To my dad, thank you for everything; here's to many more adventures together.

This thesis is dedicated to the late John R. Hunter and his love of all things of nature.

"Let's be havin' you!"

Delia Ann Smith CH CBE

Abstract

Gravity currents are sensitive to interactions with seafloor topography and changes to the degree of flow confinement: both factors impart first-order controls on flow behaviour and sedimentation patterns. The form of seafloor topography and range of sediment gravity flow types varies markedly across different geomorphic elements of the deep sea. The resulting flow-topography interactions control the routeing and burial of sediment and microplastics in the deep sea. However, the present understanding of flow-topography interactions and microplastic transfer processes in all deep sea environments remain poorly understood. This thesis presents a new process-product model for flow interactions with complex canyon-margin topography, a new mechanistic model from physical experiments of flow-topography interactions in unconfined settings, and uses modern seafloor sediment cores from the Whittard Canyon to assess the role canyons play in transferring microplastics into the deep sea. The localised heterogeneity in the deposit type and architecture related to mass-wasting of a canyon-margin documented in the Rosario Formation, Mexico, is poorly accounted for in existing canyon-fill models and highlights the role of transient storage of particulate matter in canyon overbanks. The new model for combined flow generation and mechanics for onlap styles documented experimentally in unconfined settings shows that sediment gravity flow behaviour and sedimentation patterns can be used to support interpretations of palaeogeographic reconstructions and sediment pathways in the deep sea. The pervasiveness of microplastic pollution throughout the Whittard Canyon and down to 10 cm sediment depth highlights how anthropogenic activity and subsurface burial processes add noise to the signal in microplastic source-to-sink models. Linking the findings from three different methods helps develop a comprehensive understanding of the role seafloor topography imparts on the delivery, transfer and burial of particulate matter in the deep sea. This work presents new insights into sediment gravity flow behaviour, and microplastic transfer, which provide criteria to support palaeogeographic reconstructions, assessments of sediment routeing patterns and microplastic flux calculations in deep-water sedimentary systems.

Table of Contents

List of Figures

List of Videos

List of Tables

Nomenclature and Abbreviations

Fr_d = densiometric Froude number

g = acceleration due to gravity (m s^{-2})

g' = reduced gravity

h = flow height (m)

h_{max} = maximum run-up height (m)

h' = topographic containment factor

Re = Reynolds number

U = mean depth-averaged velocity (m s^{-1})

U_{max} = maximum streamwise velocity (m s^{-1})

P_a = density of the ambient water (kg m^{-3})

P_s = mean depth-averaged density of the current (kg m^{-3})

μ = dynamic viscosity (kg m^{-1} s^{-1})

FTIR = Fourier transform infrared

HCS = hummocky cross-stratification

HDT(S) = high density turbidity current(s)

 LDT(s) = low density turbidity current(s)

m.a.t. – meters above thalweg

MCZ = Marine Conservation Zone

Mt = million tonnes

MTD(s) = mass transport deposit(s)

SGF(s) = sediment gravity flow(s)

Chapter 1   Introduction

Sediment gravity flows (SGFs) transport and bury particulate matter (*e.g.,* sediment, organic carbon, and pollutants) sourced from terrestrial and shallow marine environments to the deep sea (Middleton and Hampton, 1973; Paull *et al.,* 2002; Wynn *et al.,* 2007; Peakall and Sumner, 2015; Maier *et al.,* 2019; Heijnen *et al.,* 2022). Seafloor topography is present at different scales throughout deep-water systems and the form (*i.e.,* orientation, gradient, and rugosity) of seafloor topography acts as a first-order control on SGF behaviour (van Andel and Komar, 1969; Thornburg *et al.,* 1990; Kneller and McCaffrey, 1999; Kneller and Buckee, 2000). Submarine canyons and channels act as conduits to globally important volumes of sediment (*e.g.,* Normark, 1970; Mutti and Normark, 1991; Deptuck *et al.,* 2003; Ribó *et al.,* 2024), organic carbon (Galy *et al.*, 2007; Talling *et al.,* 2023; Hage *et al.,* 2024), and pollutants (Paull *et al.*, 2002; Zhong and Peng, 2021, Pierdomenico *et al.,* 2023), and the deep-sea floor acts as the ultimate repository; with each environment hosting complex seafloor topography (Gorsline and Emery, 1959; van Andel and Komar, 1969). Therefore, it is important to understand how seafloor topography throughout deep-water systems influences SGF behaviour and how it controls the transfer, transient storage and burial of particulate matter through time.

Changes to the direction and velocity of SGFs upon incidence with seafloor topography control the dynamics of erosion and deposition, and thus the character of the deposits. Studies of modern systems, primarily of submarine canyons and channels, have provided direct evidence of particulate matter being transferred to the deep-sea via episodic SGFs (*e.g.,* Paull *et al.,* 2010, 2018; Talling *et al.,* 2015; Maier *et al.,* 2019; Heijnen *et al.,* 2022) and canyon-flushing events (Canals *et al.,* 2006; Azpiroz-Zabala *et al.,* 2017; Mountjoy *et al.,* 2018; Maier *et al.,* 2024; Ruffell *et al.,* 2024; Ribó *et al.,* 2024). Other studies have shown how both the presence of seafloor topography (*e.g.,* mass-transport deposits, terraced overbanks, and fault scarps) (*e.g.,* Paull *et al.,* 2013; Maier *et al.,* 2018; Tek *et al.,* 2021; Pope *et al.,* 2022; McArthur *et al.,* 2024), and the geomorphology of submarine canyons and channels (*e.g.,* channel sinuosity, thalweg gradient, and canyon wall steepness) (*e.g.,* Peakall *et al.,* 2007; Wynn *et al.,* 2007; Micallef *et al.,* 2014) can control the routeing pathways, and the short- and long-term storage of particulate matter in the deep-sea. Outcrop studies have detailed flow-topography interactions at varying scales. Basin-scale variations in onlap patterns and facies distributions have been linked to changes in the degree of basin confinement (*e.g.,* Gorsline and Emery, 1959; van Andel and Komar, 1969; Ricci Lucchi and Valmori, 1980; Covault and Romans, 2009; Marini *et al.,* 2015; Dodd *et al.,* 2018), and

allogenic and autogenic signal changes (*e.g.,* Soutter *et al.,* 2019). The generation of mixed grain-size bedforms (*e.g.,* Baker and Baas, 2020; Stevenson *et al.,* 2020; Taylor *et al.,* 2024a), hybrid event beds (Talling *et al.,* 2004; Hodgson, 2009; Kane and Ponten, 2012; Kane *et al.,* 2017; Pierce *et al.,* 2018), hummock-like structures (Tinterri, 2011; Tinterri *et al.,* 2022; Taylor *et al.,* 2024a), and sediment waves (Wynn *et al.,* 2002a; Fildani and Normark, 2006; Dennielou *et al.,* 2017; Hofstra *et al.,* 2018; Maier *et al.,* 2020) have been linked to process-product models of SGFs undergoing flow transformations due to changes in the degree of flow confinement, the entrainment of mud, and upon incidence with topography. Key to the understanding of how flow-topography interactions vary with time and control the behaviour of SGFs are scaled, physical models, that have focused primarily on the processes of flow reflection (*e.g.,* Pantin and Leeder, 1987; Edwards *et al.,* 1994; Kneller *et al.,* 1997), deflection (*e.g.,* Kneller *et al.,* 1991), and blocking/ponding (*e.g.,* Al Ja'aidi *et al.,* 2004; Patacci *et al.,* 2015; Stevenson *et al.,* 2015).

The presence of microplastics in deep-sea sediments (*e.g.,* Woodall *et al.,* 2014; Kane *et al.,* 2020) and efficiency of sediment transport via SGFs (*e.g.,* Middleton and Hampton, 1973; Stevenson *et al.,* 2013) has led to the hypothesis that microplastic transport to the deep-sea is primarily via SGFs (Kane and Clare, 2019; Pohl *et al.,* 2020). Microplastics are plastic particles less than 1 mm in size, with variable shapes (*i.e.,* from elongate microfibres to spherical microbeads) and densities (*e.g.,* Polypropylene [PP] has a density of approximately 900 kg m^{-3} and Polyethylene Terephthalate [PET] approximately 1370 kg m^{-3}). Microplastics are subject to the same transport mechanisms of natural sediment grains (*e.g.,* Waldshläger *et al.,* 2022) and have been observed to have been ingested by deep-sea organisms (Rist *et al.,* 2016; Taylor *et al.,* 2016). Therefore, it is important to better understand how microplastics respond to sediment transport and burial processes in order to include microplastics when calculating particulate matter storage and burial in the deep sea, and for identifying ecosystems vulnerable to microplastic pollution.

However, there are spatio-temporal resolution gaps that exist with modern, outcrop, and physical modelling approaches owing to a sparsity of direct measurements outside of canyon and channel environments, the incomplete three-dimensional stratigraphic record, limited sedimentological constraint on microplastic transfer processes, and challenges associated with scaling real-world processes to laboratory analogues, especially in unconfined settings. Therefore, the understanding of how flow-topography interactions dictates the behaviour of SGFs and the transfer of particulate matter throughout deep-water environments is incomplete.

This thesis presents and synthesises the results from:

i. Scaled, physical experiments of saline density currents interacting with a simple topographic slope to understand flow processes in an unconfined, basin floor setting.

ii. An outcrop study of the exceptionally well-preserved Rosario Formation, Mexico, to assess how topography in a canyon-confined overbank controls sediment gravity flow behaviour and deposit heterogeneity.

iii. Modern seafloor samples from the Whittard Canyon, NE Atlantic to determine how different near-bed deep-sea flows, shallow subsurface processes, and submarine canyon topography control the transport and burial of microplastics in the deep-sea.

The ambition for this thesis is to address the following research questions:

1.1 How does topography control sediment gravity flow behaviour and sedimentation?

Rationale: Sediment gravity flows (SGFs) are the principal mechanism for the transport of particulate matter into the deep-sea (Curray and Moore, 1971; Middleton and Hampton, 1973; Wynn *et al.*, 2007), resulting in the largest sediment accumulations on Earth (Curray and Moore, 1971; Emmel and Curray, 1983). However, the loci of deposition and depositional character of SGFs is strongly controlled by seafloor topography (Alexander and Morris, 1994; Kneller, 1995; Kneller and McCaffrey, 1999, McCaffrey and Kneller, 2001; Mulder and Alexander, 2001), imparting a first-order control on SGF behaviour. Better understanding of how the nature of the seabed topography controls SGF behaviour is crucial for deciphering bed-scale processes, developing process-product models, and palaeogeographic reconstructions of deep-water sedimentary systems.

The behaviour of a SGF changes profoundly both with variations in the degree of flow confinement (Mutti and Normark, 1987, 1991; Posamentier and Kola, 2003; Stevenson *et al.*, 2015; Hodgson *et al.*, 2022) and upon incidence with topography (van Andel and Komar, 1969; Thornburg *et al.*, 1990; Kneller and McCaffrey, 1999; Kneller and Buckee, 2000; Apps *et al.*, 2004). Observations from deposits show that upon incidence with topography, SGFs can accelerate, becoming more erosive and bypass-dominated (*e.g.,* Kneller, 1995; Kneller and McCaffrey, 1999; Amy *et al.*, 2004; Jobe *et al.*, 2017), have increased superelevation (*i.e.,* ability of the flow to run-up surfaces several times their flow depth) following density decoupling of stratified flows (*e.g.,*

Piper and Normark, 1983; Fildani *et al.,* 2006; Soutter *et al.,* 2021a), and can become completely ponded (*e.g.,* Haughton, 1994; Patacci *et al.,* 2015; Southern *et al.,* 2015; Tinterri *et al.,* 2022; Siwek *et al.,* 2023). How a flow responds to interactions with topography is dependent on the character of the primary flow (*i.e.,* concentration, velocity, and thickness) and the topographic configuration (*i.e.,* orientation, gradient, and rugosity).

Using the deposits from SGFs to answer the above research question does however have inherent challenges, related to the poor exposure of exhumed ancient systems and low-resolution seismic reflection data. This knowledge gap limits understanding of the process-product models of bedforms interpreted to record the interaction of SGFs with seafloor topography and palaeogeographic reconstructions of basin confinement. Following the recognition of distinct facies variations and complex palaeocurrent dispersal patterns in the stratigraphic record, attributed to the interaction of SGFs with topography (Pickering and Hiscott, 1985; Alexander and Morris, 1994; Kneller *et al.,* 1991; Hodgson and Haughton, 2004), physical modelling approaches have helped to better understand the process-product models associated with flow reflection, deflection, acceleration, and ponding processes (*e.g.,* Pantin and Leeder, 1987; Kneller *et al.,* 1991, 1997; Edwards *et al.,* 1994; Kneller, 1995; Kneller and McCaffrey, 1995; Amy *et al.,* 2004; Patacci *et al.,* 2015; Soutter *et al.,* 2021a). The earliest physical models primarily focused on the generation of hydraulic bores, solitons and solitary waves in the formation of flow reversals (*e.g.,* Pantin and Leeder, 1987; Kneller *et al.,* 1991; Edwards *et al.,* 1994), and the changes to flow velocity and direction in the response to interactions with topography (*e.g.,* Alexander and Morris, 1994; Kneller and McCaffrey, 1995; Al Ja'aidi *et al.,* 2004; Amy *et al.,* 2004). A major caveat to many of the previous physical models is the confined, two-dimensional aspect ratio of the flume tanks, thus inhibiting observations of unconfined SGFs to be made. In practice, the principles from the previous models are best applied to confined-basin settings (*e.g.,* Kneller and McCaffrey, 1999; Amy *et al.,* 2004; Tinterri *et al.,* 2016, 2022; Soutter *et al.,* 2019; Siwek *et al.,* 2023). This is particularly important for the formation of combined flows (*i.e.,* highly multidirectional flows generated from the superimposition of multiple flow components) in deep-water systems. Previous models for combined flow generation in deep-water systems are linked to the flow-topography interactions and the generation of internal waves with an oscillatory flow component superimposed with the unidirectional parental flow (Tinterri *et al.,* 2016, 2022). However, whether these models for flow-topography interactions and the generation of combined flows hold in more unconfined basin settings has not been explored thoroughly, using three-dimensional flume tanks. Except for Soutter *et al.* (2021a), results from large, three-dimensional flume tanks are not available. Soutter *et al.* (2021a) focused on the

depositional patterns up- and down-dip of flow-surmountable topography oriented orthogonal, oblique and parallel to the parental flow. New process-product models for flow-topography interactions that tie SGF behaviour to bed-scale processes are needed to improve the accuracy of palaeogeographic reconstructions.

1.2 How does the feedback between flow-topography interactions vary with time?

Rationale: Deep-water sedimentary systems are subject to changes in allogenic factors such as sediment supply rates, accommodation, and sea-level rise/fall (Hajek and Straub, 2017). These changes are commonly recorded through the temporal evolution of the basin, via basin-margin onlap models and facies variations (*e.g.,* Puigdefàbregas *et al.*, 2004; Apps *et al.*, 2004; Soutter *et al.*, 2019). However, autogenic signal changes are also imprinted in the stratigraphic record and can be localised to intrabasinal topography. The noise contributed by autogenic signals affects the accuracy of particulate matter calculations in the deep-sea (*e.g.,* Galy *et al.*, 2007), sediment routeing pathways, and palaeogeographic reconstructions. Therefore, a better understanding of flow-topography interactions through time is vital.

Complex topography exists throughout all the geomorphic elements of deep-water sedimentary systems, from submarine canyons, through channels, to lobes and abyssal plain settings. Topography created from pre- and syn-depositional tectonic deformation (*e.g.,* Haughton, 1994; Hodgson and Haughton, 2004) is tied to allogenic processes. However, more localised topography generated by the depositional relief from mass transport deposits (MTDs) (Armitage *et al.,* 2009; Martínez-Doñate *et al.,* 2021; Allen *et al.,* 2022), and levees and lobes (*e.g.,* Groenenberg *et al.,* 2010; Kane and Hodgson, 2011) is also common and can often be tied to autogenic processes. Well documented in deep-water systems is the occurrence of MTDs, common in both exhumed, ancient (*e.g.,* Armitage *et al.,* 2009; Kneller *et al.,* 2016, Valdez Buso *et al.,* 2024), subsurface (*e.g.,* Bull *et al.,* 2019; Nwoko *et al.,* 2020; McArthur *et al.,* 2024) and modern (*e.g.,* Pope *et al.,* 2022) studies. MTDs not only create space from the evacuation of material, but also create topography at their margins and on the upper surfaces. How subsequent flows of different magnitudes interact with the evacuated space and MTD relief, and other forms of topography (*e.g.,* basin margins and fault scarps) through time is recorded by localised facies and onlap variations.

Submarine canyons play a vital role in the delivery and storage of particulate matter in the deep-sea. However, understanding how flow-topography interactions evolve through time in

submarine canyons at a fine resolution is limited by a lack of three-dimensional outcrop exposure and low-resolution subsurface data. Submarine channel-levee environments display predictable lateral changes in deposit architecture and facies variations through time (*e.g.,* Kane and Hodgson, 2011; Hansen *et al.,* 2015, 2017a) and provide a more complete record of channel evolution from incision through fill to burial, through the preservation of fine-grained material from SGFs that escaped the confinement of the channel thalweg. However, the spatio-temporal changes in deposit geometry and type in submarine canyons are more complex. Submarine canyon axes are dominated by sediment bypass processes (*e.g.,* May and Warme, 2007; Di Celma, 2011; Janocko and Basilico, 2021; Bouwmeester *et al.,* 2024) and thus provide an incomplete record of SGF processes, and canyon-confined overbanks are highly dynamic environments, hosting complex topography and a range of flow types. Outcrop-scale studies of submarine canyon typically focus on canyon axes to determine SGF processes and complex flow-topography interactions. However, the lack of three-dimensional constraints make developing process-based models of submarine canyon fills through time and exporting the models to other submarine canyons challenging.

Resolving the spatio-temporal gaps in how topography is created and removed in deep-water systems, especially in submarine canyons, and the effects this has on SGF behaviour and routeing is crucial for palaeogeographic reconstructions and calculating sediment, organic matter, and micropollutant fluxes to the deep-sea.

1.3 What role do submarine canyons play in the source-to-sink pathways of microplastics?

Rationale: Submarine canyons are the most proximal parts of deep-water sedimentary systems, playing a vital role in the transfer of particulate matter sourced from terrestrial and shallow marine environments to the deep-sea (Daly, 1936). Despite there being more than 9000 mapped submarine canyons globally (Harris and Whiteway, 2011) and their crucial role in source-to-sink pathways of sediment (Nyberg *et al.,* 2018), little is known about microplastic transport and burial processes in submarine canyons, and the processes that control microplastic fluxes to the deep-sea.

Submarine canyons are largely considered as net-erosional features, with SGFs acting to bypass particulate matter from shallow marine environments to the deep-sea (Amblas *et al.,* 2022). The signal of other hydrodynamic processes (*e.g.,* internal tidal currents) is often superimposed on SGF behaviour in submarine canyons (Hall *et al.,* 2017; Maier *et al.,* 2019; Normandeau *et al.,* 2024; Soutter *et al.,* 2024), and due to the enhanced biodiversity often

observed close to submarine canyons, they are also subject to intense anthropogenic activity (*e.g.,* benthic trawling) (Paradis *et al.*, 2017; Daly *et al.*, 2018).

Turbidity currents are responsible for generating Earth's largest sediment accumulations (Curray and Moore, 1971; Emmel and Curray, 1983) and are hypothesised to play a crucial role in the transfer and burial of microplastics on the deep seafloor (Kane and Clare, 2019; Pohl *et al.,* 2020; Zhang *et al.*, 2024); the deep seafloor is considered as the ultimate sink to microplastic pollution (Eriksen *et al.*, 2014; Woodall *et al.*, 2014; Jambeck *et al.*, 2015; van Sebille *et al.*, 2015). However, more recently, the potential for submarine canyons to be permanent and/or transient sinks to sediment (Fildani, 2017), and therefore microplastic repositories, has also been explored. Transport of sediment, organic carbon, and pollutants has been documented in submarine canyons (*e.g.,* Normark, 1970; Paull *et al.*, 2002; Zhong and Peng, 2021; Pierdomenico *et al.*, 2023; Talling *et al.*, 2023). However, the processes that govern microplastic transport via turbidity currents have only been documented experimentally (Pohl *et al.*, 2020), and there is no record of how submarine canyon topography influences SGF behaviour with respect to microplastic transport and burial, and how processes in the shallow subsurface in submarine canyons act to bury microplastics in surficial sediments.

The size, shape, and density characteristics of microplastics bear similarities and differences to natural sediment grains and they are hypothesised to be subject to the same sedimentary processes that act to control sediment transport and burial, including vertical settling, bedload transport, and notably transport and burial via turbidity currents (Waldschläger *et al.*, 2022 and references therein). Microplastic pollution is pervasive throughout Earth's oceans (Taylor *et al.*, 2016), however it has been shown that there is no direct link that exists between microplastic concentration in deep-sea sediments and distance from microplastic source (*e.g.,* Woodall *et al.*, 2014; Kane *et al.*, 2020). This suggests that other processes in the deep sea control the source-to-sink pathways of microplastics, as is observed by deep thermohaline currents in the Tyrrhenian Sea (Kane *et al.*, 2020). Currently, little is known about how processes in the shallow subsurface effect microplastic burial rates, and an outstanding question remains; How are microplastics incorporated into sediment that pre-dates the mass-production of plastic in the 1950's (*e.g.,* Dimante-Deimantovica *et al.*, 2024)?

Turbidity currents in submarine canyons have been documented to be efficient conveyors of particulate matter to the deep-sea. Yet, it has also been recognised that submarine canyons also have the potential to be transient sinks (Fildani, 2017), both by sequestering particulate matter

up-dip of landslide dams and reducing down-canyon fluxes (*e.g.,* Pope *et al.,* 2022), and in storing particulate matter prior to canyon-flushing events (*e.g.,* Canals *et al.,* 2006). The tectonic margin type of a submarine canyon needs to be considered when assessing their role in source-to-sink pathways as this can lead to buffered particulate matter supply (Kane and Clare, 2019), as does the role of subsurface processes because this can lead to the shredding of the environmental signal of plastic pollution. Understanding microplastic delivery, transport, and burial processes is critical for assessing the routeing pathways of microplastics, calculating more accurate microplastic fluxes to the deep-sea and identifying ecosystems vulnerable to microplastic pollution.

1.4   Aims and objectives

This thesis aims to provide an insight into how seafloor topography controls the behaviour of gravity flows in deep-water systems, and the sedimentological and anthropogenic factors that control microplastic transfer in the deep-sea.

This thesis uses three distinct data acquisition methods to address the overarching aims. Investigations into deep-water sedimentary systems are based upon observations from an incomplete stratigraphic record of exhumed systems, relatively low-resolution seismic reflection data, physical models with challenges associated with scaling relationships, and sparse direct measurements from modern systems. Each of these methods has resolution gaps and a range of spatio-temporal scales. Linking the observations from these normally isolated methods has become more prevalent in recent times (Kneller, 1995; Amy *et al.,* 2004; Bakke *et al.,* 2013; Hage *et al.,* 2018; Soutter *et al.,* 2021a). This thesis seeks to synthesise the findings from an exhumed system, physical models, and a modern system, with the focus being centred on the role that seafloor topography and geomorphology impart on the delivery of particulate matter and depositional patterns of SGFs throughout deep-water sedimentary systems.

These aims will be addressed with the research questions outlined above, and with the following chapter-specific aims and objectives:

1.4.1   Chapter 3: Unconfined gravity current interactions with orthogonal topography: Implications for combined-flow processes and the depositional record

The aim of Chapter 3 is to document how independently changing the angle of a topographic slope positioned orthogonal to the incoming gravity current affects the flow processes at the base of, and on, the slope surface using scaled, unconfined saline density currents. The objectives are to:

i.   Assess how the angle of containing frontal topography affects density current evolution and the generation of combined flows.

ii.   Investigate how the mechanisms of flow reflection, deflection and divergence, operate on the slope surface and influence interactions with the incoming flows at the base of slope in unconfined settings.

iii.   Discuss the effects of combined flows on the deposit character and onlap geometry in deep-water systems.

Based on the results, a new sedimentological model is developed for the generation of combined flow in unconfined gravity currents, formed in the absence of an oscillatory flow component invoked by the generation of internal waves, and instead by the superimposition of reflected, deflected, and divergent flow components with the parental flow.

1.4.2   Chapter 4: Abrupt downstream changes in submarine canyon-margin architecture

The aim of Chapter 4 is to document the downstream heterogeneity in canyon-confined overbank deposits related to mass-wasting of a submarine canyon-margin from the Rosario Formation, Baja California, Mexico. The objectives of this study are to:

i.   Assess the stratigraphic evolution of canyon-confined overbank deposits with increasing lateral distance away from the canyon axis.

ii.   Use stratigraphic logging and high-resolution photogrammetric models to describe and compare the localised heterogeneity in facies and architecture at the canyon-margin between two principal outcrops located approximately 250 m apart.

iii.   Interpret and discuss the mechanisms for canyon wall failure and how flow-topography interactions varied through time.

This study provides insights into how the heterogeneity of canyon-confined overbank deposits, regarded as monotonous and predictable successions in channel-levee systems, increases locally following the interaction of SGFs with debrites emplaced in the overbank following mass-wasting of the canyon-margin.

1.4.3   Chapter 5: Pervasive microplastic pollution in a land-detached submarine canyon

The aim of Chapter 5 is to decipher the processes that control microplastic transport and burial in a land-detached submarine canyon, using sediment cores from two across-canyon transects of the Whittard Canyon, NE Atlantic. Here, microplastic and sediment grain-size analysis, and

sediment accumulation rates are integrated with high-resolution bathymetric mapping. The objectives of the study are to:

  i. Map the distribution of microplastic particles throughout two distinct reaches of the canyon and identify how microplastic concentrations vary with increasing sediment depth.
 ii. Detail the grain-size trends associated with the microplastic distribution and concentration and integrate the findings with the sediment accumulation rates recorded in the canyon.
iii. Interpret and discuss how microplastic transport and burial processes in the canyon, anthropogenic forcing on the continental shelf, and submarine canyon topography control the transfer of microplastics to the deep-sea.

This study presents a new model that documents how sedimentological processes and anthropogenic forcing control the delivery, transfer and burial of microplastics in surficial sediments in submarine canyons and shred the signal of historical plastic production in the subsurface.

Chapter 2   Background and literature review

This literature review chapter has four parts:

i.   An introduction to sediment gravity flow processes and deposits, with a particular focus on turbidity currents (**Section 2.1**).

ii.   A review of the influence of seafloor topography on sediment gravity behaviour, with a particular focus on previous physical modelling attempts **(Section 2.2)**.

iii.   An overview of submarine canyons, including the modern and ancient record, and their importance in deep-water sedimentary systems **(Section 2.3)**.

iv.   A review of the role the deep-sea plays in the source-to-sink pathways of microplastics **(Section 2.4)**.

2.1   Sediment gravity flows

Sediment gravity flows (SGFs) are produced where gravity acts upon the density contrast between a sediment-laden fluid and the ambient fluid, thus driving the flow downslope and transporting sediment to deep-water (below storm wave-base) (Middleton and Hampton, 1973; Lowe, 1982; Kneller and Buckee, 2000). A range of SGF types have been identified and differentiated based on their particle support mechanisms (*i.e.,* controlled by a combination of matrix strength, buoyancy, pore pressure, grain-to-grain interactions, turbulence, and bed support) (Mulder and Alexander, 2001). Two end-member flow types are commonly differentiated: turbulent (Kuenen and Migliorini, 1950; Bouma, 1962; Kneller and Branney, 1995; Kneller and McCaffrey, 1999; Eggenhuisen *et al.,* 2017) or laminar (Hampton, 1972; Sohn, 2000; Baas *et al.,* 2009), with transitional flows (Baas and Best, 2002; Baas *et al.,* 2009; Sumner *et al.,* 2009) sitting within the continuum (Fig. 2.1).

Figure 2.1: Variation in sediment gravity flow type, structure, velocity and resultant deposit. Modified from Haughton *et al.* (2009).

2.1.1 Turbidity currents

2.1.1.1   Flow Processes

In sub-aqueous SGFs, where mixtures of sediment and other particulate matter are maintained in suspension by turbulence, they are named turbidity currents. The turbulence is generated at the base of the flow, in the lower 'wall-region' by bottom shear, and in the upper 'jet-region' in the free shear zone where ambient water is entrained (Altinakar *et al.,* 1996).

Turbidity currents have a general structure comprising a head, body and tail (Fig. 2.2). The head interacts with and entrains the ambient fluid, and as a result the mean velocity and sediment concentration is highest in the body, and decreases towards the tail (Middleton, 1967; Kneller and Buckee, 2000). More recent observations of natural turbidity currents document how the head may in some cases be the fastest part of the flow, shown by a high-concentration, fore-running basal flow cell (Azpiroz-Zabala *et al.,* 2017); hence the structure of turbidity currents

remains an active research theme (Luchi *et al.,* 2018; Paull *et al.,* 2018; Pohl *et al.,* 2019; Hereema *et al.*, 2020).
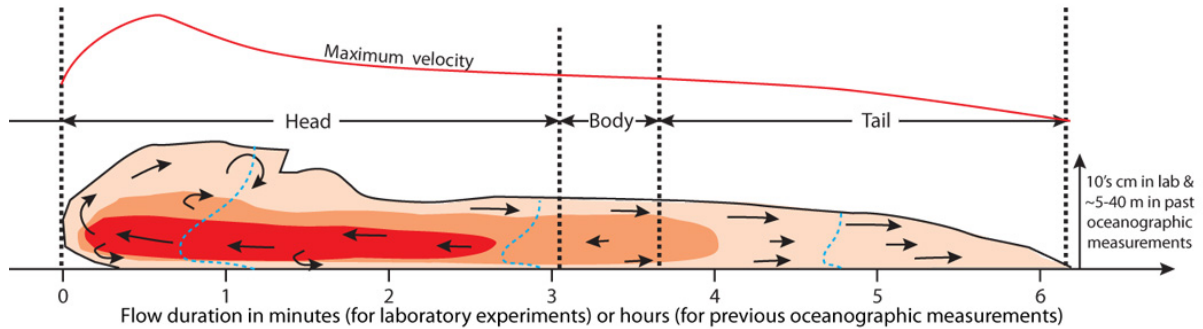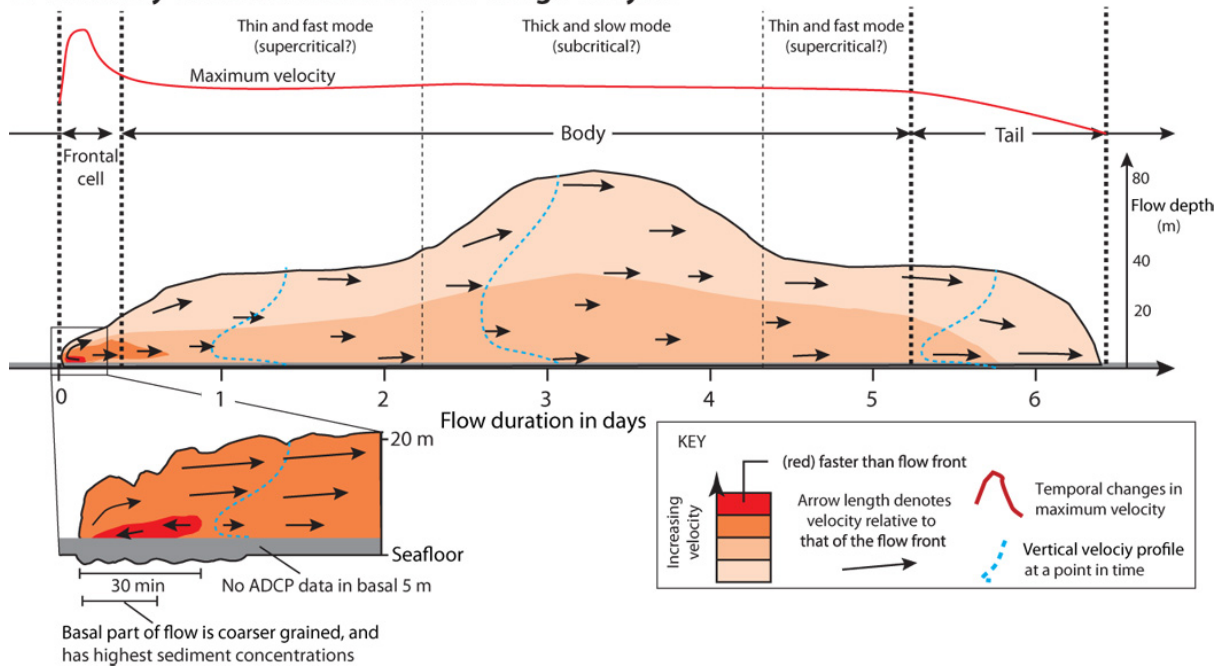
Figure 2.2: Turbidity current structure. (A) laboratory experiments of a surge-like turbidity current, (B) Sustained turbidity current directly-monitored in the Congo Canyon. From Azpiroz-Zabala *et al.*, 2017.

Turbidity currents can be categorised as either low-density or high-density based on their sediment concentration. Low-density turbidity currents have lower sediment concentrations (<<10% sediment volume) and are entirely supported by fluid turbulence throughout the entire flow height (Mulder and Alexander, 2001). Sediment transport in low-density turbidity currents occurs as long as the fully turbulent flow has the ability to move sediment particles of a particular terminal settling velocity in suspension (*i.e.*, flow competence) (Kneller and McCaffrey, 1999), or

else deposition will occur. In contrast, high-density turbidity currents have higher sediment concentrations (>~10% sediment volume), which suppresses near-bed turbulence, thus the dense, lower-layer is supported by a combination of fluid turbulence, sediment grain-to-grain interaction, hindered settling, and the development of excess pore pressure (Kuenen and Migliorini, 1950; Lowe, 1982; Mulder and Alexander, 2001; Talling *et al.,* 2012). Deposition in high-density turbidity currents can occur regardless of the flow's competence and occurs if the amount of turbulence is not enough to keep all the sediment in suspension (*i.e.*, exceeding the flow's capacity, thus rapidly depositing the entire grain-size range (Hiscott, 1994).

During the passage of turbidity current over a fixed point, velocity variations are common and result in the turbidity currents being termed 'unsteady' and 'non-uniform' with respect to time and space (Kneller, 1995). Such changes in turbidity current behaviour can be transient (seconds to minutes) and are known as surges, whereas where the flow velocity remains constant over hours to days, they are termed quasi-steady or sustained (Hughes Clarke*,* 1990; Kneller, 1995; Kneller and Branney, 1995). Turbidity currents will continue downslope until they either 'subside', due to the reduction in the density contrast between the flow and ambient fluid through ambient fluid entrainment and/or deposition (Parker *et al.,* 1986; Middleton, 1993; Talling *et al.,* 2012), or 'ignite' through erosion and incorporation of sediment as they flow, thus allowing them to maintain their excess density contrast and run-out further downslope (Parker *et al.,* 1986; Middleton, 1993; Hereema *et al.,* 2020).

2.1.1.2   *Deposits*

The deposits from low-density turbidity currents are termed low-density turbidites (LDTs) (Mulder and Alexander, 2001; Baas *et al.,* 2011). Vertical density stratification occurs in low-density turbidity currents due to the preferential settling of larger grains, with coarser grains at the base and finer-grains distributed more homogeneously throughout the height of the flow (*e.g.,* García, 1994; Baas *et al.,* 2005; Tilston *et al.,* 2015). As the flow wanes and shear velocities decrease, this results in layer-by-layer deposition, with progressively finer grains being deposited (Kneller and Branney, 1995) and forming a LDT ('Bouma Tb-e' of Fig. 2.3B). LDTs are typically thin (<40 cm) (Talling, 2001) and are often characterised by tractional structures including ripples (Baas *et al.,* 2011). LDTs have been observed in distal and margin environments, hypothesised to represent flows becoming more dilute due to ambient water entrainment and loss of sediment downslope or away from axial environments (*e.g.,* Walker, 1967; Mutti, 1977; Boulesteix *et al.,* 2019). LDTs are also associated with channelised environments, forming levees

where the upper dilute parts of a flow overspill or are stripped from the confining channel (Mutti, 1977; Normark *et al.*, 1983; Pirmez and Imran, 2003; Kane and Hodgson, 2011).

The deposits from high-density turbidity currents are termed high-density turbidites (HDTs) (Fig. 2.3B). Deposition through a loss of flow capacity causes the suppression of near-bed turbulence and consequently prevents the formation of tractional bedforms (Baas *et al.*, 2011). Instead, deposits with poorly-defined boundaries and that often contain truncated fluid-escape structures are common (Kneller and Branney, 1995). Such structures are indicative of pore water escape from a loosely packed and rapidly aggrading bed sheared by an over-riding flow (*e.g.*, Lowe, 1982; Kneller and Branney, 1995). HDTs are often relatively thick, poorly-sorted, ungraded and structureless (Middleton and Hampton, 1973), making them difficult to distinguish from sand-rich debrites (*e.g.*, Shanmugam, 1996; Amy *et al.*, 2005). However, 'traction carpets' (*e.g.*, Dzulynski and Sanders, 1962), spaced-stratification (*e.g.*, Hiscott and Middleton, 1980), and internal erosion surfaces and scour fills (*e.g.*, Lowe, 1982) have all been observed in HDTs. HDTs have been observed in proximal areas and at points of rapid flow deceleration, where high-energy and high-concentration flows are common; characteristic of channel axes (*e.g.*, Jobe *et al.*, 2017), lobe axes (Hodgson *et al.*, 2006), and channel mouth transition zones (*e.g.*, Hodgson *et al.*, 2022).
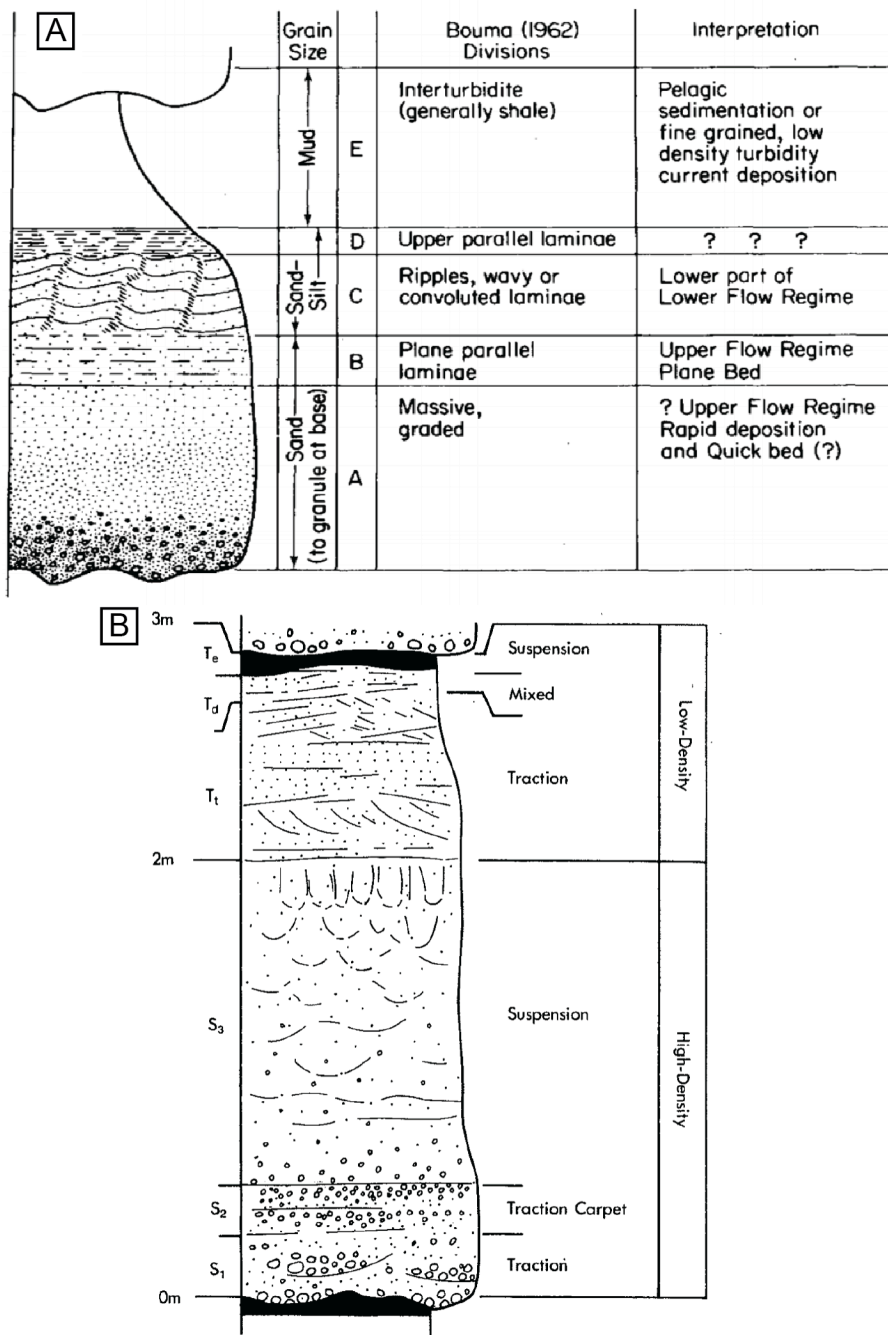
Figure 2.3: (A) The Bouma sequence (Bouma, 1962) – the first idealised model for deposition from a waning turbidity current. From Middleton and Hampton (1973). (B) The model from Lowe (1982) for deposition from a turbidity current.

2.1.2 Laminar flows

Laminar flows, such as debris flows are those in which turbulence is suppressed and sediment is supported instead by a matrix of high yield-strength fluid and fine sediment (*i.e.,* mud) (Middleton and Hampton, 1973; Baas *et al.,* 2009), and due to the high density of the flow, by grain-to-grain interactions and hindered settling (Sumner *et al.,* 2009). Laminar flow conditions typically occur when electrostatic bonds between clay minerals cause the suppression of turbulence, resulting in a non-Newtonian flow rheology (Wang and Larsen, 1994). In cohesionless flows (*i.e.,* mud poor) laminar flow conditions may arise if the sediment concentration is sufficient for grains to interlock and generate frictional strength (Amy *et al.,* 2005). The *en masse* deposition from laminar flows (*i.e.,* the flow 'freezes' as it decelerates) occurs as the shear stress, or 'driving gravity stress' (Middleton and Hampton, 1973) applied to the flow fails to overcome the yield or frictional strength of the flow (Lowe, 1982; Postma, 1986, Amy *et al.,* 2005). The dilution of debris flows can transform them into turbidity currents (Hampton, 1972; Ribo *et al.,* 2024) and *vice versa* (Haughton *et al.,* 2003; Talling *et al.,* 2004; Hodgson *et al.,* 2009; Fonnesu *et al.,* 2018).

The deposits of laminar or debris flows (*e.g.,* debrites) (Fig. 2.1) are typically ungraded and very poorly sorted, often with irregular erosional bases (Talling *et al.,* 2012). Debrite thickness and clast size is highly variable, with clast sizes ranging from sand-grade clasts (*e.g.,* Talling *et al.,* 2012) to km-scale mega clasts (*e.g.,* Hodgson *et al.,* 2019), and is dependent on the yield strength of the parental debris flow. Features, including folding (*e.g.,* Sobiesiak *et al.,* 2016) and faulting (*e.g.,* Bull *et al.,* 2009) are also common in debrites and linked to the deformation of the cohesive flow during transit (*e.g.,* Jackson, 2011).

2.1.3 Transitional flows

Transitional flows sit in the continuum between fully turbulent and laminar flows, defined as flows with transient turbulent behaviour (Wang and Plate, 1996; Baas and Best, 2002; Kane and Ponten, 2012) and are attributed to the presence of fine sediment (*i.e.,* clay- and silt-sized particles in the flow. Transitional flow rheology typically arises when a fully turbulent flow increases its relative concentration of mud as it flows down-dip, either by the erosion and entrainment of mud and/or the deposition of coarser sediment up-dip (Marr *et al.,* 2001; Haughton *et al.,* 2003). Baas *et al.* (2009) subdivided transitional flows into four categories: (i) turbulence enhanced transitional flow (TETF), (ii) lower transitional plug flow (LTPF), (iii) upper transitional plug flow (UTPF), and (iv) quasi-laminar plug flow (QLPF); based on a flow velocity *versus* mud concentration phase diagram (Fig. 2.4).
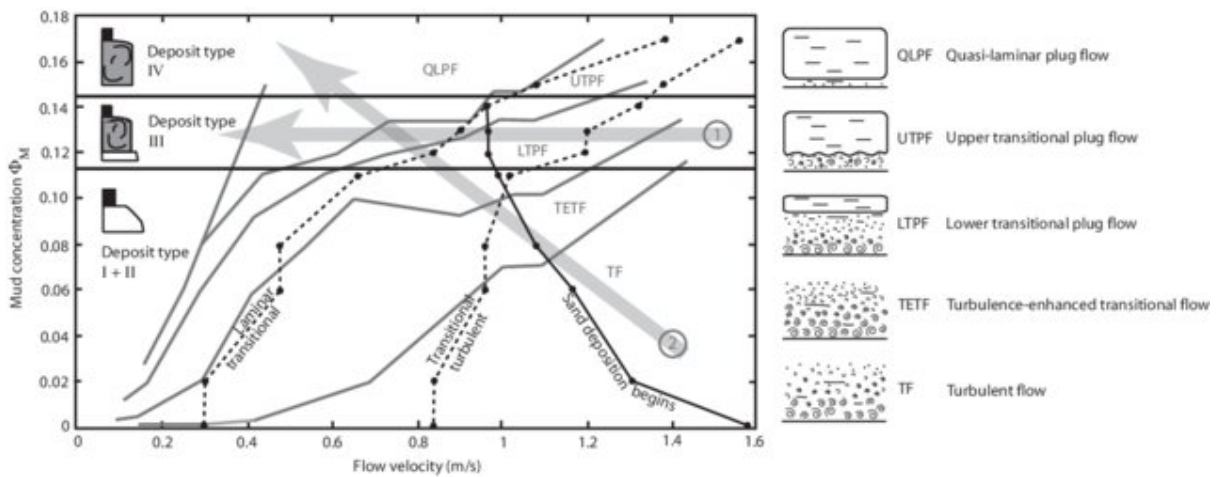
Figure 2.4: Experimental relationship between flow velocity, flow structure, and mud concentration, and the resultant deposit. The arrows show trajectory of flows that would deposit a linked turbidite-debrite. From Baas *et al.* (2009) and Sumner *et al.* (2009).

The deposits from transitional flows may record the longitudinal evolution of decreasing sand content and /or increasing mud content, often in the form of a clean basal sand overlain by an increasingly thick mud-rich, debritic layer. This was explored in detail by Haughton *et al.* (2003), naming the deposits 'hybrid event beds' (HEBs). Alternatively, HEBs may record a vertical segregation of the flow at-a-point (*e.g.*, Baas *et al.*, 2011), or a combination of vertical segregation of suspended load, and longitudinal segregation of bedload (Baas *et al.*, 2021b). The complex balance between cohesive and turbulent forces, and the type/concentration of mud can be observed at the bedform-scale, producing a suite of distinct and predictable bedform sequence that point to the evidence of transitional flows in the absence of HEBs (Baas *et al.,* 2016; Baker *et al.,* 2017; Baker and Baas, 2020; Taylor *et al.,* 2024a).

2.1.4 Mass-transport

Large-scale slope failures can generate large masses of lithified and unlithified sediment within deep-water sedimentary systems (Hampton *et al.,* 1996; Moscardelli and Wood, 2008). The deposits from such events are generally termed submarine landslides or mass-transport deposits (MTDs). Depending on the source sediment and degree of disaggregation, MTDs can either be termed debrites, slides or slumps (Nardin *et al.,* 1979). MTDs generate major seafloor topography, which can affect sediment routeing pathways and the rheological properties of the parental flow (Kneller *et al.,* 2016; Martínez-Doñate *et al.,* 2021; Valdez Buso *et al.,* 2024) (Fig. 2.5). The identification of individual MTDs is generally not possible in geophysical and subsurface

data, thus mass transport complexes (MTCs) is used as a term to describe the deposits of numerous mass-wasting events (Pickering and Corregidor, 2005; Moscardelli and Wood, 2008).
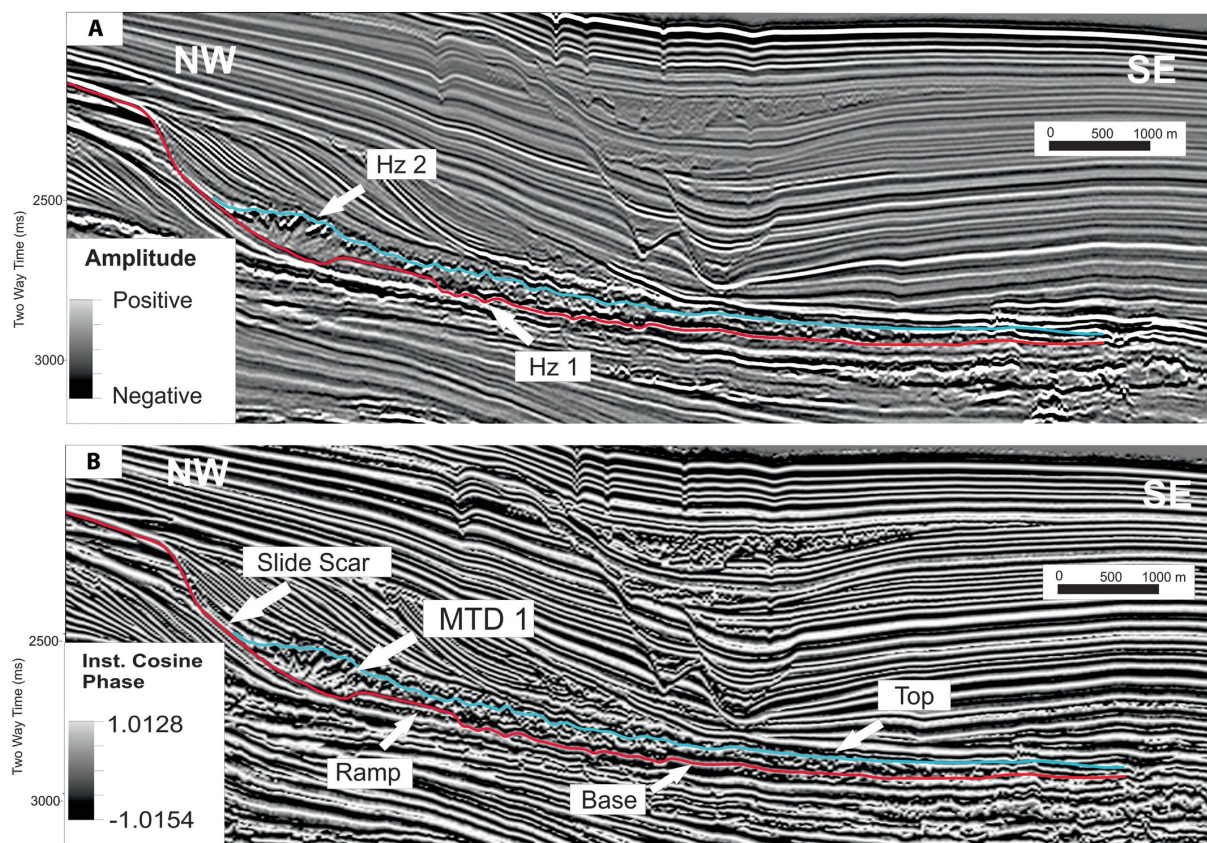
Figure 2.5: Seismic image of mass-transport deposit. (A) In-line showing the mapped horizons. (B) Interpreted surfaces and MTD characteristics using Instant Cosine Phase attribute. From Valdez Buso *et al.* (2024).

2.2   The influence of topography on deep-water sedimentary systems

2.2.1   The effects of topography on sediment gravity flow behaviour

Sediment gravity flows are the primary agents of particulate matter transport from the continents to the deep-sea. Any changes to the character of the slope, commonly following the interaction of SGFs with seafloor topography, act to dictate the velocity and direction of these flows, often reflecting, deflecting, constricting, or ponding SGFs (*e.g.,* Kneller *et al.,* 1991; Edwards *et al.,* 1994; Patacci *et al.,* 2015; Tinterri *et al.,* 2016; 2022; Dorrell *et al.,* 2018a; Soutter *et al.,* 2021a), and thus altering the erosional and depositional character of SGFs. Well-documented phenomena related to SGF interactions with seafloor topography include: the generation of subcritical bores upon incidence of supercritical flows with topography (Edwards *et al.,* 1994), the suppression of

turbulent forces and promotion of laminar forces during flow deceleration and the entrainment of mud (Barker *et al.*, 2008; Sumner *et al.*, 2009; Patacci *et al.*, 2014; Southern *et al.*, 2017; Bell *et al.*, 2018; Taylor *et al.*, 2024a), and flow stripping that leads to different sediment concentrations and thicknesses of the decoupled flow (Piper and Normark, 1983; Fildani *et al.*, 2006; Soutter *et al.*, 2021a). Seafloor topography exerts a first-order control on SGF behaviour and may be generated by high-relief fault scarps and folds (*e.g.,* Haughton, 2000; Hodgson and Haughton, 2004; Cullen *et al.*, 2020), at the trailing edges, and atop, mass-transport deposits (*e.g.,* Armitage *et al.*, 2009; Martínez-Doñate *et al.*, 2021; Allen *et al.*, 2022), seamounts (*e.g.,* Seabrook *et al.*, 2023), and salt and mud diapirism (*e.g.,* Kneller and McCaffrey, 1995; Toniolo *et al.*, 2006; Cumberpatch *et al.*, 2021; Howlett *et al.*, 2021).

Changes to a SGF's competence or capacity upon incidence with seafloor topography will alter the loci and character of the deposits (Allen, 1991; Hiscott, 1994; Kneller and McCaffrey, 1995; 1999). Using the deposit characteristics from SGFs can help to indicate both the degree of basin confinement (*i.e.,* confined or unconfined) (Fig. 2.6), and the gradient, orientation, and rugosity of more localised seafloor topography. In this thesis the definition of an unconfined flow (as used in Chapter 3) follows that of Tőkés and Patacci (2018) (Fig. 2.6D), in which the flow volume is markedly smaller than the basin capacity, and in the case of Chapter 3 the flow interacts with high-relief intrabasinal topography that acts to partially contain the flow. This definition is different to that used by Southern *et al.* (2015) who would define such a configuration as confined and uncontained. Figure 2.6E has been adapted from Tőkés and Patacci (2018) to include the topographic configuration used in Chapter 3.
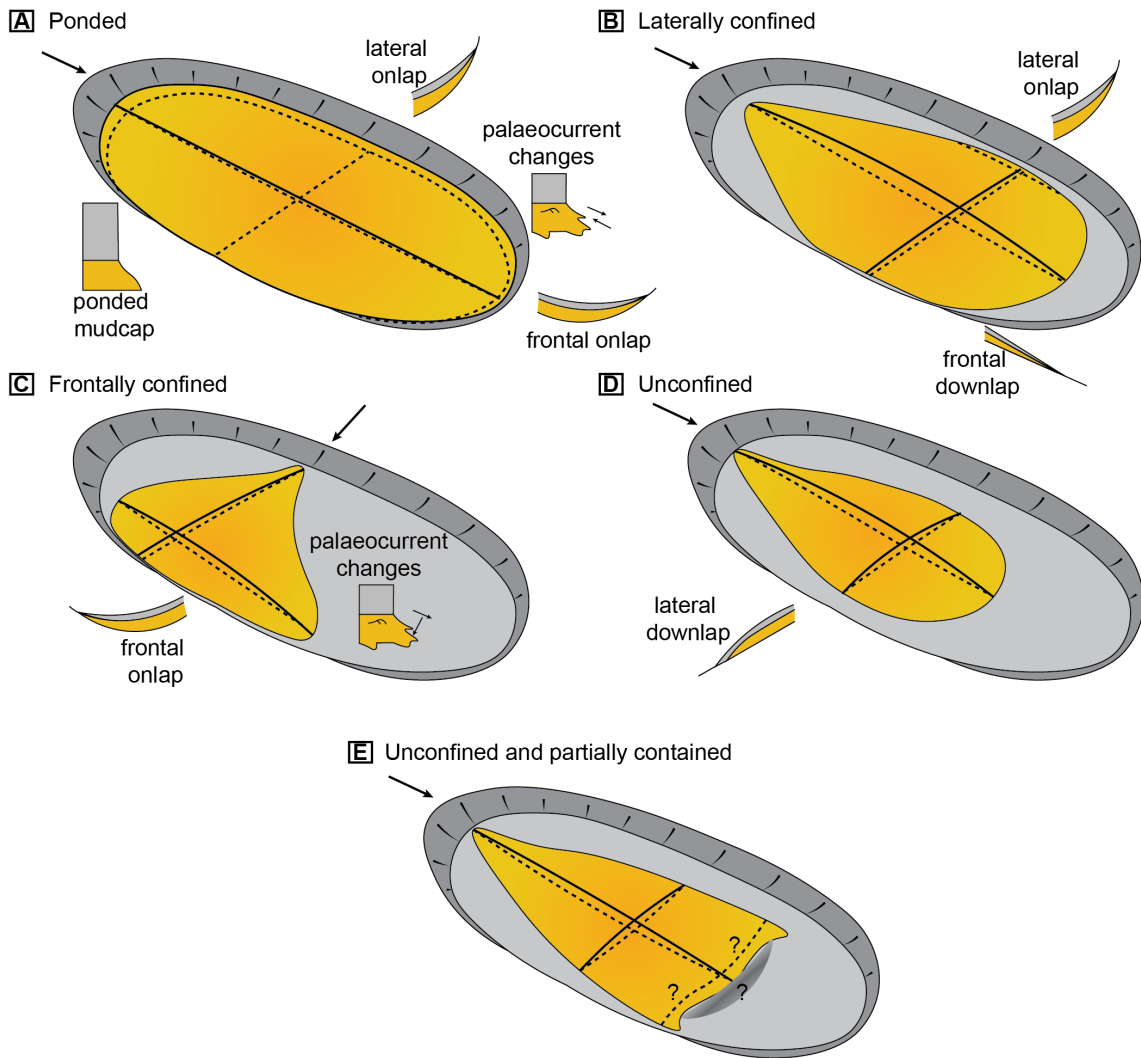
Figure 2.6: Different types of flow confinement following the definition of Tőkés and Patacci (2018) (A) Ponded. Following the definition of Southern *et al.* (2015) such a configuration would be defined as confined and contained. (B) Laterally confined. (C) Frontally confined. (D) Unconfined. Following the definition of Southern *et al.* (2015) such a configuration would be defined as unconfined and uncontained. (E) The flow confinement and topographic containment style used in Chapter 3. The question marks indicate that uncertainty in onlap patterns and facies styles related to unconfined gravity currents interacting with partially containing topography. Adapted from Tőkés and Patacci (2018).

A wide range of facies types and complex palaeocurrent records have suggested the interaction of SGFs with topography, however the incompleteness of the stratigraphic record, coupled with low-resolution seismic reflection data makes understanding process-product

models and exporting observations to the basin-scale level challenging. Thus, physical models aim to bridge this resolution gap.

2.2.2 Previous experimental models

Evidence of flow interactions with topography has been observed from bathymetric surveys of the Baja California Seamount Province (*e.g.,* Menard, 1957), and of flow reflections from turbidite successions in the Cloridorme Formation, Canada (*e.g.,* Pickering and Hiscott, 1985), the Contessa Bed of the Marnoso Arencea (*e.g.,* Ricci Lucchi and Valmori, 1980), and the ponded sediments of the Mid Atlantic Ridge (*e.g.,* van Andel and Komar, 1969). The paradigm holds that flow reversals are caused by reflections of the primary flow against seafloor topography, rather than an independent current sourced from the opposite direction. Trying to understand the mechanics of flow interactions with topography on the effects on turbidity current evolution, and the resulting deposits has been the focus of many, previous physical experiments (*e.g.,* Pantin and Leeder, 1987; Kneller *et al.*, 1991; Edwards *et al.*, 1994; Kneller, 1995; Kneller and McCaffrey, 1995; Kneller *et al.*, 1997; Amy *et al.*, 2004; Brunt *et al.*, 2004; Patacci *et al.*, 2015; Soutter *et al.*, 2021a). The flume tank dimensions, style of topography, flow density and focus of the previous physical experiments and of the flume tank used in Chapter 4 are documented in Figure 2.7.

The earliest works focusing on flow reversals in gravity currents were centred around the generation of hydraulic bores, here also encompassing the terms solitons and solitary waves (*e.g.,* Pantin and Leeder, 1987; Kneller *et al.*, 1991; Edwards *et al.*, 1994). Upon incidence of the primary flow with an orthogonal slope (*e.g.,* Pantin and Leeder, 1987; Edwards *et al.*, 1994) and a nominally oblique slope (*e.g.,* Kneller *et al.*, 1991), the generation of hydraulic bores was described semi-quantitatively using time-lapse photography, and in the case of Edwards *et al.* (1994) with additional particle tracking. In addition to the solitons and solitary waves (Type A bores of Edwards *et al.* (1994)) described by Pantin and Leeder (1987) and Kneller *et al.* (1991), respectively, Edwards *et al.* (1994) describe two other hydraulic bore types: Type C) a bore that resembles the appearance of the primary flow, and Type B) a bore with a profile in the continuum of solitons and Type C bores. The experiments discussed above were performed in either experimental basins with narrow, elongate (*i.e.,* two-dimensional) planforms or small three-dimensional planforms, meaning the flows had the inability to truly expand radially, and in each scenario the reflection of the primary flow was perpendicular to the strike of the topographic surface. These models have since been exported to help explain turbidite facies variations in a host of deep-water sedimentary systems (*see* Section 2.2.3). Whether these models for flow reversal/reflection hold in unconfined settings, as defined by Figure 2.6, is explored in Chapter 3.
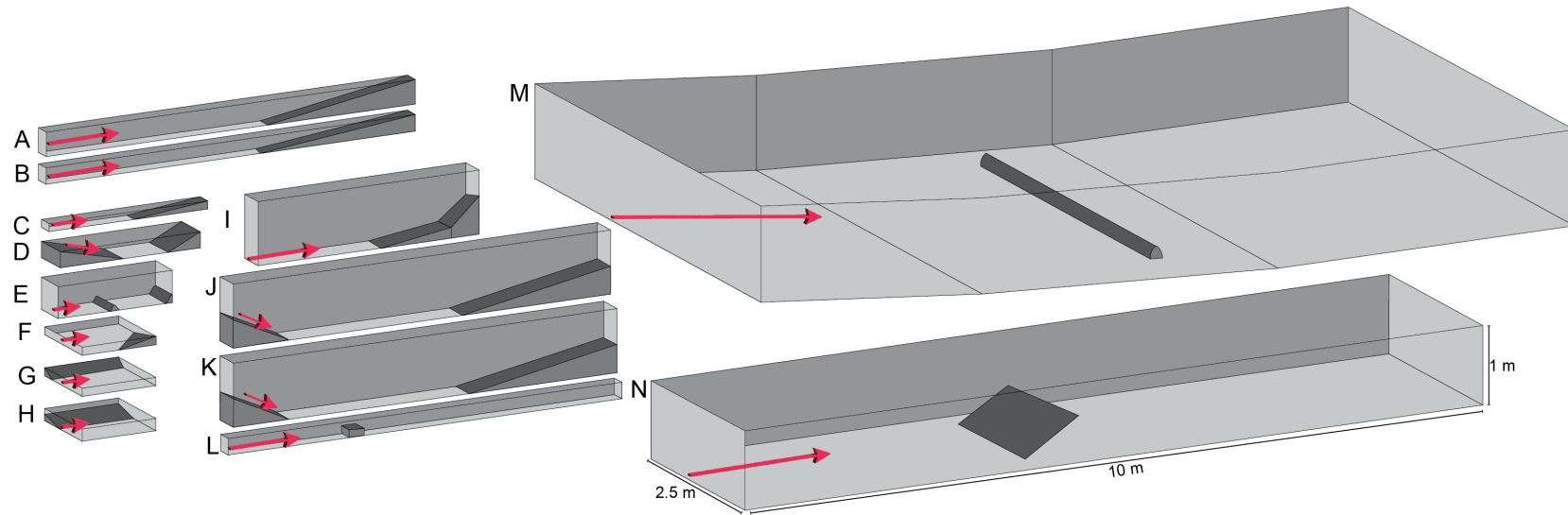
Figure 2.7: Scaled diagrams of flume tanks previously used in physical models that document the interaction of gravity flows with topography. For comparative reasons the flume tank documented in Chapter 3 is also included. Table 2.1 includes the additional information related to each flume tank experiment. (A) Pantin and Leeder (1987), (B) Edwards *et al.* (1994), (C) Kneller *et al.* (1997), (D) Muck and Underwood (1990), (E) Brunt *et al.* (2004), (F) Kneller *et al.* (1991), (G) Kneller (1995), (H) Amy *et al.* (2004), (I-K) Patacci *et al.* (2015), (L) Stevenson and Peakall (2010), (M) Soutter *et al.* (2021a), and (N) Chapter 3, Keavney *et al.* (2024). The red arrow is the direction of the primary flow.

Table 2.1: Associated table for Figure 2.7 documenting the dimensions, orientation of the topography relative to the direction of the incoming parental flow (Or is orthogonal, Ob is oblique, and Pa is parallel), the slope angle, the dense medium (whether it is a saline or sediment flow) and the density or excess density (E.D.) of the flow, and the focus of the study. Chapter 3 of this thesis (Keavney *et al.*, 2024) also recorded the density of the gravity current 3 m downstream of the inlet channel. The measured density was 1002.6 kg m^{-3} following the entrainment of water and subsequent mixing.

Diagram	Authors	Dimensions	Orientation	Slope angle	Dense medium	Focus of study
		[l x w x d] (m)		(°)	(density, kg m^{-3})	
A	Pantin and Leeder (1987)	5, 0.20, 0.30	Or	7-10	Saline (11.7, 30.0, 31.0 E.D.)	Internal soliton generation
B	Edwards et al (1994)	5, 0.20, 0.20	Or	5-10 and 15-20	Saline (1012-1178)	Hydraulic bore generation
C	Kneller *et al.* (1997)	2.15, 0.20, 0.10	Or	15	Saline (1064)	Internal solitary wave behaviour
D	Muck and Underwood (1990)	1.9, 0.50, 0.20	Or	28	Saline (N/A)	Flow behaviour upslope
E	Brunt *et al.* (2004)	1.55, 0.45, 0.40	Or	N/A	Sediment (1050)	Fill-and-spill models
F	Kneller *et al.* (1991)	1, 1, 0.1	Ob	20	Saline (178 E.D.)	Solitary wave generation
G	Kneller (1995)	1, 1, 0.1	Pa	30	Saline (1030)	Solitary wave generation
H	Amy *et al.* (2004)	1, 1, 0.15	Pa	10	Sediment (1080)	Deposit geometry
I	Patacci *et al.* (2015)	3, 0.35, 0.80	Or	6	Sediment (3% concentration)	Ponding processes
J	Patacci *et al.* (2015)	5.12, 0.35, 0.80	Or	10	Sediment (3% concentration)	Ponding processes
K	Patacci *et al.* (2015)	5.20, 0.35, 0.80	Or	15	Sediment (3% concentration)	Ponding processes
L	Stevenson and Peakall (2010)	5.34, 0.20, 0.20	Or	N/A	Sediment (1% E.D.)	Lofting processes
M	Soutter *et al.* (2021a)	11, 6, 1.20	Or, Ob, Pa	25 +- 5	Sediment (1290)	Deposit geometry
N	Chapter 3	10, 2.5, 1	Or	20, 30, 40	Saline (1025)	Flow processes on slope

The record of physically modelling the interaction of more unconfined SGFs with seafloor topography is limited (*e.g.,* Soutter *et al.,* 2021a), owing to the rarity of 3D flume tanks. Thus, numerical modelling has been utilised to help bridge the knowledge gap (*e.g.,* Howlett *et al.,* 2019). In Howlett *et al.* (2019) and Soutter *et al.* (2021a) the incoming flows were able to surmount the topographic slope. Soutter *et al.* (2021a) explored using sediment-laden gravity currents (17% by volume concentration) in a 3D flume tank, the patterns of erosion and deposition around an erodible topographic slope in a horizontal basin, downstream of an experimental platform with an 11° slope (Fig. 2.8). The topographic slope was systematically positioned orthogonal, oblique, and parallel to the incoming flow. When compared to the unconfined reference experiment, the aspect ratio of the deposit increases in the case of interactions with a parallel slope and on the upstream side of the oblique topography, attributed to enhanced sediment bypass at the upstream edge of the slope. In both the oblique and orthogonal settings, the incoming flow was able to surmount the topography, generating a deposit downstream of the slope. In the orthogonal case, the denser material onlapped against the slope, whereas the increased superelevation of the more dilute, upper region of the flow facilitated the fine-grained material to be bypassed downstream of the topography.
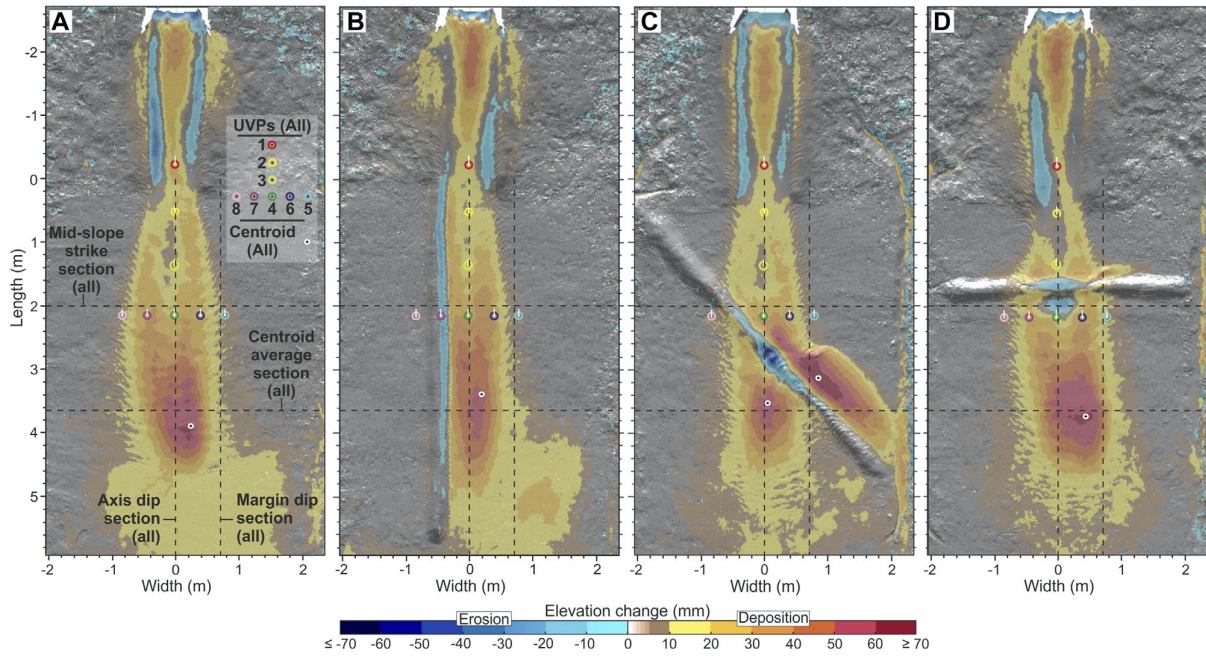
Figure 2.8: Difference maps for the experimental runs performed by Soutter *et al.* (2021a). The maps are constructed by subtracting the laser scan derived elevation of the pre-experiment tank surface from the post-experiment tank surface. (A) Unconfined, (B) laterally confined, (C) obliquely confined, and (D) frontally confined. Erosion is shown in blue and deposition is shown in yellow, orange and red. From Soutter *et al.* (2021a).

Soutter *et al.* (2021a) also explored how upstream and downstream hydraulic jumps, resulting from changes in the flow's criticality upon incidence with the topography, may be represented in the stratigraphic record. However, a critique of the experimental methods of Soutter *et al.* (2021a) brings these results into question. Here, Soutter *et al.* (2021a) calculate the densiometric Froude number by defining the flow height as the height of the flow at ½ of the U_{max} (maximum downstream velocity). The determination of U_{max} is likely to be over-estimated in this instance due to the assumption that the vertical velocity component of the gravity flow is zero, an artefact of having the Ultrasonic velocity profilers oriented 60° to the vertical. Vertical velocities can account for approximately 10% of the downstream velocity (Nomura *et al.*, 2019). Consequently, this leads to the under-estimation of flow height. Figure 2.7 shows that the flow height calculated as ½ the U_{max} is lower than the true height of the flow (*i.e.,* the height at which the flow reaches zero at the top of the flow). This is an artefact of the Ultrasonic Doppler velocity profilers not capturing the top of the flow. Combined, this would have the effect of reducing the densiometric Froude number and suggests that the flows may in fact be subcritical. This is further complicated by Soutter *et al.* (2021a) using the input density of the flow to calculate the reduced gravity of the flow, and therefore assuming no decrease in the density of the flow from the input

channel to the topographic barrier via the entrainment of ambient water into the gravity current. A decrease in the reduced gravity may yet make the flows supercritical.
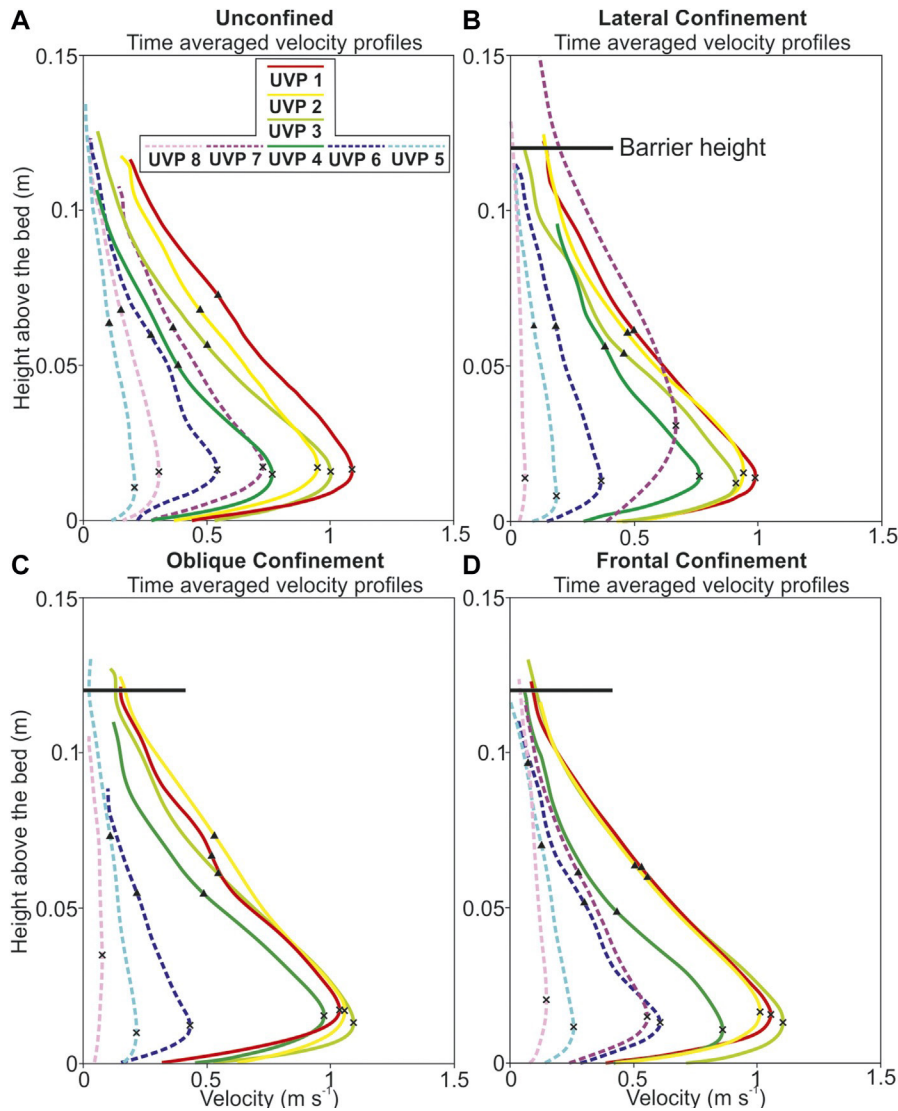
Figure 2.9: Time-averaged velocity profiles for the experimental runs performed by Soutter *et al.* (2021a). Dashed lines indicate velocity measurements taken laterally to the primary flow direction. (A) Unconfined, (B) laterally confined, (C) obliquely confined, and (D) frontally confined. The cross on the time-averaged velocity profiles is the U_{max}, and the triangle is the flow height. Modified from Soutter *et al.* (2021a).

There is an absence of physical experiments that capture unconfined gravity currents interacting with insurmountable topographic slopes. Bridging this knowledge gap will help to further develop bed-scale process-product models and the understanding of SGF dynamics following flow-topography interactions: both of which can be exported to aid interpretations of the stratigraphic record.

2.2.3 The stratigraphic record of flow-topography interactions

Evidence of flow reflection, deflection, and ponding following the interaction of SGFs with seafloor topography have all been identified in the stratigraphic record (*e.g.,* van Andel and Komar, 1969; Ricci Lucchi and Valmori, 1980; Pickering and Hiscott, 1985; Kneller, 1991) In the Marnoso Arencea Formation, Italy, following the interaction of SGFs with structural highs within the confined basin, flow reflection produces a range of distinct facies (Tinterri *et al.,* 2016, 2022). Of note is the formation of bedforms hypothesised to be formed under combined flow conditions. Combined flows are formed by the superimposition of unidirectional and multidirectional and/or oscillatory flow components, generating a high-degree of spatial and temporal flow variability. The original model for combined flows is based on observations from shallow-marine, shoreface environments and linked to the oscillatory motion of waves (*e.g.*, Clifton, 1976). In deep-water settings, the current model for the generation of combined flows is linked more to the interaction of a unidirectional SGF with topographic slopes and generation of internal waves with an oscillatory flow component (Tinterri *et al.,* 2016, 2022). In deep-water settings, the resulting bedforms include biconvex ripples, megaripples, and hummock-like features. Such bedforms have been documented in several other deep-water sedimentary systems (Fig. 2.10) (*e.g.,* Privat *et al.,* 2021, 2024; Tinterri *et al.,* 2022; Martínez-Doñate *et al.,* 2023; Siwek *et al.,* 2023; Taylor *et al.,* 2024a, 2024b). The generation of combined flows in the instance of Tinterri *et al.* (2016, 2022) is attributed to the superimposition of a unidirectional flow component with an oscillatory flow component following the reflection of the primary flow against topography and the generation of internal waves/hydraulic bores. This process-product model is proposed based on the observations made experimentally, primarily by Kneller *et al.* (1991), Edwards *et al.* (1994), and Patacci *et al.* (2015), and by the model of hummocky cross-stratification formation in shallow water systems (*e.g.,* Arnott and Southard, 1990; Duke *et al.,* 1991; Dumas and Arnott, 2006; Wu *et al.,* 2024).
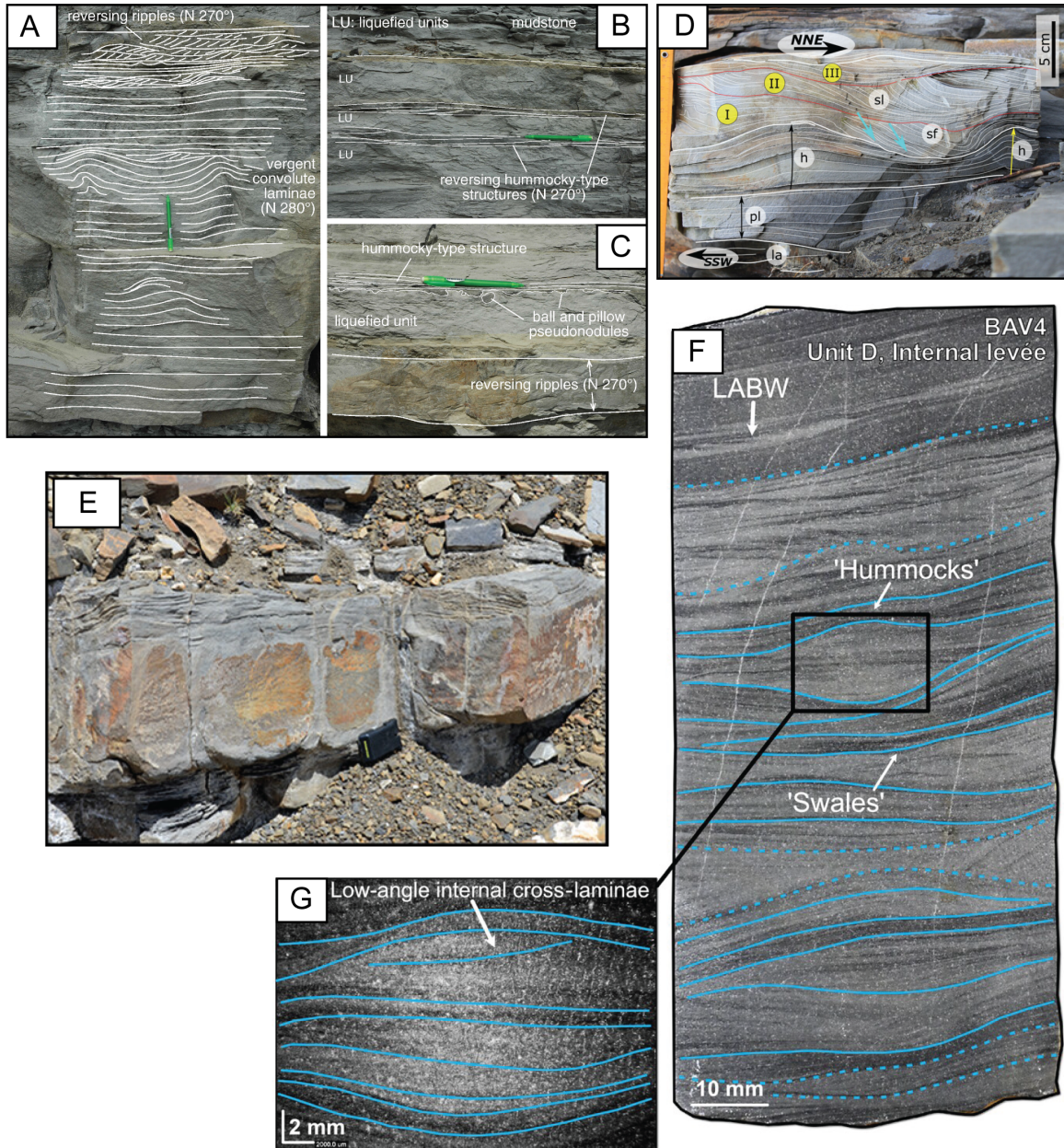
Figure 2.10: Photographs of hummock-like bedforms documented in deep-water sedimentary systems. (A), (B) and (C) Hummock-type structures in the contained reflected beds of the Marnoso Arenacea Formation, Italy [modified from Tinterri *et al.* (2016)]. (D) Quasi-symmetrical hummocks [h] in the ponded turbidite beds of the Fore Magura Unit, Polish Outer Carpathians [modified from Siwek *et al.* (2023)]. (E) Hummock-like bedforms in the Neuquén Basin, Argentina [modified from Martínez-Doñate *et al.* (2023)]. (F) and (G) Hummock-like bedforms from the Karoo Basin, South Africa [modified from Taylor *et al.* (2024a)]. The nomenclature for hummock-like bedforms adopted in photographs (A), (B), (C) and (D) is adopted from the respective studies.

Here, flow deflection is defined as the oblique change in direction of the primary flow upon incidence with topography. Whereas flow reflection/reversal is defined by a change in the obverse direction to the direction of the primary flow. The effect of flow deflection on SGF behaviour has also been observed in the stratigraphic record (Edwards *et al.*, 1994; Haughton, 1994; Kneller, 1995; Kneller and McCaffrey, 1999; McCaffrey and Kneller, 2001; Hodgson and Haughton, 2004; Puigdefàbregas *et al.*, 2004; Jobe *et al.*, 2017; Martinez-Doñate *et al.*, 2023). McCaffrey and Kneller (2001) determined that the confining slope in the Braux System, France, was oriented oblique to the direction of the incoming flow, insomuch that the complex palaeocurrent dispersal recorded by erosional and depositional structures track parallel to the base of the confining slope. The development of enhanced zones of sediment bypass related to the constriction and acceleration of SGFs upon incidence with oblique topography has also been observed in the stratigraphic record (*e.g.,* Kneller, 1995; Kneller and McCaffrey, 1999; Jobe *et al.,* 2017) and supported experimentally by Soutter *et al.* (2021a).

Ponded SGFs can also be termed 'confined and contained' SGFs (Fig. 2.6a) (Haughton, 1994; Patacci *et al.*, 2015; Southern *et al.*, 2015; Tinterri *et al.*, 2022). The generation of a flat-topped suspension cloud with internal circulation patterns and wavy internal interfaces was observed experimentally by Patacci *et al.*, (2015). Features of ponded SGF recorded in the stratigraphic record include: basal sandy turbidites with tractional and combined-flow bedforms representing flow-topography interactions being overlain by massive mudstones representing the collapse of a mud-rich suspension cloud (Muzzi Magalhaes and Tinterri, 2010; Tinterri *et al.*, 2022) and in the case of Haughton (1994) sandstone beds with tractional features being overlain by massive, dewatered sandstones following increased sediment fallout rates as the flow progressively became ponded.

2.2.4 Onlap patterns

The termination styles of SGF deposits can help elucidate the style of topographic confinement, magnitude of the parent SGF, and stability of the topographic slope. Onlap is defined by Mitchum (1977) as "a base-discordant relation in which initially horizontal strata terminate progressively against an initially inclined surface, or in which initially inclined strata terminate progressively against a surface of greater initial inclination". Following the earlier works of McCaffrey and Kneller (2001), Smith and Joseph (2004), Gardiner (2006), and Patacci (2010), Bakke *et al.* (2013) presented six different termination styles that can be resolved at seismic resolution. Three termination styles are presented for sand-prone stratigraphic units: (i) simple onlap, (ii) draping

onlap and (iii) bed thickening (Fig. 2.11). Bakke *et al.* (2013) hypothesise that the simple onlap style is present with steep palaeotopography and high magnitude SGFs, whereas with decreasing slope angle and flow magnitude, draping onlap prevails. Bed thickening is apparent where the slope is unstable and actively failing. Bakke *et al.* (2013) also suggest three pinchout styles for heterolithic stratigraphic units: (i) advancing pinchout, (ii) convergent pinchout and (iii) convergent thickening.
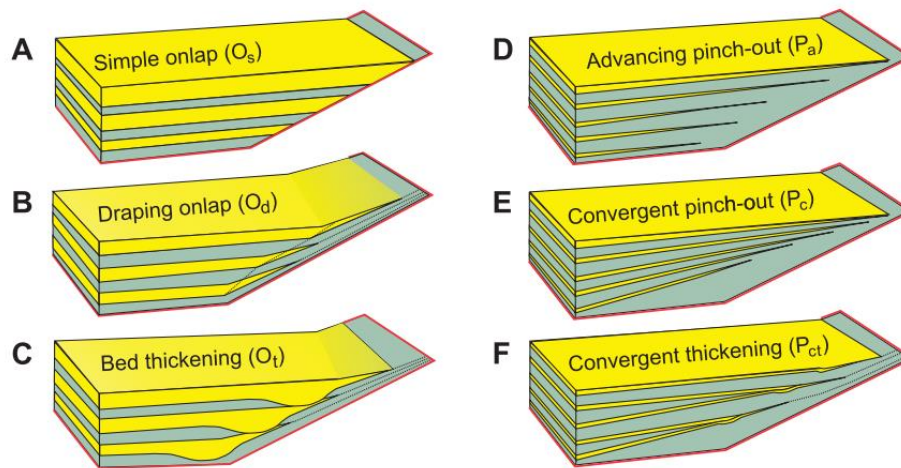
Figure 2.11: Illustrations of possible deep-water termination styles close to topographic highs. From Bakke *et al.* (2013).

The facies type and distribution, palaeocurrent dispersal, and onlap type can be used to aid in reconstructing the scale of basin confinement and form of intrabasinal topography (Pickering and Hiscott, 1985; Kneller *et al.*, 1991; Hurst *et al.*, 1999; Amy *et al.*, 2004; Smith and Joseph, 2004; Gardiner, 2006; Marini *et al.*, 2015; Soutter *et al.*, 2019; Tinterri *et al.*, 2022). In addition to palaeogeographic reconstructions, understanding the degree of basinal and local topography and how it influences SGF behaviour is important in assessing the design criteria for seafloor infrastructure and the source-to-sink pathways of particulate matter in the deep sea.

2.3   Submarine canyons

The geomorphic elements of submarine canyons and the terminology used in this thesis are presented in Figure 2.12. Submarine channel and lobes are also included in Figure 2.12 and discussed in Section 2.3.5.
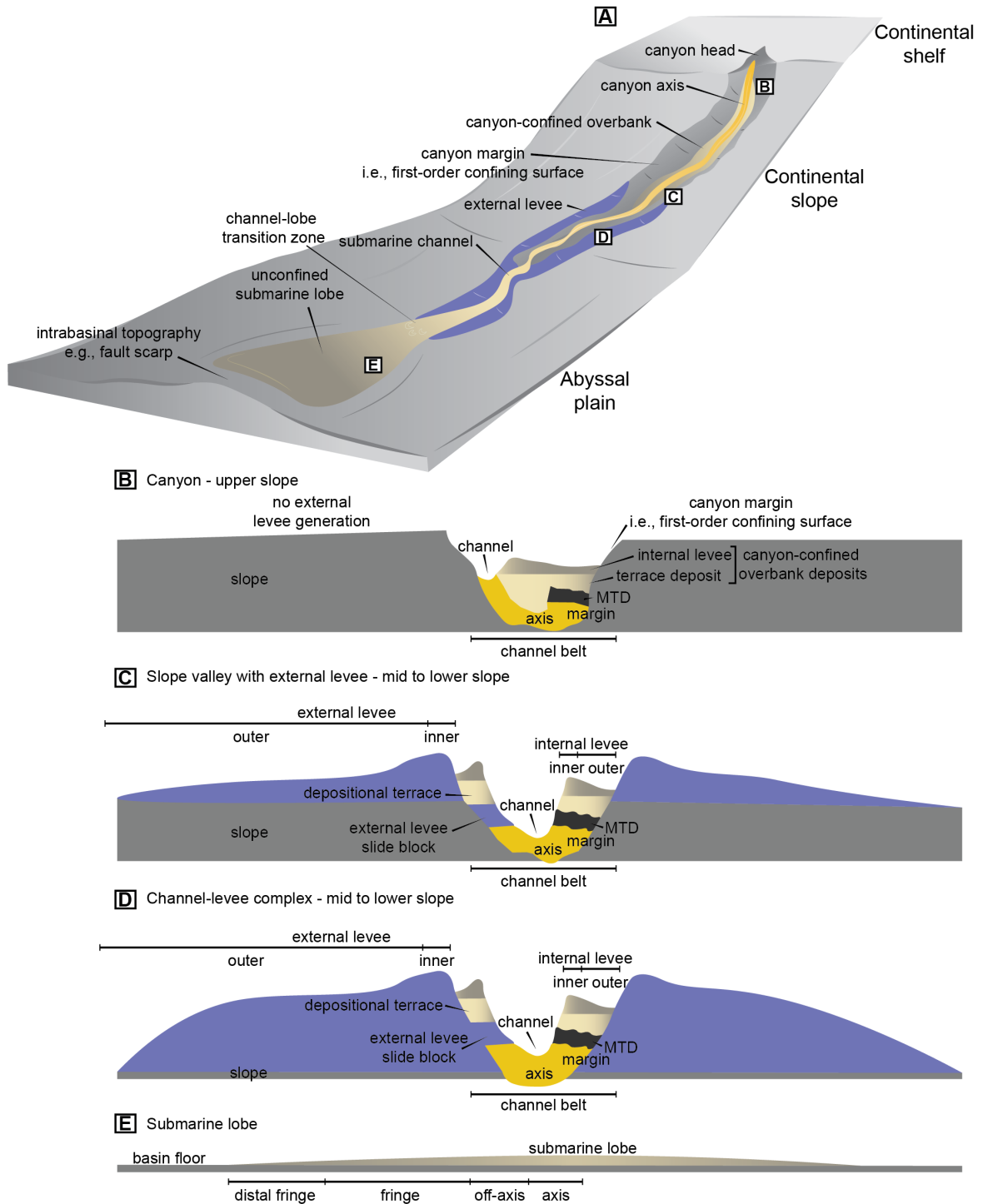
Figure 2.12: (A) Conceptual diagram of deep-water sedimentary systems, including (B) canyons, (C) slope valleys, (D) channel-levee complexes, and (E) lobes. The terminology adopted here used throughout this thesis. Modified from Hansen *et al.* (2015) and W. Taylor *per comms.*

2.3.1   What are submarine canyons?

Submarine canyons are an important conduit for sediment (Normark, 1970), organic carbon (Talling *et al.*, 2023), nutrient (Heezen *et al.*, 1955), and pollutant (Paull *et al.*, 2002; Zhong and Peng, 2021; Pierdomenico *et al.*, 2023) transport to the deep sea. Submarine canyons typically occur on the upper-slope and are connected to the shelf edge (Wynn *et al.*, 2007). They have been identified in the ancient and modern record, and to date there are over 9000 mapped, modern submarine canyons globally, observed on both passive and active margins (Harris and Whiteway, 2011) (Fig. 2.13). Canyons are erosional, quasi-linear features that incise into the continental shelf and/or slope, extending up to hundreds of kilometres in length, tens of kilometres in width, and several kilometres deep (Harris and Whiteway, 2011). Canyons can be categorised as: (i) shelf-incised and river-connected, (ii) shelf-incised and land-detached and (iii) slope incised ('blind') (Harris and Whiteway, 2011). Canyons form because of three main processes: (i) prolonged erosion from SGFs, (ii) retrogressive slope failure (mass-wasting events) and (iii) subaerial exposure during low sea-levels (Daly *et al.*, 1936; Farre *et al.*, 1983; Pratson *et al.*, 1994; Pratson and Coakley, 1996; Fagherazzi, 2004; Piper and Normark, 2009). A comprehensive literature-based study recently proposed however, that most of the canyon-fed systems had their canyons cut with part or all the continental shelf flooded, generally during rising and highstand of sea level (Fisher *et al.*, 2021). Shelf-incised canyons are more common on active margins due to high volumes of sediment input and typically form short, steep canyons (Sømme *et al.*, 2009; Harris and Whiteway, 2011) (Fig. 2.13). Even land-detached canyons (*e.g.,* Whittard Canyon) have been shown to be equally as active in terms of turbidity current frequency and magnitude as shelf-incised, land-attached canyons (*e.g.,* Monterey Canyon and Congo Canyon) (Heijnen *et al.*, 2022).
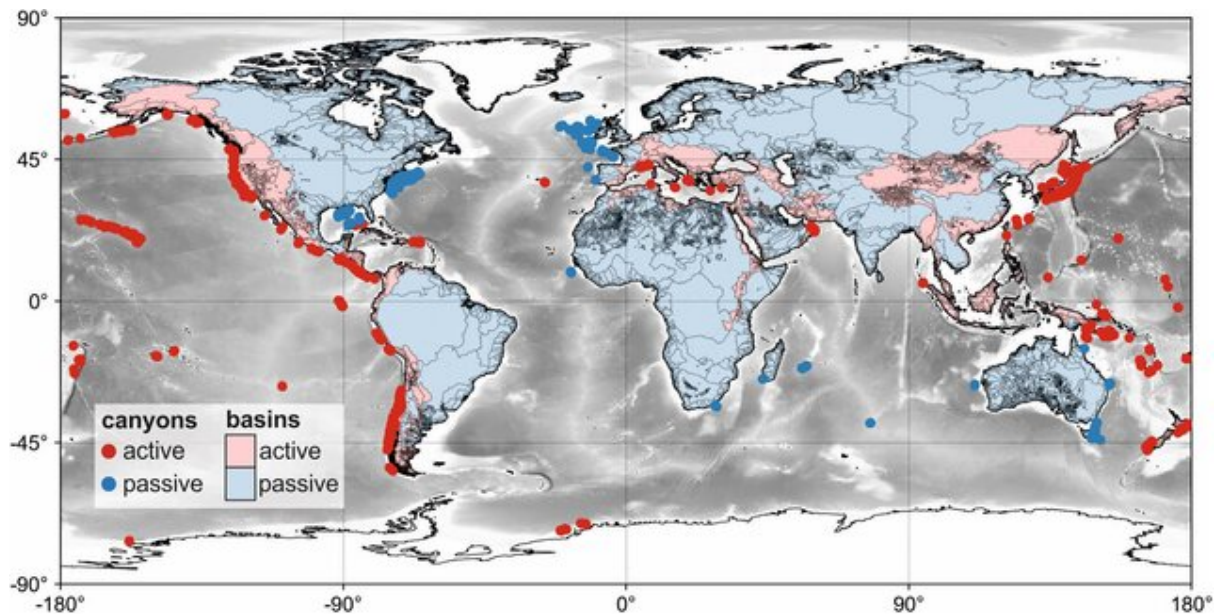
Figure 2.13: Map of the global distribution of submarine canyons and the drainage-basin delineation. Red dots indicate canyons formed on active margins and blue dots indicate canyons formed on passive margins. The lighter shades are shallow bathymetry, and the darker shades are deeper bathymetry. From Soutter *et al.* (2021b).

2.3.2   Direct monitoring in modern submarine canyons

Recent technological advancements have enabled the direct monitoring of velocity and concentration measurements of SGFs (Talling *et al.*, 2023 and references therein) and other near-bed deep-sea flows, including deep internal tides (Xu and Noble, 2009; Hall *et al.*, 2017; Maier *et al.*, 2019) and nepheloid layers (Wilson *et al.*, 2015) in submarine canyons. High-resolution bathymetric maps have also been created to better understand the physiography of canyons (Fig. 2.14). Although these measurements are sparse relative to the number of mapped submarine canyons, they have been able to elucidate a more comprehensive understanding of SGF and deep-sea flow frequency, magnitude, and dynamism (Azpiroz-Zabala *et al.*, 2017; Paull *et al.*, 2018; Lo Iacono *et al.*, 2020; Heijnen *et al.*, 2022), compared to previous models (Normark and Piper, 1991). The generation of mixed systems, owing to the dynamism and superimposition of SGFs with other near-bed deep-sea flows (*e.g.,* internal tidal currents) is hypothesised to be under-represented in the deep-water geological record (Zhenzhong and Eriksson, 1991; Shanmugam, 2003; Soutter *et al.*, 2024).
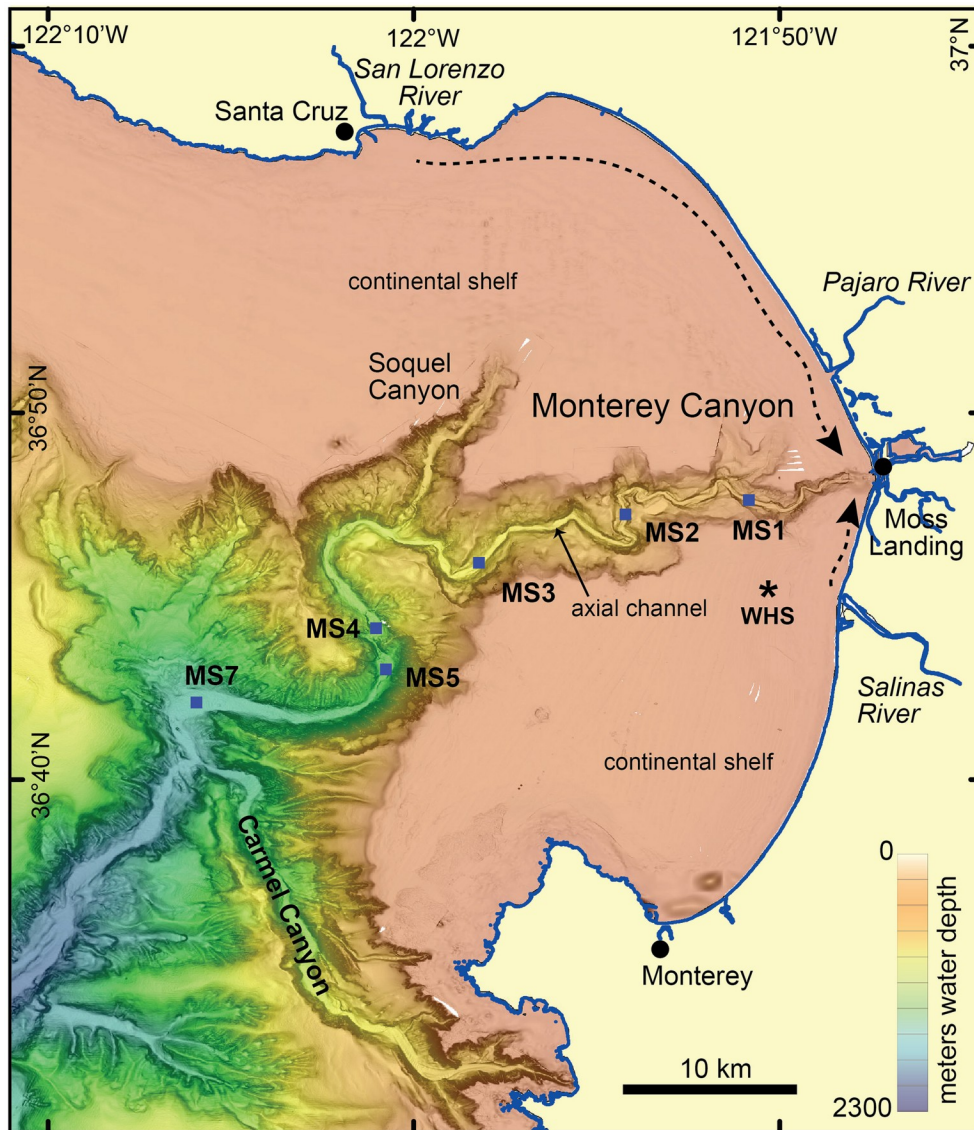
Figure 2.14: Map of the Monterey Canyon, offshore central California. Blue squares indicate locations of the Coordinated Canyon Experiment moorings. Dashed arrows depict littoral transport paths into Monterey Canyon. WHS: wave height sensor. From Maier *et al.* (2019).

Modern submarine canyons are composed of an axis or axial channel and a terraced overbank, with terrace surfaces often extending hundreds of metres above the canyon thalweg (Maier *et al.*, 2018), and typically being overlain by fine-grained SGF deposits (Hansen *et al.*, 2015). Following repeat bathymetric surveying and by using hydrodynamic moorings in Monterey Canyon, a powerful, through-going turbidity current with velocities exceeding 7 m s^{-1} was documented, revealing that erosion was focused in the sandy, axial channel, whereas the muddy, terraced flanks displayed no resolvable elevation change (Paull *et al.*, 2018). The canyon walls are steep, and often, near vertical escarpments that are prone to mass-wasting, such that

landslides have been documented to 'dam' submarine canyons, causing the canyon axis to reroute (Pope *et al.*, 2022) (Fig. 2.15). Modern canyons have also been documented to host important, vulnerable ecosystems (Biachelli *et al.*, 2010; Johnson *et al.*, 2013; Fernandez-Arcaya *et al.*, 2017). The positioning of canyons at the continental shelf to slope transition and the delivery of nutrients by SGFs makes submarine canyons and the surrounding interfluves targets for fishing fleets. Benthic fishing activity close to submarine canyons has been shown to cause resuspension of sediment on the continental shelf and high on the canyon walls (Puig *et al.*, 2014; Daly *et al.*, 2018), and provides a source of marine litter directly to canyons (Xue *et al.*, 2020).
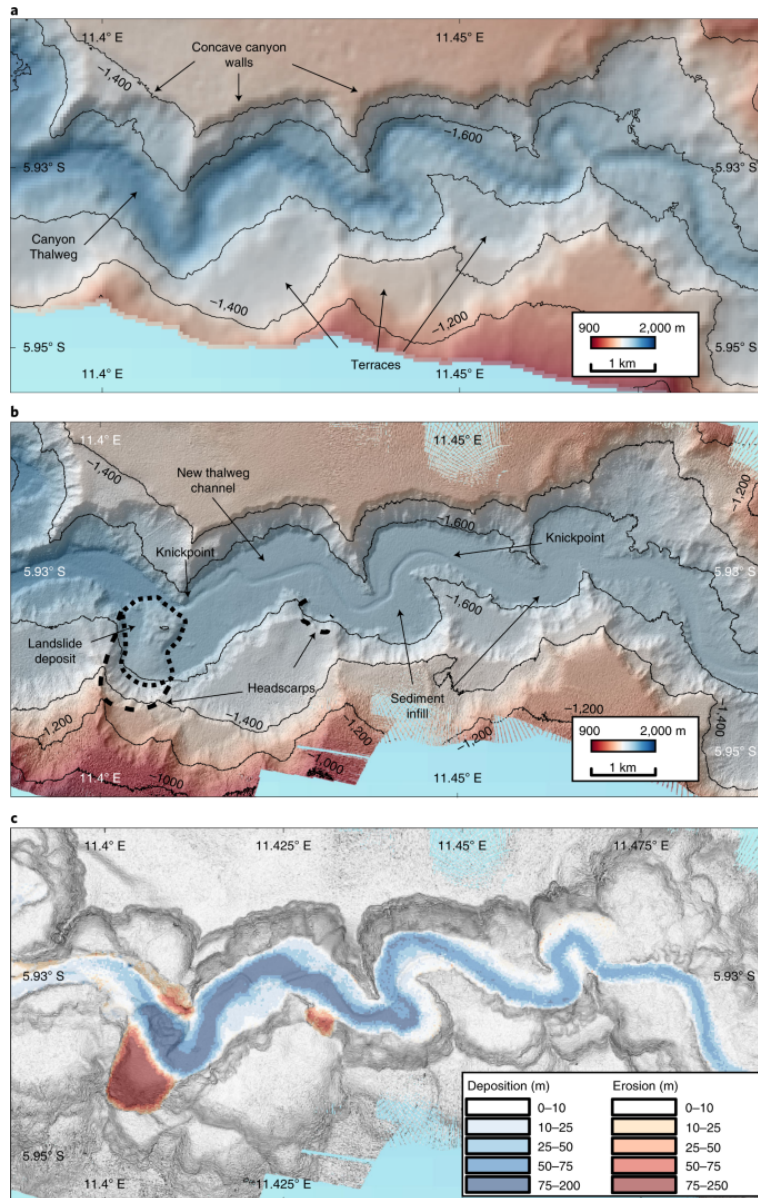
Figure 2.15: Bathymetric maps from the Congo Canyon. (A) Data derived from 2005, (B) Data derived from the same area in 2019. A canyon flank landslide that has dammed the overbank and axis is shown. The landslide-dam has resulted in the trapping of sediment leading to infilling up-canyon of the landslide-dam. (C) Difference map from the 2005 data and the 2019 data, overlain on a hillshade map to allow the patterns of erosion and deposition to be characterised. From Pope *et al.* (2022).

2.3.3 Exhumed submarine canyons

When exhumed, ancient canyon fills are characterised by axial fills composed of coarser-grained sandstones and conglomerates, indicative of the repeated cut-and-fill stages, resulting from high-magnitude events eroding the canyon floor and bypassing sediment downslope (May and Warme,

2007; Di Celma, 2011; Maier *et al.*, 2012; Jobe *et al.*, 2018; Janocko and Basilici, 2021; Bouwmeester *et al.*, 2024). Laterally to the axis, the inner-canyon margin is characterised by slump-dominated deposits that act to both provide obstacles to subsequent flows, but also provide a source of finer-grained material that can be transported down-canyon (Anderson *et al.*, 2006). The evidence of episodic, erosive SGFs is further supported by observations from the modern Monterey Canyon of decametre-long crescentic-shaped bedforms and knickpoints; formed by erosion from cyclic steps (Paull *et al.*, 2010). Canyon-confined overbank areas act to provide a more complete, organised record of canyon evolution, in the form of finer-grained material deposited from flows that overspilled the canyon axis (Taylor *et al.*, 2024b). The more episodic, lower-magnitude flows fail to traverse the full length of the canyon and typically 'die-out' in the upper-canyon reaches. Only the rarer, higher magnitude flows traverse the length of the canyon, depositing further down-slope (Jobe *et al.*, 2018). The heterogeneity of canyon-confined overbank deposits has been shown to increase towards the canyon margin (*i.e.*, first-order confining surface), due to mass-wasting events and the emplacement of mass-transport deposits into the canyon-confined overbank sub-environment (*see* Chapter 4).

Although the preservation potential of coarser-grained axial fills is enhanced at outcrop compared to finer-grained canyon overbank environments, exposures of the former typically lack 3D constraints and are strongly linked to bypass-dominated processes. This coupled with the more complete stratigraphic record typically preserved in canyon overbank environments, means that 3D exposures of canyon overbank and margins can markedly aid the development of process-based models of submarine canyon fills.

2.3.4 The importance of submarine canyons

Canyons are the most proximal component of deep-water depositional systems, playing a vital role in connecting terrestrial and shallow marine environments to abyssal depths (Daly, 1936; Kuenen, 1938; Middleton and Hampton, 1973; Simpson, 1997; Fildani *et al.*, 2017). At their terminus, submarine canyons typically feed submarine channel-levee systems and lobes, which in their totality host the largest sediment accumulations on Earth (Curray and Moore, 1971; Emmel and Curray, 1983). Furthermore, submarine canyons have been documented to have higher levels of oxygen and nutrient enrichment compared to open slope locations at the same water depths (Vetter and Dayton, 1998; Rex *et al.*, 2006; De Leo *et al.*, 2010). As a result, submarine canyons host biodiverse faunal assemblages, under-pinning critical marine ecosystems. Understanding the role submarine canyons play in the transient storage and flushing of particulate matter to the deep sea is vital for palaeogeographic reconstructions, calculating

sediment, carbon, and pollutant budgets, and informing the design criteria of seafloor infrastructure. Changes to the planform geometry of submarine canyons, and localised topography in canyon overbank environments and at abyssal depths profoundly influences SGF behaviour.

2.3.5 The connection of submarine canyons to submarine channels and lobes

Submarine channels often evolve downslope from the terminus of submarine canyons (Fig. 2.16), yet this is a source of ambiguity, hence, following Wynn *et al.* (2007) they are here differentiated by being in a relatively distal slope position compared to canyons, with a lower cross-sectional area and gentler axial gradient. Channel-levee systems, where external levees are constructed beyond the first-order confining surface, act as conduits for continued transport of particulate matter further into the deep sea (Menard, 1955; Peakall *et al.*, 2000; Hansen *et al.*, 2016).
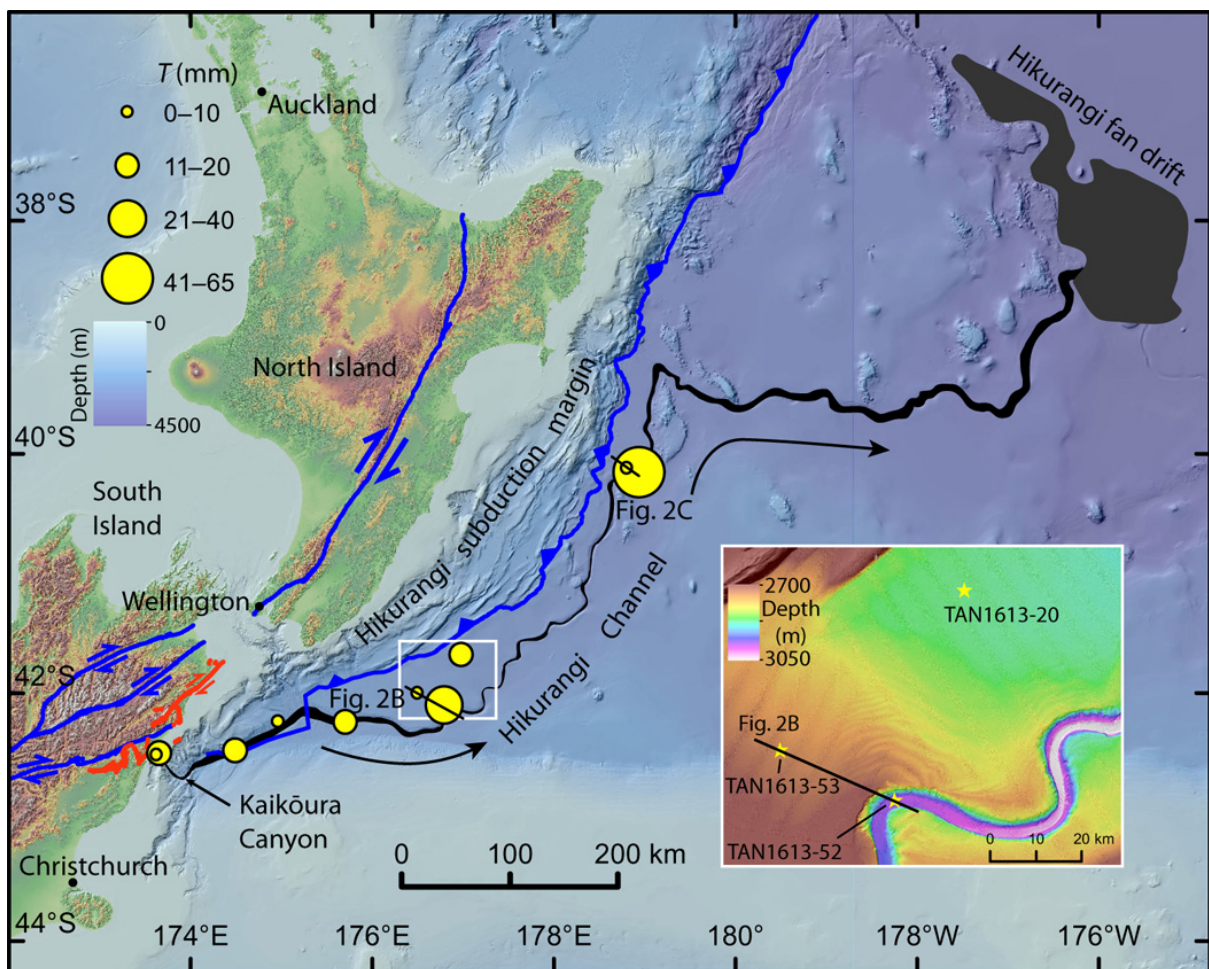
Figure 2.16: The 1500 km-long Hikurangi Channel offshore New Zealand. Note its connection to the Kaikōura Canyon. From Mountjoy *et al.* (2018).
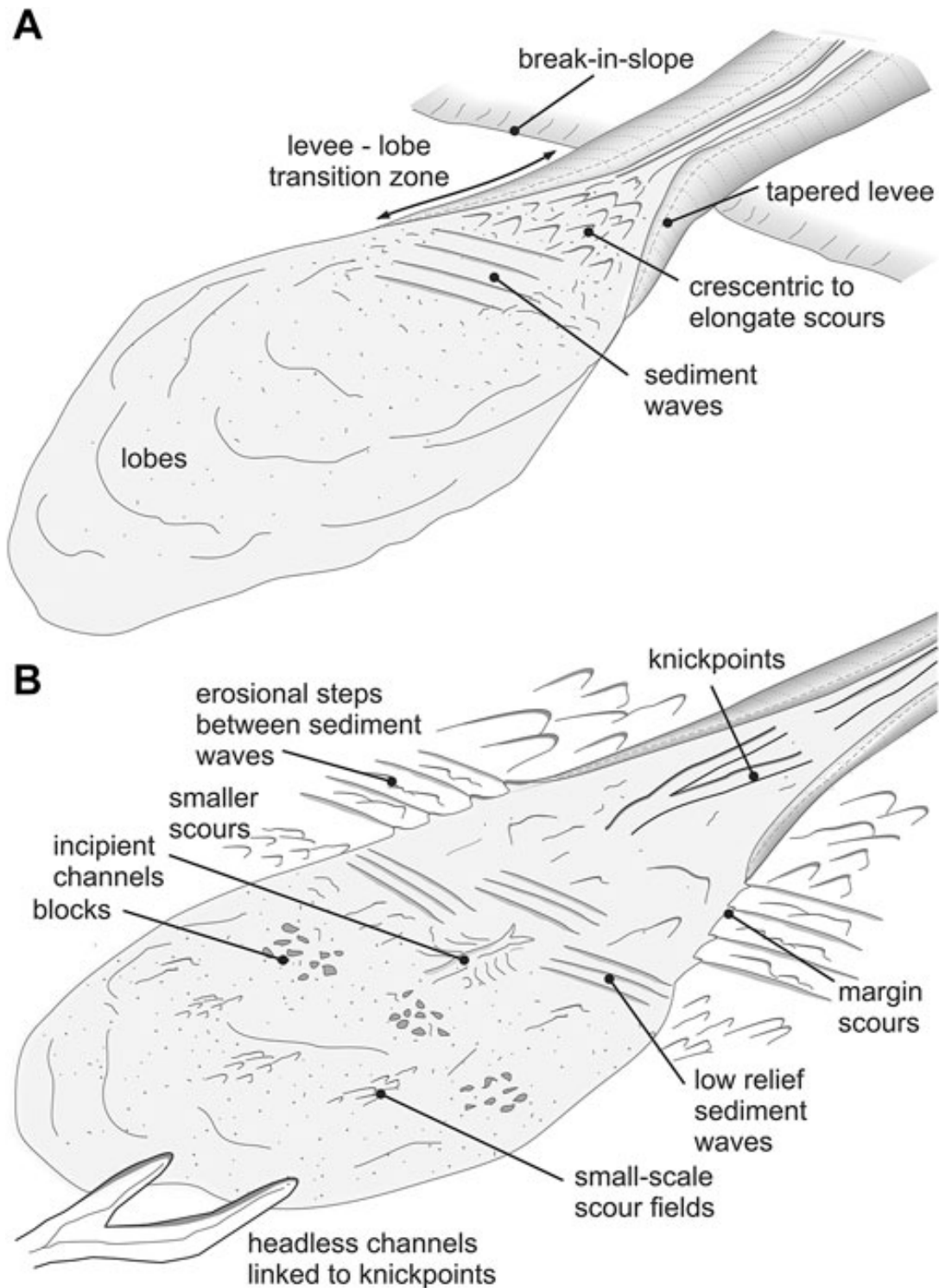
Figure 2.17: Diagram of end-member channel mouth systems. (A) Channel-lobe transition zones based on Wynn *et al.* (2002a) and Brooks *et al.* (2018). (B) Channel-mouth expansion zones based on Maier *et al.* (2020). From Hodgson *et al.* (2022).

At the mouth of submarine channels, typically at a marked break-in slope, the transitional area between submarine channels and lobes is termed the channel-lobe transition zone (CLTZ) (Wynn *et al.*, 2002a; Fildani and Normark, 2004; Maier *et al.*, 2020). There are a range of different CLTZ configurations defined by Hodgson *et al.* (2022) (Fig. 2.17). The sudden change in the degree of flow confinement makes CLTZs crucial in the source-to-sink pathways of particulate matter.

Submarine lobes are the most distal expressions of deep-water sedimentary systems (Normark, 1978; Mutti, 1992; Spychala *et al.*, 2017a). As SGFs exit the confinement of submarine channels and pass through CLTZs they spread radially and decelerate (Normark, 1978). As a result, the deposits thin and fine, both laterally and distally (Deptuck *et al.*, 2008; Spychala *et al.*, 2017a). Submarine lobe environments can be subdivided based on the longitudinal and latitudinal evolution of the SGFs that build them (Spychala *et al.*, 2017a) (Fig. 2.18).
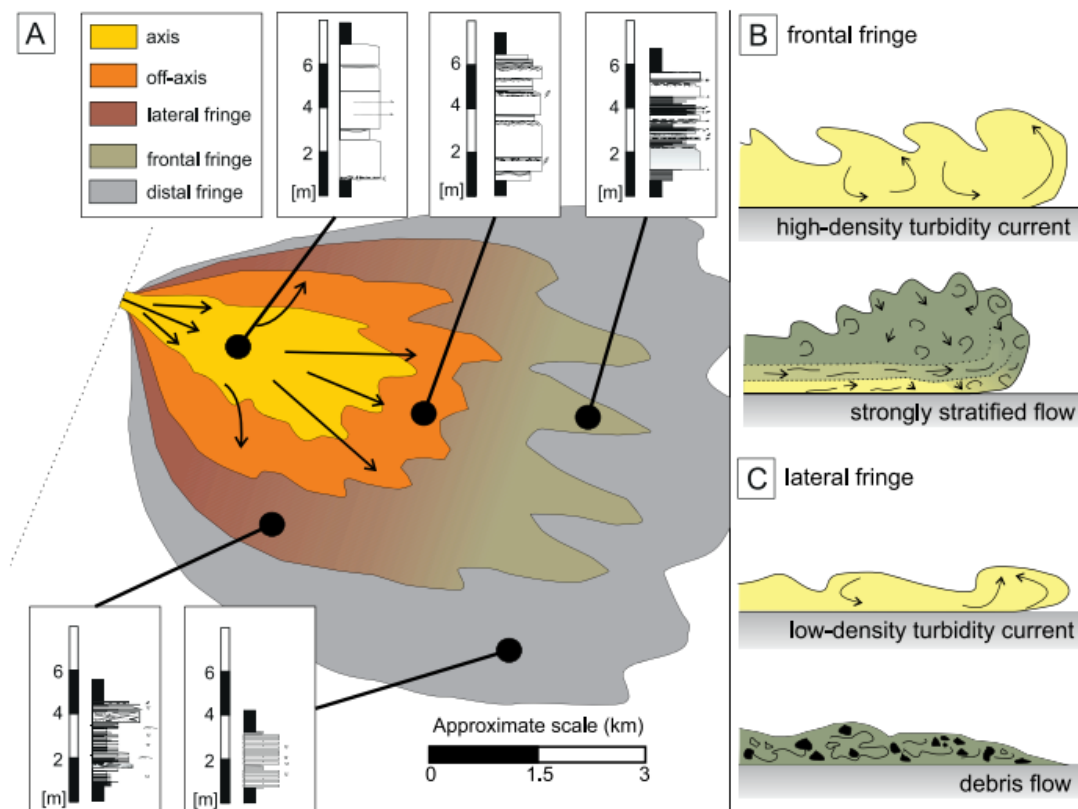
Figure 2.18: Facies associations related to submarine lobe sub-environments. From Spychala *et al.* (2017a).

2.4 Microplastic transfer in deep-water sedimentary systems

2.4.1 Historic plastic production

Plastic production has increased from 50 million tonnes (Mt) in 1976 to more than 400 Mt in 2022 and is forecasted to exceed 500 Mt per year by 2050 (PlasticsEurope, 2023). The ubiquity of plastic in modern, everyday life is owed to its versatility and low cost. An estimated 70% of all plastic ever produced is now however, considered as waste (Geyer *et al.,* 2017). Although approximately 12% and 9% of this waste has been incinerated or recycled, respectively, an estimated 4900 Mt of plastic has accumulated in landfill or due to waste mismanagement, in the natural environment (Geyer *et al.,* 2017). Plastic pollution has been observed in nearly all of Earth's environments (Taylor *et al.,* 2016), including the polar regions (Zarfl and Matthies, 2010; Bergmann *et al.,* 2022) and in deep ocean trenches (Peng *et al.,* 2020). Of all the plastic debris in the marine environment, 10-25% is estimated to be from ocean-based sources and 75-90% from land-based sources (Duis and Coors, 2016).

2.4.2 What are microplastics?

Microplastics particles are plastic particles < 1mm in diameter (Fig. 2.19) and can be primary or secondary in origin. Primary microplastics are formed as manufactured particles, commonly in the form of microbeads, as used in cosmetic applications (Zitko and Hanlon, 1991) and nurdles used in plastic production (Jiang *et al.,* 2022). Secondary microplastics form via the breakdown of macroplastics via physical weathering and/or chemical degradation (Cole *et al.,* 2011), and commonly take the form of synthetic and semi-synthetic fibres (Finnegan *et al.,* 2022). Semi-synthetic fibres (*e.g.,* rayon and chlorinated rubber) have been documented to be as pervasive as synthetic plastic fibres in the natural environment (Woodall *et al.,* 2014; Finnegan *et al.,* 2022) and have similar ecotoxicological effects on organisms (Jiang *et al.,* 2024). Semi-synthetic fibres are used in both clothes manufacturing and cigarette filters. Microplastic pollution is pervasive in the natural environment. Crucial to understanding the effects of microplastic pollution on organisms and humans, is identifying microplastic sources, the transport pathways, and burial processes.
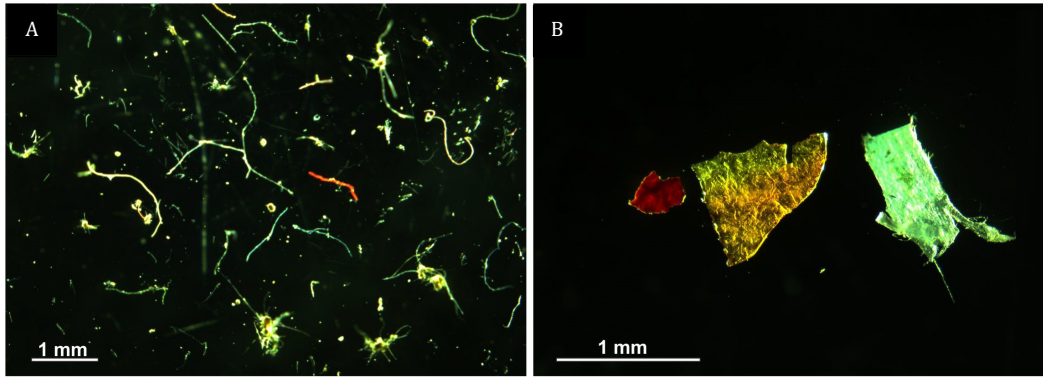
Figure 2.19: Photographs of microplastics collected from seafloor sediment cores collected in the Tyrrhenian Sea. (A) Microfibres and (B) Microplastic fragments. From Kane and Clare (2019).

2.4.3   Microplastic source-to-sink pathways

Rivers are hypothesised to be key agents in the transfer of sediment and terrestrially sourced macro- and micro-plastics to coastal settings (*e.g.,* Strokal *et al.,* 2023), although wind-blown transport of airborne plastic is also common (*e.g.,* Bullard *et al.,* 2021). Riverbeds and floodplains have been considered as sites of transient storage of microplastics, sequestered, until flooding events and riverbank erosion remobilises particulate matter (*e.g.,* Hurley *et al.,* 2018). Repeat sampling of the upstream catchment of the River Mersey, UK found that an estimated 70% of the microplastic load stored as bedload was exported during a catchment-wide flooding event, calculated to be 43 ± 14 billion microplastic particles (Hurley *et al.,* 2018). When terrestrially sourced microplastics reach coastal settings, is it hypothesised that estuarine, deltaic, and shallow marine processes are capable of reworking microplastic sequestered in sediment and transporting sediment and microplastic further seaward via longshore drift and cross-continental shelf currents, where it can be stored on the continental shelf or at submarine canyon heads (Rohais *et al.,* 2024). The rates of sediment and microplastic storage in coastal and shallow-marine settings, and the transfer to deep-marine settings is strongly dictated by the tectonic configuration of the margin (Kane and Clare, 2019). The factors controlling the efficiency of microplastic transfer to the deep-sea include: (i) margin relief, (ii) shelf width, and (iii) connectivity to fluvial input (Kane and Clare, 2019) (Fig. 2.20), but should also consider where the microplastics are sourced from.
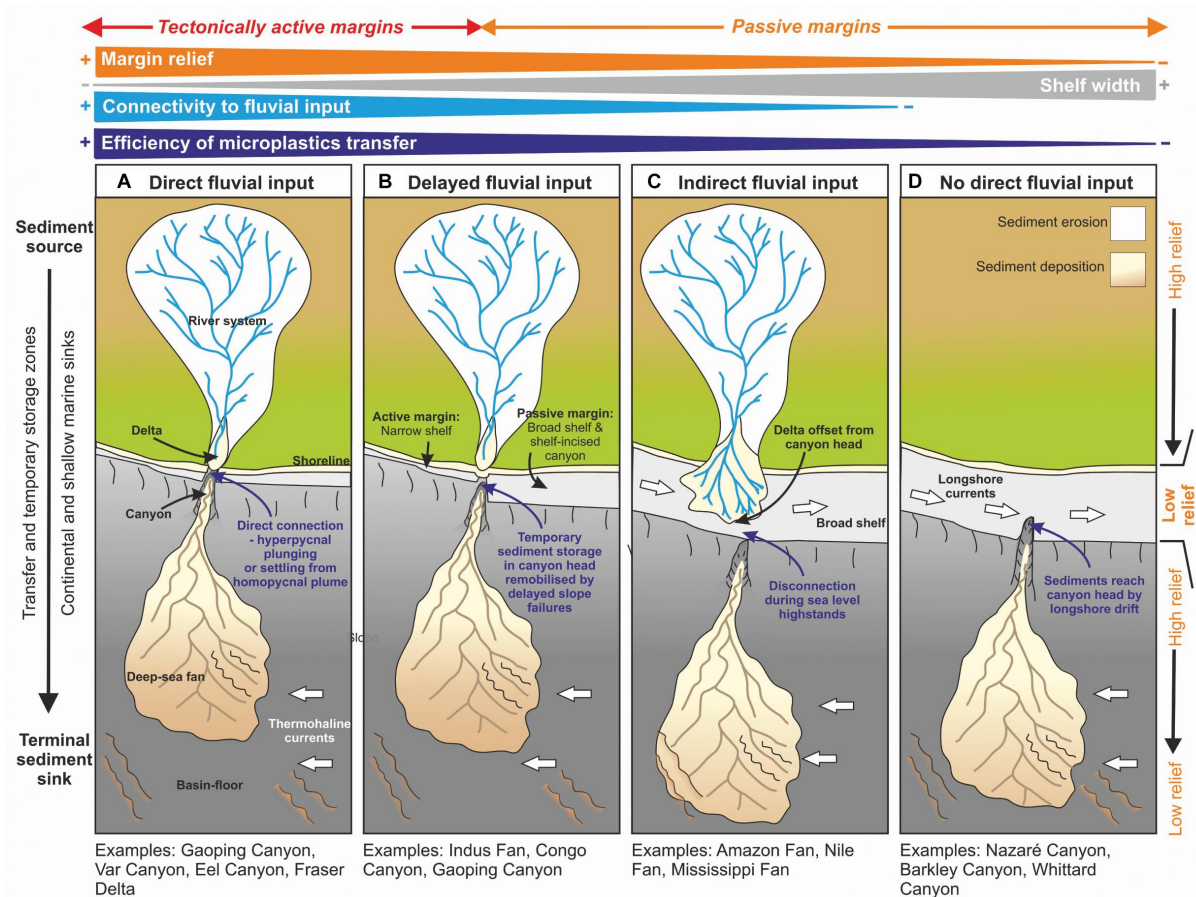
Figure 2.20: Schematic diagram showing the efficiency of microplastic transfer from terrestrial to deep-marine realms. (A) Direct fluvial input to the canyon head, (B) delayed fluvial input as sediment is stored transiently in the canyon head, (C) indirect fluvial input due to the canyon being offset from the river mouth, and (D) no direct fluvial feeder, sediment is sourced from longshore drift. The proximity to marine sources of microplastics is not considered. From Kane and Clare (2019).

SGFs are hypothesised to be the primary agent of sediment and microplastic transfer from terrestrial and shallow-marine environments to the deep-sea, with submarine canyons acting as the conduits (Kane and Clare, 2019; Pohl *et al.*, 2020). However, microplastic transfer via turbidity currents has only been documented experimentally (Pohl *et al.*, 2020). The density and shape characteristics of microplastics, like those of organic matter, would suggest that SGFs would be highly capable of transporting microplastics through submarine canyons and to the deep-sea. The role of transient microplastic storage in submarine canyon and channel overbanks,

and canyon-flushing events is yet to be resolved, however it is hypothesised to be crucial when attempting to accurately calculate microplastic fluxes to the deep-sea and microplastic burial rates in sediment.

2.4.4 Microplastic transport processes in the deep-sea

An estimated 13.5% of the global marine plastic budget is microplastic (Koelmans *et al.*, 2017). Of this global budget, 1% is estimated to be found on the ocean surface, in 'ocean garbage patches' (Eriksen *et al.*, 2014; van Sebille *et al.*, 2015). This poses the questions - where is the missing 99% and what processes control microplastic distribution? The deep seafloor is hypothesised to be the ultimate depositional sink to most of this plastic pollution, residing both on and within sediments on the deep seafloor (Thompson *et al.*, 2004; Koelmans *et al.*, 2017; Choy *et al.*, 2019). Sampling of deep seafloor surficial sediments reveals that microplastic distribution and concentration does not correlate with the extent of overlying surface garbage patches or with distance from source (*e.g.,* Kane *et al.*, 2020). This suggests that vertical settling of microplastics through the water column is not the only process controlling microplastic distribution and concentration in marine environments (Thompson *et al.*, 2004; Pham *et al.*, 2014; Kane and Clare, 2019; Kane *et al.*, 2020). Instead, it is hypothesised that SGFs transport sediment and microplastic to the deep-sea (Kane and Clare, 2019; Pohl *et al.*, 2020; Zhang *et al.*, 2024). Furthermore, it has been shown that microplastics are preferentially concentrated within deep sea physiographic settings (Kane *et al.*, 2020). Similarly to how oceanic gyres control the distribution of surface garbage patches, deep near-bed thermohaline currents (*i.e.,* bottom currents) have been documented to control microplastic distribution on the deep seafloor (Kane *et al.*, 2020).

Although both micro- and macroplastics had been documented in deep seafloor sediments (Woodall *et al.*, 2014; Kane *et al.*, 2020; Zhong and Peng, 2021; Pierdomenico *et al.*, 2023), the extent to which physical transport processes were responsible for concentrating microplastics into distinct physiographic domains remains unclear. The work of Kane *et al.* (2020) integrated deep seafloor sediment samples with bathymetric, oceanographic, and sedimentological data to bridge the existing knowledge gap. Microplastics were observed to be focused in zones where bottom currents interacted with complex seafloor topography, where near-bed shear stresses were low and sediment accumulation rates were increased (*e.g.,* mounded drifts) compared to zones of erosion and bypass (*e.g.,* contour-parallel moats) (Kane *et al.*, 2020). Bottom currents have also been documented to play a crucial role in the delivery of oxygen and nutrients to the deep sea, and hence the depositional environments host important biodiversity hotspots (Treigner *et al.*, 2006). It stands to reason that SGFs, namely turbidity

currents, in submarine canyons are hypothesised to be major conveyors of microplastics to the deep sea, given the crucial role submarine canyons play in sediment transport processes. The role that other near-bed deep-sea flows (*e.g.,* internal tides), shallow subsurface processes (*e.g.,* bioturbation), and external anthropogenic forcing (*e.g.,* benthic trawling) play in controlling microplastic transfer to the deep sea is explored in Chapter 5.

The knowledge gap related to understanding microplastic transport processes and potential mobility in the subsurface, and the crucial role submarine canyons play in source-to-sink pathways means that calculations of microplastic fluxes in the deep-sea may be inaccurate, and the routeing pathways of other particulate matter (*e.g.,* organic carbon) and the effects of microplastic ingestion by organisms may be poorly understood.

2.4.5 Microplastic burial and the ecotoxicological effects in the deep sea

The more quiescent deep-sea settings (*e.g.,* abyssal plains, deep-sea trenches, and canyon/channel overbanks) are considered as long-term storage sites of microplastics, rather than the more bypass-dominated, higher-energy environments. However, processes in the shallow subsurface, including bioturbation (Courtene-Jones *et al.,* 2020) and hyporheic transfer (*i.e.,* the transport of surface waters through sediment pore space in flow paths that return to the water surface and are driven by a pressure gradient flowing over the bed) (Frei *et al.,* 2019) may act to increase the preservation potential of microplastic by burying them into older sediments. Once buried it is hypothesised that microplastics can enter the food-chain via trophic transfer from benthic organisms (Taylor *et al.,* 2016). Microplastics also have the potential to act as vector particles for various toxins, including persistent organic pollutants (POPs) and heavy metals (Campanale *et al.,* 2020). The consumption of microplastics by marine organisms has been documented in polychaetes, molluscs, fish, and whales (Taylor *et al.,* 2016) (Fig. 2.21). The pathways for trophic transfer remain unclear, however it is evident that they are entering the food-chain, with potentially deadly consequences for the organisms (Al Mamun *et al.,* 2023).
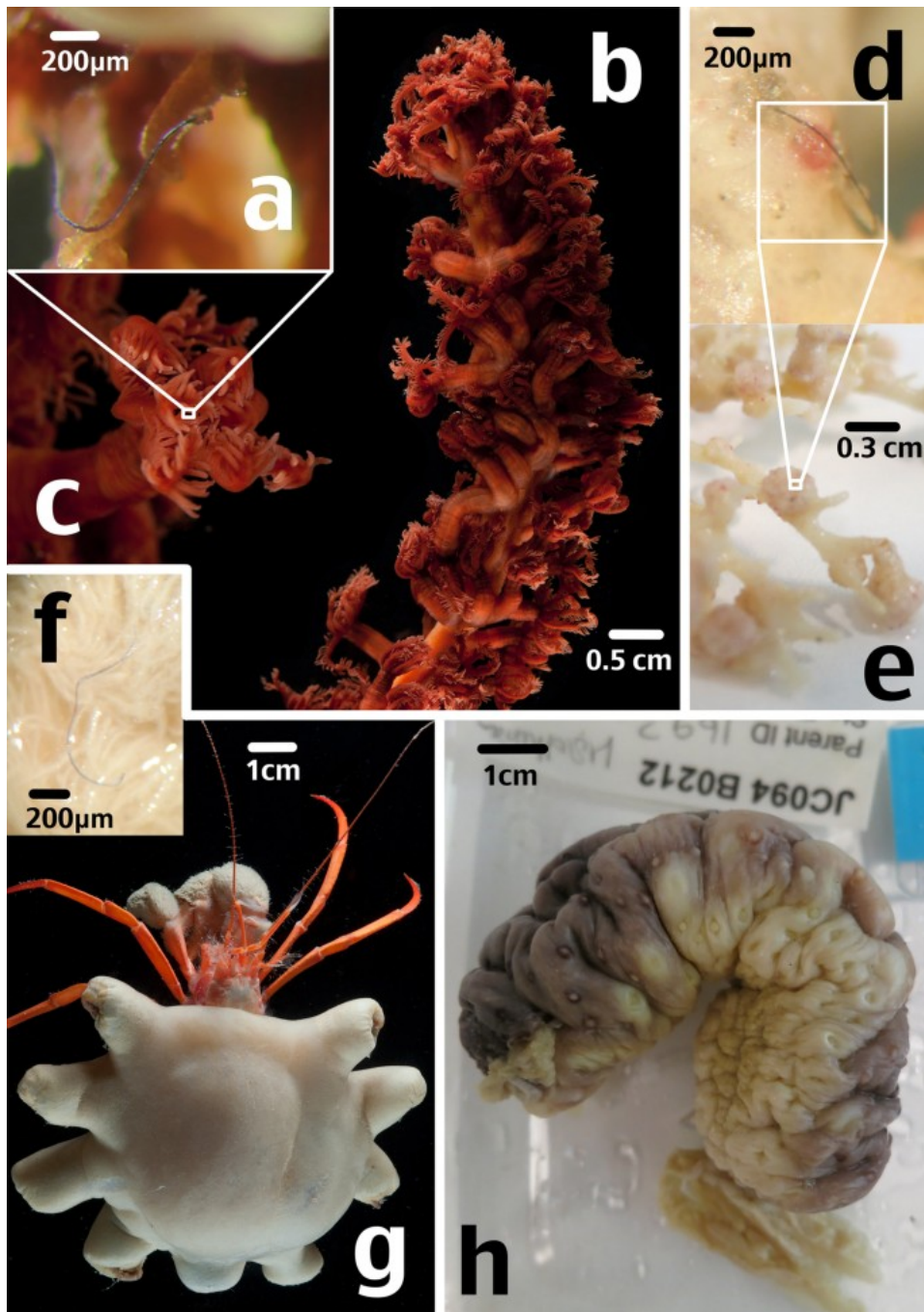
Figure 2.21: Photographs of organisms found to have ingested microfibres and microfibres in situ. (A) Blue microfibre from mouth area of sea pen polyp, (B) sea pen, (C) sea pen polyp, (D) black microfibre embedded in surface of zoanthid, (E) zoanthids on bamboo coral skeleton, (F) blue microfibre on feeding maxilliped of hermit crab, (G) hermit crab, and (H) sea cucumber. From Taylor *et al.* (2016).

Chapter 3 Unconfined gravity current interactions with orthogonal topography: Implications for combined-flow processes and the depositional record

3.1 Summary

Turbidity current behaviour is affected by interactions with seafloor topography. Changes in flow dynamics will depend on the orientation and gradient of the topography, and the magnitude and rheology of the incoming flow. A better understanding of how unconfined turbidity currents interact with topography will improve interpretations of the stratigraphic record, and is addressed herein using three-dimensional flume tank experiments with unconfined saline density currents that enter a horizontal basin before interacting with a ramp orientated perpendicular to flow direction. The incoming flow parameters remained constant, whilst the slope angle was independently varied. On a 20° slope, superelevation of the flow and flow stripping of the upper, dilute region of the flow occurred high on the slope surface. This resulted in a strongly divergent flow and the generation of complex multidirectional flows (*i.e.,* combined flows). The superelevation and extent of flow stripping decreased as the slope angle increased. At 30° and 40°, flow reflection and deflection, respectively, are the dominant flow process at the base of slope, with the reflected or deflected flow interacting with the parental flow, and generating combined flows. Thus, complicated patterns of flow direction and behaviour are documented even on encountering simple, planar topographies orientated perpendicular to flow direction. Combined flows in deep-water settings have been linked to the interaction of turbidity currents with topography and the formation of internal waves with a dominant oscillatory flow component. Here, combined flow occurs in the absence of an oscillatory component. A new process model for the formation and distribution of hummock-like bedforms in deep-marine systems is introduced. This bedform model is coupled to a new understanding of the mechanics of onlap styles (draping versus abrupt pinchout) to produce a spatial model of gravity-current interaction, and deposition, on slopes to support palaeogeographic reconstructions.

3.2 Introduction

Turbidity currents are the principal mechanism for sediment transfer from shallow-water to deep-water environments (Kuenen and Migliorini, 1950; Middleton and Hampton, 1973;

Simpson, 1997), resulting in the largest accumulations of sediment on Earth (Curray and Moore, 1971; Emmel and Curray, 1983). Seafloor topography, which acts as a first order control on turbidity current behaviour, may be generated by depositional relief associated with mass transport deposits (*e.g.,* Armitage *et al.,* 2009; Martínez-Doñate *et al.,* 2021; Allen *et al.,* 2022), levées and lobes (*e.g.,* Groenenberg *et al.,* 2010; Kane and Hodgson, 2011), folds and faults (*e.g.,* Haughton, 2000; Hodgson and Haughton, 2004; Cullen *et al.,* 2020), salt and mud diapirism (*e.g.,* Kneller and McCaffrey, 1995; Toniolo *et al.,* 2006; Howlett *et al.,* 2021; Cumberpatch *et al.,* 2021), seamounts (*e.g.,* Seabrook *et al.,* 2023) and abyssal plain mountains (*e.g.,* Harris *et al.,* 2014).

Turbidity current behaviour is strongly influenced by the flow characteristics (*i.e.,* velocity, thickness, concentration) and the nature of the seabed topography (*i.e.,* gradient, form, substrate) (*e.g.,* Kneller *et al.,* 1991; Edwards *et al.,* 1994; Patacci *et al.,* 2015; Tinterri *et al.,* 2016, 2022; Dorrell *et al.,* 2018a; Soutter *et al.,* 2021a). Turbidity currents can be reflected, deflected and/or ponded, generating spatial variations in flow competence and capacity, and hence the loci of deposition and depositional character (Allen, 1991; Hiscott, 1994; Kneller and McCaffrey, 1995, 1999). Recent technological advances have enabled direct velocity measurements of natural turbidity currents, and estimations of their concentration; however, these measurements have solely been acquired in submarine canyons or channels (*e.g.,* Talling *et al.,* 2023, and references therein). To date, no such measurements have been made where unconfined flows interact with seafloor topography, although palaeocurrent records from deposits show that complicated flow fields are established (*e.g.,* Pickering and Hiscott, 1985; Kneller *et al.,* 1991; Hodgson and Haughton, 2004).

The superimposition of unidirectional, and multidirectional and/or oscillatory flow components (*i.e.,* combined flows), produces distinctive bedforms with a high degree of spatial and morphological variability (Clifton, 1976). Such bedforms include hummocky cross-stratification (HCS) (*e.g.,* Arnott and Southard, 1990; Duke *et al.,* 1991; Dumas and Arnott, 2006; Wu *et al.,* 2024) and sigmoidal-cross lamination in small-scale and large-scale ripples (*e.g.,* Yokokawa, 1995; Dumas and Arnott, 2006; Tinterri, 2006, 2007). Hummock-like structures, large asymmetrical ripples, biconvex ripples and symmetrical megaripples have been documented in several deep-water systems (*e.g.,* Privat *et al.,* 2021, 2024; Tinterri *et al.,* 2022; Martínez-Doñate *et al.,* 2023; Siwek *et al.,* 2023; Taylor *et al.,* 2024a), and are typically postulated to have formed as a result of the generation of combined flows (*cf.* Mulder *et al.,* 2009). However, the combined flow paradigm in deep-water systems is based upon two-dimensional experimental observations.
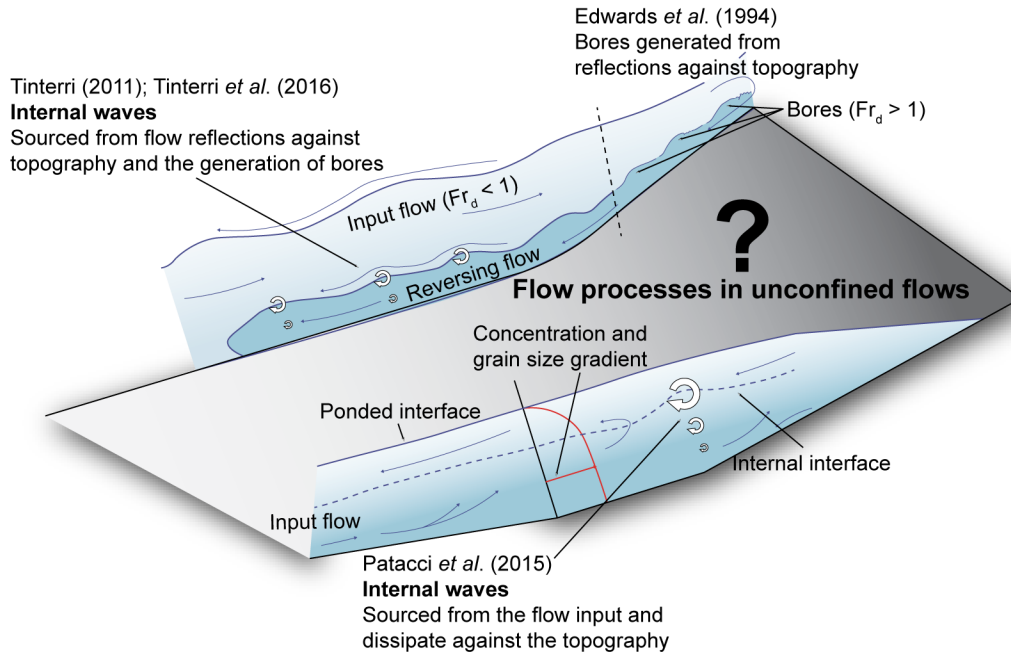
Figure 3.1: Schematic diagram of existing models proposed for the generation of internal waves in turbidity currents. The generation of internal waves in ponded turbidity currents in two-dimensional experimental conditions was demonstrated by Patacci *et al.* (2015). Tinterri (2011) and Tinterri *et al.* (2016) derived their model from outcrop following flow reflections against topography, following observations by Edwards *et al.* (1994) on the generation of bores. The question mark indicates the existing uncertainty in unconfined (three-dimensional) flow process behaviour.

Observations from 2D experiments of turbidity currents rebounding against topographic slopes (*e.g.,* Pantin and Leeder, 1987; Edwards *et al.,* 1994; Kneller and McCaffrey, 1995; Kneller *et al.,* 1997) have been used to support outcrop-based models for the formation of combined flows and the formation of hummock-like structures in deep-water systems (Fig. 3.1) (*e.g.,* Tinterri, 2011; Tinterri *et al.,* 2016, 2022; Privat *et al.,* 2021, 2024; Martínez-Doñate *et al.,* 2023). Tinterri (2011) suggests that flow transformations following the deceleration of flows upon incidence with slopes produce a hydraulic jump, akin to bores described semi-quantitatively with time-lapse photography and particle tracking by Edwards *et al.* (1994). It is hypothesised that the superimposition of the subcritical, unidirectional turbidity current, and an oscillatory flow component from the internal waves generated by supercritical upstream-migrating bores, produces combined flow in density currents (Tinterri, 2011; Tinterri *et al.,* 2016). Whether the same mechanisms for combined flow generation are active following the interaction of 3D,

unconfined density currents with planar containing topography has not been explored experimentally. Understanding the flow process interactions of unconfined low-density gravity currents with orthogonal containing slopes is therefore crucial for interpreting turbidity current evolution and onlap geometries, and bedform and facies variability in 3D space on slopes.

Although previous physical experiments have varied flow parameters and topographic configuration to examine turbidity current flow dynamics and deposits (*e.g.,* Kneller *et al.*, 1991, 1997; Edwards *et al.*, 1994; Amy *et al.*, 2004; Brunt *et al.*, 2004; Patacci *et al.*, 2015; Howlett *et al.*, 2019; Reece *et al.,* 2024) only one has investigated the interaction of 3D, unconfined gravity currents with simple, planar topographic slopes (Soutter *et al.,* 2021a). Soutter *et al.* (2021a) explored the depositional patterns around erodible basinal topography. With the basinal topography positioned orthogonal (90°) to the primary flow direction, and with sediment-laden gravity flows (17% by volume concentration), the denser material within the flow was observed to onlap the base of the containing slope, whereas the low density, finer grained material bypassed down-dip as it surmounted the topographic barrier (Soutter *et al.,* 2021a). Notably, the high concentration SGFs and steep angle of the experimental platform (11°) produced gravity currents on the slope and the proximal basin floor of the flume tank, upstream of the topographic barrier, with basal 'slip-velocities' (*i.e.,* the streamwise velocity measured at the base of the flow is not zero). This suggests that the SGFs of Soutter *et al.* (2021a) are more akin to grain-flows and debris-flows (*sensu* Méjean *et al.,* 2022).

In contrast, the experiments herein, are low-density, fully-turbulent, gravity currents that were unable to surmount the containing topographic slope. This experimental configuration permits observations of unconfined gravity current dynamics and evolution both at the base of, and on, the slope surface, which has not been previously explored. The influence of the topographic containment on flow processes is expressed by the topographic containment factor (h'), where $h' = h / h_{max}$, and h is flow height and h_{max} is the maximum run-up height. The containment factor increases as the slope angle increases from 20° to 30° to 40°. Increasing the slope angle affects the degree of flow stripping, and the velocity structure and evolution on the slope surface and at the base of the slope.

The aim of the current study is to document the interaction between scaled, unconfined saline density currents and partially containing orthogonal topography using 3D flume tank experiments. The objectives are to: (i) assess how the angle of the containing frontal topography (independently varied at 20°, 30°, and 40°) affects density current evolution and the generation

of combined flows; (ii) investigate how the mechanisms of flow reflection and deflection, and the novel observation of flow divergence, operate on the slope surface and influence interactions with the incoming flow at the base of the slope in unconfined settings; and (iii) discuss the effect of combined flows on the deposit character and onlap geometry in deep-water settings.

3.3   Methods

3.3.1   Experimental set-up

Experiments were performed in the Sorby Environmental Fluid Dynamics Laboratory, University of Leeds, UK, using a 10 m long, 2.5 m wide and 1 m deep flume tank (Fig. 3.2A and B). A 1400 L saline solution (2.5% excess density) was prepared in a 2000 L mixing tank. The saline solution was pumped (using an inverter controlled centrifugal pump) into the main tank through an inlet pipe centred on the experimental platform and into a straight-sided 0.62 m long, 0.26 m wide channel, before the flow debouched into the main tank. The main tank and inlet channel were both set on a horizontal basin floor (*i.e.,* 0° slope angle). The main tank was filled with tap water to a depth of 0.6 m. The pump speed was manually adjusted when the flow rate deviated from the reference value of 3.6 l s^{-1}. The flow rate variability was accurate to ±0.05 l s^{-1} of the reference value throughout the duration of the experiment (<2% error) (Table 3.1).
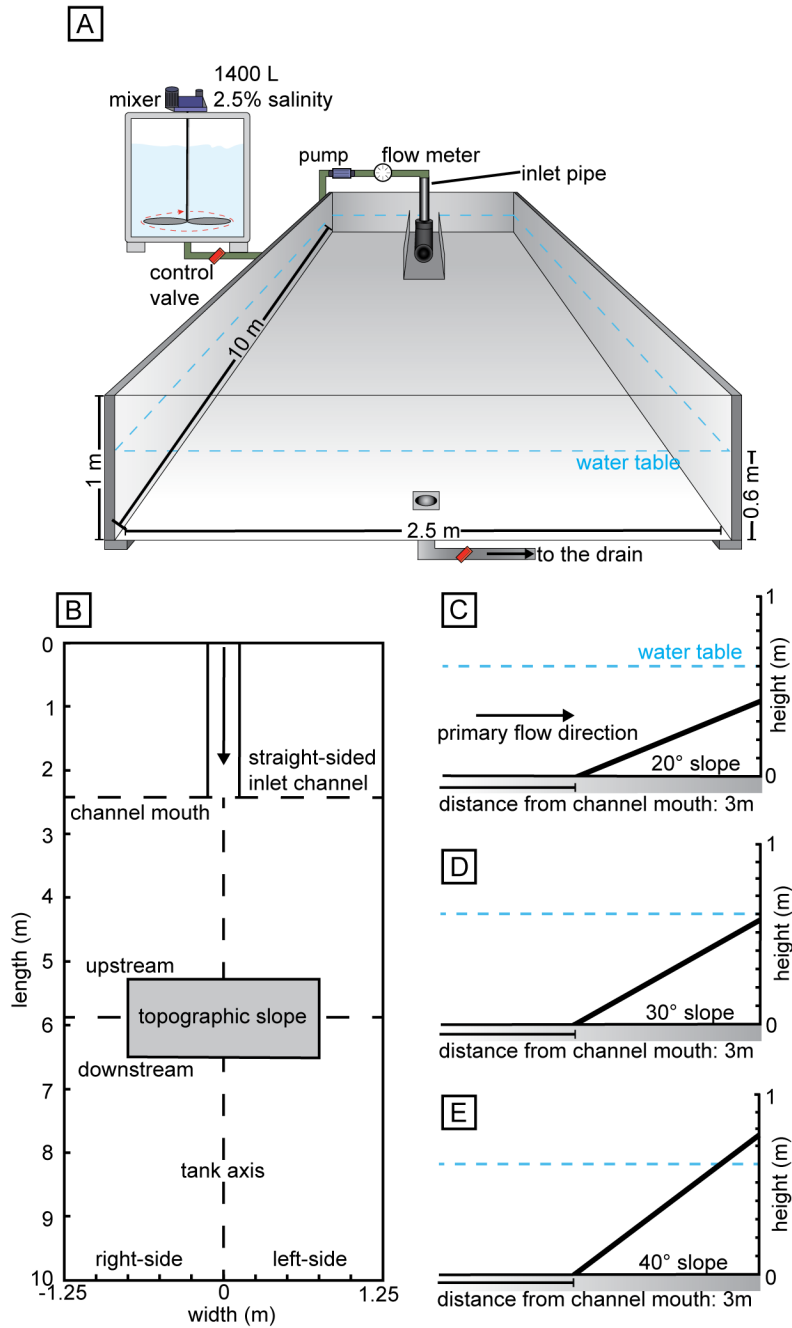
Figure 3.2: (A) Flume tank and mixing tank configuration. (B) Plan view of flume tank and slope position. Right-side and left-side is with respect to the primary flow direction. (C) to (E) Configurations of the 20°, 30° and 40° topographic slopes.

Table 3.1: Experimental configuration and data instrumentation (Ultrasonic Doppler velocity profiler (UVP), Acoustic Doppler velocity profiler (ADV) and density siphon) positions for all experiments. The instrumentation was placed along the tank axis. Unconfined-b and Unconfined-c: each instrument was positioned 3 m downstream of the channel mouth. For the experiments with the topographic slope, the slope was positioned 3 m downstream of the channel mouth and perpendicular to the primary flow direction. The reference values for mean flow rate (l s^{-1}) and the excess density of the input current (%) were 3.6 l s^{-1} and 2.5%, respectively.

Run	Slope angle (°)	Instrumentation (height up-slope (m))	Mean flow rate (l s^{-1})	Input Current density (%)
Unconfined-a	-	Visualisation	3.61	2.50
Unconfined-b	-	UVP	3.60	2.50
Unconfined-c	-	Density siphon	3.60	2.50
FC-20a	20	ADV (0)	3.61	2.50
FC-20b	20	ADV (0.10)	3.60	2.49
FC-20c	20	ADV (0.15)	3.61	2.50
FC-20d	20	Visualisation	3.60	2.51
FC-20e	20	Density siphon (0)	3.60	2.50
FC-20f	20	Density siphon (0.10)	3.60	2.50
FC-30a	30	ADV (base)	3.59	2.49
FC-30b	30	ADV (0.10)	3.60	2.50
FC-30c	30	ADV (0.20)	3.59	2.49
FC-30d	30	Visualisation	3.59	2.49
FC-40a	40	ADV (0)	3.59	2.49
FC-40b	40	ADV (0.08)	3.59	2.50
FC-40c	40	ADV (0.14)	3.60	2.49
FC-40d	40	Visualisation	3.58	2.50

3.3.2 Unconfined flow properties

Three initial experiments were performed without any containing topography. Firstly, the unconfined flow was visualised for the full duration of the experiment through the free-water surface, using an overhead camera above the flume tank (Video 3.1). Fluorescent tracer dye was used to aid visualisation of the flow. Measurements of the flow were recorded along the tank axis, at 3 m downstream of the channel mouth, to provide a base case for comparison with the flows interacting with the containing topography (Fig. 3.3A and B; Table 3.2). An Ultrasonic velocimeter Doppler profiler (UVP) (Met-Flow, UVP DUO, 4 MHz, Met-Flow SA, Lausanne, Switzerland) was used to record the instantaneous downstream flow velocity (Fig. 3.4A and B). The UVP recorded the multiplexed velocity output from a vertically stacked array of 10 transducers from the entire

flow height (*see* Table 3.2 for details of UVP parameters). Positive values of streamwise velocity are measured as the flow travels into the basin (Fig. 3.3A). A Nortek Vectrino Acoustic Doppler velocity profiler (ADV) (Nortek Group, Rud, Norway) was used to record the instantaneous flow velocities of the unconfined flow at 3 m downstream of the channel mouth, before the flow interacted with the slope. Where the ADV was used, positive streamwise velocities are measured as the flow travels towards the slope, whereas negative values record flow reversal. Additionally, for the ADV data (Fig. 3.3B), positive and negative values of cross-stream velocity data correspond to left-lateral and right-lateral movement of the flow, respectively, while positive and negative values of vertical velocity data correspond to the up – and down – movement of the flow, respectively. Such cross-stream and vertical data are not available from the UVP, which measures streamwise velocity only. Flow density was also measured (Fig. 3.4G and H), using an array of 12 siphons, and also for two additional experiments performed with frontally containing topography (Fig. 3.4I). Siphon sampling was initiated 5 s after the head passed, and lasted for 30 s. Twelve stacked siphons with 5 mm diameter tubing were deployed over a 0.095 m height, with the lowermost siphon 0.005 m above the base of the tank floor (Fig. 3.4G). The siphon array was connected to a peristaltic pump set to a constant withdrawal rate. The fluid was collected in sample pots and the density was measured using an Anton Paar DMA 35 portable densitometer (Anton Paar GmbH, Graz, Austria), with a resolution of 0.1 kg m^{-3}. The density was measured at a background temperature of 12°C, where the ambient density of water is 999.58 kg m^{-3}.

placeholder image for Video 1 (timestamp: 9 s)
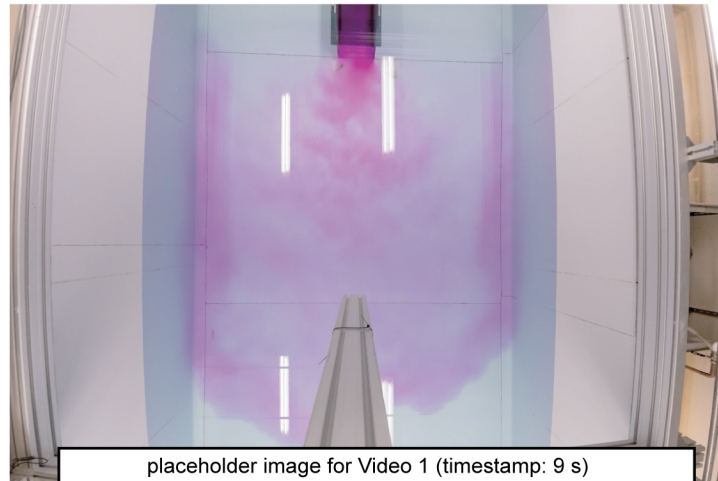
Video 3.1: Time-lapse video of the evolution of the unconfined density current throughout the experimental run (3X playback speed). The field of view is the full width of the tank (2.5 m). To aid flow visualisation, the input flow is dyed with fluorescent, purple tracer dye. The flow is observed to exit from the channel at the channel mouth and begins to radially expand into the basin. At 3 m from the channel mouth, the incoming head of the flow is unconfined. For the subsequent experiments with the orthogonal slope, the leading edge of the base of slope was positioned at 3 m from the channel mouth. https://youtu.be/KMpQTdzNNGc
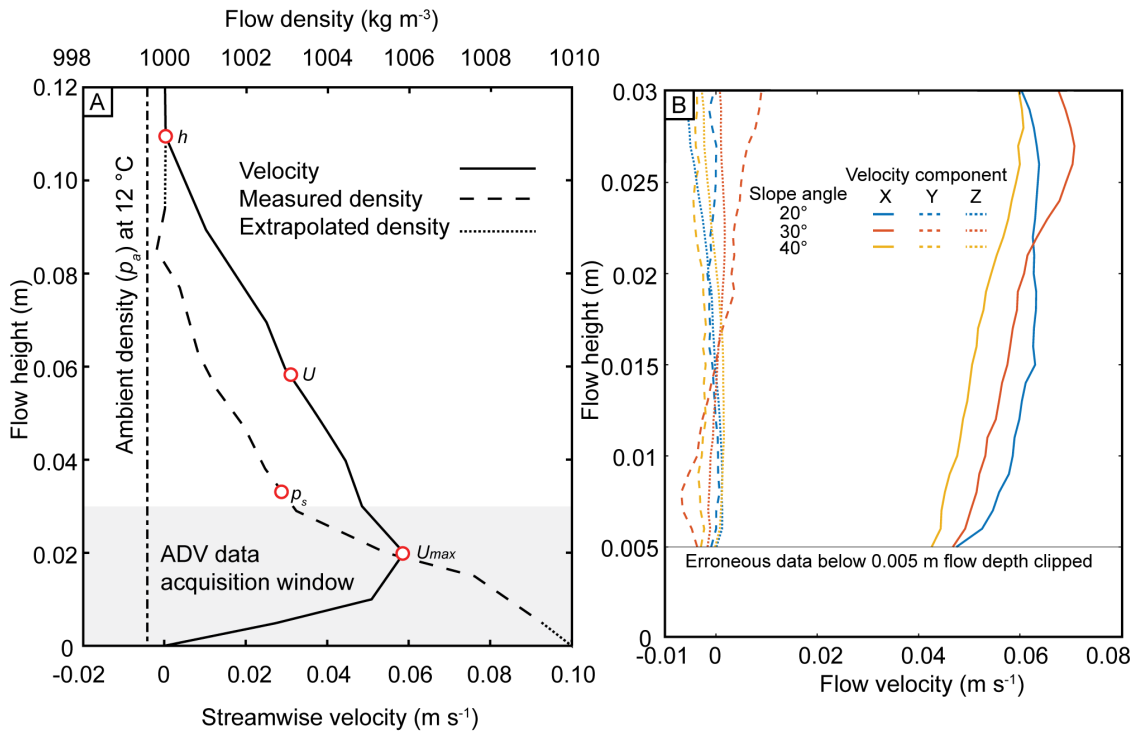
Figure 3.3: Comparative velocity profiles measured along the tank axis, 3 m downstream of the channel mouth. (A) Time-averaged streamwise velocity [using the Ultrasonic Doppler velocity profiler (UVP)] and density profiles of the unconfined flow. Both measurements were initiated 5 s after the head passed, and lasted for 30s. U_{max}, U and h denote the maximum streamwise velocity, depth-averaged streamwise velocity and flow height, respectively. For the density profile, p_s is the depth-averaged density. The dashed line indicates the measured density data, and the dotted line is density data extrapolated below 0.05 m flow depth and above 0.09 m flow depth. The density of the ambient water (p_a) as measured at a background temperature of 12°C, where the ambient density of water is 999.6 kg m^{-3}. (B) 5 s time-averaged velocity profiles [using the Acoustic Doppler velocity profiler (ADV)] measured from the first 5 s from the head of the flow at the 3 m position (base of slope), prior to the collapse of the flow downslope. The three components of measured velocity, *i.e.,* streamwise (X), cross-stream (Y) and vertical (Z) are indicated.

Table 3.2: Parameters for the Ultrasonic Doppler velocity profiler (UVP) and Acoustic Doppler velocity profiler ADV used in the current study. UVP is used to quantify instantaneous flow velocities of the unconfined flow, measured 3 m downstream of the channel mouth and along the tank axis. ADV is used to measure the instantaneous flow velocities 3 m downstream of the channel mouth along the tank axis, at the base of each slope configuration, and two positions on each slope surface.

UVP parameters		ADV parameters	
Instrument name	Met-Flow UVP Monitor 4	Instrument name	Vectrino Doppler Velocimeter
Sampling frequency	4 Hz	Sampling frequency	100 Hz
Probe height above tank floor	1, 2, 3, 4, 5, 6, 7, 9, 11, 13 cm	Speed of sound in water	1465 m s^{-1}
Velocity of ultrasound in water	1480 m s^{-1}	Number of transducers	4
Number of bins	128	Number of cells	31
Number of profiles per transducer	1000	Cell start below head of probe	40 mm
Sampling period	11 ms	Cell end below head of probe	70 mm
Velocity range	256 mm s^{-1}	Cell size	1 mm
Minimum velocity	-128 mm s^{-1}	Velocity range (streamwise)	500 mm s^{-1}
Maximum velocity	128 mm s^{-1}	Horizontal velocity range	497 mm s^{-1}
Minimum measurement distance	4.99 mm	Vertical velocity range	130 mm s^{-1}
Maximum measurement distance	99.71 mm	Instrument run time	240 s

3.3.3 Froude scaling

Calculations of the Reynolds number (Re) and densiometric Froude number (Fr_d), permit the Froude scaling of experimental saline density currents with natural turbidity currents (Yalin, 1971) (*see* Table 3.3). Here, the measured parameters of the unconfined flow 3 m downstream of the channel mouth were used. The measurements were initiated 5 s after the head passed, and lasted for 30 s. Froude scale modelling considers the Reynolds number (Re) relaxed compared to natural systems, but still within the fully turbulent regime, whereas the densiometric Froude number (Fr_d) is held as similar (*e.g.,* Graf, 1971; Peakall *et al.,* 1996). In this study, the Reynolds number is taken to be:

$$Re = \frac{p_s U h}{\mu}$$

(1)

where p_s is the mean depth-averaged density of the gravity flow measured using the density siphon array, U is the mean depth-averaged velocity, μ is dynamic viscosity, and h is the height at which the streamwise velocity recorded by the UVP reaches zero at the top of the flow. The depth-averaged density and velocity values are calculated by taking measurements at regularly-spaced

intervals (0.05 m) from the profiles in Fig. 3.3A, for the velocity over the full depth of the flow recorded by the UVP, and for the density over the available depth profile and extrapolated points at the base and top of the flow (Fig. 3.3A). The flow height was 0.11 m.

The Reynolds number is used as an indicator of turbulence, where Re >2000 represents a fully-turbulent flow (Simpson, 1997). Based on the unconfined reference experiments, the modelled flow had a Reynolds number of 3203 (Re = 3203), 3 m downstream of the channel mouth (*i.e.,* a fully turbulent flow).

The Froude number (Fr) describes the ratio of inertial to gravitational forces for stratified flows. To indicate which of these forces is dominant, flows of Fr >1 are termed supercritical, while flows of Fr <1 are termed subcritical (Ellison and Turner, 1959). Hydraulic jumps occur when flows transition from supercritical to subcritical, here the critical Froude number (Fr_c), is denoted by Fr_c = 1, although this can vary in strongly stratified density currents (*e.g.,* Sumner *et al.,* 2013; Cartigny *et al.,* 2014). For turbidity currents, the densiometric Froude number (Fr_d) is used to account for the reduced gravity (g') derived from the density difference between the flow and the ambient fluid (Kneller and Buckee, 2000):

$$Fr_d = U / \sqrt{g'h} \qquad (2)$$

$$g' = g(p_s - p_a)/p_a \qquad (3)$$

where g is acceleration due to gravity, and p_a is the density of the ambient fluid, measured at 12°C.

Based on the unconfined reference experiments, the modelled flow had a densiometric Froude number of 0.50 (Fr_d = 0.50) (*i.e.,* a subcritical flow). This value, and the visually-observed hydraulic jump following debouching of the flow at the channel mouth, may be considered analogous to basin floor flows that have passed through the channel-lobe transition zone, experiencing a loss in flow confinement (*e.g.,* Komar, 1971; Hodgson *et al.,* 2022).
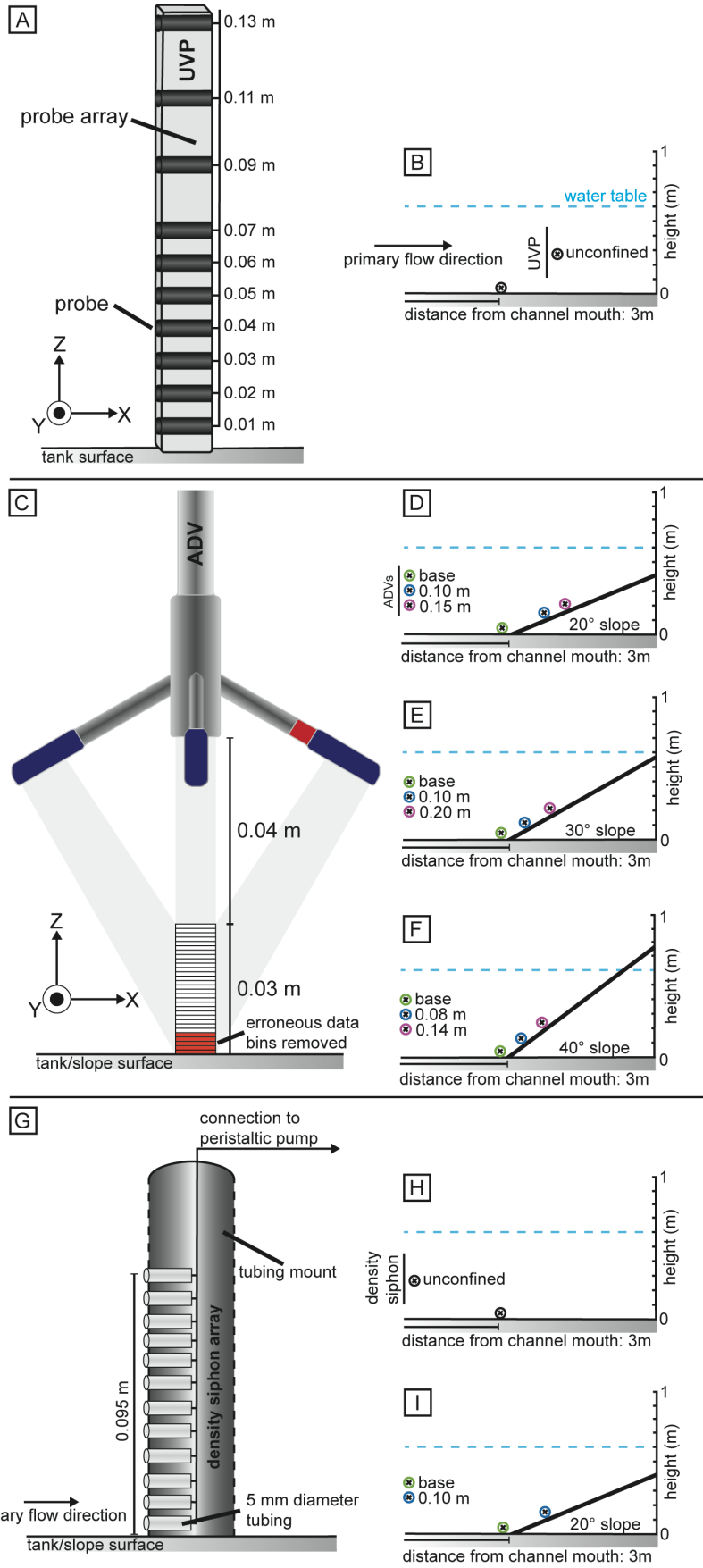
Figure 3.4: (A) Schematic diagram of the Ultrasonic Doppler velocity profiler (UVP), with the probe heights annotated. (B) Configuration of the UVP used to quantify the velocity of the unconfined density current. (C) Schematic diagram of the Acoustic Doppler velocity profiler (ADV). The basal 0.03 m is the data acquisition window of the ADV instrument. (D), (E) and (F) Configuration for the 20°, 30° and 40° slopes respectively, with the three ADV positions annotated. For (A) and (C), X, Y and Z are with respect to the velocity components. (G) Schematic diagram of the density siphon array. The siphon array was connected to a peristaltic pump set to a constant withdrawal rate to measure the density of the flow for the duration of the experiment. (H) and (I) Configuration of the siphon array used to quantify the density of the unconfined flow and for the 20° slope.

Table 3.3: Reynolds Number (Re) and Densiometric Froude Number (Fr_d) calculations. The Ultrasonic velocimeter Doppler profiler (UVP) measurements were recorded 3 m downstream of the channel mouth, along the flow's axis, and were initiated 5 s after the head of the unconfined passed, and lasted 30 s.

Parameter	
Mean depth-averaged density of current (P_s) (kg m^{-3})	1002.6
Density of ambient (P_a) (kg m^{-3})	999.6
Mean depth-averaged streamwise velocity (U) (m s^{-1})	0.029
Flow height (h) (m)	0.11
Dynamic viscosity (μ) (kg m^{-1} s^{-1})	0.001
Acceleration due to gravity (g) (m s^{-1})	9.81
Reynolds number (Re)	3203
Densiometric Froude number (Fr_d)	0.50

3.3.4 Containing topography

The topography was created using a linear, non-erodible slope. The 1.5 m wide planar slope, not spanning the full width of the 2.5 m wide flume tank, was positioned orthogonal (90°) to the primary flow direction and across the tank axis, 3 m downstream of the channel mouth (Fig. 3.2B). The angle was independently varied at 20°, 30° and 40° (Fig. 3.2C to E). The slope had a bevelled leading edge, thus minimising the step at the base of slope. For the 20°, 30° and 40° slope configurations the maximum height of the slope was 0.410, 0.585 and 0.760 m, respectively. The containment factor (h') value for all three slope configurations describes a flow unable to

surmount the containing topographic slope (Fig. 3.5). Due to the width of the slope (1.5 m) compared to the width of the tank (2.5 m), the flow is partially-contained.

The use of 20°, 30° and 40° slope angles herein is motivated by outcrop examples of onlap angles, previous experimental models and the water depth of the experimental basin. The modelled flows herein are more dilute than in previous experiments on topographic interaction of density currents (*e.g.,* Pantin and Leeder, 1987; Kneller *et al.,* 1991; Edwards *et al.,* 1994; Kneller, 1995; Patacci *et al.,* 2015), making them more mobile upslope. This coupled with the maximum water depth of the flume tank (0.6 m) meant that slope angles less than 20° were difficult to achieve without the flow surmounting the topographic slope or the flow travelling upslope and interacting with the free-water surface. Examples of similar slope angles used in previous experimental studies, include: 20° (Kneller *et al.*, 1991), 25° ± 5° (Soutter *et al.,* 2021a), 28° (Muck and Underwood, 1998) and 30° (Kneller, 1995). In Annot, France, the basin margin slope angle is between 10° and 30° (Sinclair, 1994; Pickering and Hilton, 1995; Joseph *et al.,* 2000; Puigdefàbregas *et al.,* 2004; Smith and Joseph, 2004; Tomasso and Sinclair, 2004; Soutter *et al.,* 2019). Locally steep topography is common in deep-water settings, *e.g.,* related to fault scarps (*e.g.,* Haughton, 1994; Hodgson and Haughton, 2004; Bakke *et al.,* 2013) and mass-transport deposits (*e.g.,* Martínez-Doñate *et al.*, 2021; Allen *et al.*, 2022). That being said, slope angles less than 10° are common in many basins (*e.g.,* Bakke *et al.,* 2013; Spychala *et al.*, 2017b), and the implications of this work for lower angle slopes are discussed later.

An initial experiment was performed using a series of GoPro Hero 10 Black cameras (GoPro, Inc., San Mateo, CA, USA) to visualise the flow at each topographic configuration. Fluorescent tracer dye was injected through a series of tubes (5 mm in diameter) on to the slope surface to aid visualisation (Videos 3.2–3.4). The dye injection tubes were inserted into an array of evenly-spaced drilled holes and were flush with the slope surface, thus minimising any surface irregularities. The rate of dye injection was controlled using a peristaltic pump, set to a constant discharge rate for all experimental runs. The net input of fluid into the tank will lead to a diffuse compensatory return flow in the upper part of the water column, however this could not be visually observed, and the orthogonal orientation of the slope stops any return flow from directly affecting the experiments. For each slope configuration, three subsequent runs with an ADV were performed to quantify the instantaneous three-dimensional flow velocities, at a frequency of 100 Hz (*see* Table 3.2 for details of ADV parameters). The ADV can measure 30 measurement points with three component velocities (downstream and cross-stream components, X and Y, respectively, and two measurements of the vertical component, Z1 and Z2, associated to the X and

Y receivers of the ADV probe, respectively) over a depth range of 0.03 m. The measurement zone starts 0.04 m below the probe head, and with the basal measurement recorded at the interface of the tank floor and the slope (Fig. 3.4C to F). The five lowermost ADV measurement points were clipped from all experimental runs due to excessive data noise resulting from signal interferences with the floor/slope. The ADV was positioned along the tank axis, at the base of each slope configuration to quantify the instantaneous velocities of the flow interacting with the topographic slope. The position of the ADV on the slope surface was dependent on the slope angle and determined with the aid of the flow visualisation videos (*see* Table 3.1 for ADV positions). For the experiments performed with the UVP and ADV the saline density currents were seeded with neutrally-buoyant, hollow glass microspheres (Sphericel 110-P8) (Potters Industries, Malvern, PA, USA) to provide an acoustic contrast to the flow, which produces the white colour to the flows observed in Videos 3.2–3.4. The lowermost ADV was located at the approximate height upslope at which a stable flow front developed. The uppermost position was located where the flow height was approximately 0.07 m thick; at flow thicknesses below 0.07 m, the precision of the ADV data measurement window is not considered accurate enough. All instantaneous velocity data recorded by the UVP and ADV were post-processed to remove any data spikes more than two standard deviations away from the mean and replaced with an 11-point moving average (*see* Buckee *et al.*, 2001; Keevil *et al.*, 2006).
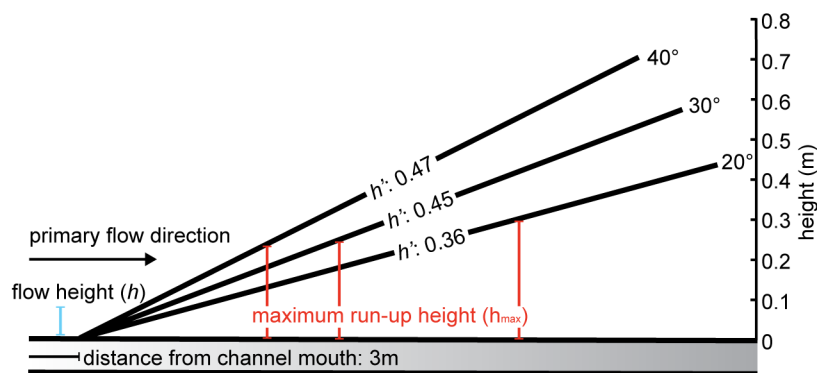
Figure 3.5: Containment factor (h') for each slope configuration ($h' = h/h_{max}$), where h = flow height (0.11 m) and h_{max} = maximum run-up height. The observed h_{max} for the 20°, 30° and 40° slopes is 0.30 m, 0.24 m and 0.23 m, respectively. For all experimental configurations, the incoming flow was unable to surmount the containing topographic slope.

placeholder image for Video 2 (timestamp: 20 s)

Video 3.2: Annotated real-time video illustrating the temporal evolution of the flow with a 20° slope. Fluorescent dye injected at a series of lateral points onto the slope surface was used to visualise the interaction of the density current and the containing topography. Gridded white lines were marked on the slope surface to aid the identification of the height at which the stable flow front developed, and the maximum run-up height (h_{max}). https://youtu.be/mqRIlQe9plU

placeholder image for Video 3 (timestamp: 17 s)
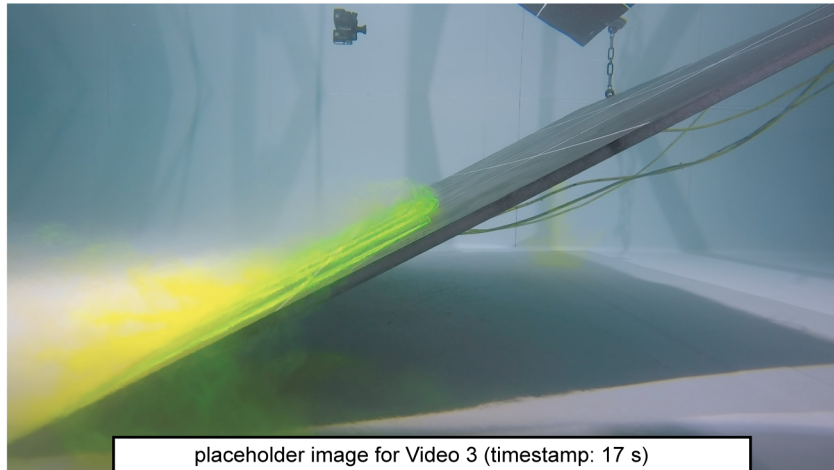
Video 3.3: Annotated real-time video illustrating the temporal evolution of the flow with a 30° slope. Fluorescent dye injected at a series of lateral points onto the slope surface was used to visualise the interaction of the density current and the containing topography. Gridded white lines were marked on the slope surface to aid the identification of the height at which the stable flow front developed, and the maximum run-up height (h_{max}). https://youtu.be/LYQUPHA_k3E

placeholder image for Video 4 (timestamp: 10 s)
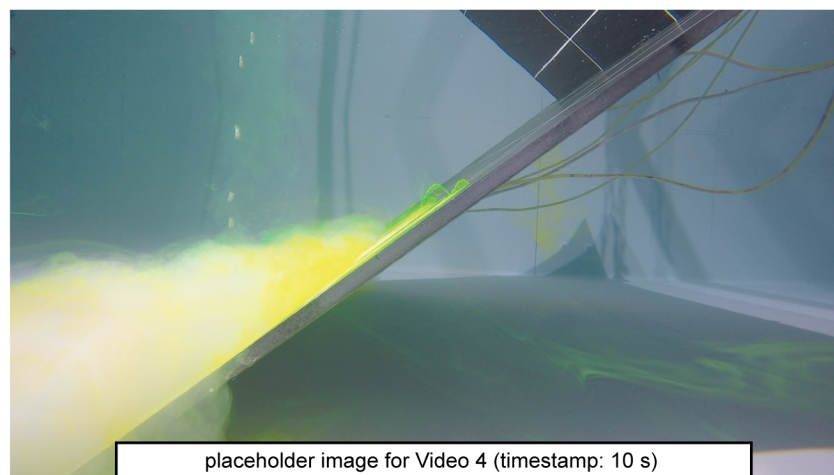
Video 3.4: Annotated real-time video illustrating the temporal evolution of the flow with a 40° slope. Fluorescent dye injected at a series of lateral points onto the slope surface was used to visualise the interaction of the density current and the containing topography. Gridded white lines were marked on the slope surface to aid the identification of the height at which the stable flow front developed, and the maximum run-up height (h_{max}). https://youtu.be/BJ5nS5pum3o

3.4   Results

3.4.1   Unconfined flow

3.4.1.1   Unconfined flow

The flow measured at 3 m downstream of the channel mouth is quasi-steady, with a radially spreading front (Video 3.1). Both the UVP velocity and density measurements of the unconfined flow were initiated 5 s after the head passed, and lasted for 30 s (Fig. 3.3A). The time-averaged streamwise velocity recorded by the UVP (Fig. 3.3A) gives a maximum streamwise velocity (U_{max}) of 0.059 m s^{-1}, at a height of 0.02 m (Fig. 3.3A). The flow height is 0.11 m, and the mean depth-averaged streamwise flow velocity is 0.029 m s^{-1} (Fig. 3.3A). Prior to the interaction of the unconfined flow with the slope, the ADV measured the three components of velocity for the incoming front of the head of the current, over a 5 s period. The U_{max} of the incoming flow is 0.065 ± 0.005 m s^{-1} (Fig. 3.3B); albeit the height over which the ADV measures may not quite capture the U_{max} position in the 40° case (see unbroken yellow velocity profile in Fig. 3.3B), and thus may be an under-estimate. Over the 5 s window in which it was recording the unconfined flow velocity, the ADV measured the cross-stream velocity component as -9% to 12% of the maximum streamwise velocity, and the vertical velocity component ranges as -9% to 2% of the maximum streamwise velocity (Fig. 3.3B). The flow is well-stratified at a distance of 3 m downstream of the channel mouth (Fig. 3.6B). The dense, basal region of the flow (0.03 m thick) is separated from the dilute, upper region of the flow (0.06 m thick) by a distinct density interface (Figs 3.3A and 3.6B). The density of the flow decreases upward from 1009 kg m^{-3} (0.9% excess density) in the basal region of the flow to 1000 kg m^{-3} at 0.09 m flow height (Fig. 3.3A).

A

primary flow direction →

distance from channel mouth: 3m

slope angle

	20°	30°	40°
initial flow reversal	□	□	□
h_{max}	×	×	×
flow front development	○	○	○

B — Unconfined-d

ambient water

dilute, upper region

density interface
dense, lower region

C — FC-20e

ambient water

flow mixing and thickening

D — FC-20f

ambient water

dilute region stripped
from dense region

density (kg m⁻³)
999.6   1012.5
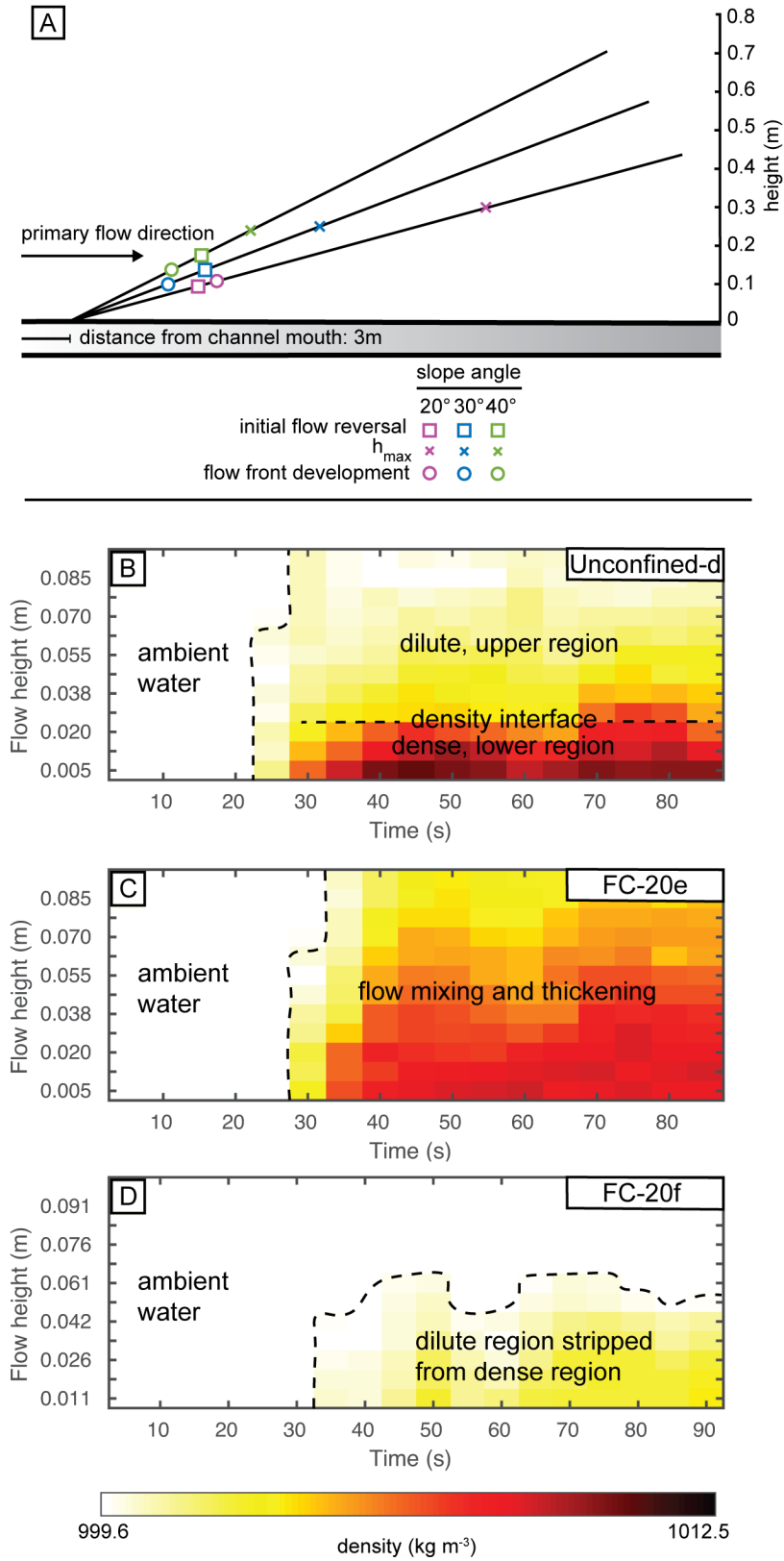
Figure 3.6: Figure caption overleaf.

67

Figure 3.6: (A) The extent of the zone of flow stripping that is generated on the slope surface for each topographic configuration. The lower limit of the zone of flow stripping is demarcated by the height of initial flow reversal. The upper limit is defined by the maximum run-up height (h_{max}) of the flow. The extent of the zone of flow stripping decreases with an increasing containment factor. (B-D) Density time series. (B) the unconfined flow recorded at the base of slope, (C) at the base of the 20° slope (FC-20e), and (D) 0.1 m upslope (FC-20f) along the tank axis.

3.4.2   Flow interactions with containing topography

The distance downstream from the channel mouth to the containing topography (3 m) and input flow parameters were uniform for all experimental runs. The slope was positioned orthogonal to the primary flow direction, with the slope angle independently varied at 20°, 30° and 40°. Comparing how changes in slope angle affect the flow velocity and density structure, and evolution, provides a better understanding of processes active at the base of, and on, the slope surface. The flow visualisation (Videos 3.2–3.4, Figs 3.7 and 3.11) permits qualitative observations of the flow processes across the width of the slope surface and at the base of slope, while, at a quantitative level, the ADV (Figs 3.8, 3.9, 3.10, 3.12 and 3.13) and density (Fig. 3.6B to D) measurements provide data on the central axis of the flow.

3.4.2.1   Lateral flow spreading on the slope surface

Upon incidence with the containing topography, the flow visualisation videos show that the superelevation (*i.e.*, ability of the flow to run-up surfaces several times their flow depth) of the flows, and the nature of the radially spreading front, differ as a function of slope angle (Videos 3.2–3.4, Fig. 3.7). At 20°, the flow continues to spread radially on the slope surface, diverging away from its central streamline, with a high degree of spreading towards the lateral edges of the slope (Video 3.2). At 20°, h_{max} occurs along the flow axis, approximately 0.30 m upslope, 2.73 times the flow height (Video 3.2, Fig. 3.7A). The initial degree of lateral flow spreading on the 30° slope is like that observed at 20° (Video 3.3). However, because of the increased containment at 30°, the component of flow reflection on the slope surface is enhanced, resulting in less lateral flow spreading (Video 3.3). At 30°, h_{max} occurs along the flow axis, approximately 0.24 m upslope, 2.19 times the flow height (Video 3.3, Fig. 3.7B). At 40°, the radially spreading head decelerates rapidly at the base of slope and is deflected along the basal edge of the slope (Video 3.4). The enhanced topographic steering generated at 40° decreases the flow's upslope momentum compared to the 20° and 30° slopes, and hence decreases the degree of lateral flow spreading on the slope. At 40°,

h_{max} occurs towards the lateral edges of the slope, approximately 0.23 m upslope, 2.10 times the flow height (Video 3.4, Fig. 3.7C).

3.4.2.2 *Degree of flow thinning and stripping*

The flow visualisation from each slope configuration, shows that the flow thins as it decelerates upslope (Videos 3.2–3.4). Density measurements 3 m downstream show a well-stratified flow with a distinct interface between the dense, basal region and the dilute, upper region of the flow (Fig. 3.6B). The density measurements recorded at 0.1 m upslope of the 20° slope show that the dilute region of the flow decouples from the dense region of the incoming flow (Fig. 3.6D) and continues to thin upslope before reaching h_{max} (Video 3.2). The thinning and density decoupling of the flow as it travels up the counter slope is akin to the process of flow stripping. Flow stripping is observed at submarine channel bends, where the upper dilute part of a flow decouples from the lower part and overtops the channel at the bend and the residual flow stays within the channel (Piper and Normark, 1983). The zone of flow stripping that develops at each slope configuration is defined qualitatively (Fig. 3.6A), using the flow visualisation (Videos 3.2–3.4), and supported quantitatively for the 20° slope using density measurements of the flow (Fig. 3.6C and D). The lower limit of the zone of flow stripping is demarcated by the height upslope at which the basal region of the flow reverses downslope (Videos 3.2–3.4), hence marking the onset of flow thinning upslope (termed 'height of initial flow reversal') (Fig. 3.6A). The upper limit of the zone of flow stripping is defined by h_{max} (Fig. 3.6A). Upon incidence with the 20° slope, the height of initial flow reversal occurs approximately 0.09 m upslope (Video 3.2). The dense region of the decelerating flow reverses downslope, causing the flow to thicken and mix as it interacts with the incoming flow at the base of slope, generating a non-stratified flow (Fig. 3.6C). The degree of flow thinning and zone of flow stripping generated on the 20° slope is enhanced compared to the 30° slope (Fig. 3.6A). At 30°, the initial flow reversal occurs approximately 0.13 m upslope (Video 3.3) and the zone of flow stripping extends to 0.24 m upslope (Fig. 3.6A). At 40° slope, the flow decelerates strongly at the base of slope and there is little decoupling observed between the dense region of the flow and the more dilute region of the flow on the slope surface (Video 3.4). The height of the initial flow reversal in this 40° case is approximately 0.18 m, slightly higher than that on the 20° and 30° slopes. Despite this, the smaller h_{max} value of approximately 0.23 m upslope led to a smaller zone of flow stripping (Fig. 3.6A). The degree of flow stripping and thinning strongly influences the character of the reversed flow at the base of slope.
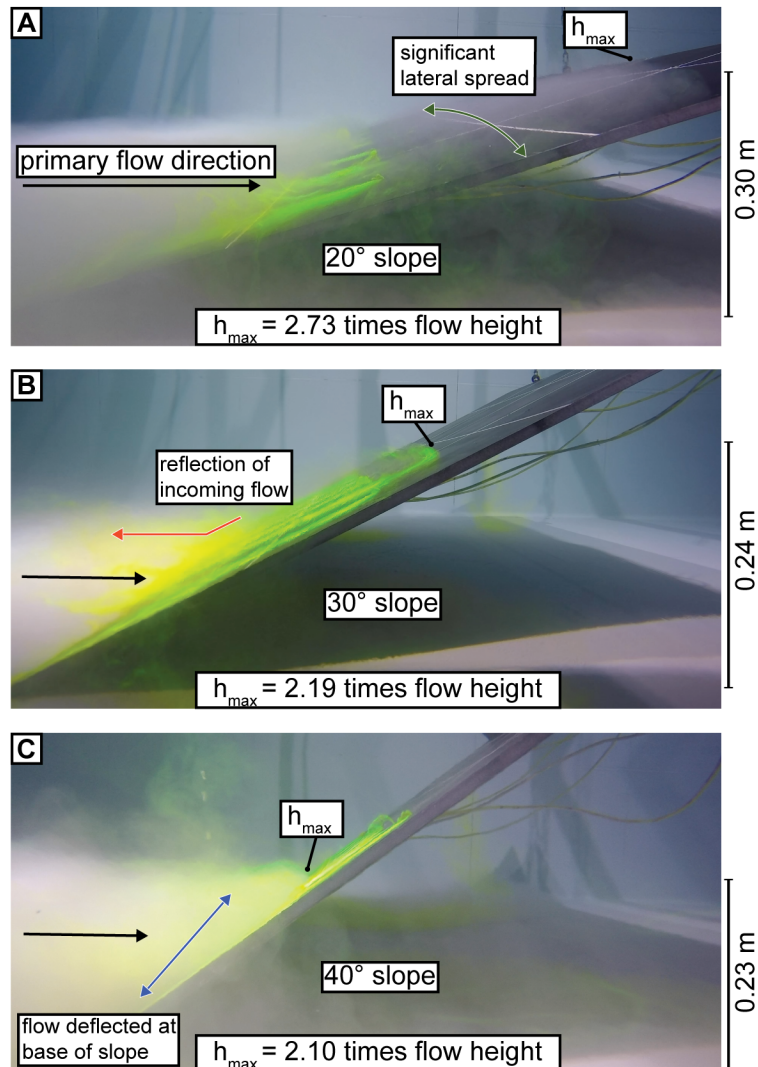
Figure 3.7: Photographs captured using underwater cameras, with the maximum run-up height (h_{max}) and degree of lateral flow spreading annotated. (A) 20° slope. (B) 30° slope. (C) 40° slope. Fluorescent dye is injected at a series of lateral points onto the slope surface using a peristaltic pump set at a constant flow rate, to aid in the visualisation of the incoming flow interacting with the slope. The h_{max} and degree of lateral flow spreading decreases as the angle of the slope, and hence the topographic containment factor, increases.

3.4.2.3   *Primary and secondary flow reversals*

The first recorded negative streamwise velocity signal corresponds to the primary flow reversal (Figs 3.8, 3.9 and 3.10). The subsequent repeated fluctuations correspond to the secondary flow reversals (Figs 3.8, 3.9 and 3.10). The flow visualisation (Videos 3.2–3.4) and depth-constrained

ADV velocity time-series data (Figs 3.8, 3.9 and 3.10) demonstrate how the magnitude of the primary flow reversal and the fluctuations of the secondary flow reversals are a function of slope angle. The magnitude of the primary flow reversal is characterised by the arrival time of the primary reversal at the base of the slope, the periodicity of the reversal, and its velocity signal.

On a slope of 20°, before the primary flow reversal is recorded at the base of slope, the parental flow decelerates due to the interaction with the weakly reversing flow as it travels downslope. The primary flow reversal occurs approximately 12 s after the parental flow initially arrived (Video 3.2), with a recorded streamwise velocity of approximately -0.03 m s^{-1} (Fig. 3.8C). The arrival of the primary flow reversal at the base of slope marks the onset of enhanced cross-stream velocity fluctuations as the reversed flow and parental flow interact and are superimposed against each other (Fig. 3.8D). The primary flow reversal is recorded at the base of slope over a 9 s window (Fig. 3.8C). Before the parental flow re-establishes at the base of slope, a 4 s period of stasis, where the streamwise velocity is negligible (Fig. 3.8C), marks the period of the greatest cross-stream velocity variability (Fig. 3.8D). At 30°, there is limited deceleration of the parental flow at the base of slope before the primary flow reversal is recorded (Fig. 3.9C). The arrival of the primary flow reversal is recorded 6 s after the parental flow initially arrived at the base of slope (Fig. 3.9B), with a streamwise velocity of approximately -0.04 m s^{-1} (Fig. 3.9C). The interaction and superimposition between the primary flow and the reversal generates an increased cross-stream velocity component at the base of slope (Fig. 3.9D). The primary flow reversal is maintained for approximately 10 s before the parental flow re-establishes (Video 3.3). At 30°, following the interaction of the primary flow reversal with the parental flow, the body of the density current appears to inflate, thickening for approximately 30 s becoming flat-topped and subsequently propagating upstream of the topographic slope (Video 3.3). The highest degree of flow thickening is observed at the 30° slope (Video 3.3). At 20° and 40°, the inflated, flat-topped cloud generated at the base of slope is maintained for approximately 10 s and 20 s, respectively, before then propagating upstream of the topographic slope and dissipating throughout the experimental basin (Videos 3.2 and 3.4). Despite the propagation of the thickened cloud upstream, no soliton wave trains or bores were observed, as has been observed in 2D experiments, involving a more confined flow (*i.e.*, within a channel) (*e.g.,* Pantin and Leeder, 1987; Edwards *et al.*, 1994; Kneller *et al.*, 1997). At 40°, the primary flow reversal arrives at the base of slope, approximately 12 s after the parental flow first arrived with a decreased streamwise velocity of approximately -0.02 m s^{-1} (Fig. 3.10C). The parental flow at the base of slope re-establishes approximately 7 s after the primary flow reversal was first recorded (Fig. 3.10C). There is negligible streamwise velocity variability in the basal 0.005-0.01 m of the flow during

the primary flow reversal (from 12–17 s of Fig. 3.10C), whereas the cross-stream velocity component during the primary flow reversal operates over the full height of the data acquisition window, at approximately 0.03 m s^{-1} (Fig. 3.10D).

A quasi-stable flow front develops on the slope surface following the primary flow reversal (Videos 3.2–3.4). The flow front is maintained for the remainder of the experiment following repeated episodes of secondary flow reversal on the slope surface and the re-establishment of the parental flow (Videos 3.2–3.4). The height upslope at which the flow front develops, the velocity structure, and the frequency of secondary flow reversals recorded on the slope surface and at the base of slope, is a function of slope angle.

At 20°, a flow front with a linear trace, forms at an average height of 0.11 m upslope, one times the flow height, across the width of the slope (Video 3.2, Fig. 3.11A). However, the height of the flow front fluctuates between 0.10 and 0.14 m upslope as the flow repeatedly reverses downslope before the flow re-establishes (Video 3.2). The streamwise velocity fluctuates between 0.02 and -0.02 m s^{-1}, and the cross-stream velocity between 0.01 and -0.01 m s^{-1} (Fig. 3.8A and B). At 30°, the flow front develops approximately 0.10 m upslope, 0.91 times the flow height, with a weakly sinusoidal trace (Video 3.3, Fig. 3.11B). At 30°, the streamwise velocity of the flow front fluctuates between 0.01 and -0.01 m s^{-1} (Fig. 3.9A), and the episodes of secondary flow reversal and re-establishment are less defined compared to the 20° slope (Fig. 3.8A). At 40°, the initial development of the flow front coincides with greatest cross-stream velocity fluctuations (approximately 0.05 m s^{-1}) of any slope configuration (Fig. 3.10B). For approximately 40 s following the establishment of the flow front, the cross-stream velocity signal is maintained at approximately 0.05 m s^{-1}, whereas the streamwise velocity signal is negligible (Fig. 3.10A and B). As the positive streamwise velocity at the flow front re-establishes after approximately 50 s (Fig. 3.10A), the cross-stream velocity becomes negative (approximately -0.02 m s^{-1}) (Fig. 3.10B). At 40°, the flow front develops approximately 0.13 m upslope, 1.19 times the flow height (Video 3.4, Fig. 3.11C).

Single-sided amplitude spectral analysis using a Fast Fourier Transform of the velocity fluctuations (*cf.* Dorrell *et al.*, 2018b), at the lowermost ADV measurement point (0.005 m above the base of the tank/slope), was used to assess the frequency of secondary flow reversals (Fig. 3.12). The lowermost ADV measurement point was used for these analyses as this is closest to the floor, and thus most representative of the conditions affecting sediment transport and deposition. Following the development of the flow front on the slope surface at the 20° and 40°

slope (>40 s into flow), low frequency oscillations in the range of approximately 10^0 to 10^{-1} Hz are observed at the middle ADV position (Fig. 3.12D and P, respectively). The increased power of the oscillations compared to the 30° slope (Fig. 3.12J) is due to the greater observed fluctuations in the streamwise velocity component (Figs 3.8A, 3.9A and 3.10A). At 20° and 40° the power spectra decrease with height up-slope (Fig. 3.12 B, H and N) and dissipates at the base of slope (Fig. 3.12F, L and R). Whereas, at 30°, the power spectra increase between the middle ADV position (Fig. 3.12J) and the base of slope (Fig. 3.12L).
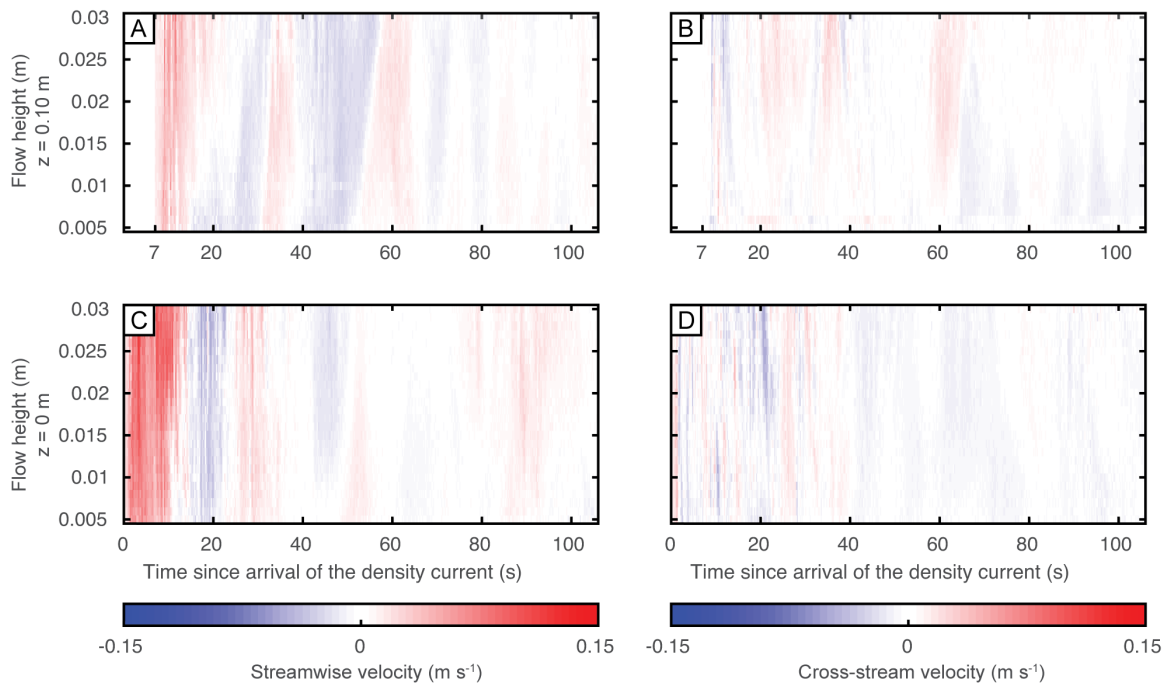
Figure 3.8: Acoustic Doppler velocity profiler (ADV) velocity time series of saline density currents interacting with the 20° slope. (A) and (B) Streamwise and cross-stream velocity time series respectively (z = 0.10 m upslope). (C) and (D) Streamwise and cross-stream velocity time series respectively (z = 0 m, base of slope). The clipped data from the first 7 s in (A) and (B) represents the time taken for the flow to travel from the base of slope to 0.1 m upslope.
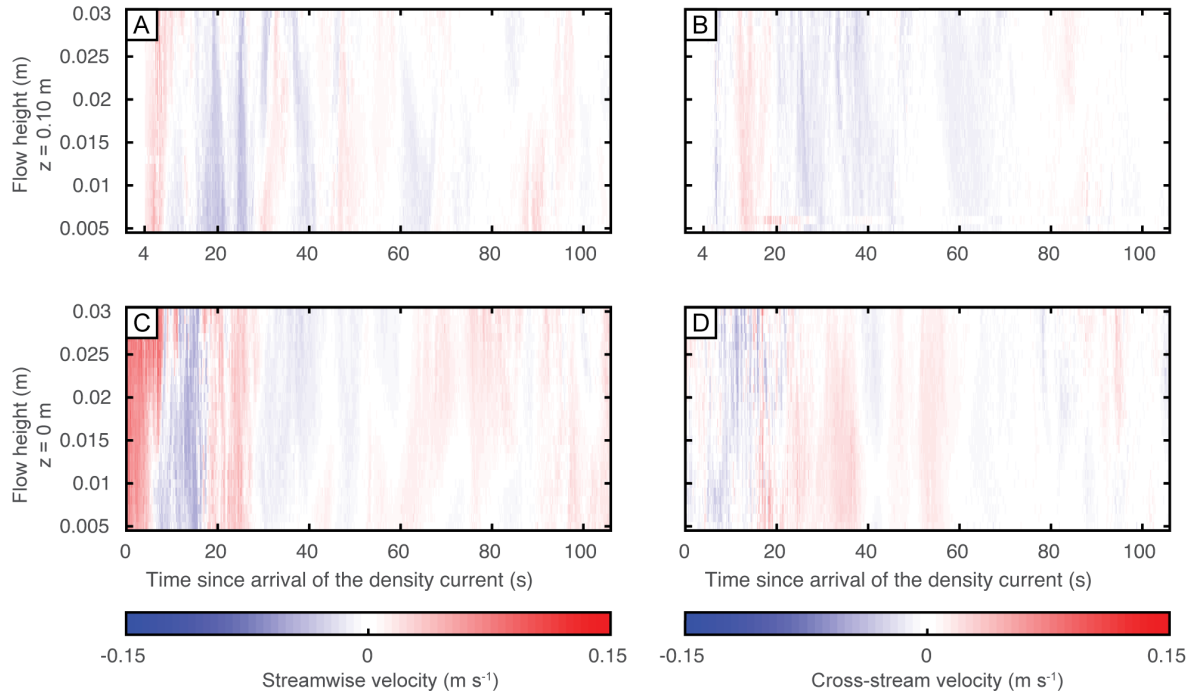
Figure 3.9: Acoustic Doppler velocity profiler (ADV) velocity time series of saline density currents interacting with the 30° slope. (A) and (B) Streamwise and cross-stream velocity time series respectively (z = 0.10 m upslope). (C) and (D) Streamwise and cross-stream velocity time series respectively (z = 0 m, base of slope). The clipped data from the first 4 s in (A) and (B) represents the time taken for the flow to travel from the base of slope to 0.1 m upslope.
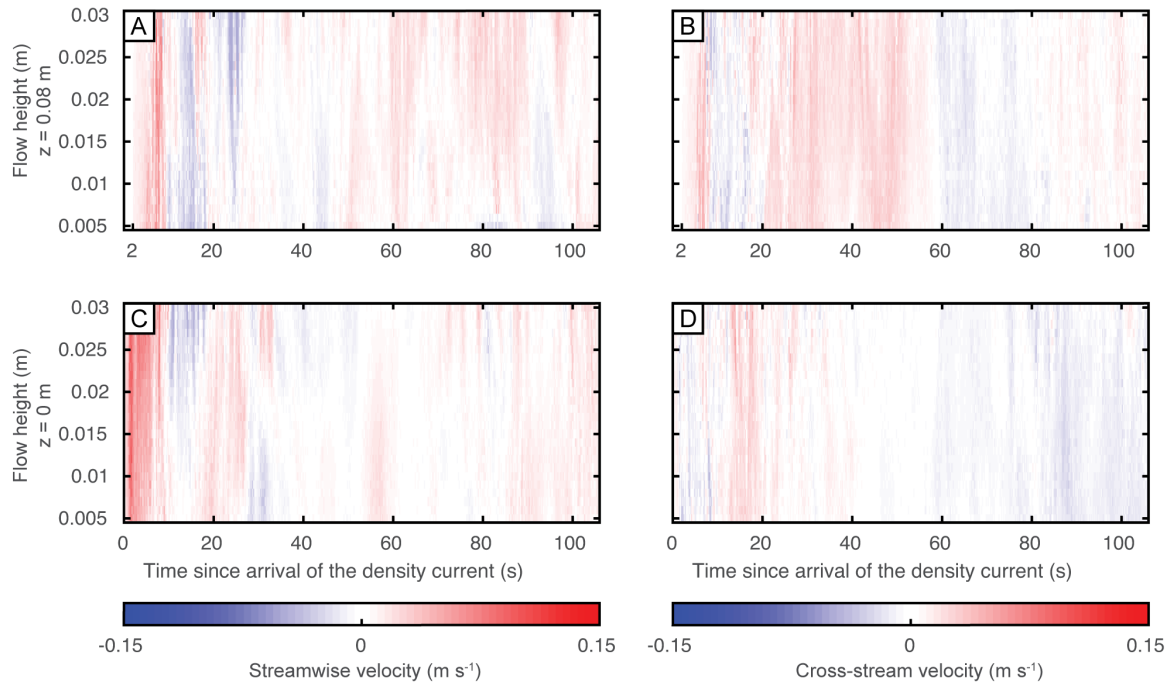
Figure 3.10: Acoustic Doppler velocity profiler (ADV) velocity time series of saline density currents interacting with the 40° slope. (A) and (B) Streamwise and cross-stream velocity time series respectively (z = 0.08 m upslope). (C) and (D) Streamwise and cross-stream velocity time series respectively (z = 0 m, base of slope). The clipped data from the first 2 s in (A) and (B) represents the time taken for the flow to travel from the base of slope to 0.08 m upslope.

3.4.2.4 *Temporal velocity variability*

Flow visualisation shows the development of complex, multidirectional flows (*i.e.*, combined flows) qualitatively, on the slope surface and at the base of slope (Videos 3.2–3.4). To better understand the generation of complex, multidirectional flows (*i.e.,* combined flows), the nature of temporal streamwise and cross-stream velocity variations with position (height) on the slope are considered. Here, analysis focusses on the lowermost ADV measurement point (0.005 m above the base of the tank/slope), as measured on the axis of the flow. The incoming flow recorded at the base of each slope (<15 s into flow) has a similar streamwise and cross-stream velocity signal (Fig. 3.13G to I). The streamwise and cross-stream velocity magnitude and variability decrease through time and with height up-slope, in all cases (Fig. 3.13). The interaction between the primary flow and the parental flow and superimposition of flow components marks the onset of increased cross-stream velocity variations at the base of the 20° and 30° slope (Fig. 3.13G and H).

At the base of the 40° slope (Fig. 3.13I), the streamwise velocity of the primary flow reversal and the cross-stream velocity variability before the establishment of the flow front (<40 s into flow) is decreased compared to the lower slope angle configurations. Whereas, on the slope surface, the ADV data from the 40° slope (Fig. 3.13F) demonstrate increased streamwise and cross-stream velocity variability compared to the lower slope angle configurations (Fig. 3.13D and E).
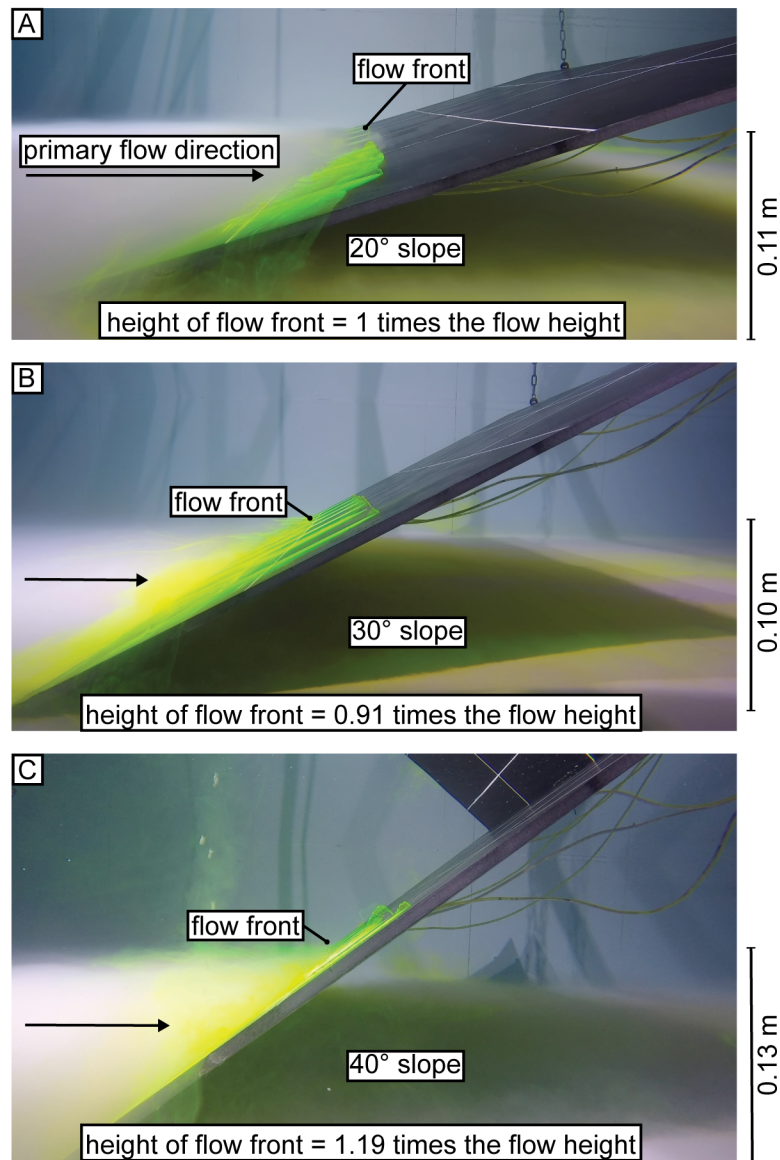
Figure 3.11: Photographs captured using an underwater camera, with the height (annotated) at which a quasi-stable flow front develops. (A) 20° slope. (B) 30° slope. (C) 40° slope. At each topographic configuration, a quasi-stable flow front develops on the slope surface following the primary flow reversal of the flow downslope and the subsequent re-establishment of the parental flow.
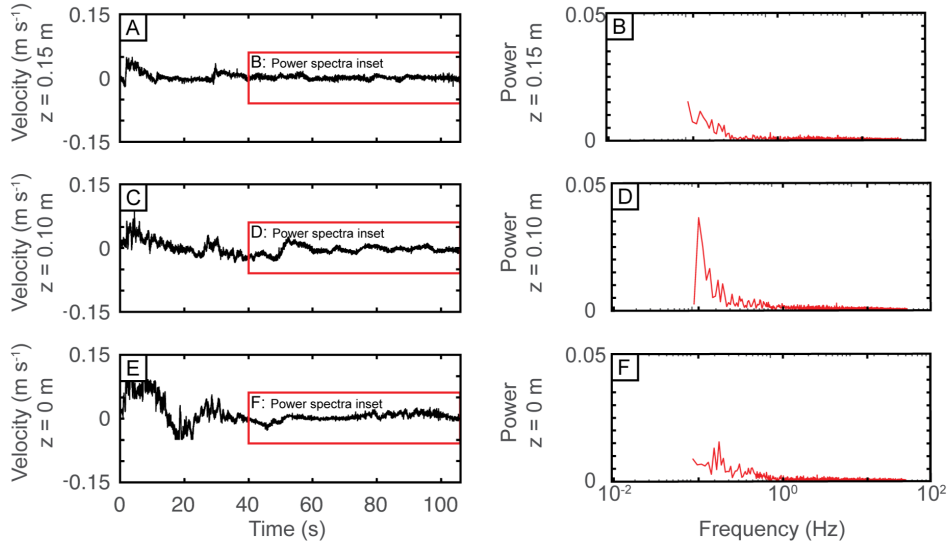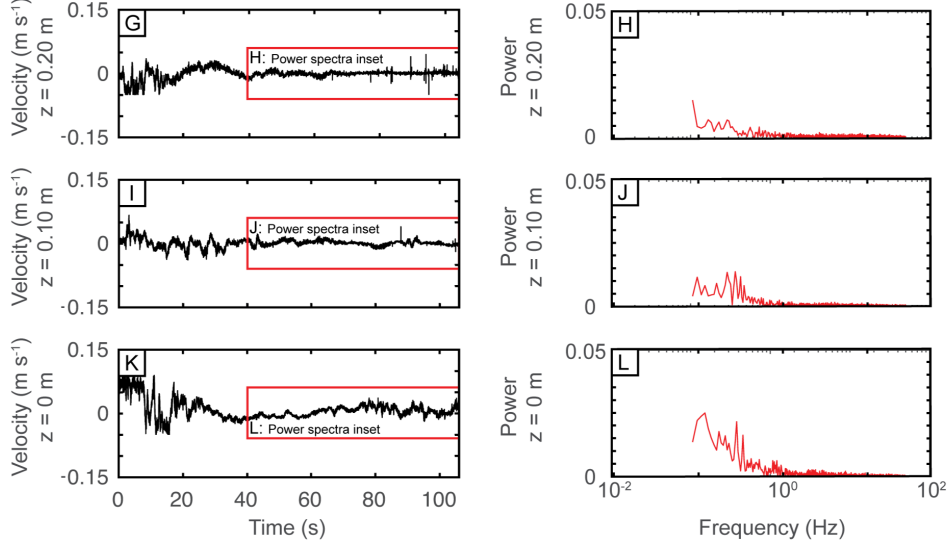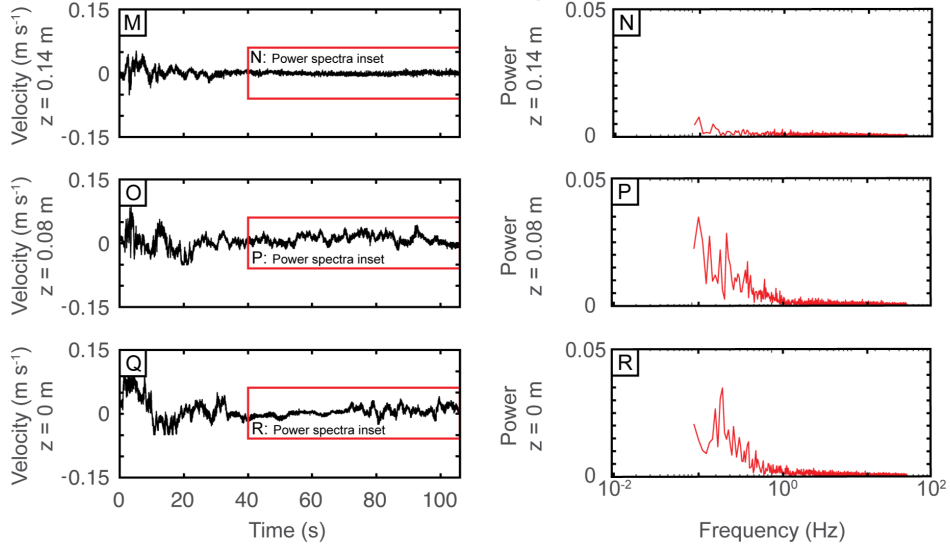
Figure 3.12: Acoustic Doppler velocity profiler (ADV) streamwise velocity time series and associated single-sided amplitude spectrum of the streamwise velocity fluctuations from each slope configuration and ADV position. The lowermost ADV data point was used (0.005 m above the base of the tank/slope surface), as this is the most representative of the conditions affecting sediment transport and deposition. (A), (C) and (E) 20° slope, (H), (J) and (L) 30° slope, and (N), (P) and (R) 40° slope, streamwise velocity time series. z = height of the ADV upslope. The inset boxes display the region used in calculating the single sided amplitude spectrum of the streamwise velocity fluctuations, (B), (D) and (F) 20˚ slope, (I), (K) and (M) 30˚ slope, and (O), (Q) and (S) 40˚ slope.
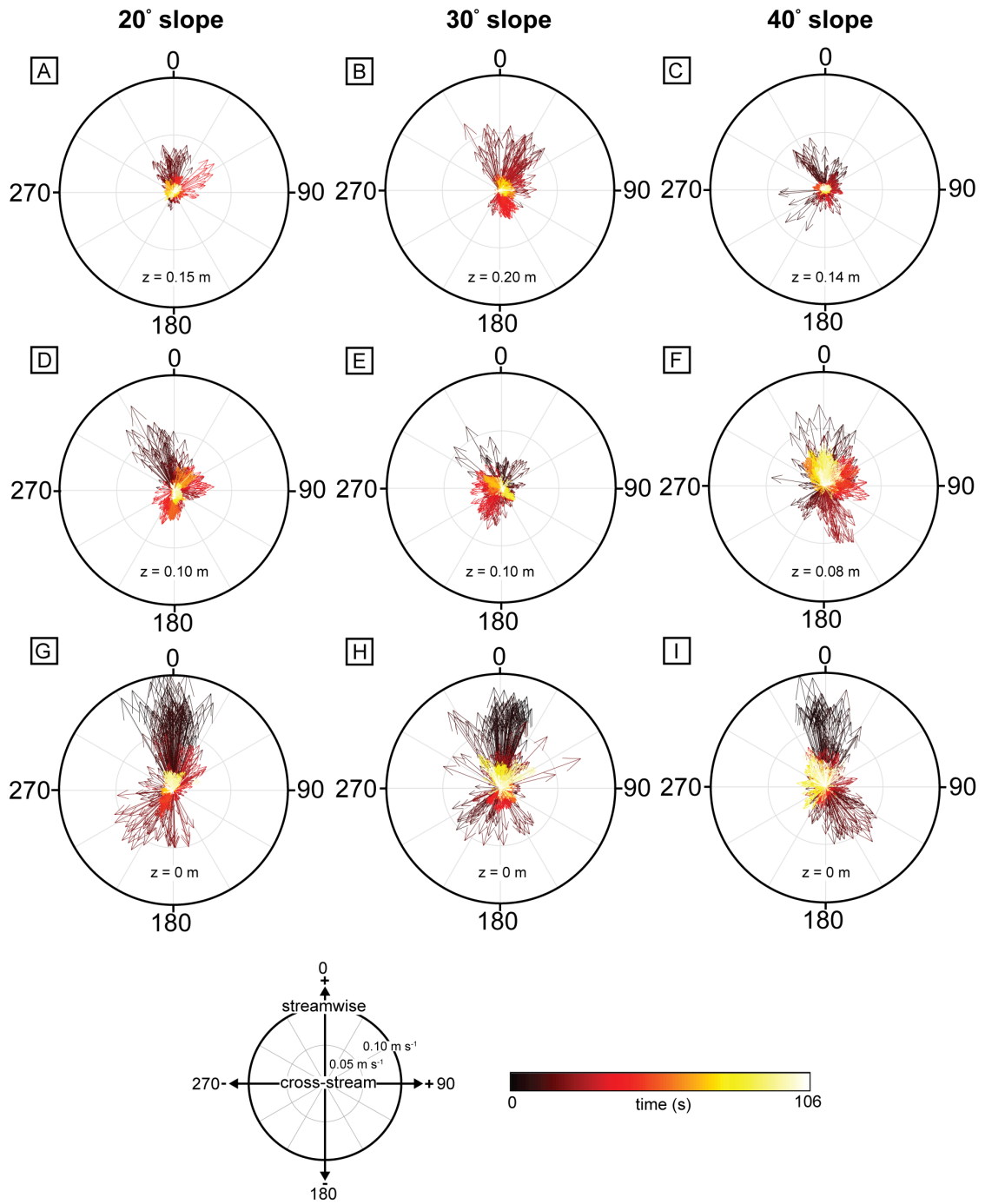
Figure 3.13: Figure caption overleaf.

Figure 3.13: Streamwise and cross-stream velocity vector variability for the duration of the experimental runs. (A), (B) and (C) at the uppermost ADV position on the slope surface, (20°, 30° and 40° respectively), (D), (E) and (F) at the middle ADV position (20°, 30° and 40° respectively), (G), (H) and (I) at the base of each slope configuration (20°, 30°, and 40° respectively). z = height of the ADV upslope. For each experimental run, the 100 Hz ADV data were decimated to 10 Hz, and the lowermost ADV data point was used (0.005 m above the base of the tank/slope surface), as this is the most representative of the conditions affecting sediment transport and deposition. The colour gradient represents time (s) in the experiments.

3.4.3 Summary of flow processes

3.4.3.1 On the slope surface

The increasing angle of the counter slope affects the velocity evolution of the density currents (Figs 3.8, 3.9 and 3.10) and the dominant flow processes that operate on the slope surface (Fig. 3.14). At 20°, the parental flow is observed to decelerate upslope, with the denser, basal region of the flow becoming weakly reflective as it reverses downslope (Video 3.2). The upper, dilute region of the flow decouples (or is 'stripped') at the density interface and continues upslope whilst rapidly thinning (Fig. 3.6C and D), with a high degree of lateral flow spreading before reaching h_{max} (Video 3.2, Fig. 3.7A). In the zone of flow stripping on the slope surface, the thin, dilute flow (Fig. 3.6D) is observed to diverge away from its axial streamline (Video 3.2), generating a complex, multi-directional flow (Fig. 3.13D). The diverging flow reverses downslope, and interacts with the parental flow and the flow components are superimposed to generate combined flows high on the slope surface (Video 3.2, Figs 3.13D and 3.14A). At 30°, a change in the dominant flow process compared to the 20° slope (Video 3.2 and Fig. 3.8C) is supported by: (i) the decreased rate of lateral flow spreading and flow thinning observed on the slope surface (Video 3.3); and (ii) the increased magnitude of the primary flow reversal recorded by the earlier arrival time and increased negative streamwise velocity of the primary flow reversal at the base of slope (Fig. 3.9C). The increased degree of containment acts to enhance the rate of deceleration at the base of slope (Fig. 3.9C) and limit the upslope-momentum of the incoming flow (Video 3.3). As a result, the flow becomes strongly reflective (Fig. 3.14B). At 40°, the observed decrease in h_{max} and the degree of flow thinning on the slope surface (Video 3.4) indicates that the increased topographic containment dramatically decreases the upslope-momentum of the incoming flow. Following the arrival of the flow at the base of slope, part of the flow is observed to flow approximately normal to the orientation of the slope (Video 3.4, Fig. 3.10C). The limited upslope-

momentum and flow deflection at the base of slope has the effect of reducing the magnitude of the primary flow reversal at the base of slope (Fig. 3.10C) compared to the 20˚ and 30˚ slope (Figs 3.8C and 3.9C, respectively), and increasing the cross-stream velocity of the flow both on the slope surface and at the base of slope (Fig. 3.14C, F and I). The superimposition of the strongly deflective flow with the parental flow generates highly multidirectional flows (*i.e.,* combined flows) both at the base of, and low down on, the slope surface (Fig. 3.13I and F).

3.4.3.2   *At the base of slope*

In all topographic configurations, highly multi-directional flows are generated at the base of each flow, both at the base of, and on, the slope (Fig. 3.13D to I), and flow inflation occurs at the base of slope (Videos 3.2–3.4). These changes in flow behaviour result from the interaction of the primary flow reversal with the parental flow (Videos 3.2–3.4). The decreased magnitude of the primary flow reversal and degree of flow inflation recorded at the base of the 20° and 40° topographic configurations is attributed to the high-degree of lateral flow spreading at 20° (Fig. 3.8C), and the reduced upslope-momentum of the flow at 40° (Fig. 3.10C). Flow divergence and flow deflection are the primary flow process at 20° and 40°, respectively (Fig. 3.14A and C). At 30°, the magnitude of the first flow reversal recorded at the base of slope is greater than the other slope configurations (Fig. 3.9C), which is attributed to flow reflection being the dominant flow process (Fig. 3.14B) and an enhanced interaction between the reflected flow and the parental flow at the base of slope (Video 3.3). The observed episodes of secondary flow reversal and flow stasis (Figs 3.8C, 3.9C and 3.10C) indicate the quasi-steady state of the density current as it inflates at the base of slope, before subsequently dissipating farther into the experimental basin, upstream of the topographic slope (Videos 3.2–3.4).

3.5   Discussion

3.5.1   Effect of topographic containment on flow processes

3.5.1.1   *On the slope surface*

Here, the incidence of unconfined, 3D density currents upon planar frontal topographic slopes is shown to result in differences in the superelevation, the degree of flow thinning, and the velocity structure of the flow between the three slope angle configurations. In previous 2D experimental studies (*e.g.,* Pantin and Leeder, 1987; Kneller *et al.,* 1991, 1997; Edwards *et al.,* 1994; Patacci *et al.,* 2015) where flows were strongly confined by the experimental basin, flow reflection has been documented as the dominant flow process with both orthogonal (*e.g.,* Pantin and Leeder, 1987;

Kneller *et al.,* 1991, 1997; Edwards *et al.,* 1994; Patacci *et al.,* 2015) and oblique (*e.g.,* Kneller *et al.,* 1991) slopes. The inability of the density currents to radially-expand in 2D experiments poorly models the behaviour of natural turbidity currents in unconfined and weakly confined settings. Where unconfined gravity currents have been documented to interact with orthogonal counter-slopes, both in physical (*e.g.,* Soutter *et al.,* 2021a) and numerical (*e.g.,* Howlett *et al.,* 2019) models, the decreased containment factor compared to the current study permits the flows to surmount the topography and bypass down-dip. The model presented here shows how the flow process regime changes from divergence-dominated, through reflection-dominated, to deflection-dominated as the slope angle increases from 20° to 30° to 40°, respectively. The new model has implications for the generation of combined flows and potentially for facies and bedforms on topographic slopes.

3.5.1.2   At the base of slope

The experiments show how a sustained flow input in an unconfined experimental setting results in the inflated density current forming at the base of slope and dissipating throughout the basin upstream of the topographic slope and/or being diverted around the basal edges of the slope; all in the absence of flow ponding. By contrast, in experimental mini-basin settings, sustained flow input results in the progressive infilling of sediment in the first basin (up-dip of the topographic sill), until complete flow ponding results in overspill into the second basin (Brunt *et al.,* 2004). The conditions for flow ponding, and the development of a marked density boundary in the suspension, are further promoted in 2D flume tank experiments due to the high degree of flow confinement and topographic containment (*e.g.,* Lamb *et al.,* 2004; Patacci *et al.,* 2015). Internal waves have been described as forming at a prominent density boundary in ponded suspensions (Patacci *et al.,* 2015).

A

thin, dilute flow high
on the slope surface

highly multidirectional flows
high on the slope surface

flow divergence

quasi-steady,
radially expanding
unconfined flow

weak reflection
at base of slope

20°

B

decreased superelevation
and flow stripping

flow thickening
at base of slope

enhanced reflection
at base of slope

30°

C

limited up-slope momentum
of the incoming flow

flow deflection
at base of slope

40°

Flow outline in cross-section

Flow outline in planview

Flow vectors measured along flow axis

Flow direction observed visually

Figure 3.14: Figure caption overleaf.

Figure 3.14: Schematic three-dimensional summary of the primary flow processes active upon the incidence of the unconfined density current, as a function of the three slope configurations. (A) 20° slope – flow divergence is active in the enhanced zone of flow stripping that forms on the slope surface. (B) 30° slope – flow reflection is the dominant process and produces a flow reversal with an increased magnitude and enhanced flow thickening at the base of slope. (C) 40° slope – flow deflection at the base of slope limits run-up potential and generates a weakly collapsing flow.

3.5.2   Absence of internal waves in unconfined density currents

The lack of distinct peaks in the frequency spectra generated at the mid-slope and base of slope positions (Fig. 3.12), and the observed absence of well-defined internal wave-like structures (Videos 3.2–3.4), suggests features including solitons and bores are not present in these unconfined density current experiments. Instead, these experiments demonstrate the generation of combined flows both on the slope surface and at the base of slope. Combined flows are generated due to the interaction of unconfined density currents with topographic slopes, and the superimposition of multidirectional flow components (Fig. 3.13), following flow thinning, deceleration and reversal on the slope surface (Videos 3.2–3.4). Solitons and internal bores recognised in 2D experiments have been linked to the generation of an oscillatory flow component and the inception of combined flow (*e.g.,* Pantin and Leeder, 1987; Edwards *et al.,* 1994; Kneller *et al.,* 1997). These observations have been invoked to explain the presence of combined flow bedforms, such as hummock-like structures and symmetrical megaripples above topographic slopes in deep-water settings following flow interactions with seafloor topography (*e.g.,* Privat *et al.,* 2021, 2024; Tinterri *et al.,* 2022; Martínez-Doñate *et al.,* 2023; Siwek *et al.,* 2023).

3.5.3   A new model for combined flow generation

A new model for the generation of combined flow in unconfined density currents has implications for interpreting the degree of flow confinement and topographic containment in deep-water systems. Here, the generation of combined flows from physical 3D experiments of density currents is explored. At 20°, compared to the 30° and 40° slope configurations, the increased degree of flow stripping, lateral flow spreading and h_{max} (Video 3.2), is observed to generate thin, dilute currents high on the slope surface (Fig. 3.6D). In this position, the diminished gravitational forces that would otherwise act to 'pull' the flow back down the slope allows for the dilute flow to spread laterally and strongly diverge away from the axial centreline (Video 3.2). The

superimposition of the multi-directional, diverging flow as it begins to reverse downslope with the unidirectional, yet radially-expanding, parental flow, produces velocity signals with a high-degree of spatio-temporal, streamwise and cross-stream velocity variability on the slope surface (Fig. 3.13D) and at the base of slope (Fig. 3.13G). At 30°, the generation of complex, multi-directional flows is focused towards the base of slope (Fig. 3.13H). The increased topographic containment leads to flow reflection and the enhanced interaction between the primary flow reversal and the parental flow (Video 3.3). At 40°, the enhanced flow deflection at the base of slope, due to the increased degree of containment, produces complex, multidirectional flows with a strong cross-stream component both at the base of slope (Fig. 3.13I) and low on the slope surface (Fig. 3.13F). Critically, the results herein document how flow reflection is not the dominant flow process in 3D, unconfined experiments on low angle slopes, unlike in previous 2D experiments (*e.g.,* Pantin and Leeder, 1987; Edwards *et al.,* 1994; Kneller *et al.,* 1997). This highlights that the superelevation of gravity currents, flow divergence and the generation of highly multidirectional flows (*i.e.,* combined flows) is likely to be further enhanced on lower angle slopes, less than 20°, with implications for bedform distribution and onlap styles discussed herein. For each topographic configuration, there is an absence of internal waves (Videos 3.2–3.4, Fig. 3.12). This variability in velocity and direction suggests that the generation of combined flows at different positions at the base of, and on, the slope is a function of the degree of topographic containment.

In deep-marine settings, one mechanism invoked for the generation of combined flows is the superimposition of high-frequency flow oscillations over periods of hours and/or days, against a unidirectional turbidity current (*e.g.,* Tinterri, 2011). These oscillations are postulated to be generated by the interaction of turbidity currents with seafloor topography, leading to the formation of internal waves. Previous field-based outcrop models (*e.g.,* Tinterri *et al.,* 2016, 2022; Privat *et al.,* 2021, 2024; Martínez-Doñate *et al.,* 2023) have invoked this model to interpret sedimentary structures. However, the model is based largely on semi-quantitative (Edwards *et al.,* 1994) and quantitative (Kneller *et al.,* 1997) observations from 2D, non-ponded flume tank experiments.

A second mechanistic model for combined flow generation exists for ponded turbidity currents, whereby the formation of internal waves is independent of flow interactions with a containing slope (*e.g.,* Patacci *et al.,* 2015). The intensity of the internal waves was attenuated with depth (Patacci *et al.,* 2015), seemingly exerting no direct influence on the bedload. The observations from the Patacci *et al.* (2015) model suggest that internal wave generation is: (i)

promoted in 2D, ponded experimental settings, due to the strong stratification focused at the internal velocity, and concentration and grain-size interface; (ii) dependent on the flow magnitude in 2D experimental settings; and (iii) not applicable to combined flow generation in 3D density current experiments. Internal wave formation in ponded suspensions is hypothesised to exploit the contrast between the velocity, and the concentration and grain-size layers (*e.g.,* Patacci *et al.,* 2015). From experimental modelling of 2D gravity currents, internal wave formation has also been observed to occur at a critical layer within the body of gravity currents, at the height of the maximum internal velocity, thus suggesting that the 'steady' body of gravity currents has inherent instabilities in the form of internal waves and may not be as steady as first assumed (*e.g.,* Marshall *et al.,* 2021, 2023). Internal wave generation has been documented to enhance flow stratification, by maintaining the momentum in the lower-part of the flow and limiting the entrainment of ambient water in the upper-part (Dorrell *et al.,* 2019). The experiments herein model low-density gravity currents with the absence of a strong density stratification. It is hypothesised that gravity currents with a stronger density stratification may have a propensity to develop internal waves and reflected bores, as has been observed in the previous 2D experiments with increased flow densities compared to the current study (*e.g.,* Kneller *et al.,* 1991; Edwards *et al.,* 1994; Kneller, 1995; Patacci *et al.,* 2015) (the effects of flow stratification regarding the implications for the formation of sedimentary structures and different onlap styles is considered in the 'Effect of flow stratification' section). Whether the same mechanisms for internal wave generation are applicable in 3D, unconfined settings with low-density gravity currents is yet to be explored.

Based on the observations from these experiments, a new model is proposed for the generation of combined flows at the base of density currents that interact with simple containing topographies. Combined flows are established following flow deceleration, thinning and spreading on the slope surface, and the superimposition of the reversing flow with the parental flow at the base of slope. Hence, combined flows in unconfined flows are generated in the absence of internal waves. The temporal nature of the complex, multidirectional flows (*i.e.,* combined flows) varies markedly in 3D space depending on the slope angle. Furthermore, the interaction of flows with non-planar seafloor relief, rugose flow fronts and unsteady flows, likely further enhance the generation of combined flows above slopes.

3.5.4 Implications for facies variations

3.5.4.1 A new model for the formation of hummocks in the deep sea

Hummock-like structures have been documented in a range of deep-marine settings, including basin-plain lobes (*e.g.,* Mulder *et al.,* 2009; Bell *et al.,* 2018), channel-lobe transition zones (*e.g.,* Hofstra *et al.,* 2018) and intraslope lobes (*e.g.,* Privat *et al.,* 2021, 2024; Martínez-Doñate *et al.,* 2023). They are dominantly aggradational and differ in their internal architecture compared to both true HCS, and to supercritical bedforms such as antidunes (see reviews in Tinterri, 2011, and Hofstra *et al.,* 2018); thus they are considered to be the product of subcritical flows. Prave and Duke (1990) and Mulder *et al.* (2009) invoke standing to weakly migrating waves formed by Kelvin–Helmholtz instabilities at the upper flow interface to explain the development of HCS-like bedforms. However, the primary model ascribed to their genesis is based on observations of bores in 2D reflected density current experiments with an oscillatory flow component being superimposed with a confined, unidirectional parental flow (*e.g.,* Edwards *et al.,* 1994), and applied to outcrop models in confined/contained-reflected basins (*e.g.,* Tinterri, 2011; Tinterri *et al.,* 2016).

The documentation of combined flow in unconfined, subcritical, density currents that interact with planar topography, which form in the absence of oscillatory flow from internal and surface waves, allows a new mechanistic model for the deposition of hummock-like structures to be proposed. Hummock-like bedforms in these settings are proposed to form via rapid sediment fallout as flows decelerate on the slope, under combined flows that show marked temporal variations in flow directions that are generated as the reversing flow is superimposed with the parental flow (Fig. 3.13). High-up on low angle slopes where the range of flow directions is diverse, and the primary current velocity is low, the hummock-like structures will be composed of convex or concave draping laminae that may largely lack cross-cutting relationships (Figs 3.15A and 3.16C), as observed in examples in outcrop and core (Privat *et al.,* 2021, 2024; Taylor *et al.,* 2024a). In part, these are analogous to isotropic hummocky-cross stratification, although the absence of cross-cutting relationships is in marked contrast to true HCS (Harms, 1969). Further down the slope where the primary flow is greater and reversals more important, cross-cutting relationships are likely to be more frequent (*e.g.,* Hofstra *et al.,* 2018), producing bedforms in part analogous to anisotropic HCS (Figs 3.15C and 3.16C). In all cases, however, higher frequency wave oscillations are not a factor in the generation of the hummocks.

A — isotropic hummock-like structures — fine sandstone — 80 mm

B — thin-bedded heterolithics — 140 mm — massive sandstone

C — anisotropic hummock-like structures — opposing ripple directions — 55 mm
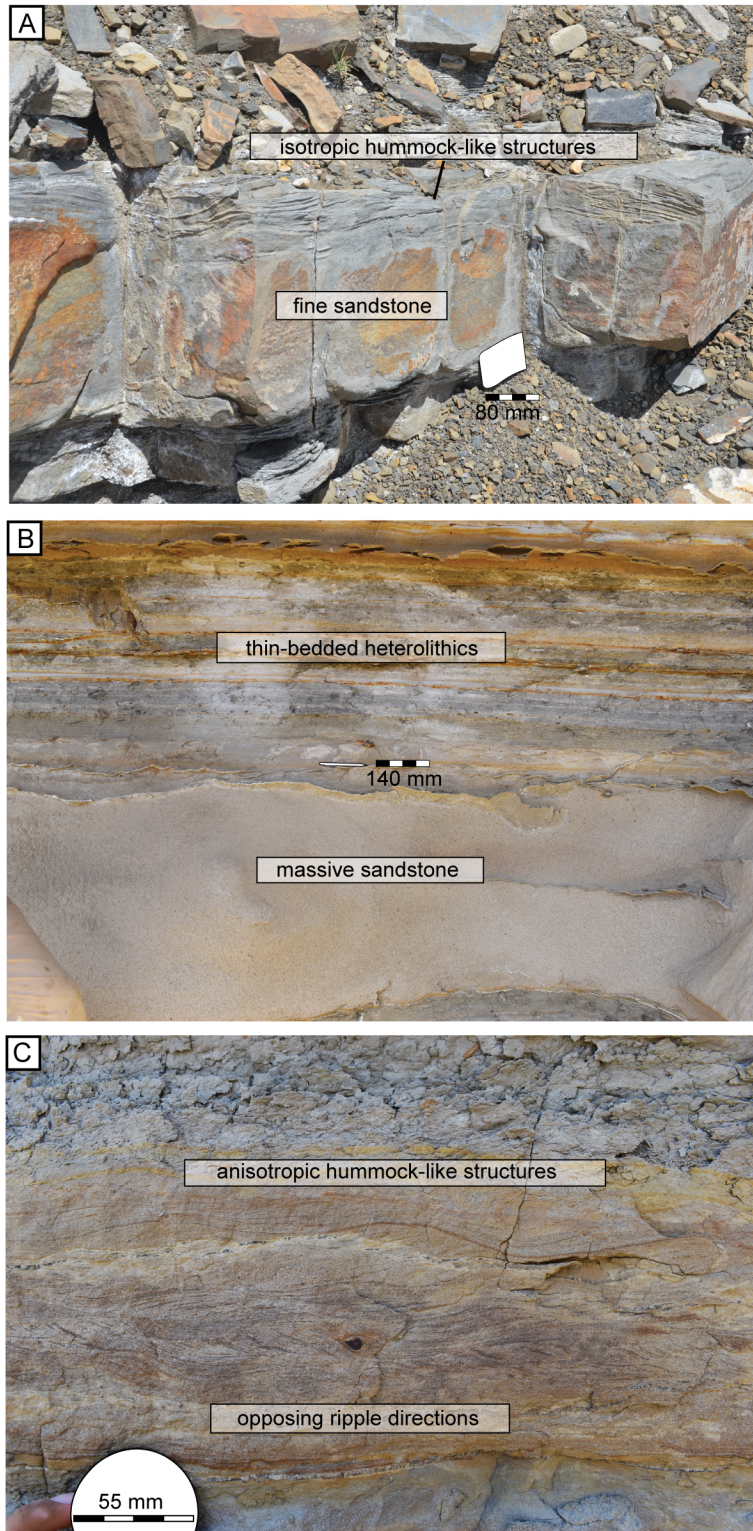
Figure 3.15: Figure caption overleaf.

Figure 3.15: Facies photographs of turbidites deposited following the interaction with containing topography. (A) Isotropic hummock-like structures displayed in bed-tops (Neuquén Basin, Argentina). (B) Thick, massive sandstone bed (Canyon San Fernando, Baja California, Mexico). (C) Fine sandstone bed displaying ripples with opposing palaeoflow directions, overlain by anisotropic hummock-like structures (Canyon San Fernando, Baja California, Mexico).

3.5.4.2 *Spatial distribution of bedforms on the slope*

As particulate currents decelerate upon incidence with seafloor topography, suspended sediment fallout rates increase, the unidirectional component of the flow decreases, and the flows become strongly multi-directional high up on the slope surface (Fig. 3.16A and B). More isotropic hummock-like structures are predicted to form under such combined flows high up on low angle slopes (Figs 3.15A, B and C), including slopes lower than 20°, where enhanced superelevation and flow divergence are hypothesised to occur. In contrast the superimposition of the primary flow reversal with the unidirectional flow at the base of each slope configuration is predicted to lead to the deposition of 2D, anisotropic hummock-like structures perpendicular to the slope (Fig. 3.15C). At 40°, the flow lines of the depletive density currents are observed to converge at the base of slope (accumulative flow), before running parallel to the slope surface (uniform flow) (*see* Kneller and McCaffrey, 1999) (Video 3.4), resulting in a quasi-uniform flow component being generated at the base of the simple orthogonal, steep slope. Towards the base of slope, the superimposition of the uniform flow component running parallel to the slope surface and the depletive, parental flow would support the generation of combined flow bedforms with multidirectional palaeoflow directions (Fig. 3.16B). Where subcritical density currents decelerate, often towards the base of impinging slopes or basin margins, outcrop (*e.g.,* Tinterri and Muzzi Magalhaes, 2011; Bell *et al.,* 2018; Tinterri *et al.,* 2022) and experimental (*e.g.,* Allen, 1971, 1973, 1975; McGowan *et al.,* 2024) observations of erosional features (*e.g.,* flutes and tool marks) can act to record the regional palaeoflow direction of turbidity currents and/or more mud-rich flows (Peakall *et al.,* 2020). As such, the 2D, hummock-like structures are hypothesised to overprint the regional palaeoflow direction at the base of slope. The new model for the generation of combined flows, and the presence of combined flow bedforms in 3D space on seafloor topography, can be used to reconstruct the form and angle of the topography (Fig. 3.16B and C).

3.5.4.3 Development of thick massive sands at the base of slope

Compared to lower angle slope configurations (Videos 3.2 and 3.3), the observed rapid flow deceleration at the base of the 40° slope, coupled with the limited up-slope momentum (Video 3.4), is hypothesised to result in high rates of suspended sediment fallout and the formation of thick massive sandstone beds (Fig. 3.15B), which terminate abruptly at the base of slope (*e.g.,* Schofield and Serbeck, 2000; McCaffrey and Kneller, 2001; Lee *et al.,* 2004) (Fig. 3.16B and C). The presence of thick massive sandstone beds at the base of slope could therefore provide evidence of flow interactions with seafloor topography. The proposed mechanism for massive sand formation at the base of slope, can be considered alongside other mechanisms for the deposition of deep-water massive sands (*e.g.,* Kneller and Branney, 1995; Cantero *et al.,* 2012; Hernandez-Moreira *et al.,* 2020).

3.5.4.4 Draping onlap of low angle slopes

The increased run-up potential of the dilute flow on the 20° slope that decouples from the co-genetic dense lower region (Fig. 3.6D, Video 3.2), demonstrates how lower-concentration flows and the more dilute regions of co-genetic flows are able to drape low-angle onlap surfaces (*e.g.,* Bakke *et al.,* 2013) (Fig. 3.16). Where the slope angle is below 20°, the superelevation of the dilute part of the flow is hypothesised to increase, further draping the onlap surface with fine-grained material high on the slope surface. As the dilute, upper region of the flow thins and decelerates upslope, the denser region has limited upslope momentum, and rapidly decelerates at the base of slope (Video 3.3). The modelled behaviour of the denser region of the flow would result in the deposition of the coarser-grained sediment fraction and the abrupt termination lower on the slope, as observed in previous experimental studies (*see* Fig. 13A and B in Soutter *et al.,* 2021a). However, the behaviour of the more dilute (*i.e.,* finer-grained) part of the flow on the slope surface was not explored in the previous experimental studies due to the configuration of the topographic slope (*e.g.,* Soutter *et al.,* 2021a). Soutter *et al.* (2019) observed in the Annot Basin, France, the abrupt pinch-out of high-density turbidites and the draping onlap of low-density turbidites on to the same onlap surface. The observations from the experiments herein show that higher on the slope surface the thin and decelerated flow would generate combined flows and lead to the deposition of the finer-grained sediment fraction (*e.g.,* silt – fine sand) and the development of isotropic hummock-like bedforms (Fig. 3.16B and C). Coupled with the new model for the generation of combined flow, the onlap style of the resulting deposits can support reconstructions of the orientation and gradient of seafloor topography in deep-water settings.

A

relative flow density
low
high

increased superelevation
and flow stripping

containing slope

basin floor

20°

generation of multi-directional flows
from superimposition of collapsing
flow with the parental flow

30°

40°

limited upslope-
momentum of flow

< 1 km

divergence of flow
away from centreline

flow reflection is the
dominant process at
the base of slope

flow is deflected
at base of slope

B

grain size
mud
sand

combined-flow bedforms
deposited on the slope surface
e.g. 3D, isotropic hummock-like
bedforms

finer-grained
material drapes
the onlap surface

containing slope

basin floor

40°
Z'

30°
Y'

20°
X'

abrupt pinch-out at
the base of slope

combined-flow bedforms
perpendicular to regional
palaeo-flow direction away
from the axis of the deposit

X

Y

Z

regional palaeo-flow direction recorded
by erosional structures at bed bases,
overprinted by combined-flow bedforms
e.g. 2D, anisotropic hummock-like bedforms

deposition of massive sand
following rapid deposition
at the base of slope

C

highly multidirectional flows high on the
slope surface leads to the deposition of
3D, isotropic hummock-like bedforms

draping onlap of finer-grained
material high on the slope surface

20°
X'

30°
Y'

40°
Z'

limited deposition on the slope surface

X

onlap surface

Y

Z

stronger bi-directionality of the flow at
base of slope leads to deposition of 2D,
anisotropic hummock-like bedforms

abrupt termination/pinch-out of
coarser-grained material at the base of
slope

Figure 3.16: Figure caption overleaf.

Figure 3.16: Summary schematic diagram showing: (A) the dominant flow processes observed from these experiments as a result of low-density gravity currents interacting with topographic slopes of varying angles; (B) the hypothetical deposit geometry for each topographic configuration, and the key facies and palaeo-current dispersal trends; and (C) the onlap styles for each slope configuration and the differences between two-dimensional anisotropic and three-dimensional isotropic hummock-like bedforms [part C modified from Tinterri, (2011)].

3.5.5 The effect of flow stratification

The present experiments utilised saline flows; however, stratification is a key aspect of SGFs, particularly those with a sand-grade component, and is more pronounced than in saline flows (Menard and Ludwick, 1951; Gladstone *et al.*, 2004; Amy *et al.*, 2005; Dorrell *et al.*, 2014). The effects of flow stratification will influence the nature of processes as flows interact with topography, albeit that the full influence is difficult to assess *a priori*. Furthermore, density profiles are absent in the few documented unconfined natural SGFs (*e.g.,* Lintern *et al.*, 2016; Hill and Lintern, 2022). There are three main aspects of the current study to be considered when assessing how flow stratification may affect flow processes. First, it is hypothesised that the effects of density decoupling and increased superelevation of the upper, dilute region of density currents is enhanced when a strongly stratified flow decelerates upon interacting with topography. Thus, increasing stratification is expected to result in dilute flows with a strong multidirectional flow component higher on the slope surface. Second, it is hypothesised that flows with a pronounced stratification have a propensity for internal wave formation and may produce distinctive bedforms up-dip of topography as internal waves propagate upstream. Finally, it is difficult to predict the patterns of sedimentation and bedform development linked to the interaction between a well-stratified flow at the base of slope with a dilute, and better mixed, less-stratified flow collapsing downslope. These factors suggest the need for future physical experiments and numerical simulations to explore the effects of more strongly stratified flows as they encounter topography, and more direct monitoring efforts in unconfined settings.

3.6   Conclusions

Froude-scaled physical models of 3D, unconfined density currents interacting with a planar orthogonal slope are used to develop a new mechanistic model for the formation of combined flows in turbidity currents. Flow visualisation and high-resolution 3D Acoustic Doppler velocity profiler (ADV) data demonstrate how flow divergence, reflection and deflection are observed to

be the dominant flow processes active above 20°, 30° and 40° slopes, respectively. The increased 'superelevation' and flow stripping active on the 20˚ slope promotes flow divergence and generates complex, multidirectional flows high on the slope surface. At 30˚, the extent of flow stripping and lateral flow spreading on the slope surface decreases, and flow reflection becomes the dominant flow process, producing an enhanced flow reversal. This generates increased streamwise and cross-stream velocity variations at the base of slope. At 40˚, the increased degree of topographic containment, limits the up-slope momentum of the flow, and instead deflects the flow at the base of slope.

The generation of complex, multidirectional flows (*i.e.,* combined flows) in the experiments herein are formed due to the superimposition of diverging, reflecting and deflecting flow components with the parental flow at the base of, and on, the slope surface. A new model is developed for the generation of combined flow in unconfined flows, which highlights the 3D nature of the flow and the behaviour of the thin, dilute flow on the slope surfaces. This contrasts with previous 2D experimental studies where combined flows are invoked from the interaction of the unidirectional input flow with an oscillatory flow component generated by internal waves following the interaction of turbidity currents with topographic counter-slopes. Observations from previous 2D experimental studies have provided the basis for the existing outcrop models that document combined flow bedforms in a host of deep-water settings. The new model for combined flow generation from these 3D experiments provides a novel mechanism for the formation and distribution of combined flow bedforms in turbidites, such as isotropic and anisotropic hummock-like bedforms, and the mechanics of draping onlaps versus abrupt pinch-outs. The onlap style of the resulting deposits when coupled with the new model for the generation of combined flow, can support enhanced palaeogeographic reconstructions and assessments of the degree of flow containment within deep-water systems.

Chapter 4 Abrupt downstream changes in submarine canyon-margin architecture

4.1 Summary

Submarine channel-levee environments can display predictable lateral changes in deposit architecture and facies variations. However, in submarine canyon settings, the interaction of sediment gravity flows with dynamic erosional and depositional topography is more complicated, and rarely documented in detail. Modern studies of submarine canyons have documented the complex planform geometry of canyon walls and their susceptibility to mass-wasting. Understanding the flow process – topography interactions is crucial for the development of process-based models for submarine canyon fills. However, outcrop-scale observations focus primarily on canyon axes, and rarely with three-dimensional constraints. The Upper Cretaceous Rosario Formation, Mexico, provides exceptional dip-oriented exposures that capture the downstream variation in sediment gravity flow interactions with a submarine canyon-margin. High-resolution photogrammetry, and a well-constrained stratigraphic framework provided by the correlation of marker beds are used to document onlap geometries and facies variations to support interpretations of flow-topography interactions. With increasing lateral distance from the canyon axis, the presence of erosional scours and amalgamation surfaces decreases in the overbank deposits, and the deposits thin and fine. At the canyon wall, thin-bedded turbidites act to drape the canyon wall, healing the topography and generating an intra-formational onlap surface, on which sand-rich deposits abruptly pinch-out. The generation of combined flow bedforms and the wide palaeocurrent dispersal compared to the canyon axis suggests flows reflected and deflected against the canyon wall. Mass-transport deposits emplaced 250 m along-strike, and up-dip of the canyon wall, acted to capture sediment gravity flows in the overbank, resulting in marked spatial deposit geometry and facies changes. The results demonstrate how variations in autocyclic flow modulation generates complicated deposit architectures, and how the complex geometry of canyon walls, generates marked and localised heterogeneity in depositional character. Better understanding of these flow-topography interactions will support interpretations of overbank canyon-fill successions from less well constrained settings.

4.2 Introduction

Submarine canyons link continental and shallow-marine sedimentary systems to the deep sea (Daly, 1936; Kuenen, 1938; Middleton and Hampton, 1973; Simpson, 1997; Fildani *et al.,* 2017),

95

acting as conduits for the transport of sediment (Normark, 1970), organic carbon (Talling et al., 2023), nutrient (Heezen et al., 1955), and micropollutants (Paull et al., 2002) to abyssal depths. Modern, subsurface, and ancient outcrop examples show how submarine canyons are highly dynamic environments, with complex planform geometries (Von der Berch, 1985), hosting different near-bed deep-sea currents (Hall et al., 2017; Paull et al., 2018; Maier et al., 2019; Heijnen et al., 2022), and being prone to mass-wasting events (Chaytor et al., 2016). Recent technological advances have enabled direct measurements of sediment gravity flows in submarine canyons, revealing their frequency (Heijnen et al., 2022) and magnitude (Paull et al., 2018; Talling et al., 2023), but are unable to document the rates of sediment bypass and storage on geological timescales.

Rare examples of exhumed submarine canyon-fills have documented axes to be coarse-grained and bypass-dominated, with unorganised stratigraphic fills (May and Warme, 2007; Di Celma, 2011; Janocko and Basilico, 2021; Bouwmeester et al., 2024). However, this heterogeneity is often only observed in two dimensions. Conversely, contemporaneous canyon overbank environments have been documented to show a more complete history of submarine canyon evolution, from incision through fill to burial, in the form of organised stacking patterns of finer-gained material from sediment gravity flows that overspilled from the canyon axis (McArthur and McCaffrey, 2019; Taylor et al., 2024b).

The complex planform geometry of submarine canyons and their susceptibility to mass-wasting events means that the three-dimensional heterogeneity in canyon overbank environments increases towards canyon walls. Subsurface and modern studies have documented the generation of mass transport deposits (MTDs) following the mass-wasting of submarine canyon-margins (Paull et al., 2013; Mountjoy et al., 2018; Pope et al., 2022) and as features related to submarine channel-margin failure (Peakall et al., 2007; Hansen et al., 2017b; Tek et al., 2021; McArthur et al., 2024), and their impact on sedimentation patterns. However, they lack the finer-scaled, detailed observations of facies and architectural heterogeneity that outcrop studies permit. The mass-wasting of submarine canyon-margins has also been documented to profoundly impact sediment routeing pathways in canyon axes, (Pope et al., 2022), as has the role of canyon-flushing events on localised patterns of erosion and deposition (Ruffell et al., 2024). Therefore, understanding canyon overbank processes is crucial in assessing the role of transient storage and canyon flushing events when estimating sediment, organic carbon, and micropollutant budgets in the deep sea.

This study uses the exceptionally well-preserved relationship between submarine canyon overbank deposits and a canyon-margin, from the Rosario Formation, Mexico (Fig. 4.1), to document the localised heterogeneity in overbank deposit facies and architecture related to submarine canyon-margin failure.
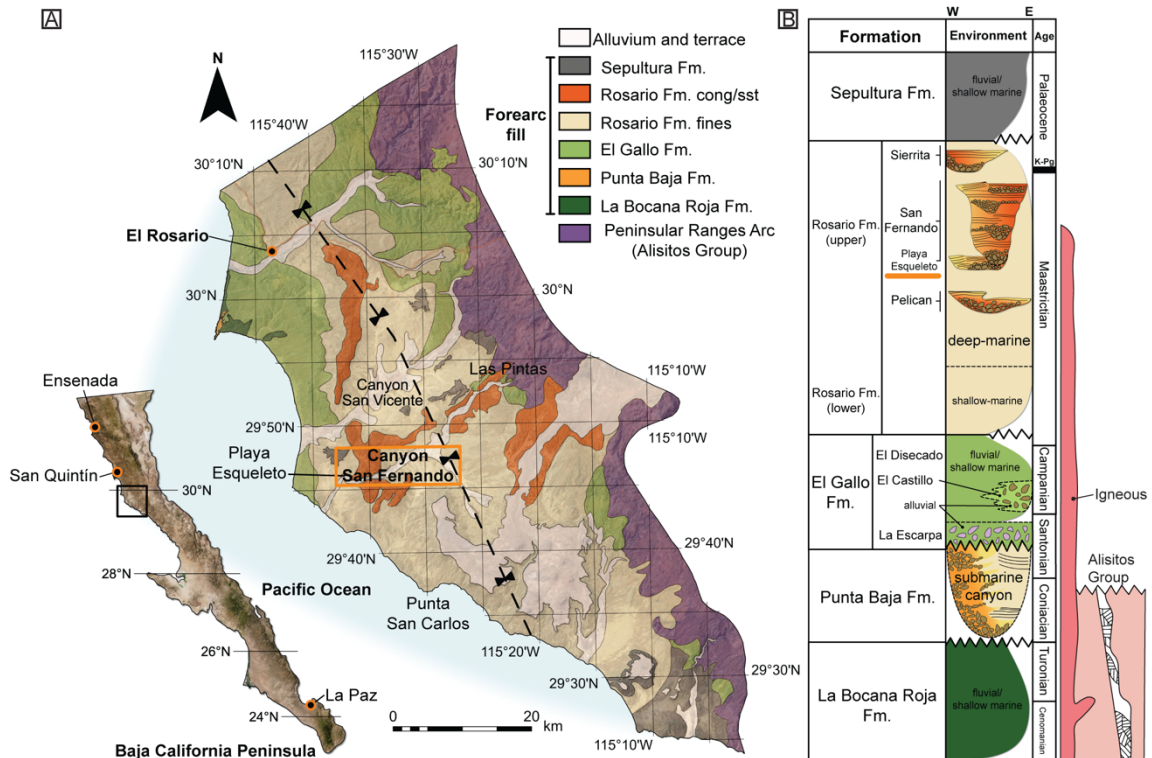
Figure 4.1: (A) Geological map of part of the Baja California peninsula, showing the main units of the Peninsular Ranges forearc basin complex. Modified from Morris and Busby-Spera, 1990 and Kneller *et al.*, 2020. (B) Stratigraphic column showing the main formations and depositional settings of the Peninsular Ranges forearc basin complex. Modified from Taylor *et al.*, 2024b.

This study uses stratigraphic logging and a high-resolution photogrammetric model from exhumed canyon-confined overbank deposits located close to the canyon axis. Two other exposures are used to assess the heterogeneity associated with sediment gravity flow interactions with canyon wall topography; one oriented oblique to depositional dip and the other approximately 250 m along strike. The Rosario Formation records the fill of a submarine canyon that formed on the active, ocean-facing tectonic margin of Baja California during the Cretaceous-Palaeogene. In Canyon San Fernando, the sedimentology of the submarine canyon axis and margin has previously been studied (Kane *et al.*, 2009), as have the overlying channel-levee

systems (Morris and Busby Spera, 1988, 1990; Morris and Busby, 1996; Dykstra and Kneller, 2007; Kane *et al.*, 2007; Kneller *et al.*, 2020) (Figs 4.2 and 4.3). However, the localised heterogeneity related to canyon-margin failure has not been documented. Here, one exposure displays the complex relationship between overbank deposits and MTDs emplaced within the canyon-belt following mass-wasting of the canyon wall (Fig. 4.3C). A second exposure lacks MTDs, and instead displays canyon-confined overbank deposits onlapping the canyon wall (Fig. 4.3C). The objectives of this study are to: (i) compare the facies and architectural differences between the two exposures; and (ii) interpret and discuss the mechanisms for canyon wall failure and how flow-topography interactions varied through time. Based on the results, a model that links facies and architecture heterogeneity with the complex topography of canyon walls is presented. This work provides a new understanding of the localised variability in canyon-confined overbank deposits in submarine slope settings, exploring flow processes and bridging the gap with lower resolution modern and subsurface datasets.

4.3   Geological Setting

The Upper Cretaceous-Palaeocene Rosario Formation constitutes part of the Mesozoic Peninsular Ranges forearc basin complex that crops out discontinuously for approximately 500 km along the Pacific coast of southern California, USA and Baja California, Mexico (Gastil *et al.*, 1975; Morris and Busby-Spera, 1990) (Fig. 4.1A). The geology of the Peninsular Ranges forearc records the evolution of an ocean-facing convergent basin margin, which developed via the eastward, oblique subduction of the Farallon plate beneath the western margin of the North American plate during the Mesozoic (Atwater, 1970; Busby *et al.*, 2002). The basin margin evolved from an intra-oceanic arc system in the late Triassic, to a fringing island arc stage during the early- to mid-Cretaceous, to a highly compressional continental arc in the Late Cretaceous (Engebretson *et al.*, 1985; Glazner, 1991; Busby *et al.*, 1998).

The central and eastern regions of the Baja California peninsula are dominated by Precambrian-Mesozoic igneous and metamorphic rocks. The Mesozoic strata record the transition from extensional intra-oceanic arc to fringing arc, and are characterised by a complex suite of igneous, volcaniclastic and carbonate rocks. In the late Cretaceous, uplift and erosion of the arc basement rocks led to an influx of sediment deposited in forearc and backarc basins on both margins of the arc (White and Busby-Spera, 1987; Busby *et al.*, 1998).

The Peninsular Ranges forearc basin developed on the ocean-facing (westward) margin of the arc. The sediment supply to these basins was tectonically-driven, following the uplift and erosion of the hinterland and lead to an influx of coarse-sediment across a relatively narrow shelf (Busby *et al.*, 1998; Kimbrough *et al.,* 2001). The forearc stratigraphy comprises: (i) the Alisitos Group (volcanic - shallow marine) (Busby, 2004), (ii) Bocana Roja Formation (fluvial - shallow marine) (Kilmer, 1963), (iii) Punta Baja (submarine canyon) (Kilmer, 1963, McGee, 1965; Boehlke and Abbott, 1986, Kane *et al.,* 2022; Bouwmeester *et al.,* 2024), (iv) El Gallo (fluvial - shallow marine) (Kilmer, 1963; Renne *et al.,* 1991), (v) Rosario Formation (shallow marine – submarine canyon – slope channel-levee complexes) (Morris and Busby-Spera, 1988, 1990; Kane *et al.,* 2009; Hansen *et al.,* 2017a; Kneller *et al.,* 2020), and (vi) Sepultura Formation (fluvial – shallow marine) (Busby, 2004) (Fig. 4.1B). Exposures of the Rosario Formation form the basis of this study.

4.3.1 The Rosario Formation in Canyon San Fernando

In the Canyon San Fernando area, the Rosario Formation represents a mid-slope submarine canyon fill overlain by a genetically-related channel-levee complex (Morris and Busby Spera, 1988, 1990; Morris and Busby, 1996; Dykstra and Kneller, 2007; Kane *et al.,* 2007) (Fig. 4.2). The Canyon San Fernando area is located approximately 30 km south of the town of El Rosario, on the Pacific coast of Baja California, Mexico (Fig. 4.1A). From herein, the submarine canyon complex is named the Playa Esqueleto Canyon (after Kane *et al.,* 2009) and the channel-levee complex as the San Fernando channel-levee complex (Fig. 4.2). The terminology used herein is also defined in Figure 4.2.
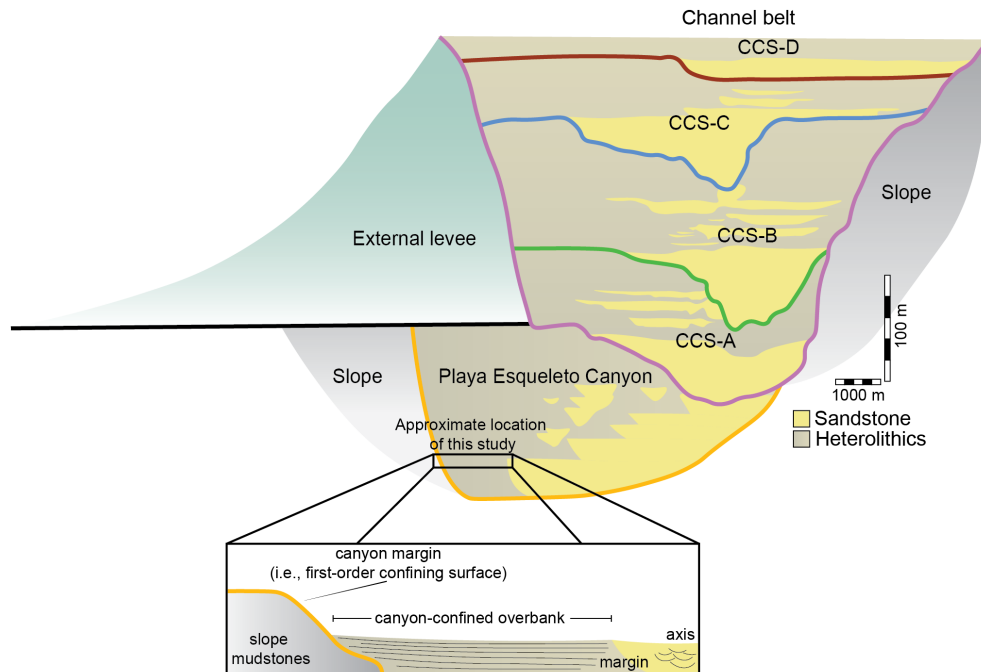
Figure 4.2: Schematic cross-section of the Canyon San Fernando slope canyon/channel system with lithologies, the Playa Esqueleto Canyon and the four channel complex sets (CCS-A to CCS-D), and the approximate location of this study (modified from Morris and Busby-Spera, 1990; Hansen *et al.* 2017a). The inset diagram of the approximate location of the study area details the terminology used here in Chapter 4.

The Playa Esqueleto Canyon eroded over 250 m into Late Campanian slope mudstones and displays complete submarine canyon confinement, bound by a first-order confining surface, with a canyon axis that migrated laterally (Kane *et al.*, 2009). In contrast, the overlying aggradationally stacked channel complex sets (CCS-A to CCS-D) are bound by an external levee on the downslope-side, acting to pin the complexes to the slope, with an incisional margin on the upslope side (Morris and Busby-Spera, 1990; Dykstra and Kneller, 2007; Kane *et al.*, 2007; Hansen *et al.*, 2015, 2017a; Kneller *et al.*, 2020). Kneller *et al.* (2020) consider the Playa Esqueleto Canyon as a separate system to the overlying channel-levee system (CCS-A to CCS-D) based on the differences in benthic foraminifera assemblages. However, although the Playa Esqueleto Canyon is older than the overlying channel-levee system, whether the Playa Esqueleto canyon system is early Maastrichtian and not late Maastrichtian (*cf*. Kneller *et al.*, 2020) is unresolvable given the absence of chronostratigraphic data. Given the similar location, orientation, and the common lateral to aggradational stacking patterns in other submarine conduits (*e.g.,* Deptuck *et al.*, 2007;

Hodgson *et al.*, 2011; Englert *et al.*, 2020; Bouwmeester *et al.*, 2024), the Playa Esqueleto Canyon and the overlying channel-levee systems are herein considered as part of the same system.

The entire canyon/channel complex set is *ca* 1 km thick and was deposited over approximately 1.6 Myr (Dykstra and Kneller, 2007). Palaeogeographical reconstructions and palaeocurrent measurements indicate that channelised flows within the canyon and channel-levee complex trended obliquely to the continental margin that faced west-south-west (Dykstra and Kneller, 2007). The uppermost channel-levee complex in Canyon San Fernando is overlain by a thick package of background slope mudstones and sandstones, associated with the abandonment of the system (Kane *et al.*, 2009).

The Playa Esqueleto Canyon axis facies is exposed to the north-east of the principal study area and is composed of clast-supported and matrix-supported conglomerates interpreted to represent the gravel-dominated thalwegs of laterally accreting channels on a submarine braid-plain, with the conglomerate facies pinching-out to the east into low relief thin-bedded heterolithic facies that onlap onto the slope mudstones (Kane *et al.*, 2009) (Fig. 4.3B). Palynology of the foraminifera-rich slope mudstones supports a palaeobathymetry of 1500-3000 m (mid-slope) (Dykstra & Kneller, 2007). The thin-bedded facies are predominantly interbedded cm-scale sandstone and mudstone turbidites (Kane *et al.*, 2009). The slope mudstones display tens of metres of local topography and evidence of failure into the canyon overbank, in the form of MTDs. The localised heterogeneity in the overbank deposits and the onlap architecture against the failed canyon wall, over several hundreds of metres is the focus of this study.

4.4 Data and methods

The dataset comprises seven sedimentary logs. Six logs (1:25 scale) were collected from two principal exposures (Fig. 4.3). Four logs (ranging from 15.03-to-29.51 m thick) were collected from a NE-SW oriented exposure, slightly oblique to depositional dip, herein referred to as the '*Exposure 1*' (*see 'Exposure* 1' in Fig. 4.3 for location). Two logs (18.50 and 21.70 m thick) from a NW-SE oriented exposure, herein referred to as the '*Exposure 2*' (*see 'Exposure* 2' in Fig. 4.3 for location). An additional log (1:5 scale) (1.9 m thick) of the thin-bedded heterolithic facies was collected (Fig. 4.5). The raw scanned images of the sedimentary logs are available, free to access in the Supplementary Material. Data collected included lithology, bed thickness, sedimentary structures and palaeocurrent measurements from ripple cross-lamination, grooves, and verging flame structures. A well-constrained stratigraphic framework provided by the correlation of marker beds and an Uncrewed Aerial Vehicle (UAV) photogrammetric model were used to

capture the facies variability and architecture of the overbank deposits close to the canyon wall contact, allowing comparison between the two investigated exposures (Fig. 4.3C). A photogrammetric model of the overbank deposits closer to the Playa Esqueleto Canyon was also constructed, to assess the lateral continuity of the deposits and facies relationships towards the axis of the system, herein referred to as '*Exposure 3*'. The UAV photogrammetric models were constructed using Agisoft Metashape (Agisoft LLC, 2024) and interpreted using Lime (Fonix Geoscience AS, 2024). Additional images captured from the models are provided in the Appendices (Figs 7.1 and 7.2). The canyon axis, and the overbank deposits preserved at all three exposures are part of the Playa Esqueleto Canyon system. Exposures *1* and *2* are in a palaeo-elevated position relative to the canyon axis and Exposure *3*.
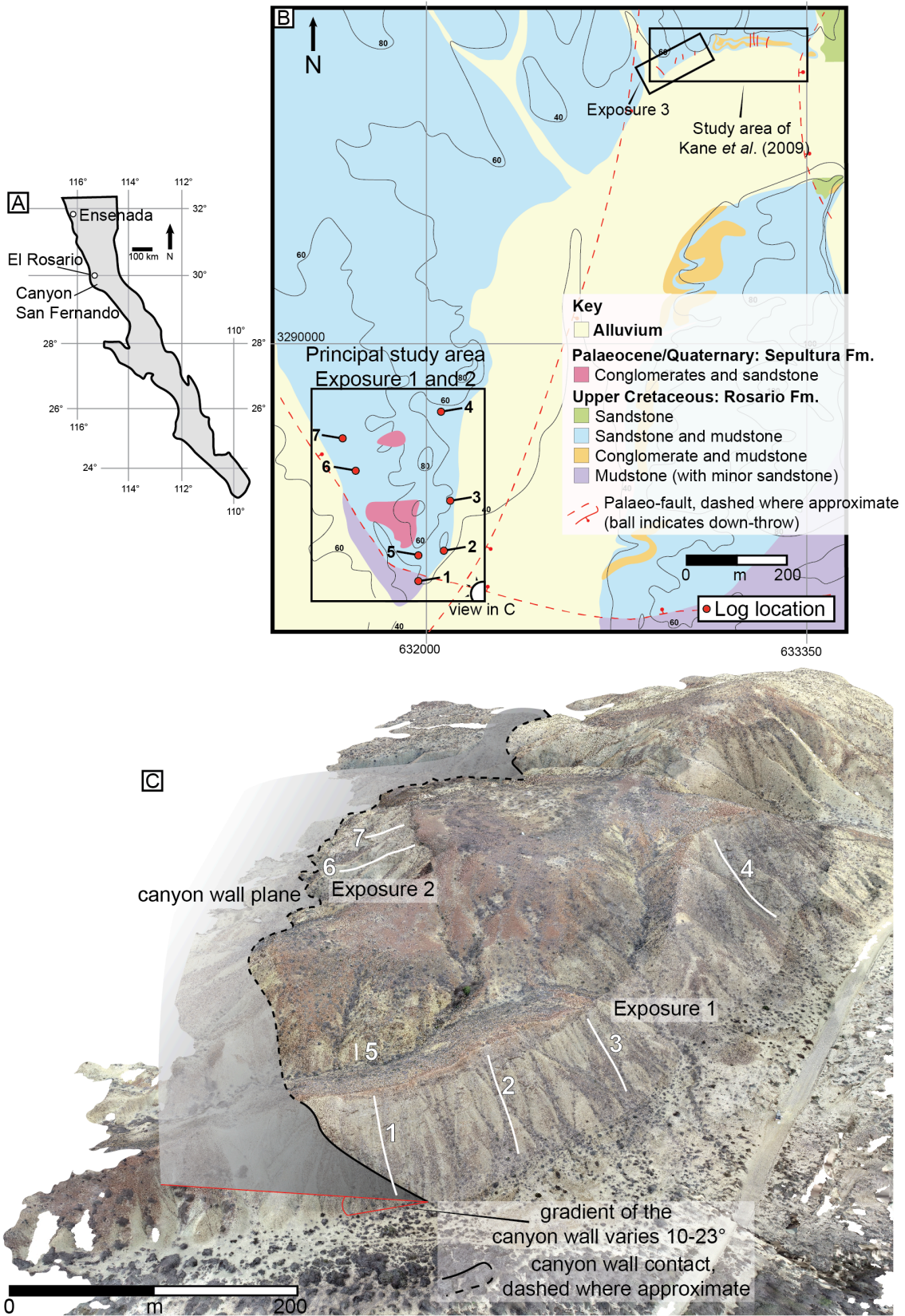
Figure 4.3: Figure caption overleaf.

Figure 4.3: Location map of Baja California with Canyon San Fernando annotated. (B) Simplified geological map of part of Canyon San Fernando, including the location of the principal study area (Exposure 1 and Exposure 2), the canyon overbank section (Exposure 3), and the axis area of Kane *et al.* (2009) (modified from Dykstra and Kneller, 2007; Kane *et al.,* 2009). (C) Annotated Uncrewed Aerial Vehicle (UAV) photogrammetric model showing the location of Exposure 1 and Exposure 2, and the location of the stratigraphic logs used in this study. Stratigraphic logs 1-4 were collected from Exposure 1. Log 5 is a high-resolution log of the thin-bedded heterolithic facies. Logs 6-7 were collected from Exposure 2.

4.5   Results

This study focusses on the changes in canyon-confined overbank sedimentology with increasing lateral distance from the axis, and the downstream heterogeneity in overbank deposit facies and architecture close to the canyon wall contact (Fig. 4.4). The stratigraphy of the Rosario Fm. in the Playa Esqueleto Canyon is described using a sedimentary facies scheme (Table 4.1). Six sedimentary facies and the palaeocurrent measurements are described to help characterise the depositional environments. For each facies, their process interpretation and a representative photograph are shown in Table 4.1 and Figure 4.5. The architectural relationship between the overbank deposits and the canyon wall surface, and MTDs emplaced within the canyon overbank are also considered.
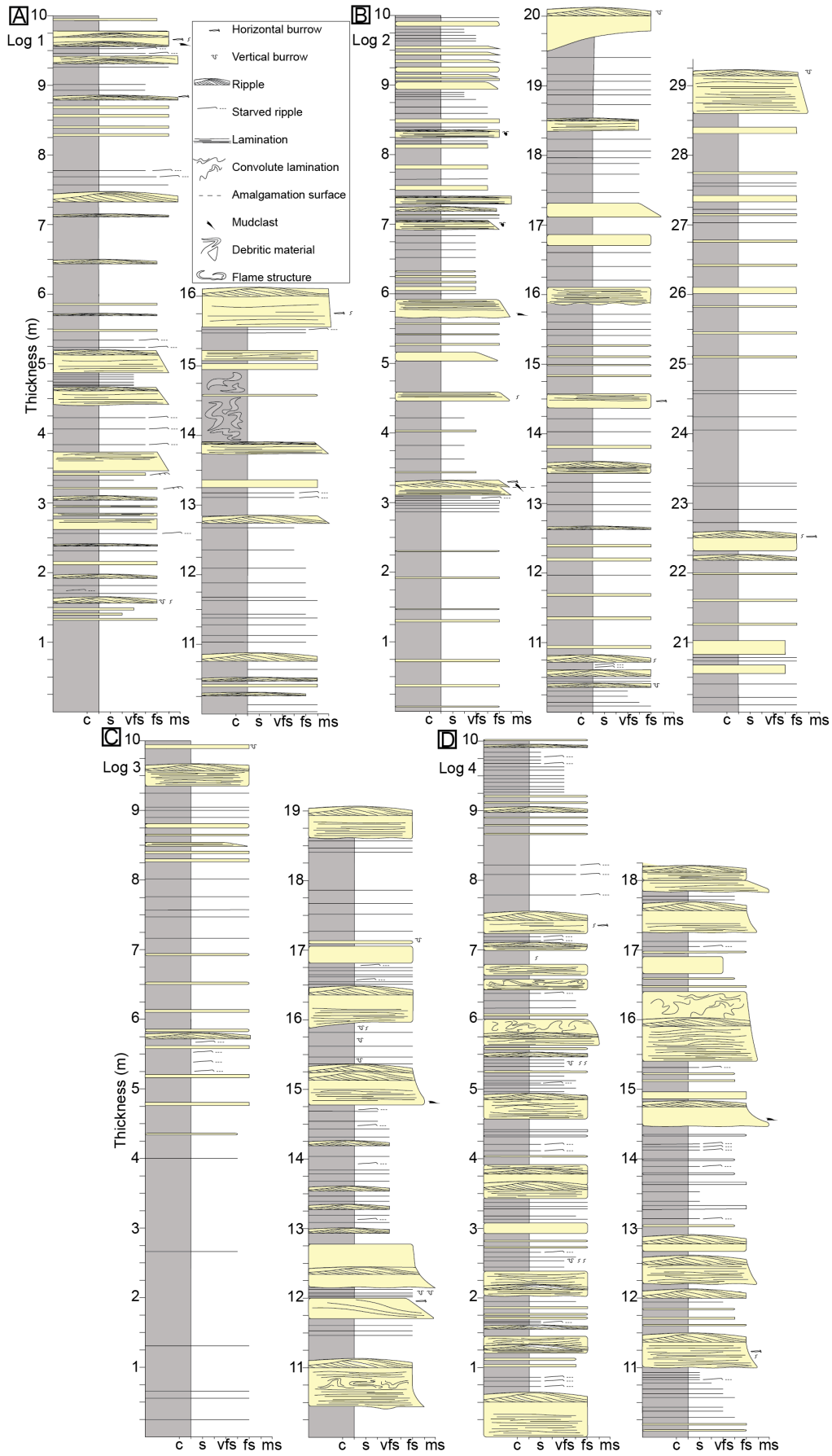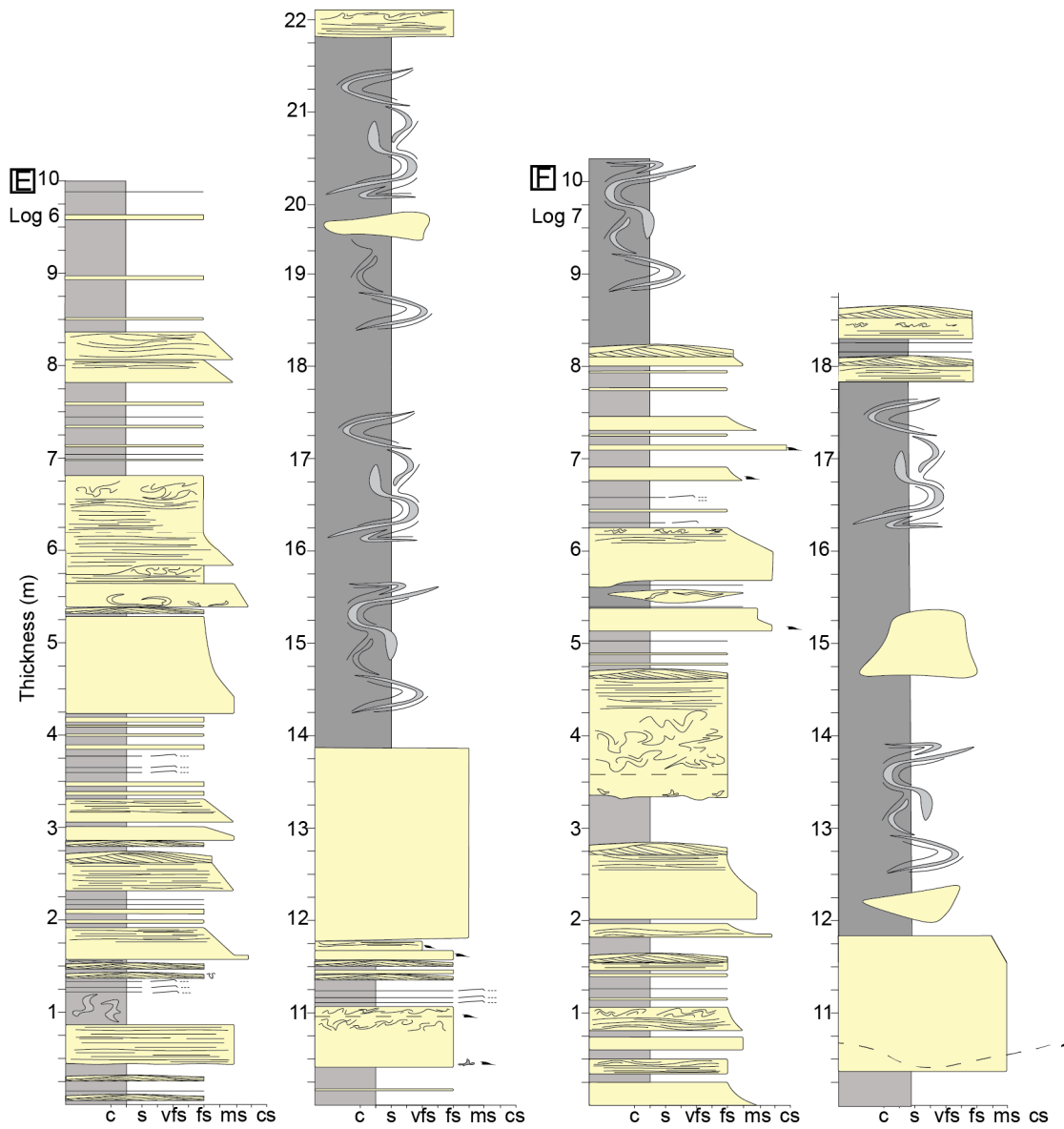
Figure 4.4: Sedimentary logs used in this study. (A-D) Sedimentary logs from Exposure 1. (E-F) Sedimentary logs from Exposure 2. For locations of sedimentary logs see Figure 4.3C. The original sedimentary logs are available in the Supplementary Material.
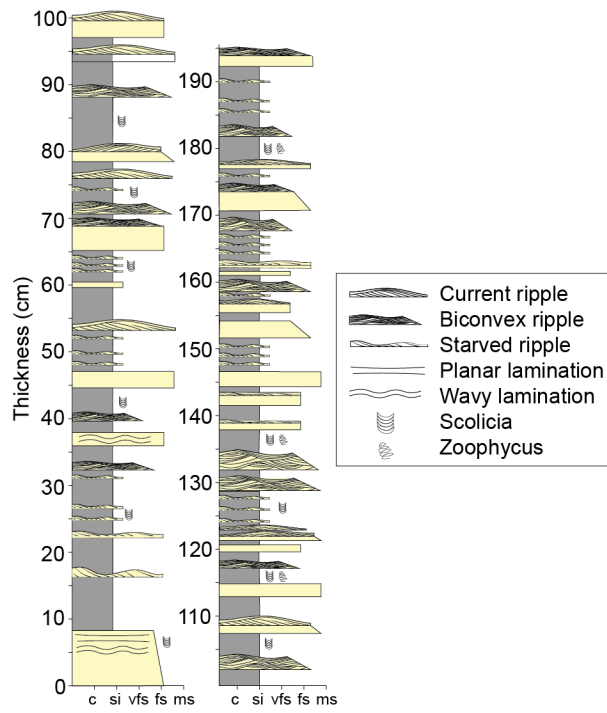
Figure 4.5: Sedimentary log of the thin-bedded heterolithics (He) facies, logged at a 1:5 scale. See Log 5 on Figure 4.3C for location. The original sedimentary log is available in the Supplementary Material.

Table 4.1: Facies table including descriptions and process interpretations for the six studied facies. Figures 4.5A–4.5E are the corresponding facies photos.

Facies code	Facies	Lithology	Thickness	Observations	Interpretations	Figure
Mu	Slope mudstones	Mudstone to fine-grained sandstone	No clear bedding	Light grey and fissile, foraminifera-rich mudstones with inter-bedded mm- to cm- scale very fine- to fine- sandstones.	Deposits form the canyon wall. Foraminifera palynology indicates deep-water agglutinated benthic forms suggesting mid-bathyal water depths (1500-3000 m), indicative of mid-slope deposition (Dykstra and Kneller, 2007; Kane *et al.,* 2009)	4.4A
He	Thin-bedded heterolithics	Sand-silt couplets of mudstone and siltstone, and very fine- to fine-grained sandstones	Successions of tens-of-cm. Mudstone and siltstone division 2-10 cm, sandstone division 1-5 cm.	Sandstones have sharp bases. High-angle climbing and low-angle symmetric ripples with opposing paleocurrent directions (ca. 50% of beds), and rounded, biconvex ripples (ca. 50% of beds). Siltstone divisions contain rare, starved, very-fine sand ripples. *Phycisiphon,* Scolicia, *Planolites, Ophiomorpha* and *Thalassinoides* trace fossils are common in the siltstone.	Siltstone deposited from dilute, low density turbidity currents (Allen, 1975; Mutti 1992). Sandstone deposited from suspension settling from fully turbulent, low density turbidity currents. Each sand-silt couplet represents one episode of overspill from the canyon axis (Kane *et al.,* 2009). High sediment fallout rates following flow interactions with topography are inferred from presence of combined flow bedforms and palaeocurrent complexities (Taylor *et al.,* 2024a). Trace fossils suggest sufficient time between subsequent flows to allow for colonisation (McArthur *et al.,* 2019).	4.4B
MeS	Medium-bedded sandstone	Very fine- to medium grained sandstone	cm to tens-of-cm	Very fine- to medium-grained, laminated and ripple cross-laminated sandstone. Where medium-grained, mildly erosional bases are occasional, whereas very fine- to fine-grained sandstone beds commonly show planar bases. When parallel lamination is not observed throughout the whole bed, often the lower half is parallel laminated and the top half is ripple. Ripples take two forms, either, rounded, biconvex ripples, or high-angle climbing ripple with sigmoidal cross-lamination.	Sandstone deposited and tractionally reworked by low-density SGFs. Combined flow bedforms on the bed tops suggests that SGFs in the canyon overbank were reflected and deflected against topography (Pickering and Hiscott, 1985; Tinterri, 2011; Tinterri *et al.,* 2022; Taylor *et al.,* 2024; Keavney *et al.,* 2024), in this case, provided by the canyon wall confining surface.	4.4C

CoS	Convolute laminated sandstone	Fine- to medium- sandstone	Tens-of-cm to 1 m	Ungraded fine sand or normally-graded fine- to medium-grained sandstone at the base of the bed with occasional cm-scale mudclasts. Upwards transition from parallel lamination, to wavy lamination, to convolute lamination, to rippled bed tops. The ripples take two forms: high-angle climbing ripples, and biconvex, rounded ripples. The full sequence is not always preserved.	Sandstone deposited from high-density SGFs. Mudclasts suggest that flows were capable of eroding and entraining the substrate (Lowe, 1982; Mutti, 1992). Structureless bed bases suggest high rate of suspension settling, perhaps due to the interaction with steep topography (Kneller and Branney, 1995; Keavney et al., 2024). Convolute lamination suggests that soft sediment deformation occurred post deposition (Gladstone et al., 2018).	4.4D
MTD	Mass transport deposit	Thin-bedded heterolithics and slope mudstones, with rafted blocks of sandstone	1-8 m	Only preserved at the complex canyon wall setting. Variable lateral continuity. The two lowermost slumps are composed of slumped thinly-interbedded heterolithics and canyon wall mudstones. The uppermost slump also contained rafted blocks of sandstone, up to 1 m thick.	Formed from the mass-wasting of the canyon wall mudstones and the material that onlapped the canyon wall surface. The presence of rafted blocks of sandstone within a chaotic, mud-to silt- dominated matrix suggests deposition under laminar flow conditions from cohesive debris flows, and thus are interpreted as debrites (sensu Talling et al., 2012). The lateral thickness variation and absence of slumps at the stable canyon wall setting suggests the slumps have highly variable 3D forms.	4.4E
MaS	Massive sandstone	Fine- to fine-medium sandstone	Tens-of-cm to >1 m	Typically fine-grained, massive sandstones with occasional cm-scale mudclasts, and with occasional medium-grained basal divisions with verging flame structures. The mudclasts often demarcate faint amalgamation surfaces. The bed tops often have very fine-grained divisions displaying convolute laminations.	The massive sandstone facies is interpreted to represent deposition from high-density SGFs. The presence of flame structures at the base of otherwise structureless, massive sandstones suggest deposition from rapidly decelerating flows (Kneller and Branney, 1995), captured by the relief above the recently emplaced, mobile mass transport deposits.	4.4F
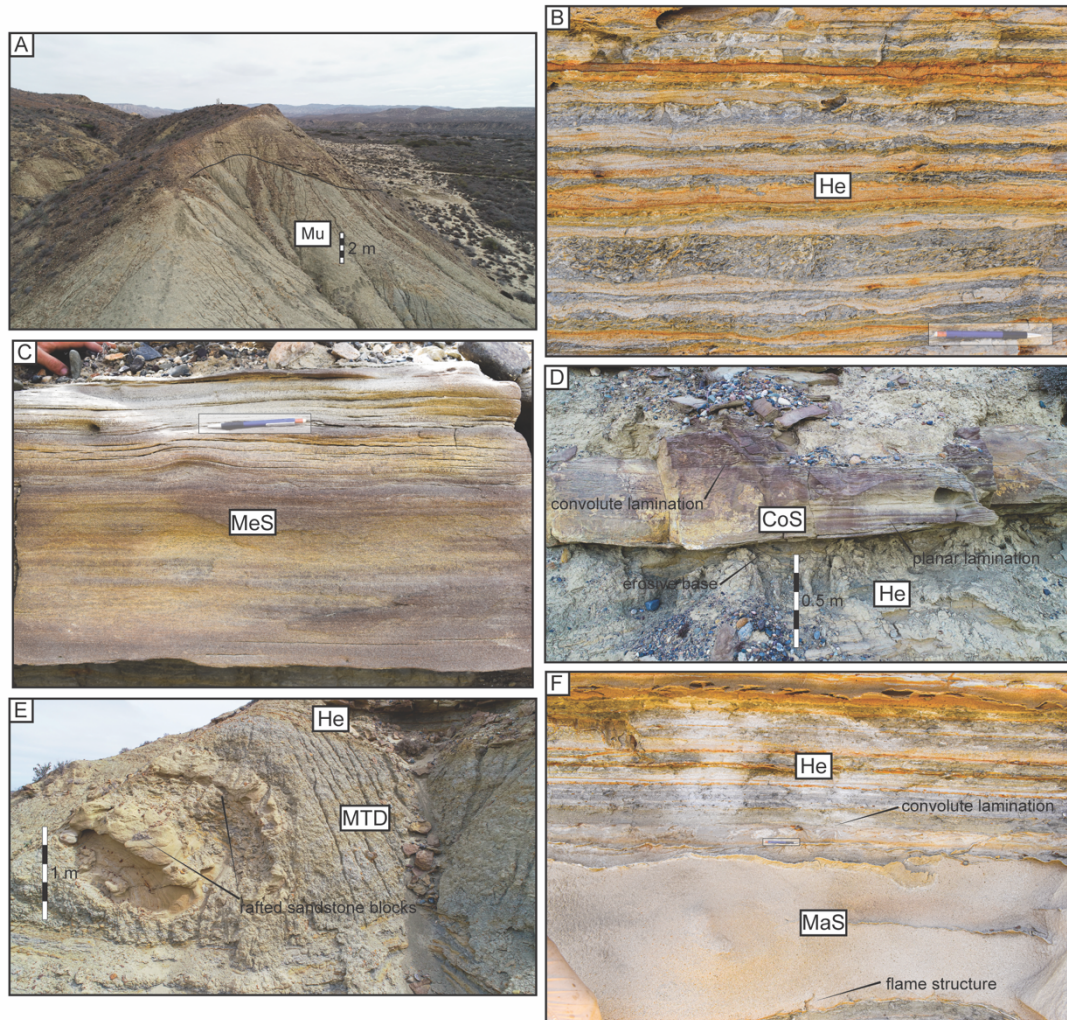
Figure 4.6: Representative photographs of the facies described in Table 4.1. (A) Slope mudstones (Mu). (B) Thin-bedded heterolithics, composed of silt-sand couplets (He). (C) Medium-bedded sandstone (MeS). (D) Convolute laminated sandstone (CoS). (E) Mass transport deposit (MTD). (F) Massive sandstone (MaS).

4.5.1   Lateral changes in overbank sedimentology

4.5.1.1   Observations

The Playa Esqueleto Canyon overbank deposits are observed 0.2 km laterally to the axis of the canyon (see '*Exposure 3*' in Fig. 4.3) and 1.2 km laterally to the canyon wall contact (see '*Exposure 1*' in Fig. 4.3). Stratigraphic logging, high-resolution photogrammetric models, and a correlation panel show that the laterally extensive thin-bedded heterolithics, medium-bedded sandstone, and convolute-laminated sandstone facies are present at all the exposures (Table 4.1; Figs 4.6–4.10). Exposure 3, close to the Playa Esqueleto Canyon axis, has a cumulative percentage of the medium-bedded sandstone and convolute-laminated sandstone facies ranging from 27-39% of the total logged stratigraphic thickness (Fig. 4.10C). The cumulative percentage decreases to 15-37% at the canyon wall contact (Exposure 1) (Fig. 4.10A). Furthermore, scours, at their maximum 1.2 m wide and cutting down up to 20 cm into the bed below, and sand-on-sand amalgamation surfaces are more common in the overbank deposits at Exposure 3 (Fig. 4.7C). Syn-depositional faults (Fig. 4.7C) and debrites tens of cm thick are also common in Exposure 3. The arithmetic mean palaeocurrent in the canyon axis is 223° (n = 536) (Kane *et al.,* 2009), whereas at Exposure 3 the arithmetic mean is 171° (median = 190°, range = 4-340°, n = 44) (Fig. 4.11C) and at Exposure 1 the arithmetic mean is 136° (median = 115°, range = 32-334°, n = 26) (Fig. 4.11A).

4.5.1.2   Interpretations

It is suggested that the sand-rich sediment gravity flows experienced a sudden loss of confinement between the canyon axis and the immediate overbank environment and that failure of material towards the canyon axis was common. The wide palaeocurrent dispersal recorded in the overbank deposits is recorded mostly by combined flow bedforms, that include rounded biconvex ripples and low-amplitude bed waves (Fig. 4.12). This indicates abundant flow reflections and deflections against the confining topography of the canyon wall and/or topography in the overbank. These predictable changes in overbank sedimentology point to the progressive deceleration and thinning of sediment gravity flows, as they become more unconfined having escaped the confinement of the canyon axis and traversing the canyon overbank environment. However, the record of predictable changes and deposit homogeneity is complicated where sediment gravity flows have interacted with the topography at the canyon wall contact.
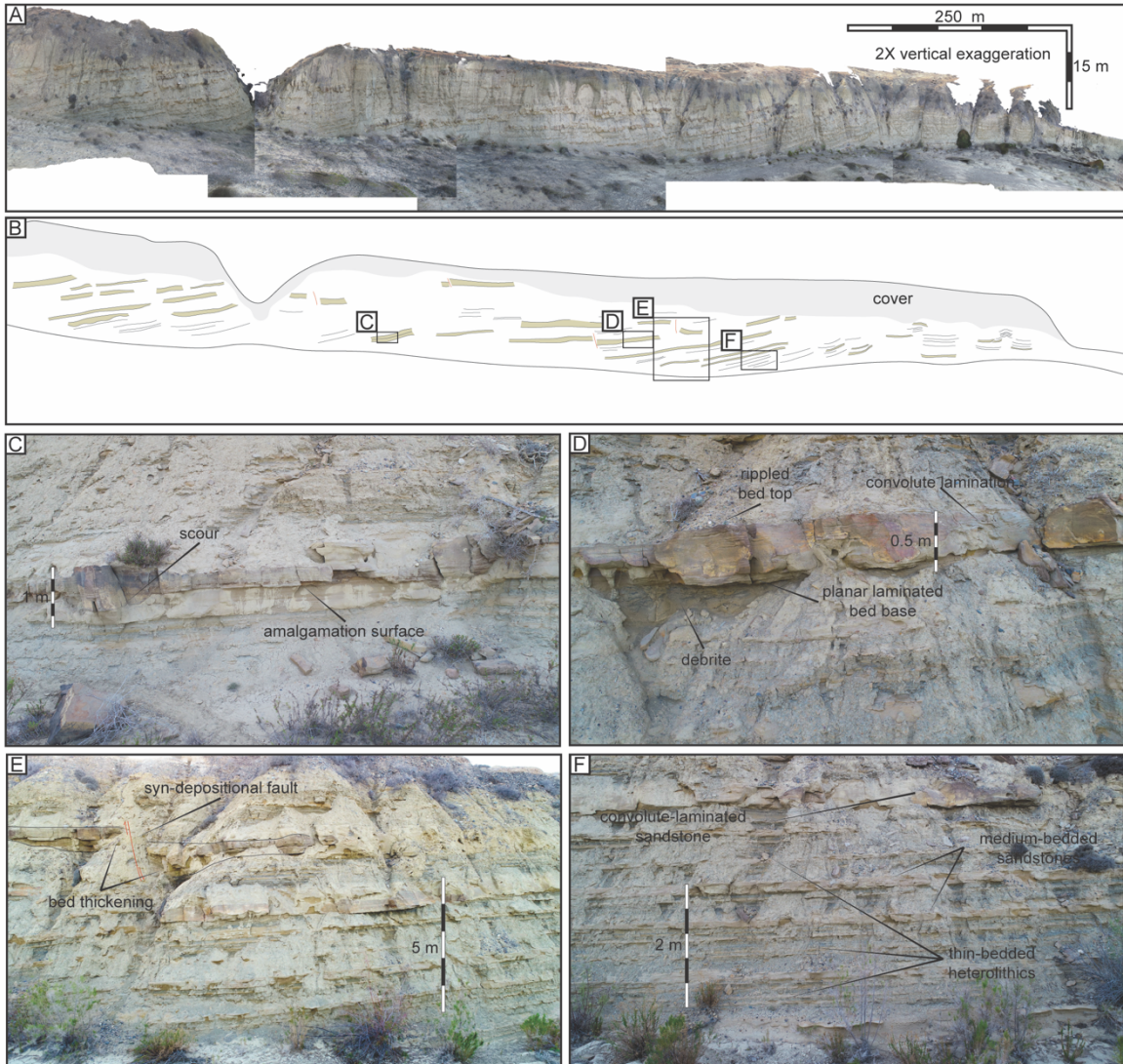
Figure 4.7: (A) Panoramic photograph of the Playa Esqueleto Canyon overbank. *See* 'Exposure 3' located in Figure 4.3C. Note the 2X vertical exaggeration. (B) Annotated line drawing of the canyon overbank. (C-F) Annotated photographs. (C) Scour and amalgamation surface. (D) Convolute laminated sandstone (CoS) facies. (E) Syn-depositional fault. (F) Representative section of the canyon overbank.

NE

?

NW

?

SE

250 m

SW

? Correlation certainty
Observed
Inferred

Exposure 2

50 m

Mudstone
Heterolithic (silt)
Heterolithic (sand)
Medium-bedded sandstone
Convolute-laminated sandstone
Debrite
Massive sandstone

5 m

Exposure 1

No exposure

50 m
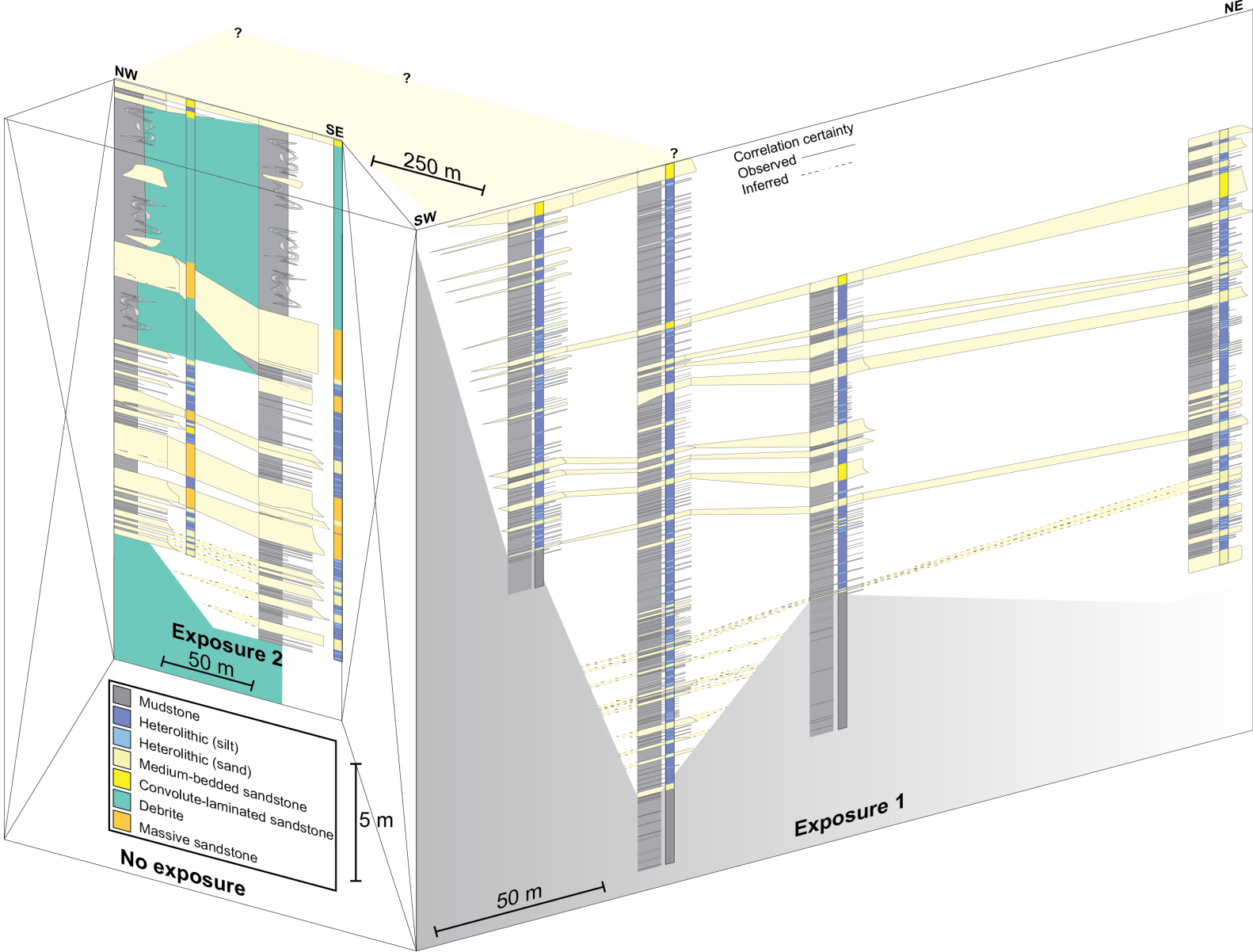
Figure 4.8: Correlation panel of Exposure 1 and Exposure 2, over a distance of approximately 200 m at Exposure 1 and 100 m at Exposure 2. The two exposures are approximately 250 m apart. The two exposures can be correlated by the convolute-laminated sandstone beds at top of the two southwesterly stratigraphic logs at Exposure 1 and the two logs at Exposure 2. The question marks indicate uncertainty in further correlating the beds due to poor exposure, and the correlation certainty of individual beds is shown using unbroken (observed) and dashed (inferred) black lines.

4.5.2   Submarine canyon-margin deposit heterogeneity

4.5.2.1   Exposure 1 – observations

At Exposure 1 (see 'Exposure 1' on Fig. 4.3 for location) the stratigraphic section is up to 29.5 m thick and characterised by the presence of slope mudstone facies (Mu) and thinly-bedded heterolithics (He) (Figs 4.7, 4.8 and 4.9A). The slope mudstone facies comprises pale grey, fissile mudstones that crop out to the south-west (Table 4.1; Figs 4.6, 4.7 and 4.9). The thinly bedded heterolithic strata onlap the mudstones (Fig. 4.9). The thinly bedded heterolithics form decimetre-scaled successions of multiple sand-silt couplets (Table 4.1; Fig. 4.6A) and comprises between 50% and 74% of the logged stratigraphic thickness (Fig. 4.10A). The siltstone divisions are generally massive, with common starved ripple trains. The siltstone packages (0.5-10 cm thick) are heavily bioturbated, displaying a high and diverse range of trace fossils (Table 4.1). Interbedded with the siltstone divisions are thin (1-5 cm thick) fine- to very fine-grained sandstone packages. The sandstone beds have sharp bases and are normally graded. The beds often display combined flow bedforms (Table 4.1; Figs 4.4B and 4.12), including, high angle climbing ripples and biconvex ripples, both displaying opposing, and diverse palaeocurrent directions (Figs 4.5B, 4.12A and 4.12B). The medium-bedded sandstone facies (MeS) are decimetre-thick very fine- to fine-grained sandstone beds, and comprises between 12% and 31% of the logged stratigraphic thickness (Table 4.1; Figs 4.6C and 4.10A). Typically, the medium-bedded sandstone facies (MeS) is parallel laminated throughout, or has a parallel laminated lower division and a rippled laminated upper division. The ripples are either high angle climbing ripples, or rounded, biconvex ripples, and both display opposing palaeocurrent directions, often within a single bed. The convolute laminated sandstone facies (CoS) comprises thickly-bedded sandstone beds (Table 4.1), present towards the top of the logged sections, which act as correlative marker datum, and make up between 3 and 6% of the logged stratigraphic thickness (Fig. 4.10A). The

beds are normally graded medium- to fine-grained sandstone and display an upwards transition from parallel, to wavy, to convolute lamination. Bed bases often contain mudclasts, and bed tops are commonly ripple laminated.
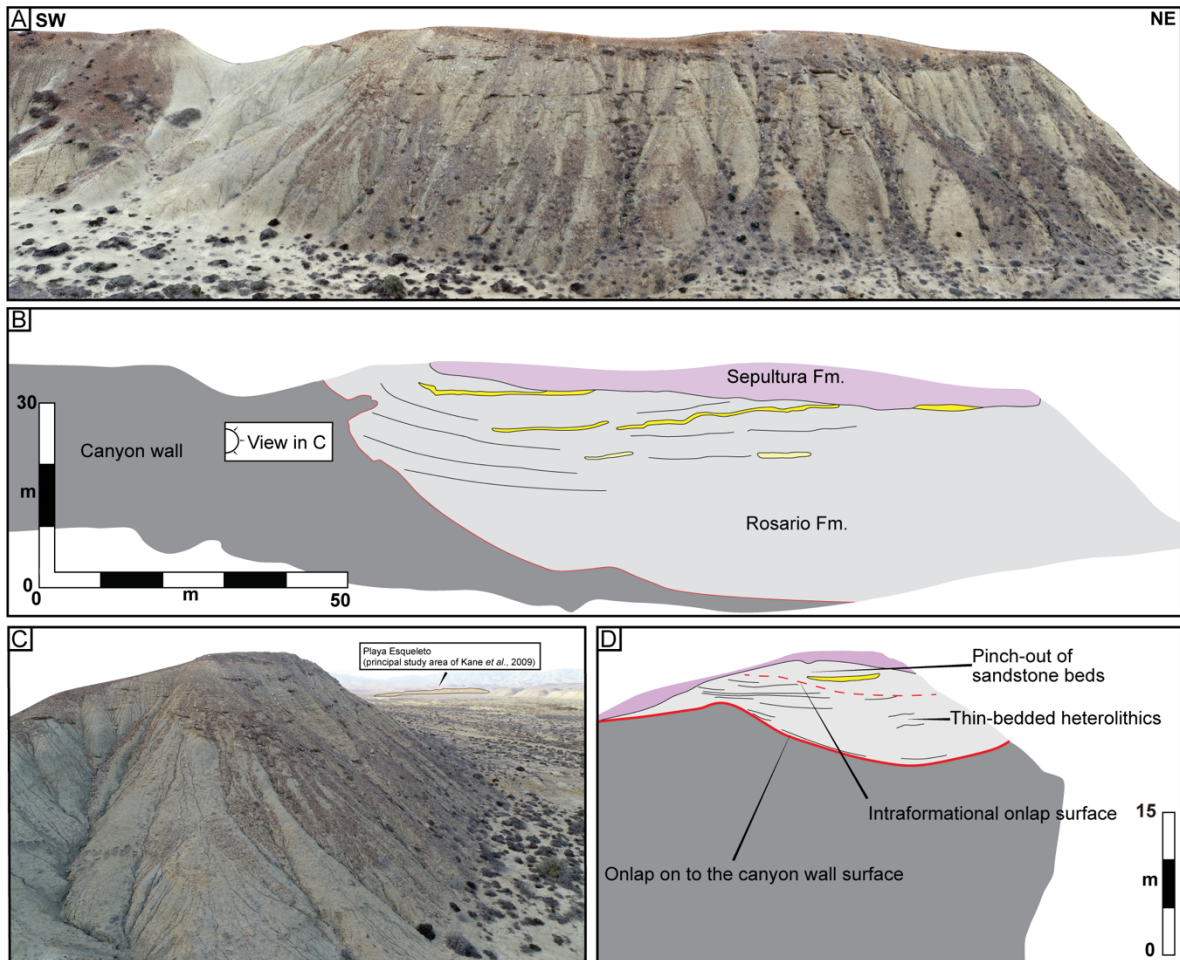
Figure 4.9: (A) Uncrewed Aerial Vehicle photogrammetric model of Exposure 1. (B) Annotated line drawing of Exposure 1. (C) Photograph of canyon wall contact and the location of canyon axis. (D) Annotated line drawing of the canyon wall contact, showing the architectural relationship between the thin-bedded heterolithic facies and the sandstone beds.

4.5.2.2   Exposure 1 – interpretations

Exposure 1 is interpreted to represent the stratigraphic relationship between overbank deposits and the slope mudstones onto which they onlap (Fig. 4.9). The stratigraphic architecture of the onlap

relationship will be revisited (*see* 'Architecture' results section). The siltstone packages that contain starved ripple trains record deposition from low-density sediment gravity flows. The absence of true ripple forms and proximity to the canyon wall surface suggests that these deposits are the most distal expression of such sediment gravity flows (Tek *et al.*, 2020; Boulesteix *et al.*, 2022). The sandstone-siltstone couplets also represent deposition from low-density sediment gravity flows (Allen, 1975; Mutti, 1992). The presence of combined flow bedforms suggests that the flows were thin and dilute (Taylor *et al.*, 2024a) and that interactions with seafloor topography in the canyon overbank (*i.e.,* the canyon wall) generated an oscillatory flow component (Tinterri *et al.*, 2022), or that flow reflections and deflections superimposed multidirectional, dilute flow components with the parental flow (Keavney *et al.*, 2024). In the canyon overbank, beyond the confinement provided by the axis, the thin-bedded heterolithic facies packages are therefore interpreted to represent the dilute, upper part of overspilling turbidity currents. The co-genetic, coarser-grained, lower parts of the sediment gravity flows are observed in the conglomeratic axis of the Playa Esqueleto Canyon, as described by Kane *et al.* (2009). The medium-bedded sandstone packages represent deposition and tractional reworking by low-density sediment gravity flows. Similarly, the presence of combined flow bedforms on bed tops suggests that sediment gravity flows in the canyon overbank reflected and deflected off topography (Pickering and Hiscott, 1985; Tinterri, 2011; Tinterri *et al.*, 2022; Keavney *et al.*, 2024), in this case, the canyon wall confining surface. The grain-size trend of the convolute laminated sandstone packages represent deposition from high-density sediment gravity flows that were subject to soft sediment deformation. The mudclasts observed near the bed bases suggest that flows were capable of eroding and entraining the substrate (Lowe, 1982; Mutti, 1992). The often structureless bed bases suggests an initially high rate of suspension settling, perhaps due to the interaction with steep topography (Kneller and Branney, 1995; Keavney *et al.*, 2024). The transition from planar, through wavy, to convolute lamination is possibly linked to flow velocity variations and pore pressure oscillations following the interaction of flows with intra-canyon topography, the entrainment of mud, and/or soft sediment deformation that occurred post deposition (*e.g.,* Gladstone *et al.*, 2018). The deposits from both low- and high-density sediment gravity flows show that the canyon overbank received a wide range of flow magnitudes, capable of breaching the confinement of the canyon axis, and all showing evidence of interactions with the topography of the canyon wall.
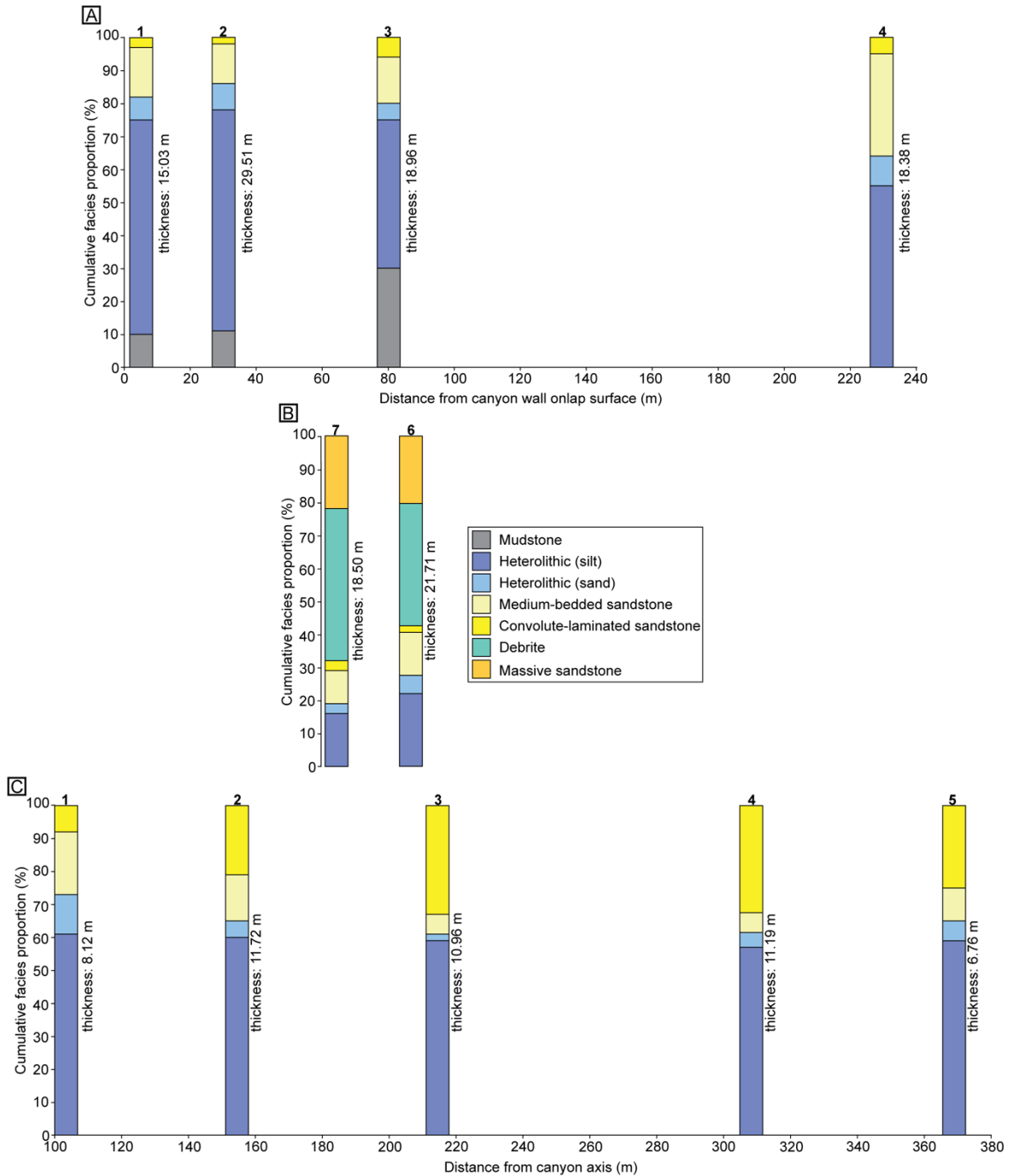
Figure 4.10: Bar plots for the cumulative facies percentages for each stratigraphic log. (A) Exposure 1 and the distance from the canyon wall onlap surface. (B) Exposure 2, where the spacing between the two logs is approximately 50 m. (C) Exposure 3 and the distance from the canyon axis.
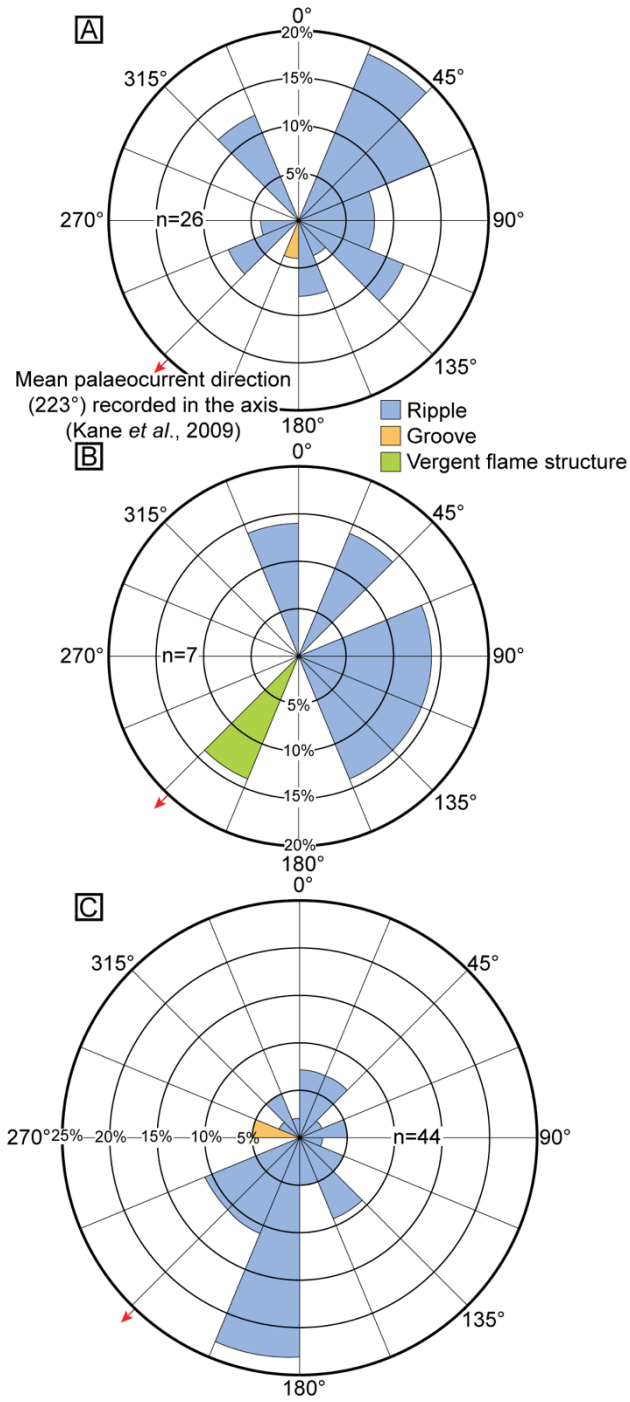
Figure 4.11: Equal area rose diagrams showing palaeocurrent directions for the three studied exposures, with the palaeocurrent recorded in the canyon axis by Kane *et al.* (2009) annotated. (A) Exposure 1. (B) Exposure 2. (C) Exposure 3.

A

sharp, erosive base

starved ripple

rounded biconvex ripple

amalgamation surface

parallel lamination

B

starved ripple

amalgamation surface

rounded biconvex ripples

sharp, erosive base

C

mudclast

skolithos trace fossil

anisotropic laminae

flame structure

soft sediment deformation

D

flame structures

E
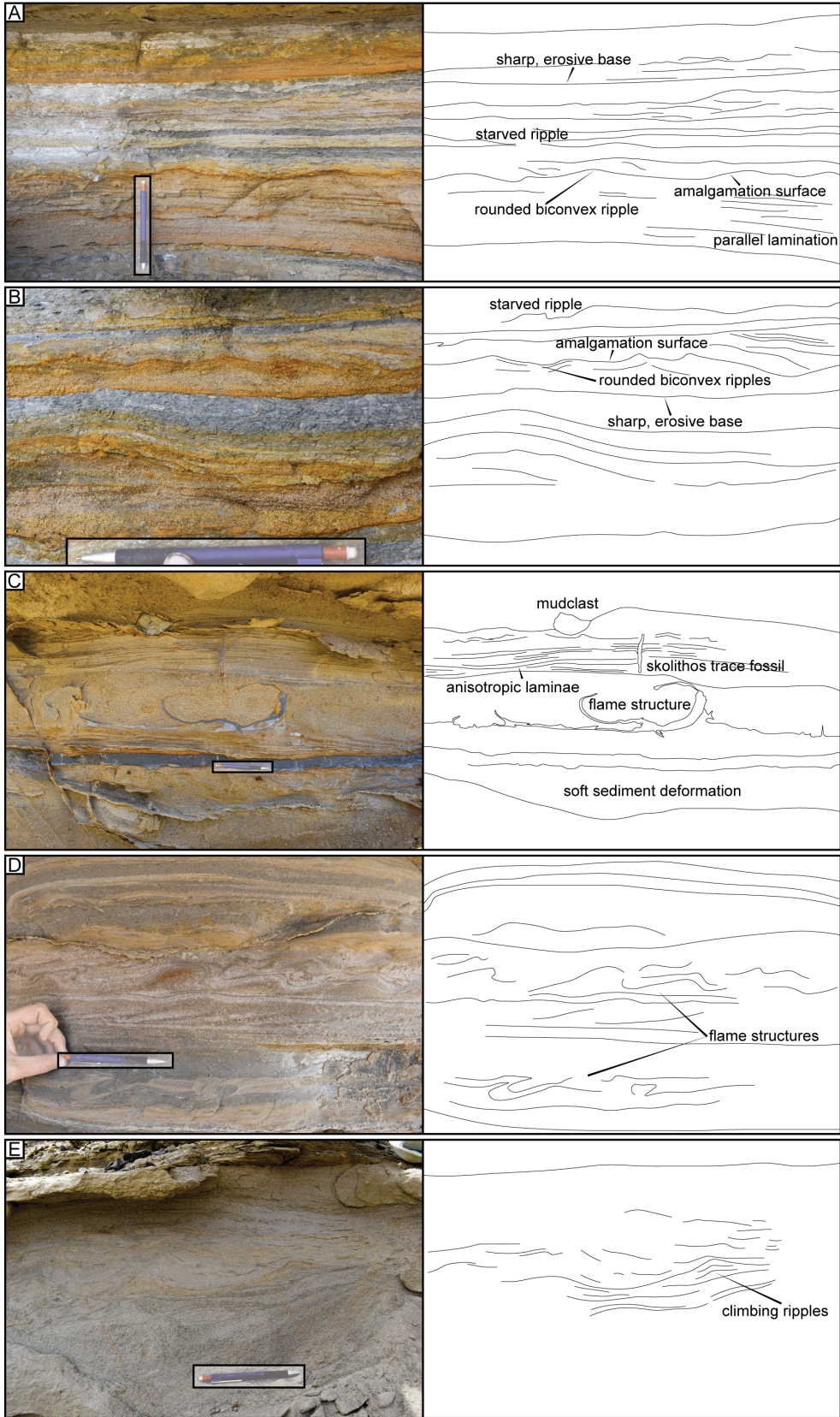
climbing ripples

Figure 4.12: Representative photographs and annotated line drawings of beds showing evidence of flow reflections and deflections. (A) and (B) Rounded biconvex ripples. (C) and (D) Flame structures. (E) Climbing ripples.

4.5.2.3   *Exposure 2 – observations*

At Exposure 2 (see Fig. 4.3 for location) the stratigraphic section is up to 21.71 m thick. The absence of the slope mudstone facies and presence of the mass-transport deposit facies (MTD) is the main difference between Exposures 1 and 2 (Figs 4.8, 4.10B and 4.13). The thinly-bedded heterolithics (He), medium-bedded sandstone (MeS), and convolute laminated sandstone (CoS) facies are present at Exposure 2 (Table 4.1; Figs 4.6 and 4.13). The sedimentary logs and photogrammetric model show that three distinct horizons of the MTD facies are present at Exposure 2. The MTD facies varies in thickness (1-8 m) and lateral extent (Fig. 4.13) and comprises 37-46% of the logged stratigraphic thickness (Fig. 4.10B). The MTD facies comprises disaggregated successions of the thin-bedded heterolithic and slope mudstone facies, as well as rafted blocks of sandstone (Table 4.1; Figs 4.13C and D), and often has an irregular, rugose upper surface. Commonly overlying the MTD facies is the massive sandstone facies (MaS), which consists of decimetre to metre thick, fine-grained sandstone beds, and comprises 21-22% of the logged stratigraphic thickness (Figs 4.10B and 4.13B). The bed bases typically contain cm-scale mudclasts and display verging flame structures (Fig. 4.12C). The massive sandstone division is typically topped by very-fine grained cm-scale caps displaying convolute laminations and flame structures (Fig. 4.12D). At Exposure 2, the arithmetic mean palaeocurrent is 147° (median = 116°) (n=7) (Fig. 4.11B).
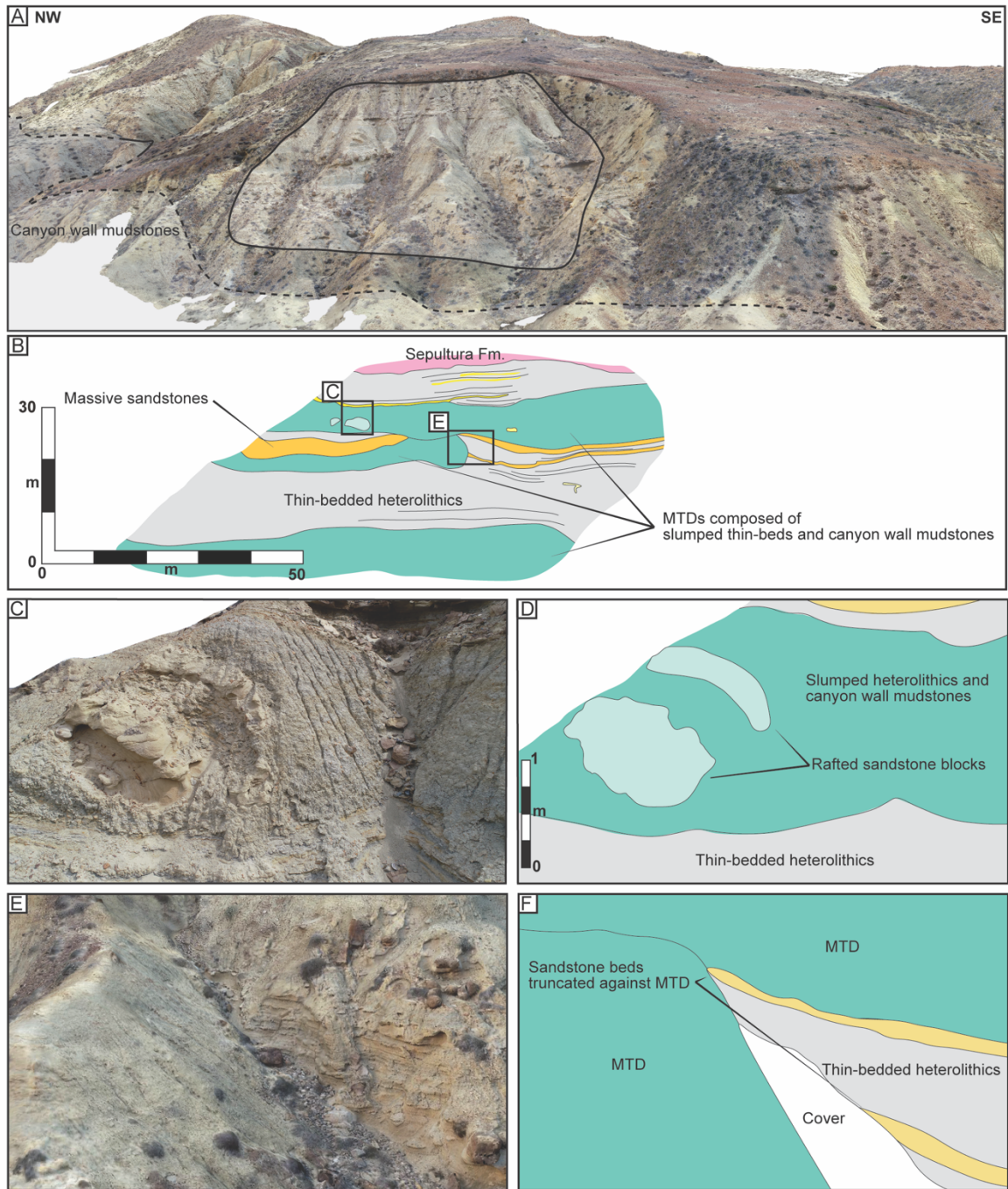
Figure 4.13: Figure caption overleaf.

Figure 4.13: (A) Uncrewed Aerial Vehicle photogrammetric model of Exposure 2. (B) Annotated line drawing of the exposure. (C) Photograph of a rafted sandstone block in the uppermost mass transport deposit. (D) Annotated line drawing of the rafted sandstone block. (E) Photograph of overbank deposits being truncated at the lateral margin of the middle mass transport deposit. (F) Annotated line drawing of the truncation.

4.5.2.4   Exposure 2 – interpretations

Exposure 2 is interpreted to represent the repeated mass wasting of the canyon wall. The presence of rafted blocks of sandstone within a chaotic, mud-to silt- dominated matrix suggests deposition under laminar flow conditions from cohesive debris flows, and thus interpreted as debrites (*see* MTD facies in Table 4.1) (*sensu* Talling *et al.,* 2012). The subsequent turbidity currents were captured and the deposits and healed the newly generated debrite relief in the canyon overbank. The absence of the canyon wall contact is due to limitations in exposure. However, the composition of the debrite suggests that the material that once onlapped the canyon wall failed locally into the overbank area. The repeated failure of the canyon wall generated debris aprons being emplaced in the overbank environment, acting as obstacles to subsequent sediment gravity flows, affecting onlap relationships (see 'Architecture' results section), and facies deposition.

The low-density turbidity currents that escaped the confinement provided by the canyon axis were able to feel the debrite relief and heal the topography, depositing the same thin-bedded heterolithics facies observed at Exposure 1. Where the medium- to high-density turbidity currents interacted with the healed topography of the debrites, the medium-bedded and convolute laminated sandstone facies were deposited. The massive sandstone facies was deposited directly above the debrite and is interpreted to represent the incoming high-density sediment gravity flow being captured by the topography and rapidly decelerating.

4.5.3   Submarine canyon-margin architecture

4.5.3.1   Exposure 1 – observations

The contact between the slope mudstones and overbank deposits is well exposed at Exposure 1 (Figs 4.3C, 4.8 and 4.9). This contact cuts down from SW-NE over approximately 20 m, forming a steep, rugose first-order NW-SE trending confining surface within the canyon. The mapping of the canyon wall and observations from the UAV photogrammetric model show that the gradient of the canyon wall varies between 10 and 23°. The thin-bedded heterolithics facies is observed to

be horizontally-bedded away from the canyon wall contact (Fig. 4.9B). At the contact, the thin-bedded heterolithics facies forms a wedge onto the canyon wall contact (Figs 4.9B and D). Towards the base of the succession, the thicker-bedded sandstone beds progressively thin towards the canyon wall contact. With increasing stratigraphic height, the thicker-bedded sandstone beds are more tabular, before abruptly pinching-out against the intraformational onlap surface (Figs 4.9B and D).

4.5.3.2 *Exposure 1 – interpretations*

The absence of any MTDs and the featureless canyon wall contact suggests that either the canyon wall had not failed at this location within the canyon, or that the canyon wall contact is a preserved slide scar from a previous mass-wasting event that has been removed or continued down canyon. Regardless, the canyon wall contact acted as the first-order confining surface in the overbank to subsequent gravity flows that escaped from the canyon axis. The more dilute, low-density turbidity currents responsible for the deposition of the thin-bedded heterolithic facies have an elevated run-up height upon incidence with topography compared to the denser, sandier flows. This has the effect of the low-density turbidity currents being able to feel and heal the topography of the canyon wall contact, before depositing, and generating an intra-formational onlap surface and modifying the angle of the original onlap surface. Subsequently, higher density flows were unable to surmount the newly generated onlap surface due to their decreased run-up potential, and instead pinch-out against the surface.

4.5.3.3 *Exposure 2 – observations*

The changes in architecture between Exposure 1 to Exposure 2 occur abruptly, over approximately 200 m downstream between exposures. The canyon wall contact does not crop out, but can be inferred from the position of slope mudstones. The three debrites have variable thicknesses and lateral extents and are composed of slope mudstones, thin-bedded heterolithics and rafted sandstone blocks (Figs 4.8 and 4.13). The lower- and upper-most debrites are laterally continuous across the exposure, whereas the middle debrite is exposed for approximately 50 m on the NW-side of the exposure and truncates the overbank deposits on the SE-side (Figs 4.8, 4.13E and 4.13F).

4.5.3.4 *Exposure 2 – interpretations*

The repeated, localised failure of the canyon wall acted to form evolving obstacles to subsequent flows in the canyon overbank. Where the debrites are laterally extensive across the width of the

exposure, the deposits from subsequent sediment gravity flows acted to heal the topography or were captured in the rugose upper surface of the debrite depending on the magnitude of the flow (*e.g.,* Martínez-Doñate *et al.,* 2021) (*see* 'submarine canyon-margin deposit heterogeneity' Results section). Where the magnitude of the mass-wasting event was decreased or the foci of failure moved, and the debrites are not laterally extensive across the exposure, the overbank deposits are truncated by the margins of the debrites. Here, the steep margins of the debrite acted as an obstacle to sediment gravity flows in the overbank, inhibiting the run-up potential and limiting deposition atop the debrite.

4.6 Discussion

4.6.1 Mass-wasting of the canyon wall

The changes in thickness and lateral extent of debrites 250 m downstream (Fig. 4.6), and change in canyon wall contact position, suggest the repeated, localised failure of the canyon wall. Where the debrites are absent, the flows could interact with the topographic surface of the exposed canyon wall. How the flow-topography interactions varied through time is discussed further in the '*onlap styles*' discussion section. The mapping of the canyon wall contact shows the approximate position of the canyon margin at Exposure 2, but it is poorly exposed (Fig. 4.3C). However, the location of Exposure 2, and the presence and composition of the three debrites suggests the failure of the canyon wall and generation of debris flows that deposited in the canyon. The evacuation scar of the canyon wall failure is hypothesised to be scallop-shaped, as suggested by the orientation of the exposures and lateral variations in debrite architecture, a common geometry of submarine slide scars (*e.g.,* Tek *et al.,* 2021; Pope *et al.,* 2022; Ayckbourne *et al.,* 2023). The debrites represent the repeated failure and up-dip translation of the canyon wall mass-wasting events into the overbank. Whereas, adjacent to the main failure, the overbank flows interact directly with the canyon wall, against the slide scar, with deposition being unaffected by the mass-wasting deposits and forming simple onlap relationships with the canyon wall (Fig. 4.9).

One hypothesis for the emplacement of the debris flows into the overbank is the oversteepening of the pre-existing deposits that onlapped against the canyon wall surface, as has been observed elsewhere in submarine canyons (Armitage *et al.,* 2010; Gales *et al.,* 2013; Bührig *et al.,* 2022) and channels (De Ruig and Hubbard, 2006; Hubbard *et al.,* 2009). However, the presence of slope mudstones in the MTDs suggests that the canyon wall itself also actively failed at the time of mass-wasting. The canyon wall contact has been hypothesised to represent either a canyon wall slide scar or an approximately syn-depositional cross canyon normal fault (Kane *et*

al., 2009). The palaeocurrent recorded in the axis of the Playa Esqueleto Canyon (arithmetic mean = 223°; n = 536, Kane *et al.,* 2009), and the orientation of the canyon wall confining surface at Exposure 1 (oblique to the depositional dip recorded in the canyon axis), suggests that the orientation of the canyon has changed downstream between the study area of Kane *et al.* (2009) and this study. This change in orientation could be due to an underlying syn-depositional cross canyon fault (Kane *et al.,* 2009), and/or by a change in the planform geometry of the canyon. Given the presence and composition of the MTDs, and the form of the canyon wall contact, the canyon wall slide scar interpretation is supported here, however localised fault activity could provide the mechanism for the onset of mass-wasting (*e.g.,* Micallef *et al.,* 2014). In the Congo Canyon, submarine landslides from the failure of the canyon wall have been observed to dam and store sediment and organic carbon upstream of the landslide deposit, before re-routeing the thalweg (Pope *et al.,* 2022). Here a section orientated oblique to depositional strike is presented. The dip profile cannot be resolved, and hence neither can the volume of the three MTDs. However, in the case of the Congo Canyon, failure of the canyon wall produced an MTD with a volume of approximately 0.09 ± 0.01 km^3 and was observed to profoundly influence sediment gravity flow behaviour (Pope *et al.,* 2022). The scale of mass-wasting events observed in the current study are hypothesised to be more in line with observations from Congo Canyon as opposed to shelf margin collapses, documented to produce MTDs with volumes of 3150 ± 600 km^3 (Collot *et al.,* 2001). However, recent observations from the Hikurangi channel-levee system documented an MTD with a volume of 19 km^3 to be the result of submarine channel wall failure (McArthur *et al.,* 2024). Given the susceptibility of canyon walls to mass-wasting events (*e.g.,* Paull *et al.,* 2013; Mountjoy *et al.,* 2018; Pope *et al.,* 2022) and the known dimensions of MTDs in other deep-water systems, MTDs have the capacity to profoundly influence sediment gravity flow behaviour, the resultant deposit geometry and sedimentology in 3D space. However, the localised heterogeneity in onlap and facies patterns observed in overbank environments cannot be resolved in seismic reflection data and from modern studies to the same degree as observed at outcrop. Recent repeat surveying of the Congo Canyon has shown how localised deposition of more than 5 m occurred in the overbank terrace environment (hypothesised to be thin-bedded turbidites) following a large canyon flushing event that eroded the canyon thalweg (Ruffell *et al.,* 2024). However, the facies variations in the terrace environment following the canyon flushing event are yet to be explored. By better understanding the patterns formed in response to interactions between sediment gravity flows and MTDs, more accurate estimations of particulate matter budgets can be made. These estimations can take into account information regarding the rates of transient storage, periodicity of canyon flushing events, and transport pathways.
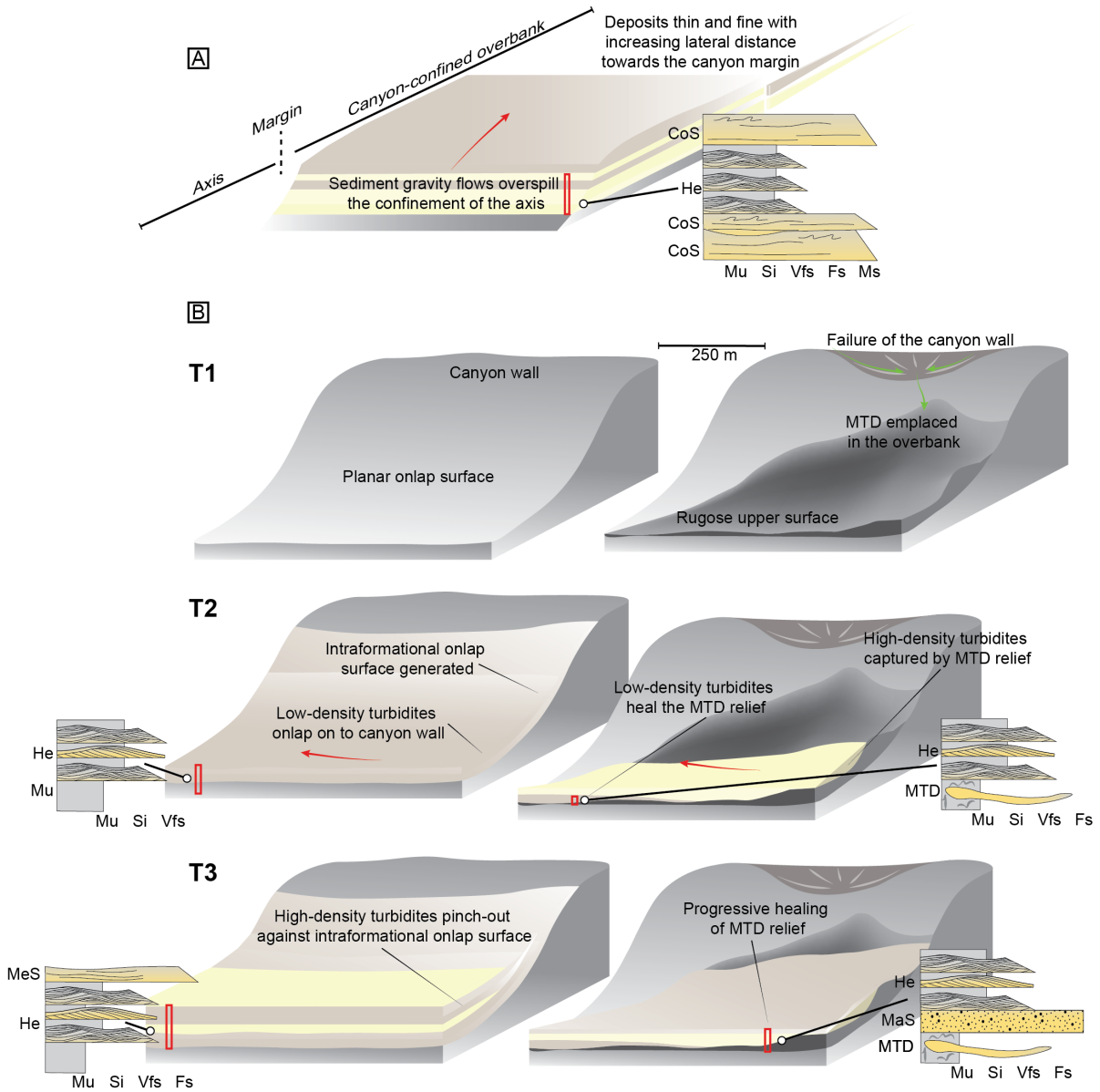
Figure 4.14: Summary schematic diagram showing the evolution of deposits in a canyon-confined overbank, with, (A) increasing lateral distance away from the canyon axis and (B) through time at the canyon margin. T1 shows the emplacement of debrites within the canyon overbank following the mass-wasting of the canyon wall. T2 and T3 document the flow-topography interactions through time between sediment gravity flows interacting with the planar canyon wall and with debrite topography.

4.6.2　Onlap styles

The onlap relationships observed between the canyon wall and the debrites is highly variable, due to the different topographic configurations and the magnitude of the SGFs (Fig. 4.13).

4.6.2.1　Onlap relationships with the canyon wall

At Exposure 1, the flow-topography interactions through time are represented by deposition from low-density turbidity currents against the canyon wall onlap surface, the generation of an intraformational onlap surface, and the subsequent pinchout of the deposits from high-density turbidity currents against the newly generated onlap surface (Fig. 4.9). The absence of debrites at the canyon wall margin permits the initial incoming flows that are mainly travelling down-canyon, and not directly up the canyon wall margin, to interact with a simple topographic surface, with little inherited complexity in gradient or form from the mass-wasting of the canyon wall. In the canyon-confined overbank environment (Fig. 4.2), with increasing distance away from the canyon axis and towards the canyon wall contact, the occurrence of deposits from bypassing turbidity currents decreases, mud-silt content increases, and deposits become thinner (Figs 4.7 and 4.9). These trends in deposit style are expected as sediment gravity flows become less confined with increasing distance away from canyon axis (Hansen *et al.,* 2017a). These predictable patterns have been observed in the overbank deposits of submarine channel-levee systems (*e.g.,* Babonneau *et al.,* 2002, 2010; Posamentier, 2003; Kane and Hodgson, 2011; Hansen *et al.,* 2015, 2017a).

The generation of the intraformational onlap surface is the result of the low-density turbidity currents riding up the canyon wall topography and depositing the thin-bedded heterolithic facies (Table 4.1; Fig. 4.9). Low-density turbidity currents, composed primarily of mud and silt, with a smaller very fine- to fine-sand component, are more capable of flow inflation and have increased run-up heights compared to more ground hugging high-density turbidity currents (Dorrell *et al.,* 2018a). The draping onlap style and presence of combined flow bedforms (Figs 4.9, 4.12A and 4.12B) suggests that upon incidence of the unconfined turbidity currents in the overbank with the canyon wall, the finer-grained component of the flow decelerated and thinned upslope, becoming highly multidirectional (as suggested by the laboratory experiments in Chapter 3).

Following the generation of the intraformational onlap surface, high-density turbidity current deposits formed the medium-bedded sandstone and convolute laminated sandstone facies (Table 4.1; Figs 4.9 and 4.14). These medium- to thick-bedded sandstone packages are

observed to abruptly pinchout against the onlap surface (Fig. 4.9B and D). The superelevation of high-density turbidity currents is hypothesised to be lower than the low-density counterparts. Furthermore, the healing of the original canyon wall onlap surface by the thin-bedded heterolithic facies modifies the angle of the newly generated onlap surface and the ability of the high-density flows to travel up the confining slope decreases, resulting in flow reflection and deflection off the onlap surface and into the overbank (Chapter 3). This not only generates highly multidirectional, combined flows, but also results in high rates of suspended sediment fallout and cyclical variations in pore pressure, that likely lead to the generation of the convolute laminated facies towards the base of the onlap surface.

The presence of a thin-bedded heterolithic drape against the canyon wall, the pinch-out geometries, and the proximity to the canyon axis suggests that canyon overbank was highly confined. This suggests these deposits, as observed in 2D, are not internal levee deposits as they have been previously considered (Dykstra and Kneller, 2007; Kane *et al.*, 2009), but are more akin to terrace deposits. Terrace deposits in submarine channel-levee systems are described as the product of fully turbulent sediment gravity flows that overspilled the channel, generating flat-lying, sheet-like deposits showing evidence of flow reflection and deflection against a confining surface in the overbank (Hansen *et al.*, 2015, 2017a). Figure 4.14 uses schematic sedimentary logs to compare the stratigraphy of the canyon thalweg studied by Kane *et al.* (2009), the depositional terraces, internal levees and external levee of the overlying submarine channel deposits studied by Hansen *et al.* (2015), and the canyon overbank deposits of this study. One of the main controlling factors in the generation of depositional terraces and internal levees, is the available space for flows to overspill into. The wedge-shaped geometry of internal levees is due to flows being able to overspill, decelerate, and deposit suspended sediment before interacting with a confining surface (Kane and Hodgson, 2011; Hansen *et al.*, 2015, 2017a); this contrasts with the unconfined nature of external levees where flows can spread more uniformly (Kane *et al.*, 2007). This would suggest that during the early, aggradational fill phase of submarine canyons, where canyons are typically more confined, the formation of depositional terraces is promoted. Through time, the gradual widening of the canyon and/or the migration of the canyon axis may generate additional accommodation in the overbank. This coupled with an allogenic signal change in the sediment input rate may lead to more internal-levee style deposition as canyons fill.

Figure 4.15: Figure caption overleaf.

Figure 4.15: (A) Schematic sedimentary logs of the Playa Esqueleto canyon thalweg, modified
from Kane *et al.* (2009) and of the internal levees, depositional terraces and distal external
levee from the submarine channel system that overlies the Playa Esqueleto Canyon,
modified from Hansen *et al.* (2015). (B) Schematic sedimentary logs of the canyon overbank
deposits described in this study from Exposure 1 and 3.

4.6.2.2   Onlap relationships with the mass transport deposits

In this study, where debrites are emplaced in the overbank, they are shown to profoundly
impact the sedimentation patterns of subsequent sediment gravity flows. Whether flows become
captured by, or act to heal, the topography of the debrites is dependent on the flow size and
concentration. The fact that the debrites are preserved in the overbank and have not been
completely reworked, further supports the hypothesis that the Playa Esqueleto Canyon was
undergoing an aggradational canyon fill phase, whereas the genetically related, overlying channel
complex sets (CCS-A to CCS-D) were dominated by sinuous channels, with limited aggradation
(Kneller *et al.*, 2020).

The thin-bedded heterolithic facies is observed to be deposited above the lower- and
upper-most debrites, first infilling and healing the topography and then generating more tabular
deposits following the progressive healing of the rugose surface (Figs 4.13B and 4.14). Low-
density turbidity currents can feel the topography of the debrites, owing to their small volume
and dilute nature. However, the deposits of high-density turbidity currents display large facies
and architectural differences when captured by debrite relief, compared to the onlap model
presented where flows interacted with the canyon wall. The massive sandstone facies is observed
above the laterally discontinuous debrite (Fig. 4.13B). Here, the upper surface of the debrite is
rugose and the massive sand facies infills the relief. This suggests that the relief acts to capture
the incoming high-density turbidity currents, causing the flow to decelerate rapidly and for
suspended sediment fallout rate to increase (Kneller and Branney, 1995). The presence of verging
flame structures at the base of the massive sand facies (Fig. 4.12C) suggests that the debrite was
unconsolidated and mobile, and recently emplaced into the overbank. On the south-east side of
the exposure, at the same stratigraphic height, deposits of the thin-bedded heterolithics and
medium-bedded sandstones facies are truncated against the margin of the debrite (Figs 4.13B
and F). Here, high-density turbidity currents are captured by the relief of the debrite, whereas the
contemporaneous flow, less affected by the topography displays different facies and architectural
relationships. Such discontinuity over a short spatial range (approximately 20 m) suggests that
the geometry and areal extent of the debrite is highly variable and that the trailing edge of the

MTD is preserved in the overbank, as opposed to more laterally continuous debrites where the deposits are shown to drape and infill the upper surface of the debrites (Fig. 4.14).

4.7   Conclusions

The changes in submarine canyon overbank deposits with increasing lateral distance from the thalweg, and the increased heterogeneity adjacent to the canyon wall, were examined using outcrop data from the Upper Cretaceous Rosario Formation, Mexico. High resolution photogrammetry and stratigraphic logging are used to confirm how as sediment gravity flows escape the canyon axis they become less confined, the presence of erosional features decreases and the deposits thin and fine with increasing lateral distance. However, at the canyon wall contact, the heterogeneity in the facies and deposit architecture increases, especially when sediment gravity flows interact with mass-transport deposits (MTDs) sourced from the mass-wasting of the canyon wall. The interaction between sediment gravity flows and the relatively simple topography of the exposed canyon wall reveals the strong and localised heterogeneity observed only 250 m downstream.

The exposed canyon wall provided a surface for the deposits from low density turbidity currents to drape, generating an intraformational onlap surface. Thin-bedded heterolithic deposits display evidence of flow reflection and deflection against the canyon wall in the form of combined flow bedforms and a wide palaeocurrent dispersal pattern, compared to that observed in in the overbank. The decreased upslope momentum of high-density turbidity currents caused the abrupt pinch-out of the deposits against the intraformational onlap surface. Over a short distance along-strike (250 m), debrites emplaced up-dip of the canyon wall acted to capture sediment gravity flows, profoundly influencing deposit character. Where low-density sediment gravity flows could feel the rugose topography of the MTDs and heal the upper surface, high-density sediment gravity flows were captured by the topography and decelerated rapidly, depositing thick, massive sands as opposed to thin-bedded heterolithics.

The complex geometry of submarine canyon walls, owing to their susceptibility to mass-wasting processes, has been documented in modern and subsurface studies. However, this is the first detailed study to document the downstream deposit heterogeneity of canyon overbank deposits adjacent to the localised failure of a submarine canyon wall. The repeated failure of canyon walls and the resulting volume of material emplaced in canyon overbanks can profoundly influence the character of overbank deposits.

Chapter 5   Pervasive microplastic pollution in a land-detached submarine canyon

5.1   Summary

Submarine canyons are important conduits for microplastic transport to the deep sea via turbidity currents. However, other near-bed oceanographic flows and sub-seafloor processes may play an important role in the transport and burial of microplastics. Analysing sediment cores from two transects across the Whittard Canyon, UK, shows that changes to submarine canyon topography and complex process-interactions control the burial of microplastics and semi-synthetic microfibres in the thalweg and on the canyon flanks. Microplastic pollution is pervasive across the canyon at both transects, from the thalweg and from 500 m higher on the flanks, despite turbidity currents being confined to the canyon thalweg. Furthermore, microplastic concentrations remain similar at sediment depths down to 10 cm. The calculated sediment accumulation rates from ^{210}Pb dating show that constant microplastic concentration with depth is irrespective of sediment age. This reveals that the huge global-increase in plastic production rates over time is not recorded, and that microplastics are present in sediments that pre-date the mass-production of plastic. The absence of silt-sized sediment and protracted sediment accumulation rates in the steep, upper-canyon, coupled with observations from hydrodynamic mooring data suggest turbidity currents are capable of bypassing sediment and microplastics further down-canyon. The turbidity currents become net-depositional once the canyon widens and the thalweg angle shallows, and the flows are less confined by the complex canyon topography. Changes to canyon topography, and the interaction of turbidity currents, deep-tidally-driven currents, and sub-seafloor processes control microplastic transport in the deep-sea and shreds any potential signal that microplastics may provide as indicators. This undermines the utility of microplastics as reliable markers of the onset of the Anthropocene.

5.2   Introduction

Plastic production increased 700%, from 50 million tonnes (Mt) in the 1970's to more than 400 Mt in 2022 (PlasticsEurope, 2023). More than 10 Mt of plastic enters the world ocean annually (Lebreton *et al.,* 2017). Microplastics (<1 mm diameter particles) represent approximately 13.5% of the marine plastic budget (Koelmans *et al.,* 2017), including primary (manufactured particles; Zitko and Hanlon, 1991) and secondary (derived from the breakdown of macroplastics; Andrady, 2011) microplastics. Semi-synthetic microfibres (*e.g.,* composed of rayon and chlorinated rubber)

are observed in deep-sea sediments (Woodall *et al.*, 2014) and are as equally persistent in the natural environment (Finnegan *et al.*, 2022), and have similar detrimental effects on biota (Jiang *et al.*, 2024) as plastic microfibres. Semi-synthetic microfibres are commonly used in clothes manufacturing and cigarette filters. From herein the term 'microfibre' is used to encompass synthetic and semi-synthetic microfibres.

Lacustrine and shallow-marine settings act as archives to calculate the rate and quantity of pollutant delivery (such as microplastics) and monitor how stresses on ecosystems have changed over time (Uddin *et al.*, 2021 and references therein). Despite being the ultimate sink for plastics (Woodall *et al.*, 2014), few studies have acquired sedimentary time-series records of microplastics in the deep sea (*e.g.,* Chen *et al.*, 2020). Furthermore, none exist in submarine canyons, which host important seafloor ecosystems (Fernandez-Arcaya *et al.*, 2017) and are the main conduits for delivering particulate matter, including pollutants, to the deep sea (Paull *et al.*, 2002; Zhong and Peng, 2021; Pierdomenico *et al.*, 2023). Avalanches of sediment, known as turbidity currents, flow through submarine canyons and are responsible for generating Earth's largest sediment accumulations (Curray and Moore, 1971), and are thought to be the main agent for microplastics transfer to, and sequestration on, the deep seafloor (Kane and Clare, 2019; Pohl *et al.*, 2020; Zhang *et al.*, 2024), yet other hydrodynamic processes can control microplastic concentrations (Kane *et al.*, 2020). It is increasingly-recognised that processes other than turbidity currents control particulate transport and burial in submarine canyons (*e.g.,* Bailey *et al.*, 2024; Palanques *et al.*, 2024). It is possible that the importance of complex submarine canyon topography, changes to the degree of flow confinement, other hydrodynamic and sub-seafloor processes, and anthropogenic activities has been underestimated. However, the role of hydrodynamic and sub-seafloor processes, and anthropogenic activities on microplastic and microfibre dispersal in submarine canyons remains unconstrained. This uncertainty results from a lack of targeted seafloor sampling and sedimentological context, and therefore limits understanding of microplastic fluxes to the deep sea, threats to deep-seafloor ecosystems, and deep-sea Anthropocene sedimentary archives.

The aims of this study are to determine microplastic and microfibre transport and burial processes in the deep-sea Whittard Canyon. To assess these processes, detailed seafloor observations from multibeam bathymetric mapping and video footage acquired from a Remotely Operated Vehicle (ROV), are integrated with analysis of four box-cores to quantify sediment accumulation rates and nine push-cores to quantify the sediment grain-size and microplastic particle concentration in surficial seafloor sediments.

5.3   Setting and methods

5.3.1   The Whittard Canyon

5.3.1.1   Canyon setting

The head of Whittard Canyon is at approximately 200 m water depth in the Celtic Sea, approximately 300 km from the nearest coast (Fig. 5.1A). Four main branches incise steeply into the shelf break, extending approximately 150 km, to approximately 3800 m water depth (Amaro *et al.*, 2016). The upper-reach of the Eastern Branch extends approximately 55 km, from the head to approximately 2960 m water depth, with steep canyon flanks and a >2° thalweg slope, with a vertical relief from flank to thalweg of approximately 1000 m. The lower-canyon reach extends to approximately 3700 m water depth, with lower gradient canyon flanks and a <2° thalweg slope, with a vertical relief from flank to thalweg of approximately 1250 m (Figs 5.1B and 5.1C). High-resolution bathymetric data enable investigation of the effects of submarine canyon geomorphology on microplastic distribution (Fig. 5.1B). The bathymetry of the Northeast Atlantic Ocean is derived from the Esri Ocean Basemap. The Digital Terrain Model data for the Whittard Canyon is based on the 2020 EMODnet digital terrain model (DTM), which has a resolution of 1/16 x 1/16 arc minute of longitude and latitude (ca. 115 x 115 metres). The bathymetry for the Eastern Branch of Whittard Canyon is derived from the GEBCO_2023 Grid, GEBCO Compilation Group (2023) GEBO 2023 Grid. All the bathymetry data are analysed using ArcGIS Pro software to mark the moorings and sample locations, and to construct the longitudinal profiles and the cross-sections of the canyons.
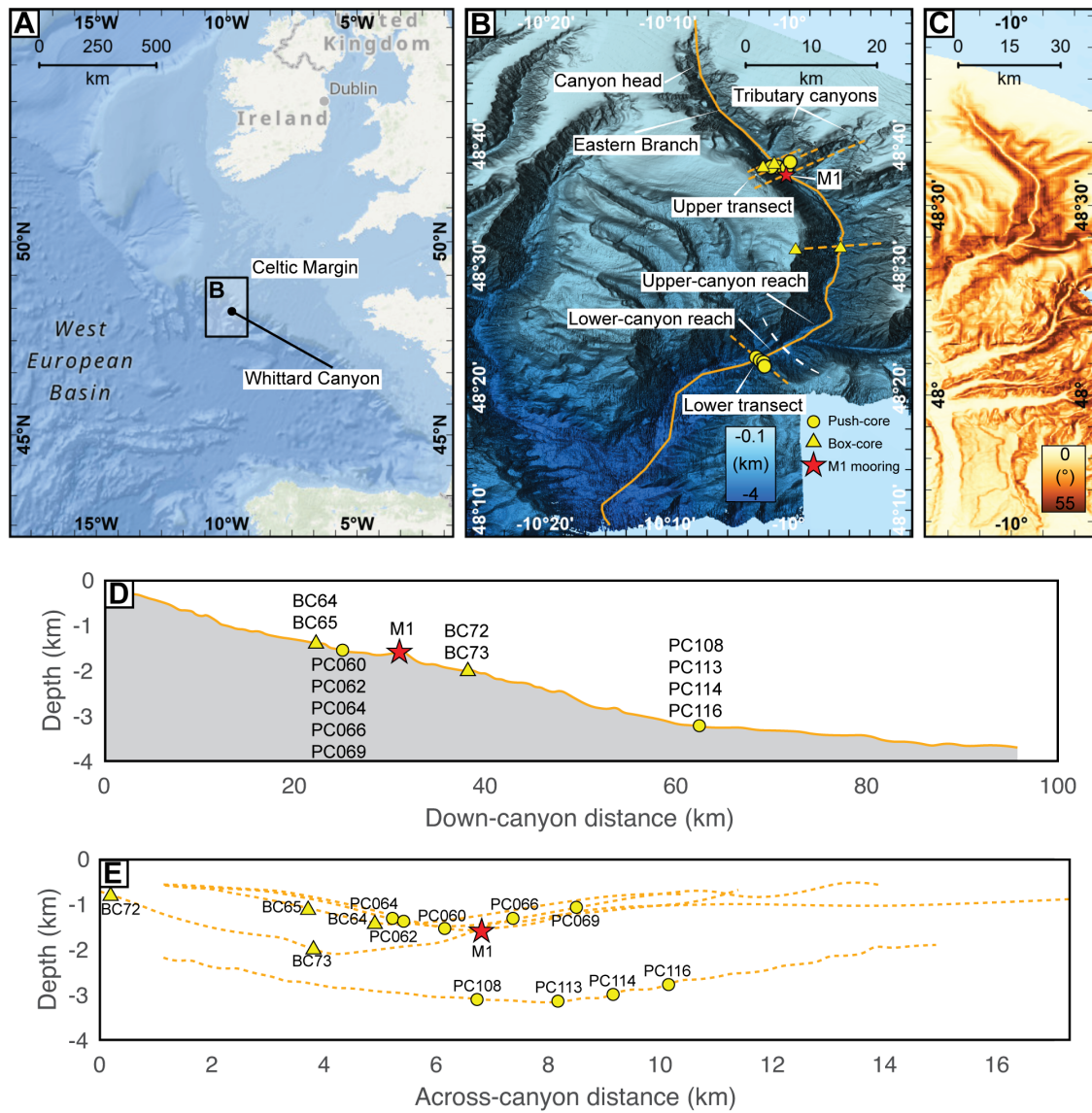
Figure 5.1: Location of data used in this study. (A) Location of Whittard Canyon. (B) Location of the cores and hydrodynamic mooring in the Eastern Branch of Whittard Canyon. (C) Slope angle map of the Eastern Branch. (D) Longitudinal profile of the canyon thalweg. (E) Cross-sections through each transect (locations on B).

5.3.1.2 Anthropogenic activity

Fishing activities that disturb the seafloor (*i.e.,* benthic trawling) are common around the head of the Whittard Canyon and on many of its interfluves; representing a source of marine pollutants (Xue *et al.,* 2020) and sediment resuspension (Daly *et al.,* 2018). Fishing activity data were

downloaded from Global Fishing Watch (GlobalFishingWatch, 2024) and formatted in estimated annual fishing effort (in hours) per 0.01 x 0.01° grids. The benthic fishing activity data were extracted. The cumulative annual trawling effort for 2013-2014 and 2023-2024 was exported for an area of 16,650 km^2 (48° - 49° N to 9° - 11° W) around the continental shelf, and Whittard Canyon was first extracted. The trawling effort for the same periods for the 661 km^2 (48° 10' 2.56" - 48° 29' 59.74" N to 9° 33' 34.59" - 9° 47' 52.25" W) area covered by The Canyons, Marine Conservation Zone was then extracted (Fig. 5.2). The Marine Conservation Zone was designated in November 2022, following the identification of vulnerable ecosystems, including burrowing megafauna and cold-water corals. The intensity of benthic trawling on the Celtic Margin has increased fivefold in the ten-year period from 2013-2014 to 2023-2024 (GlobalFishingWatch, 2024; Fig. 5.2).
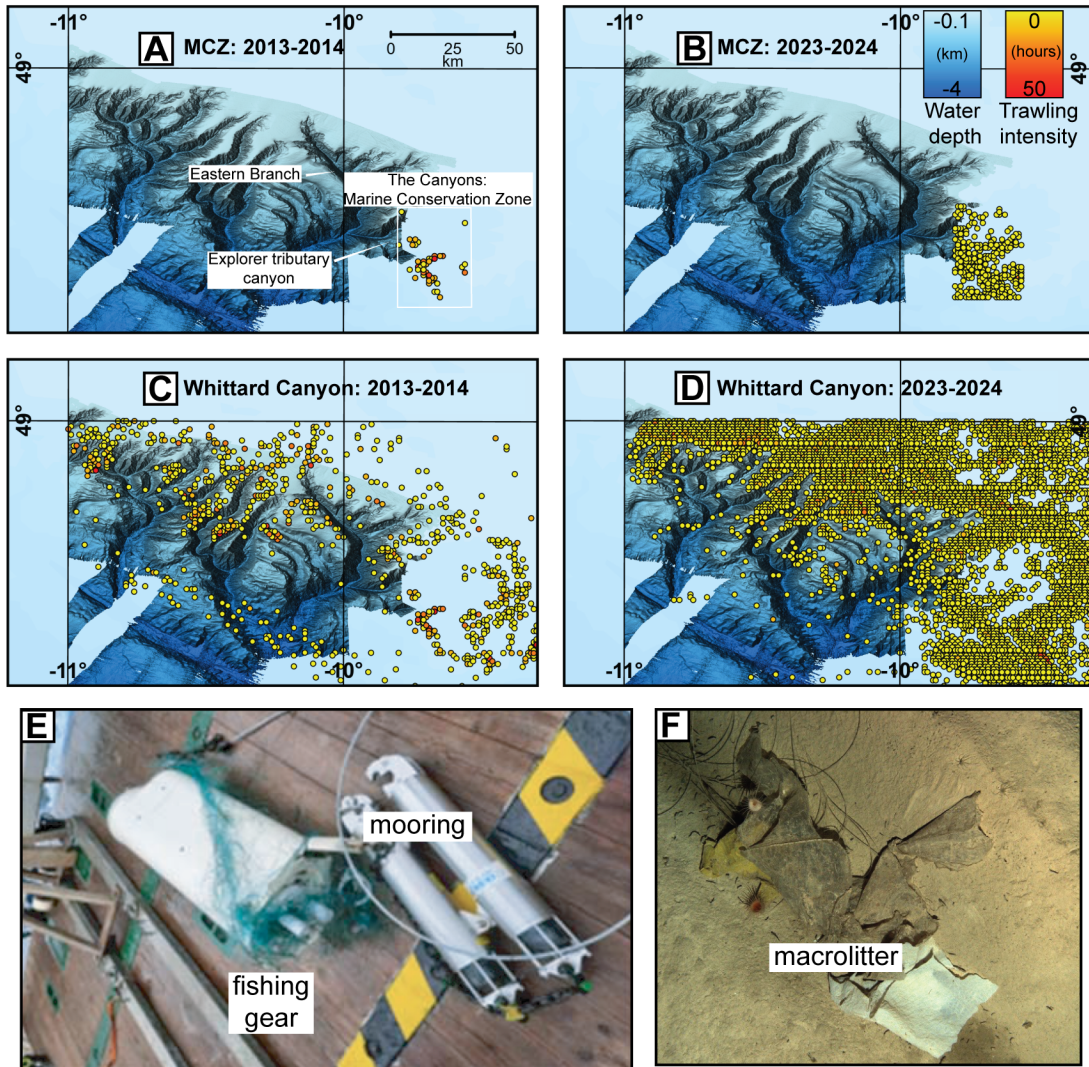
Figure 5.2: Intensity of benthic trawling as recorded by Global Fishing Watch. (A) Marine Conservation Zone (MCZ) 2013-2014. (B) MCZ 2023-2024. (C) the Whittard Canyon 2013-2014. (D) Whittard Canyon (2023-2024). (E) Photograph of the ADCP mooring wrapped in discarded fishing gear (modified from Heijnen *et al.,* 2022). (F) Macrolitter observed in the Porcupine Abyssal Plain (approximately 4800 m water depth).

5.3.1.3   Turbidity current and internal tide monitoring

A moored downward-looking 600 kHz Acoustic Doppler Current Profiler (ADCP) (M1 mooring – Fig. 5.1B: 30 m above seabed; 1500 m water depth) in the Eastern Branch recorded near-bed hydrodynamic conditions from June 2019 – June 2020, including vigorous (up to 1 m s^{-1}) internal tides and six turbidity currents. The ADCP was deployed by RRS Discovery (Expedition DY116). The ADCP data are available via the British Oceanographic Data Centre (*see* Supplementary

Material). These turbidity currents had maximum down-canyon velocities of 1.5-5.0 m s^{-1}, flow thicknesses ranging between 15 m and >30 m, and accumulated quartz-rich, fine sand in a sediment trap 10 m above seabed (Heijnen *et al.*, 2022; Fig. 5.3A). At M2 (21 km further down-canyon from M1) two of the six turbidity currents were not monitored, as they had either dissipated before reaching M2 or were too thin for detection. The frequency and speed of the turbidity currents recorded during the sampling period document how the Whittard Canyon experiences turbidity current activity analogous to land-attached canyons, despite being land-detached (Heijnen *et al.*, 2022).
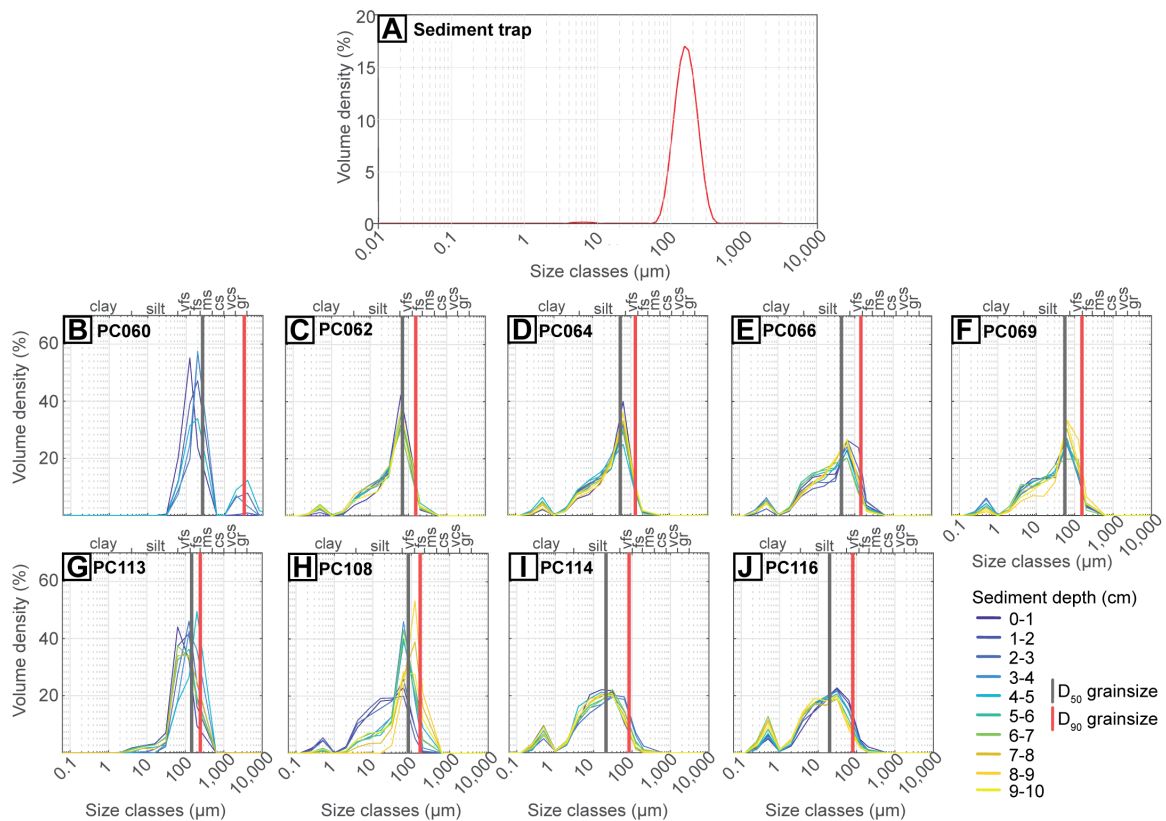
Figure 5.3: Grain-size distribution plots. (A) The sediment trap at the M1 mooring site of Heijnen *et al.* (2022). (B-J) The push-cores of the current study.

5.3.2   Sediment push-core recovery

Nine push-cores were collected from the Eastern Branch of Whittard Canyon using the Remotely Operated Vehicle (ROV) ISIS (Fig. 5.1B). Five precisely-located push-cores were collected along an across-canyon transect in the upper-canyon reach (24.9 km from the head, 1062-1546 m water depth), and four from an across-canyon transect in the lower-canyon reach (62.3 km from the

head, 2773-3204 m water depth) (Figs 5.1B, 5.1D and 5.1E). The push-cores were recovered from the upper-transect on the 21st August 2022, and from the lower-transect on the 2nd September 2022 and subsampled by the research scientists on-board the RRS James Cook (Expedition 237). All 9 push-cores were subsampled at 1 cm depth-intervals, down to 10 cm, depending on core recovery (subsample n=83), for microplastic particles and microfibres, and grain-size analysis.
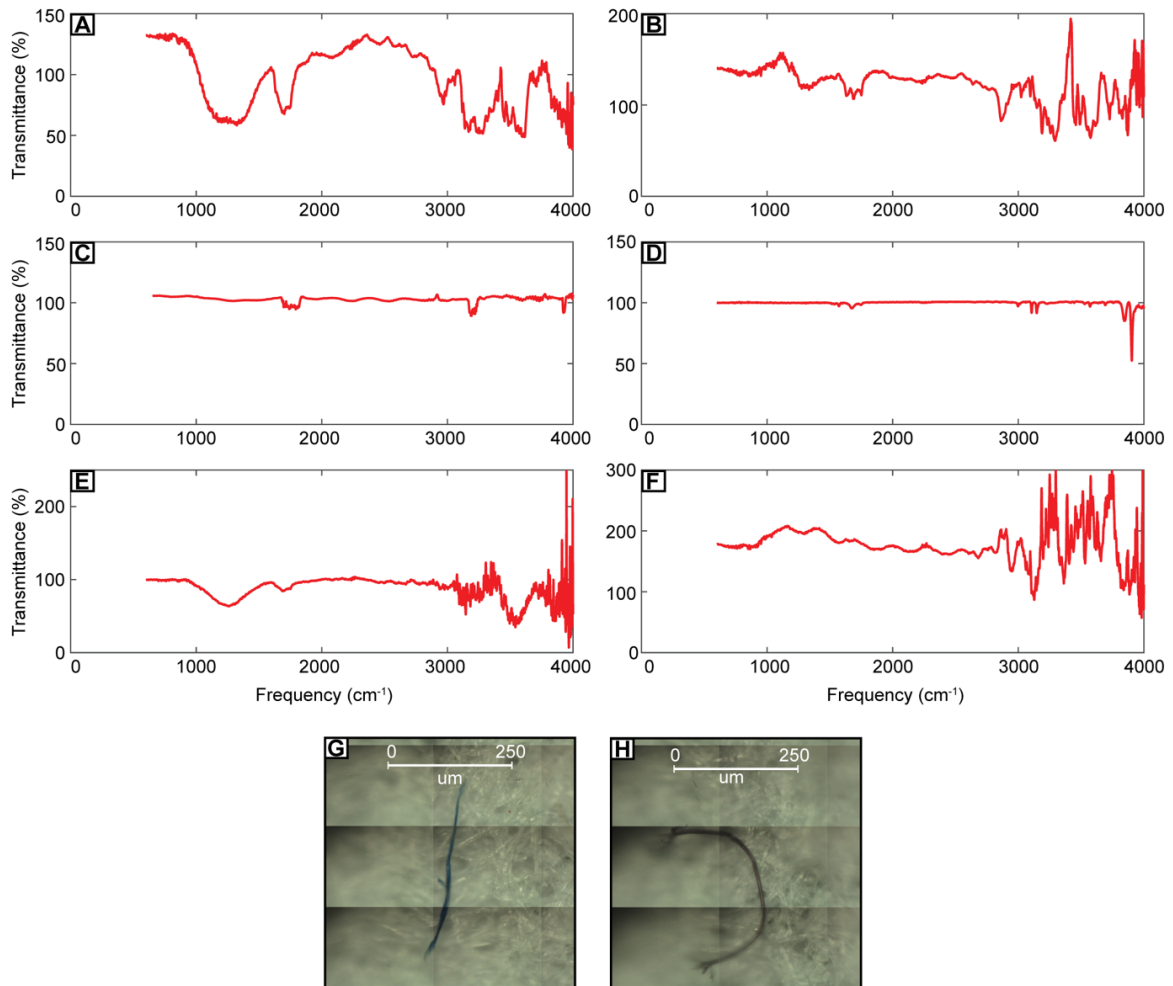
Figure 5.4: Fourier transform infrared (FTIR) spectroscopy spectra and microscope photographs of microfibres. (A) Rayon FTIR spectra. (B) Polyester FTIR spectra. (C) Polyethylene FTIR spectra. (D) Polystyrene FTIR spectra. (E) Chlorinated rubber FTIR spectra. (F) Polypropylene FTIR spectra. (G) Photograph of polyester microfibre. (H) Photograph of rayon microfibre.

5.3.3   Laboratory methods

5.3.3.1   Microplastic and microfibre extraction, identification and quantification

The 1 cm sediment core horizons had variable weights and water content, so samples were dried overnight in a drying oven set to 50°C. The dried samples were weighed, and for comparative purposes the weight and microplastic content were normalised to 50 g. Sediment samples were then stored in glass beakers and covered with aluminium foil. Samples were added to a 1 L glass beaker with approximately 700 mL of a dense $ZnCl_2$ solution (1.6 g cm^{-3}) and disaggregated using a magnetic stirrer, and mixed until the sediment/$ZnCl_2$ solution was homogenised. The microplastics were extracted from the sediment using a Sediment Microplastic Isolation (SMI) unit following a protocol developed for microplastic extraction (Coppock *et al.*, 2017) and modified following Nel *et al.* (2019). The solution was added to the SMI unit, and the beaker was rinsed with $ZnCl_2$ solution to flush any remaining sediment/microplastic. Prior to each use, the SMI unit was disassembled and thoroughly rinsed with Class 1 Milli-Q de-ionised water. Following settling overnight, the headspace supernatant was isolated by closing the ball valve of the SMI unit and rinsing with extra $ZnCl_2$ solution to flush any remaining microplastics before vacuum filtering over a Whatman 541, 22 μm filter paper. The prepared filter paper was then placed in a labelled petri dish and covered. Throughout the duration of the microplastic extraction procedure, all individuals wore white, cotton laboratory coats and latex gloves. All the microplastic extraction stages were performed in a clean laboratory in a fume cupboard. When the sediment samples were mixing in the 1 L beaker, and settling in the SMI units they were covered with aluminium foil to limit airborne microplastic contamination. When it was not possible during the sample preparation to cover the sediment sample with aluminium foil, an opened petri dish with a blank, Whatman 541, 22 μm, filter paper was placed in the fume cupboard and used as a contamination control procedural blank. When the prepared filter paper was exposed during the microplastic identification stage, a second contamination control procedural blank was also collected, again using an opened petri dish with a blank, Whatman 541, 22μm, filter paper, placed in the microscopy laboratory (Table A1).

The prepared filter papers, both from the sediment extraction process and the airborne contamination control blanks were analysed in a clean microscopy laboratory using a Zeiss Axio Zoom, V16 stereomicroscope at 20-50X magnification. From herein the definition a 'microplastic' defined by Kane *et al.* (2020) is used, which represents a plastic or semi-synthetic particle between 1 μm and 1 mm. Filter papers were traversed systematically to identify microplastics based on the following criteria: (i) no visible cellular or organic structures; (ii) a positive reaction

to the hot needle test (de Witte *et al.*, 2014); (iii) maintenance of structural integrity when touched or moved. Microplastics were categorised based on their colour and type, including, whether they were microfibres, microplastic fragments (including films), or microbeads (Table A2).

5.3.3.2   *Fourier transform infrared spectroscopy*

Microplastics were visually identified using optical microscopy and a subset of particles were analysed using Fourier transform infrared (FTIR) spectroscopy for polymer confirmation (Fig. 5.4). Identification of polymer composition was conducted on a subsample (n=13) of the extracted microplastics and microfibres using a PerkinElmer Spotlight 400 FTIR spectrometer using transmittance mode. The analytical region was positioned over the identified particle, the particle was imaged, and then scanned over a spectrum range of 4000-650 cm^{-1}, with a resolution of 4 cm^{-1} at a rate of 16 scans per analysis. The acquired spectra produced from the analysed particles were then processed and compared using the PerkinElmer Spectrum IR software with a standard reference library to assign polymer type (Fig. 5.4 and Table A3).

5.3.3.3   *Grain-size analysis*

The grain-size of 79 of the 83 push-core samples were analysed using a Microtrac FLOWSYNC particle sizer (Microtrac MRB). The grain-size of the four remaining samples (PC060B-E) were analysed using the dry sieving method due to the FLOWSYNC particle sizer having an upper particle limit of 2000 μm, and the fragmented shell material in the samples exceeded this upper limit. The FLOWSYNC particle sizer uses tri-laser diffraction to measure particle size distribution with a lower particle limit size of 0.01 μm. The samples were subjected to a small amount of ultrasonic dispersion. Three aliquots were analysed to ensure that each sample was completely dispersed. The grain-size distribution, indicating the volume percentage of grains in a certain size interval, was constructed (Fig. 5.3 and Table A2). The grain-size percentiles were exported from the FLOWSYNC software and are documented in Table A2.

5.3.3.4 ^{210}*Pb dating and sediment accumulation rates*

Sediment accumulation rates derived from ^{210}Pb dating of box-cores were recorded at four positions within the upper-canyon reach; two in the thalweg and two on the canyon flanks (Fig. 5.5). Sediment accumulation rates are calculated from the four box-cores (BC64, BC65, BC72, and BC73) (Fig. 5.5E-H and Table A4; locations on Fig. 5.1B), using ^{210}Pb dating. The box-cores were collected during the research cruise 64PE421 conducted by NIOZ (the Royal Netherlands

Institute for Sea Research) from the 14th May 2017 – 25th May 2017. The recovery rate of the box-cores varied by location.
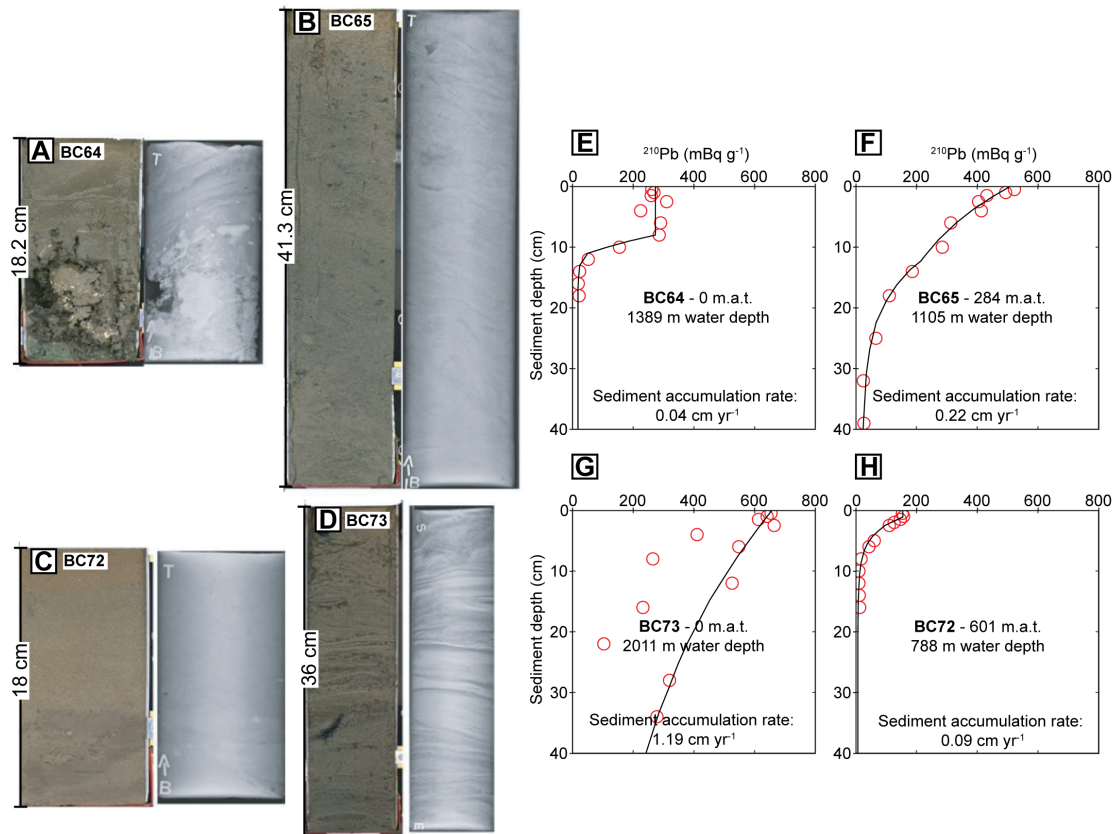
Figure 5.5: (A-D) Core photographs and X-ray scans of the box-cores used in 210Pb dating. (E-H) the sediment accumulation rate plots for the box-cores. (A and E) Box-core 64. (B and F) Box-core 65. (C and G) Box-core 72. (D and H) Box-core 73. m.a.t. is metres above thalweg. The total 1 s error data are included in Appendix Table A4.

The profiles of 210Pb are determined by alpha-spectrometry from 210Po. 210Pb is a naturally occurring radionuclide, part of the 238U decay series, with a half-life of 22.3 years. 210Po is extracted from the sediment by leaching with concentrated HCl or by total digestion using HNO_3 and HF. The 210Po is collected and counted with an alpha detector and the 210Pb profiles are plotted on a cumulative mass scale with an exponential curve. Where the 210Pb profiles deviate from the exponential curve, it is prudent to apply a conventional one-dimensional, two-layer vertical eddy diffusion model (following Carpenter *et al.* (1982)). The model assumes: (i) a constant rate of 210Pb supply (Appleby and Oldfield, 1978) and (ii) a constant initial sedimentation rate (Krishnaswarmy *et al*, 1971). A change in the gradient of the exponential

curve may be due to sediment mixing processes in the sediment mixed layer (*e.g.,* bioturbation), as is observed in BC64 and BC65, however this is accounted for in the model (Carpenter *et al.,* 1982). The sandier intervals of the box-cores hold a lower ^{210}Pb signature, so they were either avoided in the sub-sampling of the core horizons or sieved below 64 μm.

5.4   Results

5.4.1   Microplastic and microfibre pollution in surficial sediments

Microplastic particles and microfibres were present throughout all nine push-cores (Figs 5.6 and 5.7). A total of 1255 anthropogenic particles were observed with optical microscopy and a subset of the particles (n = 13) was verified with FTIR spectroscopy. Microfibres were the dominant microplastic type (microfibres = 91.3%, fragments = 5.7%, microbeads = 3.0%). Herein, the microplastic and microfibre count quantifies as the number of particles per 50 g of dry sediment weight (particles/50 g). FTIR spectroscopy confirms 62% of the anthropogenic particles are plastic, with common polymers including polyvinyl butyral, polyvinylchloride, and acrylic. The remaining 38% comprise semi-synthetic polymers, including chlorinated rubber and rayon (Fig. 5.4 and Table A3).
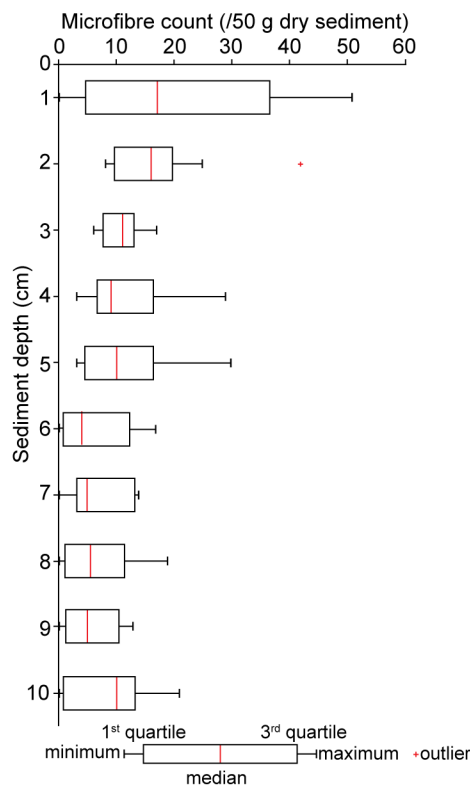
Figure 5.6: Box plot for microfibre concentration and sediment depth for all push-cores.

5.4.2   Microplastics in the thalweg

In push-core 060 (PC060) (34 metres above thalweg (m.a.t.) at the upper-transect; Fig. 5.8A), the grain-size range is 31-8000 μm, and the arithmetic mean gravel% and sand% are 9.6% and 90.3%, respectively; the granule-sized particles are fragmented shells (Fig. 5.3B and Table A2). Microfibre count in PC060 increases with sediment depth from 4 to 30 microfibres/50 g (Fig. 5.7C). In PC113 (0 m.a.t. at the lower-transect), the grain-size range is 2-200 μm, and the arithmetic mean sand% and silt% are 92.4% and 7.6%, respectively (Fig. 5.3G and Table A2). Microfibre count in PC113 decreases by 62.5% with sediment depth (Fig. 5.7F).

The sediment accumulation rates in BC64 (1389 m water depth, 0 m.a.t.) and BC73 (2011 m water depth, 0 m.a.t.) are 0.04 cm yr^{-1} and 1.19 cm yr^{-1}, respectively (Fig. 5.5). Therefore, it could take 8.4-to-250 years to accumulate 10 cm of sediment in the canyon thalweg, meaning sediments containing microplastics in the thalweg may pre-date the mass production of plastic in the 1950's. The mobility of sediment within the thalweg can be observed in a photograph captured by the ROV ISIS during the recovery of PC060; a high level of suspended sediment is recorded in the water column of the thalweg following the passing of a turbidity current down-canyon (Fig. 5.8A).
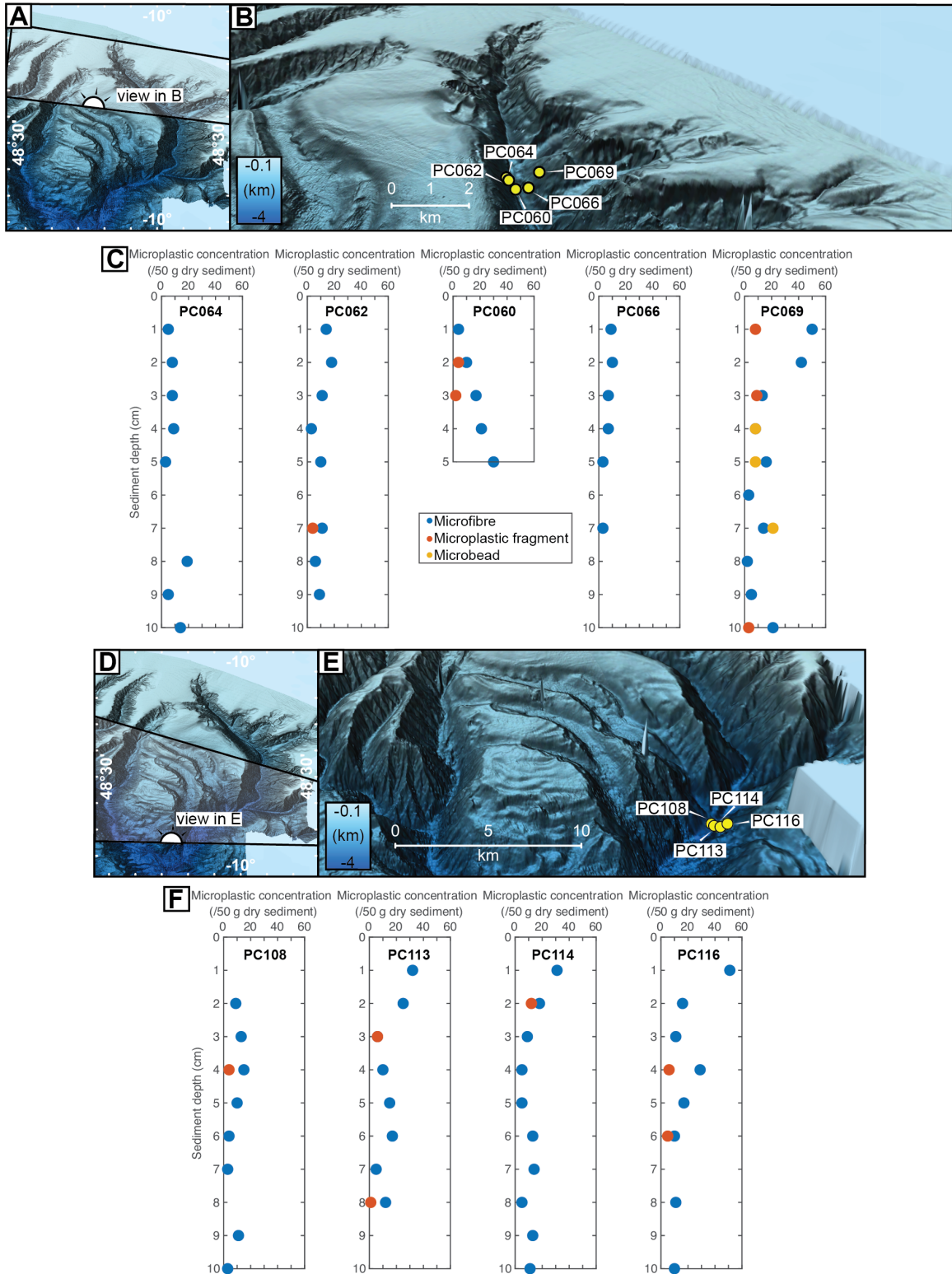
Figure 5.7: Figure caption overleaf.

Figure 5.7: Microplastic count with sediment depth for the push-cores located in Whittard Canyon. (A, B, D, and E) Location maps and high-resolution bathymetric maps of the Eastern Branch. 3X vertical exaggeration. (C and F) Microplastic trends for each push-core.

Table 5.1: Table for the push-cores collected from the upper-canyon and lower-canyon transects used for grain-size and microplastic analysis. Push-core number, height of the push-core above the thalweg, and the water depth of the push-core.

Upper-canyon transect		
Push-core	Meters above thalweg	Water depth (m)
064	277	1303
062	220	1360
060	34	1546
066	321	1259
069	518	1062

Lower-canyon transect		
Push-core	Meters above thalweg	Water depth (m)
108	52	3152
113	0	3204
114	209	2995
116	431	2773
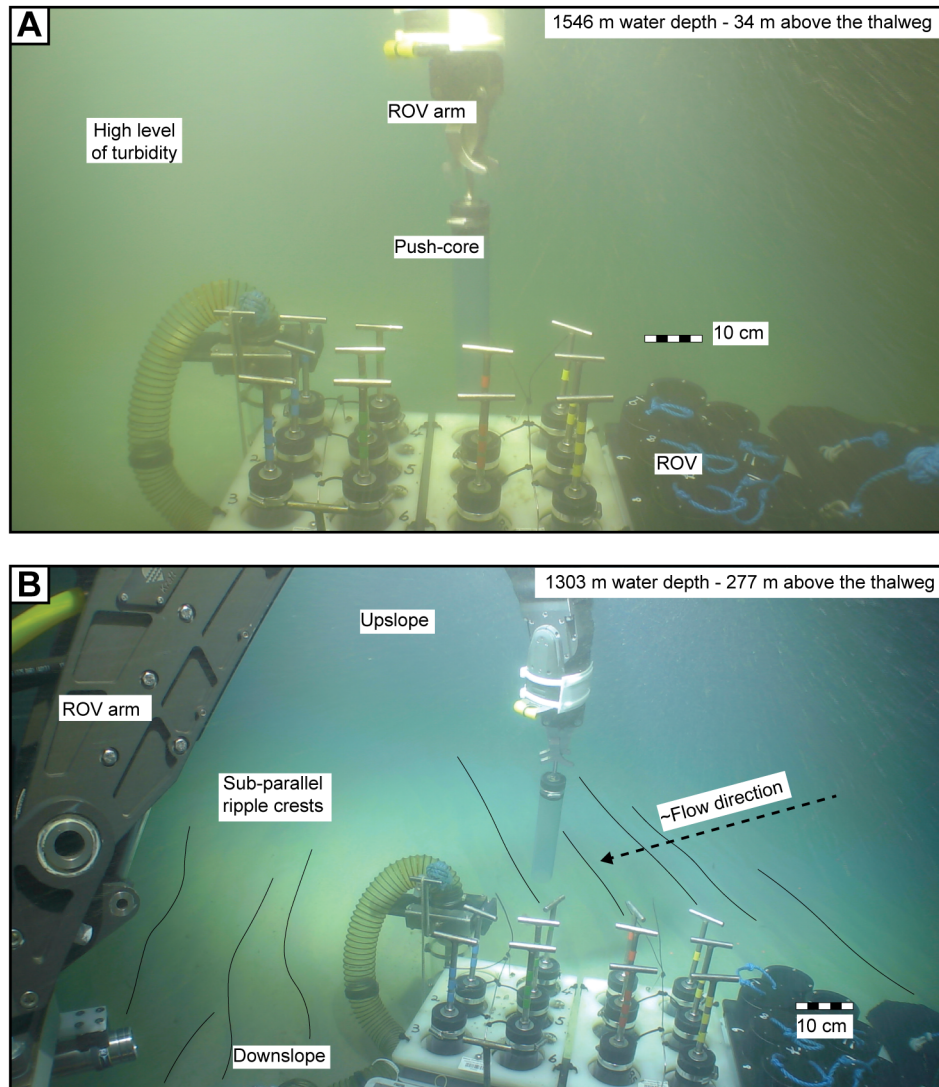
Figure 5.8: Photographs taken of seabed push-core sampling from the Remotely Operated Vehicle. (A) Canyon thalweg at the upper-transect. (B) Canyon flanks at the upper-transect.

5.4.3 Microplastics on the canyon flanks

At the upper transect, push-cores (PC062, PC064, and PC066, located 220, 277, and 321 m.a.t., respectively; Fig. 5.8B) have a grain-size range of 0.25-200 μm (clay-to-fine sand) (Fig. 5.3), and an arithmetic mean sand% of 54.9%, 43.8%, and 39.9%, respectively (Table A2). Microfibre count in these cores is low and uniform, ranging from 0-19/50 g with an arithmetic mean of 7/50 g (Fig. 5.7C). PC069 (518 m.a.t.) is located near the tributary canyons at the upper transect; the grain-size range is also 0.25-200 μm, yet despite its increased height above the thalweg, the arithmetic mean sand% is 47.6% (Fig. 5.3F and Table A2). PC069 contains the greatest range of microplastic

types, and an arithmetic mean microfibre count of 18/50 g (Fig. 5.7C). At the lower transect, push-cores (PC114 and PC116, located 209 and 431 m.a.t., respectively) have the same grain-size range as the canyon flank push-cores at the upper transect, but with an arithmetic mean sand% of 17.2% and 16.5%, respectively (Table A2). In these push-cores the microfibre count decreases with depth by 64.5% and 80.3%, respectively (Fig. 5.7F).

The sediment accumulation rates in BC65 (1105 m water depth, 284 m.a.t.) and BC72 (788 m water depth, 601 m.a.t.) are 0.22 cm yr^{-1} and 0.09 cm yr^{-1}, respectively (Fig. 5.5). Therefore, it could take 45-to-111 years to accumulate 10 cm of sediment on the canyon flanks and means sediment on the canyon flanks may pre-date the mass-production of plastic. On the canyon flanks at the upper transect, 277 m.a.t., and thus above the known thickness of the turbidity currents recorded by Heijnen *et al.* (2022), the crest orientation of sub-parallel ripples observed on the seafloor suggests a flow direction approximately perpendicular to the direction of turbidity current transport (Fig. 5.8B). This suggests that other hydrodynamic processes capable of sediment transport are also active on the canyon flanks (*e.g.,* internal tides).

5.5   Discussion

5.5.1   Microplastic transport and burial processes

Microplastic pollution is pervasive throughout the Eastern Branch down to 10 cm sediment depth. Almost all push-cores show a gradual decline in microplastic concentration with depth, despite the marked differences in sediment accumulation rates and the 700% increase in the background plastic production rate. Microplastics are hypothesised to be transported to the canyon head via cross-continental shelf currents and via vertical settling from marine sources, but their subsequent redistribution and burial cannot solely be explained by turbidity currents.

From the observed grain-size trends in the canyon thalweg (notably the absence of sediment <31 μm in PC060) it is suggested that the frequent (sub-annual) and fast (up to 5 m s^{-1}) turbidity currents serve to bypass and winnow silt-sized sediment and microplastic particles further down-canyon. As the Whittard Canyon widens and the thalweg slope angle decreases throughout the upper-canyon domain and into the lower-canyon, the bypassing turbidity currents are hypothesised to experience a decrease in the degree of flow confinement and become more depositional. Although the true thickness of four of the six recorded turbidity currents could not be determined due to limitations with the ADCP mooring, Heijnen *et al.* (2022) observed the turbidity currents to decrease in thickness down-canyon. However, microplastics were recorded

at elevations up to 518 m.a.t., (at the up-canyon transect) and 431 m.a.t., (at the down-canyon transect), both over an order of magnitude above the recorded thickness of measured turbidity currents. Turbidity currents over 100 m thick have been recorded in other submarine canyons (*e.g.*, Sumner and Paull, 2014), yet there remains an uncertainty in the true maximum thickness of the turbidity currents in Whittard Canyon. This suggests that other processes are important in the Whittard Canyon, and need be considered in other submarine canyons (Fig. 5.9). The presence of sand in the canyon flank push-cores, and increased sand% 518 m.a.t., suggests that sediment is not sourced exclusively from hemipelagic fallout, and points to sediment and microplastics stored on the Celtic Margin being transported via episodic turbidity currents in the tributary canyons and/or by sediment resuspension linked to benthic trawling and cascading into the Whittard Canyon (Figs 5.3F and 5.9). Internal tides break against the steep topography of the canyon flanks in the upper-canyon and are focused into the canyon thalweg (Amaro *et al.*, 2016), thus providing a mechanism for resuspending sediment and microplastics throughout the canyon. The location of BC72 (Figs 5.1D and 5.1E), high on the canyon flank opposite the Celtic Margin and the tributary canyons, could help to explain the low sediment accumulation rates.

The observed uniformity of the gradual decline in microplastic concentration with sediment depth suggests, however, that sub-seafloor processes also control microplastic burial processes in the deep sea. Hyporheic transfer of microplastics has been demonstrated in riverbeds (Frei *et al.*, 2019). In sub-seafloor settings, hyporheic transfer is driven by pressure gradients, as exist between the base of turbidity currents and the seabed (Eggenhuisen and McCaffrey, 2012) and is invoked here as a control on the stratigraphic distribution of microplastics (Fig. 5.9E). Furthermore, sediment resuspension via internal tidal pumping on the canyon flanks may generate a sufficient pressure gradient with the seabed to drive hyporheic transfer of microplastics through sediment pore space, where turbidity currents are not active. Microplastic infiltration depth increases positively with sediment grain-size (Waldschläger and Schüttrumpf, 2020), hence hyporheic transfer may be enhanced in the canyon thalweg compared to the canyon flanks (Fig. 5.9E).

Bioturbation may also play a role in controlling the vertical distribution of microplastics in the sub-seafloor. The uppermost 10 cm of BC64 and BC65 (Figs 5.5A and 5.5B) are bioturbated. Sediment and microplastic mixing by bioturbation have been documented experimentally (Näkki *et al.*, 2017) and is hypothesised to occur in deep-sea sediments (Courtene-Jones *et al.*, 2020). The depth of the bioturbated layer extends to 10 cm in modern marine sediments, with individual burrows extending deeper (Tarhan *et al.*, 2015) and may be enhanced on the canyon flanks, due

to more favourable conditions for organisms to colonise compared to the thalweg (Fig. 5.9E). Bioturbation and hyporheic transfer are likely important in transferring microplastic particles into pre-1950's deep-sea sediments; the latter supported in lakes where bioturbation is absent (Dimante-Deimantovica *et al.,* 2024).

Transport processes

A Cross-continental shelf currents

Microplastic flushed into the canyon

Microplastic stored in the canyon head and on the continental shelf

⅃ Microplastic
Mud
Grain-size
Sand

B Microplastic settling through water column

Surface waters

Hemipelagic fallout

Processes on the seabed rework hemipelagic sediment

Seabed

C Turbidity current active in the thalweg

Microplastic concentration profile | Sediment concentration profile | Turbidity current velocity profile

Flow direction

Low High   Low High   Low High

Seabed

Microplastics transported via turbidity currents

D Internal tides active above thalweg

Up-canyon current   Down-canyon current

Coarser sediment, and microplastics delivered from the continental shelf

turbidite

Seabed

Tidal pumping resuspends sediment

E **Sub-seafloor processes**

Hyporheic transfer   Bioturbation

Sediment surface

Post-1960's

Pre-1960's

Flow over the seabed drives a pressure gradient and transfer microplastic through sediment pore spaces

Burrowing organisms can mix microplastics into deeper sediment

F **Anthropogenic forces**

Fishing activity on the continental margin

Trawling of the seabed can resuspend sediment and be a source of microplastics

Figure 5.9: Synthesis of microplastic transport and burial processes in submarine canyons. (A-D) Transport processes. (E) Sub-seafloor processes. (F) Anthropogenic forces.

5.5.2   The influence of submarine canyon topography on microplastic transfer processes

The hypothesised transition from bypass-dominated to net-depositional turbidity currents is linked to changes in the geomorphology of the Whittard Canyon, as the thalweg angle shallows and the canyon widens, the turbidity currents become less confined. More localised complex topography within the canyon may also play an important role in controlling microplastic transfer within the canyon. Topographic lows in the thalweg may act to capture sediment and microplastics transported by turbidity currents. Additionally, as is observed in both modern (*e.g.*, Pope *et al.*, 2022) and ancient studies of submarine canyons (*e.g.*, Bouwmeester *et al.*, 2024), and in Chapter 4, the complex topography of mass-transport deposits can act to capture sediment, and is hypothesised to trap microplastics too. There is evidence of localised canyon flank failure and submarine landslide debris in the thalweg of the Whittard Canyon (*e.g.*, Carter *et al.,* 2018). This may suggest that: (i) sediment and microplastic deposited and buried on the canyon flanks may be remobilised and transported further down-canyon when mass-wasting events occur, (ii) the evacuated space on the canyon flanks may act to capture subsequent flows, and (iii) sediment and microplastic may become trapped up-dip of topographic obstacles in the canyon thalweg. The down-canyon changes to the canyon geomorphology, possible influence of complex canyon topography, and role of subsurface processes all need to be accounted for considering the role submarine canyons play in the transfer of microplastics to the deep-sea. However, the interplay of these processes complicates calculating microplastic fluxes and determining routeing pathways.

5.5.3   Shredding of microplastic signals in the deep-sea

It is suggested that sediment transport and burial processes, and anthropogenic forcing, act as nonlinear filters that shred the environmental signal of increasing plastic production rates through time in submarine canyons. The efficiency of microplastic transfer from land-based sources to the Whittard Canyon is relatively low, given the land-detached nature of the canyon. This suggests that microplastic pollution in land-detached canyons, of which there are more than 5000 globally (Harris and Whiteway, 2011), is dominantly marine-sourced, and that such systems receive a buffered supply of terrestrially-sourced microplastics. Given the dynamism of hydrodynamic processes in submarine canyons, complex canyon topography, the buffered supply of microplastics to land-detached canyons and the mobility of microplastics in the sub-seafloor,

the efficacy of using microplastics as anthropogenic tracer particles and calculations of microplastic fluxes in land-detached canyons is questionable.

5.6   Conclusions

The results show that microplastic pollution is pervasive in Whittard Canyon, to 10 cm sediment depth in both the thalweg, and on canyon flanks hundreds of metres above the thalweg. While turbidity currents are a major agent in the transfer of microplastics, the turbidity currents in Whittard Canyon are tens of metres thick (Heijnen *et al.,* 2022), suggesting other processes and sources of microplastics are important. Additional sources include hemipelagic settling, and sediments on the continental shelf resuspended by benthic trawling and entering tributary canyons. Transport and resuspension of microplastics by internal tidal pumping likely occurs across the entire canyon water depth. Almost all the push-cores show a gradual decline in microplastic concentrations down to 10 cm, despite the 700% increase in global plastic production since the 1970's. Where low sedimentation accumulation rates are recorded, much of the sediment in box-cores pre-dates plastic production. This suggests mobility of microplastics in the sub-seafloor, with likely processes including bioturbation and hyporheic transfer. The observed distribution of microplastics in Whittard Canyon demonstrates they are not entirely flushed through canyons, but may be permanently or transiently stored, and be mobile within the sediment bed. These results suggest that microplastics incorporated in deep-sea sediments may be a poor record of canyon particulate flux and that identifying the Anthropocene boundary using microplastics in these sediments may not be straightforward.

Chapter 6   Synthesis and future work

This chapter addresses the research questions outlined in Chapter 1 within the context of the results presented in Chapters 3-5. Figure 6.1 addresses the research questions outlined in this thesis and how the synthesis of the results from exhumed systems, physical models and modern systems are used to better understand the role seafloor topography imparts on the delivery of particulate matter and on the depositional patterns of SGFs in deep-water systems. The key implications for process-product models, palaeogeographic reconstructions and the routeing pathways of particulate matter in the deep-sea are discussed, and the future research directions highlighted by this study are also proposed.
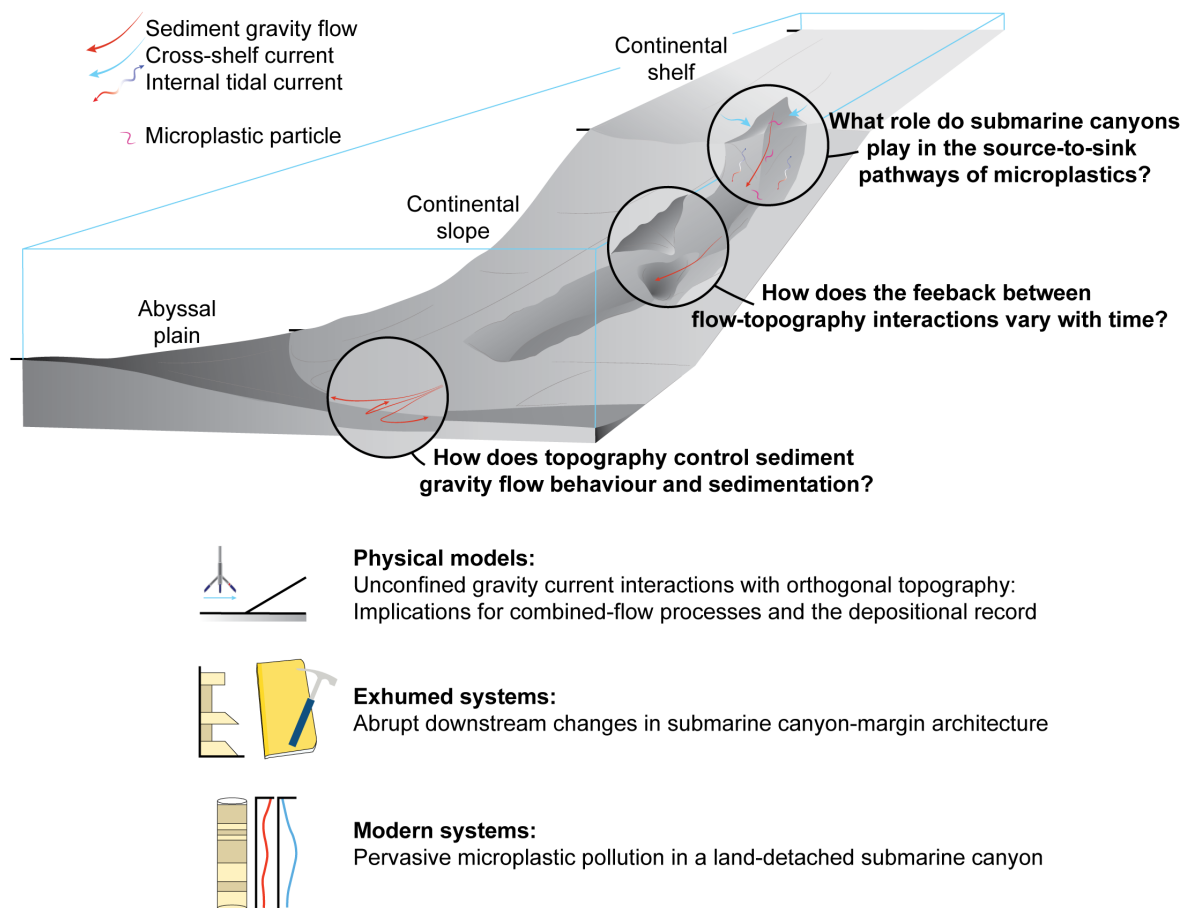
Figure 6.1: Schematic diagram showing the linkages between the research questions and different methods addressed throughout this thesis.

6.1 How does topography control sediment gravity flow behaviour and sedimentation?

Changes to sediment gravity flow behaviour can occur when flows experience a change in the degree of flow confinement (Mutti and Normark, 1987; Mutti and Normark, 1991; Posamentier and Kola, 2003; Stevenson *et al.*, 2015; Hodgson *et al.*, 2022) and when they interact with seafloor topography (van Andel and Komar, 1969; Thornburg *et al.*, 1990; Kneller and McCaffrey, 1999; Kneller and Buckee, 2000; Apps *et al.*, 2004). Chapters 4 and 5 explore how complex topography and changes to flow confinement in submarine canyons affect SGF behaviour and the delivery of particulate matter to the deep-sea. Additionally, previous experimental models have focused on how simple topography influences SGF behaviour using observations from 2D flume tanks (Fig. 2.5) that are exported to a host of deep-water basins. Chapter 3 addresses this by presenting results from physical experimental models designed as an analogue for flow-topography interactions in unconfined settings. The synthesis of how topography influences SGF behaviour in Chapters 3–5 helps to develop new insights into how particulate matter is delivered to the deep-sea and new process-product models of SGF behaviour in unconfined settings.

6.1.1 Complex flows above simple slopes

Chapter 3 presents a new model for combined flow (*i.e.*, highly complex, multidirectional flows) generation in unconfined settings, based on the interaction of subcritical density currents with topography and superimposition of flow components (*see* 'A new model for combined flow generation'). This has implications for the mechanisms of onlap styles and spatial models for deposition on, and at the base of, slopes (Fig. 3.16). Previous models attribute combined flow generation in deep-water systems to the development of an oscillatory flow component resulting from the formation of internal waves following flow-topography interactions being superimposed with the parental, unidirectional flow (*e.g.,* Pantin and Leeder, 1987; Kneller *et al.*, 1991, 1997; Edwards *et al.*, 1994; Kneller, 1995; Kneller and McCaffrey, 1995), and with internal waves being intrinsic to ponded suspensions with a strong stratification (*e.g.,* Patacci *et al.*, 2015) (Fig. 3.1). The previous models are based on observations made in 2D flume tanks where flows are unable to truly expand radially. However, the model has been exported to numerous deep-water basins where combined flow bedforms (*e.g.,* hummock-like structures, large asymmetric ripples, biconvex ripples, and symmetrical megaripples) have been documented (*e.g.,* Privat *et al.*, 2021, 2024; Tinterri *et al.*, 2022; Martínez-Doñate *et al.*, 2023; Siwek *et al.*, 2023; Taylor *et al.*, 2024a). The new model presented in this thesis documents the generation of combined flows formed from the superimposition of the multidirectional reversing flow on the slope surface and

the incoming parental flow, in the absence of internal waves. Chapter 3 shows that the previous model of an oscillatory flow component being generated by flow-topography interactions does not hold in unconfined settings with low density gravity currents.

Upon entering a horizontal basin, the subcritical density currents interacted with a topographic slope positioned orthogonal to the primary flow direction, 3 m downstream of the channel mouth (Fig. 3.2). The slope angle was independently varied at 20°, 30°, and 40°. High resolution Acoustic Doppler velocity profiling, density profiling, and video-captured flow visualisation document that, on a 20° slope, the superelevation of the flow and flow stripping of the upper dilute region of the flow occur high on the slope surface. This causes the flow to spread laterally (diverge) and collapse downslope before interacting with and being superimposed with the parental flow, thus generating combined flows. The processes observed on the 20° slope are likely to be further enhanced on lower angle slopes. The superelevation and extent of flow stripping decreases as the slope angle increases. At 30° and 40°, flow reflection and deflection, respectively, are the dominant flow processes towards the base of slope. The superimposition of the reflected or deflected flow with the parental flow generates combined flows.

How flow-topography interactions affect SGF behaviour and sedimentation in Chapter 3 are summarised in Figure 3.16. With regards to onlap styles, on lower angle slopes (20° and less) draping onlap is enhanced due to the increased run-up height of dilute, thin flows high on the slope surface. Whereas more abrupt pinchouts are expected where flows rapidly decelerate upon incidence with steeper slopes. The type and spatial distribution of combined flow bedforms may also act as an indicator of flow-topography interactions. It is expected that high-up on low angle slopes the decreased velocity of the primary current and generation of highly multidirectional flows may produce isotropic hummock-like bedforms with convex and concave laminae that lack cross-cutting relationships. Whereas, towards the base of slope, where the unidirectional flow component is stronger, cross-cutting relationships are likely to be more frequent, producing anisotropic hummock-like bedforms.

Further synthesis of Chapter 3 suggests that there are other important parameters regarding SGF interactions with topography that affect sedimentation patterns, including: substrate rheology, erosion of topography, and different flow densities. SGFs traversing mud-prone substrates are capable of entraining cohesive mud and decelerate because of turbulence damping (Stevenson et al., 2020; Baas et al., 2021a; Taylor et al., 2024a). Flow deceleration would limit the run-up height of flows upon interaction with topography and may produce distinctive

combined-flow bedforms, such as low-amplitude bed waves, sinusoidal lamination, and hummock-like bedforms lower down on the slope surface (Taylor et al., 2024a). The height and erodibility of topography also affects SGF behaviour. Where SGFs surmount topography, the finer-grained material is bypassed down-dip, whereas the coarser material is trapped up-dip, onlapping the topography (Soutter et al., 2021a). Where topography is susceptible to erosion, it is suggested that a wider sediment grain-size range of the parental flow is transferred down-dip, that the eroded material may be entrained into the flow, and that less material is stored up-dip of the topography. The effects of flow stratification are discussed in Section 3.5.5, and how flows of different densities respond to topography is explored in Section 6.1.2. With increasing flow density and density stratification, the run-up height, degree of density decoupling, and propensity for internal waves to form, are all hypothesised to increase and thus, generate distinctive bedforms and sedimentation patterns.

Using scaled, physical models provides an excellent basis for understanding simple flow-topography interactions and the effects on SGF behaviour and sedimentation. This is particularly important for unconfined settings due to the absence of direct monitoring attempts of SGF interactions with topography. To better understand the effects of flow-topography interactions with more complex, dynamic topography on SGF behaviour, the deposits from ancient SGFs can be studied.

6.1.2   Flow interactions with complex topography

How SGFs interact with complex topography is documented in Chapter 4. The generation of debris flows in a canyon-confined overbank following the mass-wasting of the canyon-margin produced complex debrite topography for subsequent SGFs to interact with. Debrites and other mass transport deposits commonly have rugose surface expressions and steep margins (*e.g.,* Armitage et al., 2009; Martínez-Doñate et al., 2021; Tek et al., 2021; Allen et al., 2022; Pope et al., 2022; McArthur et al., 2024). How SGFs of a similar magnitude interacted with the simpler canyon-margin topography can also be explored in the absence of debrite topography, approximately 250 m down-canyon due to strong 3D outcrop constraints. The effects of SGFs interacting with different topographic styles over short length scales are expressed by the localised heterogeneity in the facies and architecture of SGF deposits.

Where SGFs interact with the canyon-margin, in the absence of debrite topography (Section 4.5.2.1 and Section 4.5.3.1), low-density turbidity currents that have escaped the confinement of the canyon axis and traversed the canyon overbank, have an enhanced upslope

transport due to their dilute nature and can run up the canyon margin surface, draping the surface with thin-bedded heterolithic deposits as a result. Higher density turbidity currents are more ground-hugging and have decreased run-up heights compared to their lower-density counterparts, and so abruptly pinching-out at the margin surface and depositing sand-rich facies. By increasing the density of the gravity flows employed in the physical experiments of Chapter 3, the run-up height of the flows in all slope angle scenarios would be lower, and result in sand-rich deposits towards the base of the slope surface.

In submarine channel-levee systems, there are predictable changes in deposit type and architecture observed down-dip and along-strike (*e.g.,* Babonneau *et al.,* 2002, 2010; Posamentier, 2003; Kane and Hodgson, 2011; Hansen *et al.,* 2015, 2017a). Although somewhat predictable changes are observed from where flows traverse canyon-confined overbanks before interacting with simple topography, submarine canyons are dynamic environments, with complex and evolving erosional and depositional topography. Consequently, complex stratigraphic relationships exist over short spatial ranges, with fine-scale variations previously unresolved in outcrop studies of submarine canyons and beyond the resolution achieved by subsurface studies. Where thin, dilute turbidity currents interacted with the complex debrite topography (Section 4.5.2.3 and Section 4.5.3.3) their dilute nature allowed them to feel and progressively heal the topography, with subsequent flows depositing more tabular thin-bedded heterolithic packages. Conversely, higher-density, sand-rich flows are captured by the topography, decelerated rapidly and deposited massive sands with highly variable thicknesses and lateral extents. In contrast, more tabular, sand-rich deposits with tractional bedforms are observed at the simple topographic configuration of the exposed canyon margin.

Although finer-scale observations of facies and architectural variations can be achieved by outcrop studies and exported to other exhumed canyon fills, complete 3D constraints are not possible; therefore, MTD volumes can only be estimated. Subsurface studies have highlighted the role MTDs in submarine canyons (*e.g.,* Pope *et al.,* 2022) and channels (*e.g.,* McArthur *et al.,* 2024) play in blocking sediment routeing pathways, locking-up sediment and other particulate matter, and limiting transfer further into the deep-sea. The processes, coupled with the repeated failure and localised heterogeneity observed in Chapter 4, suggests that the emplacement and excavation of MTDs in submarine canyons plays an important role in the transient and localised storage of sediment and particulate matter to the deep-sea, and may be poorly accounted for in flux calculations.

6.1.3   Changes to the degree of flow confinement

Chapter 5 documents how the interaction between turbidity currents and internal tides, and sub-subsurface processes control the distribution of microplastic throughout the Whittard Canyon and with increasing sediment depth. The changes to submarine canyon geomorphology influence the behaviour of SGFs and the delivery of sediment and microplastics further into the deep-sea. Down-canyon changes in the degree of flow confinement are linked to the widening of the canyon and the shallowing of the thalweg gradient. The decrease in the degree of flow confinement sees SGFs transition from bypass-dominated in the upper-canyon reach to deposition-dominated further down-canyon. The effects changes in flow behaviour have on the transfer of microplastic to the deep-sea are further explored in Section 6.3. However, changes to the degree of flow confinement are not exclusive to down-canyon trends in canyon confinement, and include: channelised confinement (*e.g.,* Piper and Normark, 1983; Peakall *et al.,* 2000; Deptuck *et al.,* 2003, 2007; Kane *et al.,* 2009; Hodgson *et al.,* 2011; Kane and Hodgson, 2011; Janocko *et al.,* 2013), external levee confinement (*e.g.,* Hansen *et al.,* 2015, 2017a), and at channel mouth expansion zones (CMEZs) and channel lobe transition zones (CLTZs) (*e.g.,* Mutti and Normark, 1987; Wynn *et al.,* 2002b; Fildani and Normark, 2004; Dennielou *et al.,* 2017; Hodgson *et al.,* 2022), with each producing distinct sedimentation patterns and an important role in the transfer of particulate matter to the deep-sea.

Both channelised and external levee confinement act as filters to overspill and flow stripping of SGFs that partially escape the conduit and the master confining surface, respectively. Finer-grained sediment and low-density particulate matter, including microplastics, are primarily transported in the upper, dilute region of SGFs relative to denser sediment grains and are therefore more able to escape confinement. However, particles with lower settling velocities have also been shown to have a more even distribution throughout the flow (*e.g.,* García, 1994; Amy *et al.,* 2005; Pohl *et al.,* 2020). This produces predictable changes, laterally from the conduit to beyond external levee confinement, down-dip, and with increasing stratigraphic height (Kane and Hodgson, 2011 and references therein). The changes in SGF behaviour and sedimentation are more predictable in more distal settings (*e.g.,* channel-levee systems) where there is a more restricted range of SGF magnitudes and increased space for overspill, compared to submarine canyons that host a wider range of SGF magnitudes, therefore complicating sedimentation patterns and the transfer of particulate matter. Profound changes to SGF behaviour also occur where flows experience a sudden loss in flow confinement at CLTZs and CMEZs, producing a range of erosional (*e.g.,* scours) and depositional (*e.g.,* sediment waves) features (Hodgson *et al.,*

2022 and references therein). Changes to the criticality of SGFs, and their erosive and depositional capabilities, have potential implications for the delivery of sediment and microplastics further into the deep-sea (Kane and Clare, 2019). Chapter 3 and the comparison to previous experimental models further shows how the degree of basin-scale confinement affects gravity flow behaviour and how models developed in confined systems do not always hold in more unconfined systems. Therefore, careful consideration is needed when applying process-product for sedimentation patterns to different deep-water systems and throughout the different geomorphic elements of such systems.

How the degree of flow confinement, both within deep-water systems and at the basin-scale (*i.e.,* whether a flow is confined or unconfined), and how SGFs respond to interactions with topography, profoundly influences SGF behaviour and sedimentation. This thesis documents how integrating methods and datasets allows new process-product models to be developed to better understand SGF processes and sediment and microplastic transport in deep-water settings.

6.2 How does the feedback between flow-topography interactions vary with time?

A better understanding of the temporal evolution of flow-topography interactions in submarine canyons and throughout deep-water systems, alongside exporting the observations from well-constrained deep-water systems and experimental models to lesser-constrained systems, are key to developing palaeogeographic reconstructions.

6.2.1 Evolution of onlap patterns

The mass-wasting of submarine canyon margins affects flow processes in canyon-confined overbanks (Chapter 4) and in the thalweg (*e.g.,* Pope *et al.,* 2022). Chapter 4 documents, comparatively, how SGFs interact with both debrite topography and the preserved canyon-margin itself, and how the flow processes vary over short spatial ranges, and through time. When SGFs interacted with the simple topography of the canyon-margin, in the absence of debrite relief, the record of flow-topography interactions through time is recorded by the onlap relationships of SGFs (Section 4.5.2.1 and Section 4.5.3.1). Thin-bedded turbidites, the result of deposition from thin, dilute, low-density turbidity currents, act to drape the canyon-margin onlap surface. The ability of low-density turbidity currents to ride high-up the canyon-margin surface, and the initial episode of deposition, generates an intra-formational onlap surface. The modification of the canyon-margin gradient and decreased superelevation of high-density turbidity currents limits

the run-up potential of the subsequent turbidity currents and the sand-rich deposits pinchout abruptly against the newly-generated intra-formational onlap surface. When debrite relief is preserved in the canyon overbank, up-dip of the failed canyon-margin, thin-bedded heterolithics again act to drape the relief and heal the topography enough so tabular sand-rich beds form from subsequent high-density turbidity current deposition (Section 4.5.2.3 and Section 4.5.3.3). When thin-bedded heterolithics do not act to drape the debrite relief, high-density turbidity currents are captured and rapidly decelerate, generating marked spatial variability in deposit type and geometry.

6.2.2 Autocyclic flow signals through time

Thin-bedded heterolithic packages, deposited from low density turbidity currents, are volumetrically significant packages in organised channel-levee successions (Kane and Hodgson, 2011; Hansen *et al.*, 2015, 2017a) and in submarine lobes (Groenenberg *et al.*, 2010; Kane *et al.*, 2017; Spychala *et al.*, 2017a; Hansen *et al.*, 2019), and have been observed to drape and heal basin margins (*e.g.,* Soutter *et al.*, 2019) and localised MTD relief (*e.g.,* Martínez-Doñate *et al.*, 2021). Submarine canyons host complex topography, both at their margins and within the overbank and thalweg, and receive a wider range of SGF sizes and magnitudes compared to channel-levee systems. The complex spatio-temporal trends in SGF behaviour and sedimentation observed over short spatial ranges and documented in Chapter 4 are linked to flow-topography interactions and autocyclic signal changes, that have not previously been documented in canyon-fill models. The geometry of the canyon-confined overbank deposits observed in Chapter 4 and their interaction with the canyon-margin suggests that they are more akin to the terrace deposits described by Hansen *et al.* (2015, 2017a) as opposed to the internal levee deposits they have previously been interpreted as by Dykstra and Kneller (2007) and Kane *et al.* (2009). The generation of terrace deposits is hypothesised to be enhanced during the early, aggradational phase of submarine canyon evolution, when canyons are typically more confined. As canyons evolve and progressively widen, the stacking patterns become more organised (*e.g.,* Taylor *et al.*, 2024b), and with increased accommodation generated in overbank environments, internal levee formation is promoted. Furthermore, allogenic signal changes resulting in a decrease in sediment supply would have a similar effect, as this would result in smaller magnitude flows entering the overbank, decelerating and thinning to form internal levee deposits. Similar patterns in flow-topography interactions and role of autogenic signal changes through time have also been recorded between submarine lobe deposits and the basin margins of the Annot Basin, SE France (Soutter *et al.*, 2019).

Although the physical models of Chapter 3 employ single, sustained saline density currents with uniform input parameters, further synthesis permits the feedback between flow-topography interactions and the response to successive SGFs to be explored. How SGFs interact with simple topography in unconfined settings, the further considerations discussed in Section 6.1.1, and the response the successive SGFs exhibit are synthesised in Figure 6.2. By assuming two successive SGFs with the same input parameters (*i.e.,* no allogenic signal change) and a simple topographic configuration, similar to that outlined in Chapter 3, the patterns of deposition, high-up on low angle slopes with distinctive combined flow bedforms (*e.g.,* isotropic hummock-like bedforms), and lower down on high angle slopes with a stronger component of flow reflection/deflection and deposition of anisotropic hummock-like bedforms, may be expected from an initial low-density SGF. A successive low-density SGFs interacting with lower angle slopes may not be strongly influenced by the depositional relief of the first flow because of the high degree of flow thinning and divergence occurring over a wide area of the slope. This could provide a possible explanation for the generation of thick, intraformational onlap surfaces composed of thin-bedded heterolithics. However, at the base of steeper slopes, the decreased run-up height and increased deceleration of the initial flow, and/or where the initial flow was sand-rich and higher-density, may lead to the deposition of thick sands at the base of slope. A subsequent SGF is hypothesised to be influenced by the depositional relief generated by the first flow and may cause the deposits of successive flows to bifurcate and back-step. The back-stepping could therefore be interpreted as an allogenic signal change of either decreasing sediment supply (*e.g.,* Ferguson *et al.,* 2020) or a sea-level increase, despite the absence of such mechanisms. How flows respond to erodible topography and deposit finer-grained material further down-dip, and how they respond to complex topography are also explored in Figure 6.2.

6.2.3   Potential for transient and permanent storage of particulate matter

The preservation of complex debrite topography in the canyon-confined overbank of the Rosario Formation suggests that the Playa Esqueleto Canyon was undergoing an aggradational phase of the canyon's evolution. This also suggests that sediment and organic carbon (and microplastics in modern canyon-fills) can be permanently stored in submarine canyon overbanks, despite canyon axes typically being dominated by erosional processes, with high rates of sediment bypass. However, it further suggests that where debrites and other MTDs are not preserved over short spatial ranges, that the debritic material and deposits from subsequent SGFs may have been remobililsed and transported further down-canyon, and that the excavated space is then filled by

subsequent SGF deposits. The dynamism of canyon-margins produces complex stratigraphic relationships and provides sites for both transient and permanent storage of particulate matter.

Like the role complex topography can play in locally locking-up particulate matter; in the thalweg of the Whittard Canyon, where there are protracted sediment accumulation rates and microplastic concentrations, it is hypothesised that localised depocentres formed in topographic lows. The topographic lows can capture particulate matter from net-depositional SGFs. Where SGFs are bypass-dominated in submarine canyons, the storage of particulate matter is hypothesised to occur predominantly on flat-lying terraces located above the thalweg. Repeat surveying in the Congo Canyon following the 2019 landslide-damming event documented by Pope *et al.* (2020), and further development of canyon-fill models and indicators of sediment bypass processes in submarine canyon thalwegs (*e.g.,* Bouwmeester *et al.*, 2024), may elucidate the roles episodic SGFs and canyon-flushing events play in excavating MTDs in submarine canyons. Further understanding how the timescales vary between canyon axes and canyon-margins can help to better constrain the role of submarine canyons play in the source-to-sink pathways of particulate matter. New insights from repeat surveying in the Congo Canyon show how approximately 2.65 km^3 of sediment was eroded from the Congo canyon-channel in 2020 by canyon-flushing turbidity currents (equivalent to 19-35% of the global sediment flux from all rivers), but that seabed erosion was 'patchy' (Ruffell *et al.*, 2024). The patterns of erosion were linked to erosion from knickpoints, thalweg erosion without knickpoints, outer-bend erosion and margin collapses. Terrace deposits in the upper-canyon of more than 5 m thickness accumulated from 2019-2020, and are hypothesised to be thin-bedded turbidites (*see* Babonneau *et al.*, 2002, 2010). The terrace deposits were not cored as part of the Ruffell *et al.* (2024) study, but future coring may help to answer outstanding questions regarding how bypassing turbidity currents in canyon thalwegs are preserved in canyon overbanks, the number of events/timescales linked to accumulating 5 m-thick deposits of thin-bedded turbidites, and the role overbanks play in the storage of particulate matter in the deep sea.

A

T1

finer sediment is bypassed down-dip of the erodible topography

finer-grained material drapes high-up the onlap material

finer sediment heals topography

basin floor

decreased run-up height

low-density SGF

high-density SGF

coarser sediment captured by topography

coarser sediment pinches-out against topography

Planar topography

Complex topography

Erodible topography

T2

apparent back-stepping of deposits from flows influenced by the depositional relief of T1

limited bifuraction of T2 deposits due to deposition from T1 across a wider area of the onlap surface

following the healing of complex topography, flows of T2 are less influenced by the relief

depositional relief of T1 causes bifurcation of the subsequent flow/deposits

B

a'

isotropic hummock-like bedforms high on the slope surface

b'

limited deposition high on the slope surface

c'

low-density component of SGFs heals the complex topography

finer-grained material bypassed down-dip of erodible topography

d'

a

anisotropic hummock-like bedforms at base of slope

b

massive sand deposited at base of slope

c

massive sand deposited where SGF captured by complex topography

d

sand component of flow pinches-out against the onlap surface

Figure 6.2: Schematic diagram showing (A) the hypothetical deposit geometry of sediment gravity flows interacting with planar topography, complex topography, and erodible topography of an initial flow (T1) and a subsequent flow of the same magnitude (T2); and (B) the onlap styles from each topographic configuration and schematic sedimentary logs with the diagnostic facies.

6.3   What role do submarine canyons play in the source-to-sink pathways of microplastics?

Microplastic pollution is pervasive across the Whittard Canyon, down to a sediment depth of 10 cm. Microplastic pollution has been documented in other submarine canyons (Woodall *et al.,* 2014; Jones *et al.,* 2022; Zhang *et al.,* 2022), and other deep-sea environments (Van Cauwenberghe *et al.,* 2013; Woodall *et al.,* 2014; Barrett *et al.,* 2020; Kane *et al.,* 2020). With the exception of Kane *et al.* (2020), these studies generally lack the sedimentological context to tie how transport and burial processes affect microplastic distribution and concentration. Submarine canyons play a crucial role in the source-to-sink pathways of particulate matter (Nyberg *et al.,* 2018), primarily as conduits transporting material further into the deep-sea via SGFs (Talling *et al.,* 2023 and references therein). However, the pervasiveness of microplastic pollution across two distinct physiographic domains of the Whittard Canyon and uniformity of the microplastic concentration with increasing sediment depth, despite the historical plastic production rate increasing 700% since the 1970's (PlasticsEurope, 2023), suggests that sedimentological processes and anthropogenic forcing are affecting microplastic distribution and concentration in submarine canyons. Further understanding the interplay between these processes can help to vastly improve the understanding of the routeing pathways of microplastics in the deep-sea (Rohais *et al.,* 2024), as crucially, it is considered as the ultimate sink to global microplastic pollution (Woodall *et al.,* 2014).

Chapter 5 integrates modern seafloor sediment cores from two distinct physiographic domains of the Whittard Canyon, high-resolution seafloor bathymetry, sediment accumulation rates derived from ^{210}Pb dating of modern seafloor sediment cores, fishing activity data, and previously published data from the direct monitoring of turbidity current (*e.g.,* Heijnen *et al.,* 2022) and internal tide (Hall *et al.,* 2017) activity. The integrated sedimentological data helps to better constrain how processes in submarine canyons act to transfer microplastics to the deep-sea. Microplastics are observed in the thalweg, where turbidity currents have been recorded (Heijnen *et al.,* 2022), and even high on the canyon flanks, over an order of magnitude higher than the known thickness of the turbidity currents. This suggests that the microplastic transport and

burial processes in submarine canyons are dynamic, contributing 'noise' and not preserving the signal of historical plastic production trends. The degree to which sedimentological processes control the delivery and burial of microplastics brings into question the roles of transient and permanent storage and transport of microplastics, and other particulate matter in submarine canyons. SGFs are efficient conveyors of sediment in submarine canyons and hypothesised to be a major agent in microplastic transport in the deep-sea (Kane and Clare, 2019; Pohl *et al.*, 2020; Zhang *et al.*, 2024). Furthermore, Chapter 3 shows how interactions with seafloor topography in unconfined settings acts to change the depositional character of SGFs and the loci of deposition, and Chapter 4 shows how the character of SGF deposits in submarine canyons is highly variable over short spatio-temporal scales. When considering the observations from the Whittard Canyon and the further synthesis of Chapter 3 and Chapter 4 and processes observed in other submarine canyons, a more complete understanding of SGF behaviour and how it affects the routeing pathways and burial of microplastics throughout deep-water systems can be made.

Turbidity current activity in the land-detached Whittard Canyon is analogous in terms of frequency and magnitude to land-attached submarine canyons *e.g.,* Monterey Canyon and Congo Canyon (Heijnen *et al.*, 2022). Not only does this challenge the paradigm that land-detached canyons are dormant during high-stand conditions (Heijnen *et al.*, 2022), the pervasive microplastic pollution observed throughout the Whittard Canyon in Chapter 5 challenges the model that microplastic transfer is inefficient in such canyons (Kane and Clare, 2019). Over three quarters of mapped global submarine canyons, of which there are more than 9000, are land-detached (Harris and Whiteway, 2011). This suggests that land-detached canyons have the potential to play a major role in the transfer of particulate matter in the deep-sea.

6.3.1 Microplastic transport processes

Turbidity currents recorded by Acoustic Doppler current profiler (ADCP) in the upper-canyon reach of the Eastern Branch of Whittard Canyon at 1591 m water depth are in excess of 30 m thick (Heijnen *et al.*, 2022). In PC060, located 34 m above the thalweg (m.a.t.) at the upper-canyon transect (1546 m water depth) (Fig. 5.6C), microfibres were observed down to 5 cm sediment depth (limited by the core recovery rate), increasing from 4 microfibres/50 g dry sediment in the uppermost 1 cm to 30 microfibres/50 g at 5 cm depth, a 650% increase. In PC060 the grain-size ranges from coarse silt to pebble-sized fragmented shells (31-8000 μm) (Fig. 5.3A). Notably the sediment accumulation rate calculated by ^{210}Pb dating of the sediments from BC64 located at 1389 m (0 m.a.t.) is 0.04 cm yr^{-1} (Fig. 5.3B), thus suggesting it could take up to 250 years to accumulate 10 cm of sediment at this location within the upper-canyon reach, therefore pre-

dating the mass-production of plastic in the 1950's. The absence of sediment finer than 31 μm and the protracted sediment accumulation rates suggest that the turbidity currents in the upper-canyon reach of Whittard Canyon are net-erosional, bypassing and winnowing finer grained sediment and microplastics further down canyon. This is further supported by an increased microfibre concentration and a grain-size range of 2-200 μm recorded in PC113 in the thalweg of the lower-canyon transect (0 m.a.t., 3204 m water depth) (Fig. 5.6F). Furthermore, the sediment accumulation rate from BC73 (2011 m water depth) is calculated as 1.19 cm yr^{-1} (Fig. 5.3B), thus suggesting that as turbidity currents become less confined with increasing distance down canyon, as the canyon widens and the thalweg slope angle decreases, that they become net-depositional, depositing finer-grained sediment and microplastics. The Whittard Canyon feeds the Whittard Channel at approximately 3800 m water depth (Amaro *et al.*, 2016). Through-going turbidity currents that have traversed the length of the Whittard Canyon are hypothesised to be slow-moving and dilute (*i.e.,* low density turbidity currents) at such water depths, with their velocity and direction dictated by changes to the degree of flow confinement and interactions with seafloor topography. In such flows, microplastics are hypothesised to be dominantly transported in the upper parts of the flows (Kane and Clare, 2019), similarly to how organic carbon is transported in turbidity currents (*e.g.,* Hage *et al.*, 2022, 2024), and thus provides a mechanism for microplastics to be transported further into the deep sea, including into channel-levee and lobe systems. When deposited in fine-grained bed tops, microplastics may become bioavailable to benthic and burrowing organisms (Wright *et al.*, 2013), or can become remobilised by subsequent turbidity currents that transform into dense, cohesive flows following the entrainment of fine-grained, cohesive material, transporting microplastics to the distal parts of lobes, as is observed with lightweight, organic material (*e.g.,* Hodgson, 2009; Kane and Pontén, 2012; Kane *et al.*, 2017). Microplastics are hypothesised to be subject to the same sedimentary processes as other types of particulate matter (Horton and Dixon, 2017; Kane and Clare, 2019; Waldschläger *et al.*, 2022) with the routeing pathways and loci of deposition governed by changes to seafloor morphology and topography (Chapter 3 and Section 6.1). Assessing how processes in the subsurface control the burial rates of microplastic, is also crucial for a better understanding of the source-to-sink pathways of microplastics and possible effects on vulnerable, deep-sea organisms.

6.3.2 Subsurface processes

The highly variable sediment accumulation rates recorded throughout the Whittard Canyon, ranging from 0.04 cm yr^{-1} to 1.19 cm yr^{-1} in the canyon thalweg, and 0.09 cm yr^{-1} to 0.22 cm yr^{-1}

on the canyon flanks (Fig. 5.3B), and the down-canyon and across-canyon grain-size trends (Fig. 5.3A) suggest that the Whittard Canyon is a highly dynamic environment despite being land-detached. This dynamism is hypothesised to be due to the interplay between turbidity current and internal tide activity. Additional anthropogenic processes on the continental shelf, such as benthic trawling, are hypothesised to capable of resuspending sediment (Daly *et al.*, 2018) and providing lateral inputs of sediment directly into the canyon via the tributary canyons, and not necessarily from sediment stored at the canyon head. Crucially, it also suggests that processes in the shallow subsurface play a vital role in burying microplastics to deeper depths, into sediments that pre-dates the mass-production of plastic. Bioturbation observed in deep-sea sediments is hypothesized to play an important role in burying microplastics to increased sediment depths (Courtene-Jones *et al.*, 2020). In modern, marine sediments the mixed zone (*i.e.,* the homogeneous zone generated by the activity of bioturbating organisms) extends to sediment depths of approximately 10 cm (Tarhan *et al.*, 2015). In the canyon axis, a high-energy environment, colonisation by benthic organisms is hypothesised to be low, and SGF events may be preserved in the strata. However, high on the canyon flanks, the more favourable conditions for colonisation may enhance the action of bioturbation and is a possible mechanism for the approximately uniform microplastic concentrations recorded hundreds of metres above the thalweg (Fig. 5.6C and F). Another possible driver of microplastics further into the subsurface is hyporheic transfer, as has been observed in fluvial systems (*e.g.,* Frei *et al.*, 2019). On the canyon flanks, this is hypothesised to be the result of the action of internal tidal pumping and in the canyon axis by the passage of SGFs. Both processes have the potential to generate a pressure gradient between the sediment surface and the shallow subsurface, driving fluid and microplastic movement through interstitial sediment pore spaces to increased sediment depth. Similarly to how there are large uncertainties in calculating organic carbon mass-balances from burial rates in the deep-sea (*e.g.,* Masson *et al.*, 2010; LaRowe *et al.*, 2020), taking into account how processes in the shallow subsurface act to bury microplastics, and affect the rates of degradation and preservation is key to understanding the source-to-sink pathways of microplastic and need to be carefully considered when calculating microplastic fluxes in the deep-sea.

6.3.3 Microplastic supply and storage considerations

Chapter 5 documents how, even in a land-detached submarine canyon, submarine canyons play a vital role in the transfer of microplastics in the deep-sea, with the caveat that submarine canyons are highly dynamic environments. The interplay between sedimentary processes and anthropogenic forcing is complex and affects the rate of microplastic delivery and storage at

various temporal scales. It also highlights that there are other elements of submarine canyon geomorphology and other transport and burial processes, not observed in the Whittard Canyon that have the potential to strongly control the source-to-sink pathways of microplastics in the deep-sea. Understanding the tectonic setting and sediment provenance is key when assessing the source-to-sink pathways of sediment. There is a need to account for how lateral inputs/outputs related to atmospheric transport processes and transient storage, for example, may affect the sediment supply signal in classic source-to-sink models (Romans *et al.*, 2016), and complicates calculations of sediment fluxes throughout sedimentary systems and further into the deep-sea. The fluvial connection and the proximity to microplastic sources is crucial in determining microplastic transfer in the deep-sea. The absence of a direct fluvial input to the Whittard Canyon would suggest that microplastic transfer is inefficient (Kane and Clare, 2019). However, the pervasiveness of microplastic pollution observed in Chapter 5 would suggest marine-sourced microplastics are a major lateral input into the source-to-sink pathways of microplastics, especially in land-detached canyons, but may also suggest that the World's land-detached submarine canyons are receiving a buffered supply of microplastics and other pollutants.

Another processes to consider is mass-wasting in submarine canyons. Mass-wasting of canyon-flanks/walls is common, documented in Chapter 4 and observed in modern studies of submarine canyons (*e.g.*, Pope *et al.*, 2022). Not only do canyon-margin failures emplace material into the canyon overbank, generating new space and topography for SGFs to be captured by (Chapter 4), they also have the capacity to block, or partially block, the canyon thalweg, trapping sediment and organic carbon up-dip of the landslide dam (Pope *et al.*, 2022). Mass-wasting events documented further into deep-water sedimentary systems, in channel-levee systems (*e.g.*, McArthur *et al.*, 2024) have the potential to modulate sediment, organic carbon, and microplastic fluxes in the deep-sea. The frequency of landslide-damming events and the rate at which they are remobilised by subsequent, episodic SGFs and canyon-flushing events are factors that need to be considered when assessing the timescales of microplastic transfer in the deep-sea.

The pervasiveness of microplastic pollution observed throughout Whittard Canyon, down to 10 cm sediment depth, coupled with the down- and across-canyon trends in concentration and distribution suggest that hydrodynamic processes, anthropogenic forcing, subsurface processes, and canyon geomorphology control the transfer of microplastic in the deep-sea (Fig. 5.7). The above factors add 'noise' to the signal when determining the source-to-sink pathways. There is a complex matrix of factors specific to submarine canyons, that includes: microplastic sources, canyon and deep-seafloor processes, and burial rates (Fig. 6.3), that needs to be carefully

considered and untangled to develop accurate routeing pathways and flux calculations for microplastics in the deep-sea.

A
- Sediment gravity flow (SGF)
- Fluvial input
- Cross-shelf current
- Internal tidal current
- Bottom current

- Microplastic particle (MP)

No fluvial connection
In-direct fluvial connection
Direct fluvial connection

Terrestrial sources of microplastics

Source

Marine microplastic sources

Lateral input from tributary canyons

Sediment stored at canyon head

Cross-shelf transport

MTDs block incoming SGFs and store particulate matter up-dip

SGFs transport MP

Submarine canyon transfer zone

Reworking by internal tides

Failure of canyon walls and emplacement of MTDs

Subsurface processes control MP burial

Deep-sea sink

Topographic steering of SGFs

Canyon-flushing events and episodic SGFs excavate MTDs

Bottom current reworking

MP are bioavailable to deep-sea organisms

B

No fluvial connnection | In-direct fluvial connection | Direct fluvial connection

Source Q_{MP} — Buffered microplastic input

Submarine canyon transfer zone Q_{MP}

The interplay between sedimentological and anthropogenic processes adds 'noise' to the signal in submarine canyons and is transferred into the deep-sea

Deep-sea sink Q_{MP}

Time

Figure 6.3: Source-to-sink model for microplastic particles in the deep-sea. (A) Schematic matrix used to assess how the characteristics of the source, submarine canyon transfer zone, and deep-sea sink affect the source-to-sink pathways of microplastics. The processes do not necessarily occur in isolation and can be present across the different submarine canyon configurations; and (B) rates of microplastic signal propagation and attenuation in different submarine canyons. Q_{MP} is microplastic supply.

6.4 Future research directions

Addressing the research questions carried through this thesis have highlighted the requirements for further work to develop a deeper understanding of the topics discussed here and how the concepts can be applied to different deep-marine systems.

6.4.1 Using the new model for combined flow generation to re-evaluate other deep-marine systems

The new model, presented in Chapter 3, for the generation of combined flows in unconfined settings and formed in the absence of internal waves, provides an opportunity to re-evaluate documented examples of combined flow bedforms in deep-water settings that are attributed to the process-models developed in two-dimensional experimental settings.

Where combined flow bedforms have been documented in structurally-complex, confined and ponded deep-water settings (Tinterri, 2011; Tinterri *et al.*, 2016, 2022; Siwek *et al.*, 2023), the previous, two-dimensional experimental models of internal wave generation following flow reflection (Edwards *et al.*, 1994) and ponding (Patacci *et al.*, 2015) have been used as the process-models to support the generation of combined flows (Tinterri, 2011; Tinterri *et al.*, 2016). These models may hold in confined settings, yet the new model in Chapter 3 is used to model flows in less confined settings, where flows are able to radially expand.

However, the models of Tinterri (2011) and Tinterri *et al.* (2016) have also been used to explain the generation of combined flows in less confined settings, for example the intra-slope lobes in the Neuquén Basin, Argentina (Privat *et al.*, 2021, 2024; Martínez-Doñate *et al.*, 2023) and where SGFs have escaped channelised confinement in the Karoo Basin, South Africa (Taylor *et al.*, 2024a). The new model presented in Chapter 3 documents the generation of combined flows following the interaction of unconfined flows with the simplest of topographic configurations. The spatial distribution and type of combined flow bedforms and onlap styles vary as a function of slope angle and can be used in future studies of deep-water settings to

account for the effects of flow-topography interactions on SGF behaviour. Where more complex topography exists and the incidence angle is oblique to the direction of the parental flow, the superimposition of diverging, reflecting, and deflecting flow components with the parental flow is hypothesised to increase, further promoting combined flow generation. The effects of this should be a focus of future experimental studies.

6.4.2   Utilising different incidence angles and particulate flows in future experiments

The physical models described in Chapter 3 were the first experiments to be conducted using a new flume tank at the University of Leeds. Consequently, the maiden experiments used the simplest topographic configuration to test flow-topography interactions in three-dimensional, unconfined settings. Previous models developed in two-dimensional and small, three-dimensional flume tanks have documented how topography oriented parallel (*e.g.,* Kneller, 1995; Amy *et al.*, 2004) and oblique (*e.g.,* Kneller *et al.*, 1991) to the incoming flow influences density current behaviour. In three-dimensional settings, using the same flume tank and input flow parameters described in Chapter 3, the effects of parallel and oblique topography on the spatial variability of combined flow generation have also been explored (Wang *et al.*, 2024). In Section 3.5.5, the effect of flow stratification on flow-topography interactions are discussed. However, how flows with a stronger stratification, increased density, and increased (or decreased) velocity and flow height, influence flow behaviour is difficult to assess *a priori*. Future work should focus on parameterising such flows and numerically model their response upon interactions with orthogonal, oblique, and parallel topography. Numerical models can help to inform machine learning techniques, and allow a wide range of flow parameters, and topographic and basin configurations to be explored.

To test the process-product models of combined flow bedform generation and the deposit geometry in relation to topographic slopes, scaled physical models of particulate gravity currents should be the focus of future experiments. Again, starting with the simplest topographic configuration (*e.g.,* Soutter *et al.*, 2021a), and later introducing more complex slopes (*e.g.,* stepped slope geometries, positive and negative relief, and erodible topography), and different flow parameters (*e.g.,* increased/decreased flow density, increased/decreased flow velocity, the sand/mud % of the flow, and the inclusion of organic matter and microplastic particles). Given the paucity of direct measurements of SGFs interacting with seafloor topography in unconfined settings, physical models act as an excellent analogue for investigating SGF behaviour and

sedimentation, determining the routeing pathways and transfer of sediment, organic matter, and micropollutants to the deep-sea.

6.4.3 Exporting stratigraphic models of canyon-confined overbanks to less constrained settings

The model of localised heterogeneity in the deposits of SGFs and resulting architecture at submarine canyon-margins, builds upon models of organised stacking patterns of finer-grained material from overspilling SGFs in canyon-confined overbanks (*e.g.,* McArthur and McCaffrey, 2019; Taylor *et al.,* 2024b) and documented examples of canyon-margin failures in modern canyons (*e.g.,* Paull *et al.,* 2013; Mountjoy *et al.,* 2018; Pope *et al.,* 2021). The three-dimensional exposure of the Rosario Formation documented in Chapter 4 permits the models of flow-topography interactions with the exposed canyon-margin surface and debrites emplaced in the canyon overbank, through time to be exported to lesser constrained settings.

Outcrop studies of submarine canyons often focus on the deposits of the canyon axis due to the increased preservation potential of coarser-grained material, however axes are typically bypass-dominated and have unorganised stratigraphic fills (May and Warme, 2007; Di Celma, 2011; Janocko and Basilico, 2021; Bouwmeester *et al.,* 2024). Where exposed, the preservation of finer-grained material in canyon-confined overbanks in Chapter 4 provides an insight into the mass-wasting mechanisms of canyon-margins, how the preservation of intra-canyon debrites can be used to interpret the stage of canyon evolution, and how depositional terraces are more likely to form in canyon-confined overbanks due to the limited space available for overspilling SGFs to form internal levees (*sensu* Hansen *et al.,* 2015).

Outcrop-scale sedimentological data are above the resolution achieved in subsurface seismic reflection studies. Furthermore, there are challenges associated with obtaining precisely georeferenced sediment and rock cores from modern and subsurface studies, respectively, and with the repeat surveying of modern submarine canyons. This often leads to compromises in the degree of lithological control on the deposits and the ability to trace seismic reflections, and hence onlap styles. A better understanding of deposit type and architecture in submarine canyon overbanks can help support interpretations of overbank canyon-fill successions when applied to future fieldwork campaigns and for revisiting outcrops of submarine canyon successions. Such models can aid in developing more accurate calculations of the flux of particulate matter in the deep-sea.

6.4.4 The study of microplastics in different submarine canyons and further considerations for sampling protocols

As first suggested in Kane and Clare (2019), microplastic delivery to the Whittard Canyon is hypothesised to be low, given its land-detached configuration and distance away from the nearest coastline (approximately 300 km). Although microplastic pollution is recorded in Whittard Canyon, submarine canyons with a land-attached configuration (*e.g.,* Congo Canyon and Monterey Canyon) would be expected to contain elevated levels of microplastic pollution, given their connection to fluvial systems and the potential losses that occur with increased transport distances and capacity for transient and permanent storage.

In the Congo Canyon, estimations of the sediment concentration of turbidity currents (Simmons *et al.*, 2020), the longest recorded turbidity currents (Talling *et al.*, 2022), organic carbon transport via turbidity currents (Rabouile *et al.*, 2017), and landslide damming (Pope *et al.*, 2021) have all been documented. In Monterey Canyon, turbidity current structure (Paull *et al.*, 2018), the downstream evolution of turbidity currents (Hereema *et al.*, 2020), and internal tide activity (Maier *et al.*, 2019; Wolfson-Schwehr *et al.*, 2023) have all been documented. The integration of these data and information from the aforementioned studies coupled with microplastic analysis would help to provide the much-needed sedimentological context that is needed for developing more accurate microplastic budgets in the deep-sea. Yet, to date there is an absence of studies of microplastic pollution in such canyons, despite the Congo Canyon and Monterey Canyon being the most studied submarine canyons in the world. Furthermore, repeat surveys of such submarine canyons would help to improve the accuracy of these budgets through time, yet as of 2021, only four of the nearly 9,500 mapped submarine canyons were being repeatably surveyed (Pope *et al.*, 2021).

The pervasiveness of microplastic pollution in the Eastern Branch of the Whittard Canyon, down to a sediment depth of at least 10 cm, and the highly variable sediment accumulation rates suggests that microplastic-bearing sediments in the deep-sea may be several- to tens-of-metres thick. In theory, the mass-production of plastic in the 1950's and the generation of microplastics suggests that microplastics preserved in sediment have the potential to be tracer particles, used to identify the onset of the Anthropocene. However, their mobility in the subsurface, both in terrestrial environments (*e.g.,* Dimante-Deimantovica *et al.* 2024) and in the deep-sea (Chapter 5) suggestions caution is required and brings into question the efficacy of microplastics as tracer particles. Longer sediment cores that capture the contact between microplastic-bearing sediments and non-microplastic-bearing sediments, and the importance of

using other tracer particles, including radionuclides (*e.g.,* ^{210}Pb, ^{137}Cs, and ^{241}Am; Li *et al.,* 2021) and foraminifera (*e.g.,* Missiaen *et al.,* 2020), in conjunction with microplastics, across a wider range of depositional environments, are suggested to help provide more accurate sediment accumulation rates, and calculations of the amount of microplastics in the deep-sea and their routeing pathways.

Furthermore, strong contamination control measures are also required for assuring the accuracy of microplastic counts and improving the microplastic flux calculations across different depositional environments. During the processing of the sediment samples used in Chapter 5, control measures were employed: on-board the research vessel, in the storage of samples, during the extraction of microplastics from sediment, and during the identification and quantification, all to limit airborne contamination of samples (Section 5.3.3.1 and Table A1). At the very least, data regarding the exposure time of samples and the quantity of microplastics should be documented in future studies to gauge the difference in contamination levels across different laboratory procedures and in developing a uniformity in the methods used throughout the discipline. Similar efforts are currently being made to develop uniform microplastic extraction methods and what units are used to document microplastic concentrations (*e.g.,* Cashman *et al.,* 2020).

Microplastics have been observed to be ingested by deep-sea organisms (Taylor *et al.,* 2016) and once ingested have the potential to passed-up the trophic levels of the food-chain (Parolini *et al.,* 2023). However, how detrimental microplastic ingestion is to organisms is unknown. Turbidity currents have been documented to be efficient conveyors of sediment (Talling *et al.,* 2023), and oxygen and nutrients to the deep-sea (Canals *et al.,* 2006). Figure 6.4 shows sea cucumbers grazing on the seabed of the Whittard Canyon at 3204 m water depth following the passage of a turbidity current. Identifying the routeing pathways of turbidity currents and understanding how microplastics are transported and buried can be used to help identify deep-sea organisms vulnerable to microplastic pollution and help to develop mitigation strategies across a wider breadth of geoscience disciplines.

Figure 6.4: Photograph taken from the video footage collected by a Remote Operated Vehicle of sea cucumbers grazing on the seabed at 3204 m water depth, following the passage of a turbidity current in the Eastern Branch of Whittard Canyon.

Chapter 7   Conclusions

This thesis has used results from physical models, and data from ancient and modern submarine canyon systems to examine the effects of topography on gravity flow behaviour and sedimentation, and the transfer of microplastics in the deep sea. The main conclusions relating to the research questions addressed throughout this thesis are listed below.

1) **How does topography control sediment gravity flow behaviour and sedimentation?**

- The behaviour of sediment gravity flows changes profoundly upon incidence with topography and with changes to the degree of flow confinement, which is recorded by the loci and type of the deposits.

- The existing process models for combined flows in deep-water settings are based on experiments performed in two-dimensional flume tanks that attribute the formation of combined flows to the interaction of the primary flow with internal waves, the latter forming an oscillatory flow component. A new mechanistic model for combined flow generation in three-dimensional settings is presented based on the interaction of subcritical, unconfined density currents with simple, orthogonal topography. The superimposition of multidirectional flow components on the slope and with the parental flow at the base of slope generates complex, highly multidirectional flows (*i.e.*, combined flows), and in each topographic configuration, in the absence of internal waves and thus an oscillatory flow component.

- The superelevation of the incoming density current and degree of flow thinning on simple, orthogonal slopes is a function of slope angle. The flow process regime changes from divergence-dominated, through reflection-dominated, to deflection-dominated as the slope angles increases from 20° to 30° to 40°. The flow-topography interactions influence the spatial variability of combined flow bedforms on the slope surface, the deposition of thick sands at the base of slope, and provides a physical explanation for the onlap styles of the deposits. The new model can support enhanced palaeogeographic reconstructions and assessments of the degree of flow confinement and topographic interactions within deep-water systems.

- The interaction of sediment gravity flows with complex debrite topography generated marked heterogeneity in the deposit type and architecture in comparison to simple, planar topography. Mass-wasting in submarine canyons is common; excavating space and generating complex topography in canyon-confined overbanks. The wide range of flow types received by canyon-confined overbanks and interaction with complex topography generate heterogeneity over short spatial ranges, which was poorly accounted for in previous canyon-fill models.

- Changes to submarine canyon geomorphology affect the delivery of microplastics to the deep sea. Down-canyon changes in the canyon width and thalweg gradient see sediment gravity flows transition from bypass-dominated in the upper-canyon to net-depositional in the lower-canyon. The decrease in the degree of confinement and switch to a net-depositional regime sees an increase in the amount of microplastics deposited in the Whittard Canyon. Intra-canyon topography has also been shown to locally store organic carbon transported via sediment gravity flows, thus suggesting similar effects on microplastic particles.

2) How does the feedback between flow-topography interactions vary with time?

- In highly dynamic submarine canyon settings, the deposits from sediment gravity flows can provide an insight into flow-topography interactions and the temporal evolution of processes in canyon-confined overbanks and for the mechanisms of canyon-margin mass-wasting.

- How successive sediment gravity flows respond to interactions with topography depends on whether the topography has been healed by previous deposits or whether the sediment gravity flow are interacting directly with the topography. The heterogeneity in deposit type and architecture is more apparent with complex topography and can change over short spatial ranges.

- Further synthesis of the physical models and the outcrop study presented here document how sediment gravity flows respond to different topographic configurations and how autogenic signal changes could be misinterpreted as allogenic signal changes.

- Understanding the mechanisms that generate complex topography, how subsequent and successive sediment gravity flows respond to topography, and how particulate matter is

locked-up throughout deep-water systems is vital in assessing the spatio-temporal trends in particulate matter delivery and storage.

3) What role do submarine canyons play in the source-to-sink pathways of microplastics?

- Submarine canyons were hypothesised to be efficient conveyors of sediment and microplastic particles to the deep sea via sediment gravity flow transport. Here, the changes to the degree of flow confinement, the interplay between hydrodynamic processes, and subsurface burial processes act to transiently and permanently store microplastics in the Whittard Canyon.

- The distribution of microplastics in the deep sea is dictated by the routeing pathways of sediment gravity flows and controlled by changes to the degree of flow confinement and steering by interactions with seafloor topography.

- Microplastic pollution is observed across the Whittard Canyon despite being land-detached, thus suggesting marine-sourced microplastics dominated over terrestrially sourced microplastics, and that land-detached submarine canyons may be receiving a buffered supply of terrestrial microplastics. Land-attached canyons, with direct or delayed fluvial inputs may transfer higher concentrations of microplastics to the deep sea than land-detached canyons.

- Processes in the shallow subsurface (*e.g.,* bioturbation and hyporheic transport) are capable of burying microplastics into sediment deposited before the mass-production of plastics in the 1950's. Such processes are poorly accounted for source-to-sink models of microplastics in the deep sea and shreds the ability of microplastics to be trace markers for the onset of the Anthropocene.

- A better understanding of microplastic transport and burial processes in the deep sea permits the development of more comprehensive source-to-sink models, used to help identify microplastic pollution hotspots and deep-marine ecosystems vulnerable to the effects of microplastic ingestion.

This thesis presents and synthesises the results from three distinct data acquisition methods and develops new models for SGF behaviour and deposition, and the transfer of microplastics in the deep-sea. The findings from physical experiments present a new model for combined flow generation, and mechanisms for combined flow bedforms and onlap styles in unconfined settings; all used to support enhanced palaeogeographic reconstructions in deep-water settings. At outcrop-scale, the localised heterogeneity in canyon overbank deposits documents the influence of complex, dynamic topography on SGF behaviour, with the results having the potential to be exported across different exhumed submarine canyon systems. In modern canyon systems, the dynamism of competing processes results in a poor record of canyon particulate flux and underestimates the transient and permanent storage potential of microplastics. These advances help to inform and can be coupled with future physical and numerical models that investigate flow-topography interactions across a host of deep-water environments. Furthermore, the results highlight the need for studies of modern systems to integrate turbidity current monitoring with micropollutant data collection and analysis. This thesis furthers the understanding of palaeogeographic reconstructions, and the routeing pathways of sediment and potentially fatal micropollutants across a host of deep-water environments.

References

Al Ja'Aidi, O.S., McCaffrey, W.D. and **Kneller, B.C.** (2004) Factors influencing the deposit geometry of experimental turbidity currents: implications for sand-body architecture in confined basins. In: Deep-water Sedimentation in the Alpine Foreland Basin of SE France: New Perspectives on the Grès d'Annot and Related Systems (Eds P. Joseph and S.A. Lomas), *Geological Society London Special Publication*, **222**, 45–58.

Al Mamun, A., Prasetya, T.A.E., Dewi, I.R. and **Ahmad, M. (2023)** Microplastics in human food chains: Food becoming a threat to health safety. *Science of the Total Environment*. **858**, 159834.

Alexander, J. and **Morris, S.** (1994) Observations on experimental, nonchannelized, high-concentration turbidity currents and variations in deposits around obstacles. Journal of Sedimentary Research, 64, 899-909.

Allen, C., Gomis Cartesio, L.E., Hodgson, D.M., Peakall, J. and **Milana, J-P.** (2022) Channel incision into a submarine landslide on a Carboniferous basin margin, San Juan, Argentina: Evidence for the role of knickpoints. *The Depositional Record*, **8**, 628-655.

Allen, J.R.L. (1971) Transverse erosional marks of mud and rocks: their physical basis and geological significance. *Sedimentary Geol*ogy, **5**, 167-385.

Allen, J.R.L. (1973) Development of flute-mark assemblages, 1. Evolution of pairs of defects. *Sedimentary Geol*ogy, **10**, 157-177.

Allen, J.R.L. (1975) Development of flute-mark assemblages, 2. Evolution of trios of defects. *Sedimentary Geol*ogy, **13**, 1-26.

Allen, J.R.L. (1991) The Bouma division A and the possible duration of turbidity currents. *Journal of Sedimentary Petrol*ogy, **61**, 291-295.

Altinakar, M.S., Graf, W.H. and **Hopfinger, E.J.** (1996) Flow structure in turbidity currents. *Journal of Hydraulic Research*, **34**, 713-718.

Amaro, T., Huvenne, V.A.I., Allcock, A.L., Aslam, T., Davies, J.S., Danovaro, R., De Stigter, H.C., Duineveld, G.C.A., Gambi, C., Gooday, A.J., Gunton, L.M., Hall, R., Howell, K.L., Ingels, J., Kiriakoulakis, K., Kershaw, C.E., Lavaleye, M.S.S., Robert, K., Stewart, H., Van Rooij, D.,

White, M. and **Wilson, A.M.** (2016) The Whittard Canyon – A case study of submarine canyon processes. *Progress in Oceanography*, **146**, 38-57.

Amblas, D., Micallef, A., Ceramicola, S., Geber, T.P., Canals, M., Casalbore, D., Chiocci, F.L., Duran, R., Harris, P.T., Huvenne, V.A.I., Lai, S.Y.J., Lastras, G., Lo Iacono, C., Matos, F.L., Mountjoy, J.J., Paull, C.K., Puig, P. and **Sanchez-Vidal, A.** (2022) 8.30 – Submarine Canyons. *Treaties on Geomorphology (Second Edition)*, **8**, 830-846.

Amy, L.A., McCaffrey, W.D. and **Kneller, B.C.** (2004) The influence of a lateral basin-slope on the depositional patterns of natural and experimental turbidity currents. In: Deep-water Sedimentation in the Alpine Foreland Basin of SE France: New Perspectives on the Grès d'Annot and Related Systems (Eds P. Joseph and S.A. Lomas), *Geological Society London Special Publication*, **221**, 311-330.

Amy, L.A., Peakall, J. and **Talling, P.J.** (2005) Density- and viscosity-stratified gravity currents: Insights from laboratory experiments and implications for submarine flow deposits. *Sedimentary Geology*, **179**, 5-29.

Anderson, K.S., Graham, S.A. and **Hubbard, S.M.** (2006) Facies, Architecture, and Origin of a Reservoir-Scale Sand-Rich Succession Within Submarine Canyon Fill: Insights from Wagon Caves Rock (Paleocene), Santa Lucia Range, California, U.S.A. *Journal of Sedimentary Research*, **76**, 819-838.

Andrady, A.L. (2011) Microplastics in the marine environment. *Marine Pollution Bulletin*, **62**, 1596-1605.

Appleby, P.G. and **Oldfield, F.** (1978) The calculation of lead-210 dates assuming a constant rate of supply of unsupported ^{210}Pb to the sediment. *CATENA*, **5**, 1-8.

Apps, G., Peel, F. and **Elliott, T.** (2004) The structural setting and palaeogeographical evolution of the Grès d'Annot basin. In: Deep-water Sedimentation in the Alpine Foreland Basin of SE France: New Perspectives on the Grès d'Annot and Related Systems (Eds P. Joseph and S.A. Lomas), *Geological Society London Special Publication*, **221**, 65-96.

Armitage, D.A., Piper, D.J.W., McGee, D.T. and **Morris, W.R.** (2010) Turbidite deposition on the glacially influenced, canyon-dominated Southwest Grand Banks slope, Canada. *Sedimentology*, **57**, 1387-1408.

Armitage, D.A., Roman, B.W., Covault, J.A. and **Graham, S.A.** (2009) The influence of mass-transport-deposit surface topography on the evolution of turbidite architecture: The Sierra Contreras, Tres Pasos Formation (Cretaceous), Southern Chile. *Journal of Sedimentary Research.*, **79**, 287-301.

Arnott, R.W. and **Southard, J.B.** (1990) Exploratory flow-duct experiments on combined-flow bed configurations, and some implications for interpreting storm-event stratification. *Journal of Sedimentary Res*earch, **60**, 211-219.

Atwater, T (1970) Implications of plate tectonics for the Cenozoic tectonic evolution of western North America. *Bulletin of the Geological Society of America*. **81**, 3513-3536.

Ayckbourne, A.J.M, Jerrett, R.M., Poyatos-Moré, M., Watkinson, M.P., Kane, I.A. and **Taylor, K.G.** (2023) The influence creeping slope failure on turbidity current behaviour. *Sedimentology*, **70**, 335-361.

Azpiroz-Zabala, M., Cartigny, M.J.B., Talling, P.J., Parsons, D.R., Sumner, E.J., Clare, M.A., Simmons, S.S., Cooper, C. and **Pope, E.L.** (2017) Newly recognized turbidity current structure can explain prolonged flushing of submarine canyons. *Science Advances*, **3**, e170020.

Baas, J.H. and **Best, J.L.** (2002) Turbulence modulation in clay-rich sediment-laden flows and some implications for sediment deposition. *Journal of Sedimentary Research*, **72**, 336-340.

Baas, J.H., McCaffrey, W.D., Haughton, P.D.W. and **Choux, C.** (2005) Coupling between suspended sediment distribution and turbulence structure in a laboratory turbidity current. *Journal of Geophysical Research: Oceans*, **110**, 1-20.

Baas, J.H., Best, J.L., Peakall, J. and **Wang, M.** (2009) A phase diagram for turbulent, transitional and laminar clay suspension flows. *Journal of Sedimentary Research*, **79**, 162-183.

Baas, J.H., Best, J.L. and **Peakall, J.** (2011) Depositional processes, bedform development and hybrid bed formation in rapidly decelerated cohesive (mud-sand) sediment flows. *Sedimentology*, **58**, 1953-1987.

Baas, J.H., Best, J.L. and **Peakall, J.** (2016) Predicting bedforms and primary current stratification in cohesive mixtures of mud and sand. *Journal of the Geological Society*, **173**, 12-45.

Baas, J.H., Best, J.L. and **Peakall, J.** (2021a) Rapid gravity flow transformation revealed in a single climbing ripple. *Geology*, **49**, 493-497.

Baas, J.H., Tracey, N.D. and **Peakall, J.** (2021b) Sole marks reveal deep-marine depositional process and environment: implications for flow transformation and hybrid event bed models. *Journal of Sedimentary Research*, **91**, 986–1009.

Babonneau, N., Savoye, B., Cremer, M. and **Bez, M.** (2010) Sedimentary architecture in meanders of a submarine channel; detailed study of the present Congo turbidite channel (Zaiango project). *Journal of Sedimentary Research*, **8**, 852-866.

Babonneau, N., Savoye, B., Cremer, M. and **Klein, B.** (2002) Morphology and architecture of the present canyon and channel system of the Zaire deep-sea fan. *Marine Petroleum Geology*, **19**, 445-467.

Bailey, L.P., Clare, M.A., Hunt, J.E., Kane, I.A., Miramontes, E., Fonnesu, M., Argiolas, R., Malgesini, G. and **Wallerand, R.** (2024) Highly variable deep-sea currents over tidal and seasonal timescales. *Nature Geoscience*, **17**, 787-794.

Baker, M.L. and **Baas, J.H.** (2020) Mixed sand–mud bedforms produced by transient turbulent flows in the fringe of submarine fans: Indicators of flow transformation. *Sedimentology*, **67**, 2645-2671.

Baker, M.L., Baas, J.H., Malarkey, J., Jacinto, R.S., Craig, M.J., Kane, I.A. and **Barker, S.** (2017) The effect of clay type on the properties of cohesive sediment gravity flows and their deposits. *Journal of Sedimentary Research*, **87**, 1176-1195.

Bakke, K., Kane, I.A., Martinsen, O.J., Petersen, S.A., Johansen, T.A., Hustoft, S., Jacobsen, F.H. and **Groth, A.** (2013) Seismic modelling in the analysis of deep- water sandstone termination styles. *The American Association of Petroleum Geologists Bulletin*, **97**, 1395–1419.

Barker, S.P., Haughton, P.D.W., McCaffrey, W.D., Archer, S.G. and **Hakes, B** (2008) Development of rheological heterogeneity in clay-rich high-density turbidity currents: Aptian Britannia Sandstone Member, UK continental shelf. *Journal of Sedimentary Research*, **78**, 45–68.

Barnes, D.K., Galgani, F., Thompson, R.C. and **Barlaz, M.** (2019) Accumulation and fragmentation of plastic debris in global environments. *Philosophical Transactions of the Royal Society*, **364**, 1985-1998.

Barrett, J., Chase, Z., Zhang, J., Banaszak Holl, M.M., Willis, K., Williams, A., Hardesty, B.D. and **Wilcox, C.** (2020) Microplastic pollution in deep-sea sediments from the Great Australian Bight. *Frontiers in Marine Science*, **7**, 576170.

Bell, D., Stevenson, C.J., Kane, I.A., Hodgson, D.M. and **Poyatos-Moré, M.** (2018) Topographic controls on the development of contemporaneous but contrasting basin- floor depositional architectures. *Journal of Sedimentary Research*, **88**, 1166-1189.

Bergamann, M., Collard, F., Fabres, J., Gabrielsen, G.W., Provencher, J.F., Rochman, C.M., van Sebille, E. and **Tekman, M.B.** (2022) Plastic pollution in the Arctic. *Nature Review Earth & Environment*, **3**, 323-337.

Bianchelli, S., Gambi, C., Zeppilli, D. and **Danovaro, R.** (2010) Metazoan meiofauna in deep-sea canyons and adjacent open slopes: A large-scale comparison with focus on rare taxa. *Deep Sea Research Part 1: Oceanographic Research Papers*, **57**, 420-433.

Boehlke, J.E. and Abbott, P.L. (1986) Punta Baja Formation, a Campanian submarine canyon fill, Baja California, Mexico. In: Cretaceous Stratigraphy Western North America: Los Angeles, Pacific Section (Ed P.L. Abbott), *Society for Economic and Paleontologists and Mineralogists*, **46**, 91-101.

Boulesteix, K., Poyatos-More, M., Flint, S.S., Taylor, K., Hodgson, D.M. and **Hasiotis, T.** (2019) Transport and deposition of mud in deep-water environments: processes and stratigraphic implications. *Sedimentology*, **66**, 2894-2925.

Boulesteix, K., Poyatos-Moré, M., Flint, S.S., Hodgson, D.M., Taylor, K.G. and **Brunt, R.L.** (2022) Sedimentologic and stratigraphic criteria to distinguish between basin-floor and slope mudstones: Implications for the delivery of mud to deep-water environments. *The Depositional Record*, **8**, 958-988.

Bouma, A.H. (1962) Sedimentology of some flysch deposits: A graphic approach to facies interpretations. New York, Elsevier, 168 p.

Bouwmeester, M.J., Kane, I., Hodgson, D., Flint, S. Taylor, W., Soutter, E., McArthur, A., Poyatos-Moré, M., Marsh, J., Keavney, E., Brunt, R.L. and **Valdez, V.** (2024) Evolution and architecture of an exhumed ocean-facing coarse-grained submarine canyon fill, Baja California, Mexico. *Sedimentology,* doi.org/10.1111/sed.13231*.*

Brooks, H.B., Hodgson, D.M., Brunt, R.L., Peakall, J., Hofstra, M. and **Flint, S.S.** (2018) Deepwater channel-lobe transition zone dynamics: processes and depositional architecture, an example from the Karoo Basin, South Africa. *Geological Society of America Bull*etin, **130**, 1723–1746.

Brunt, R.L., McCaffrey, W.D. and **Kneller, B.C.** (2004) Experimental modelling of the spatial distribution of grain size developed in a fill-and-spill mini-basin setting. *Journal of Sedimentary Research*, **74**, 438–446.

Buckee, C., Kneller, B. and **Peakall. J.** (2001) Turbulence structure in steady, solute-driven gravity currents. In: *Particulate Gravity Currents* (Eds W. McCaffrey, B. Kneller and J. Peakall), *International Association of Sedimentologists Special Pub*lication, **31**, 173-187.

Bührig, L.H., Colombera, L., Patacci, M., Mountney, N.P. and **McCaffrey, W.D** (2022) A global analysis of controls on submarine canyon geomorphology. *Earth Science Reviews*, **233**, 104150.

Bull, S., Cartwright, J. and **Huuse, M.** (2009) A review of kinematic indicators from mass-transport complexes using 3D seismic data. *Marine and Petroleum Geology*, **26**, 1132-1151.

Bull, S., Browne, G.H., Arnot, M.J. and **Strachan, L.J.** (2019) Influence of mass transport deposits (MTD) surface topography on deep-water deposition: an example from a predominantly fine-grained continental margin, New Zealand. In: *Subaqueous mass movements and their consequences* (Eds A. Georgiopoulou, L.A. Amy, S. Benetti, J.D. Chaytor, M.A. Clare, D. Gamboa, P.D.W. Haughton, J. Moernaut and J.J. Mountjoy), *Geological Society London Special Publication*, **500,** 147-171.

Bullard, J.E., Ockelford, A., O'Brien, P. and **McKenna Neuman, C.** (2021) Preferential transport of microplastics by wind. *Atmospheric Environment*, **245**, 118038.

Busby, C. (2004) Continental growth at convergent margins facing large ocean basins: a case study from Mesozoic convergent-margin basins of Baja California, Mexico. *Tectonophysics,* **392**, 241-277.

Busby, C., Smith, D., Morris, W. and **Fackler-Adams, B.** (1998) Evolutionary model for convergent margins facing large ocean basins: Mesozoic Baja California, Mexico. *Geology*, **26**, 227-230.

Busby, C.J., Yip, G., Blikra, L. and **Renne, P.** (2002) Coastal landsliding and catastrophic sedimentation triggered by Cretaceous-Tertiary bolide impact: A Pacific margin example? *Geology*, **30**, 687-690.

Callow, R.H.T., McIlroy, D., Kneller, B. and **Dykstra, M.** (2013) Integrated ichnological and sedimentological analysis of a Late Cretaceous submarine channel-levee system: The Rosario Formation, Baja California, Mexico. *Marine Petroleum Geology*, **41**, 277-294.

Campanale, C., Massarelli, C., Savino, I., Locaputo, V. and **Felice Uricchio, V.** (2020) A Detailed Review Study of Potential Effects of Microplastics and Additives of Concern on Human Health. *International Journal of Environmental Research and Public Health*, **17**, 1212.

Canals, M., Puig, P., de Madron, X.D., Heussner, S., Palanques, A. and **Fabres, J.** (2006) Flushing submarine canyons. *Nature*, **444**, 354-357.

Cantero, M., Cantelli, A., Pirmez, C., Balachandar, S., Mohrig, D., Hickson, T., Yeh, T., Naruse, H. and **Parker, G.** (2012) Emplacement of massive turbidites linked to extinction of turbulence in turbidity currents. *Nature Geoscience*, **5**, 42-45.

Carpenter, R., Peterson, M.L. and **Bennett, J.T.** (1982) ^{210}Pb-derived sediment accumulation and mixing rates for the Washington continental slope. *Marine Geology*, **48**, 135-164.

Carter, G.D.O., Huvenne, V.A.I., Gales, J.A., La Iacono, C., Marsh, L., Ougier-Simonin, A., Robert, K. and **Wynn, R.B.** (2018) Ongoing evolution of submarine canyon rockwalls; examples from the Whittard Canyon, Celtic Margin (NE Atlantic). *Progress in Oceanography*, **169**, 79-88.

Cartigny, M.J., Ventra, D., Postma, G. and **Van Den Berg. J.H.** (2014) Morphodynamics and sedimentary structures of bedforms under supercritical-flow condition: new insights from flume experiments. *Sedimentology*, **61**, 712-748.

Cashman, M., Ho, K.T., Boving, T.B., Russo, S., Robinson, S. and **Burgess, R.M.** (2020) Comparison of microplastic isolation and extraction procedures from marine sediments. *Marine Pollution Bulletin*, **159**, 111507.

Chaytor, J.D., Demopoulos, A.W.J., ten Brink, U.S., Baxter, C., Quattrini, A.M. and **Brothers, D.S.** (2016) Assessment of canyon wall failure processes from multibeam bathymetry and Remotely Operated Vehicle (ROV) observations, U.S. Atlantic continental margin. In: *Submarine mass movements and their consequences, advances in natural and technological hazards research* (Eds G. Lamarche, J. Mountjoy, S. Bull, T. Hubble, S. Krastel, E. Lane, A. Micallef, L. Moscardelli, C. Mueller, I. Pecher and S. Woelz), Cham, Switzerland, 103-113.

Chen, M., Du, M., Jin, A., Chen, S., Dasgupta, S., Li, J., Xu, H., Ta, K. and **Peng, X.** (2020) Forty-year pollution history of microplastics in the largest marginal sea of the western Pacific. *Geochemical Perspective Letters*, **13**, 42-47.

Choy, C.A., Robison, B.H., Gagne, T.O., Erwin, B., Firl, E., Halden, R.U., Hamilton, J.A., Katija, K., Lisin, S.E., Rolsky, C. and **Van Houtan, K.S.** (2019) The vertical distribution and biological transport of marine microplastics across the epipelagic and mesopelagic water column. *Science Advances*, **9**, 7843.

Clark, J.D. and **Pickering, K.T.** (1996) Architectural Elements and Growth Patterns of Submarine Channels: Application to Hydrocarbon Exploration. *American Association of Petroleum Geologists Bulletin*, **80**, 194-220.

Clifton, H.E. (1976) Wave-formed sedimentary structures, a conceptual model. In: *Beach and Nearshore Sedimentation* (Eds R.A.J. Davies and R.L. Etherington), *SEPM Special Publication, 24, 126-148.* SEPM Society for Sedimentary Geology, Tulsa, OK.

Cole, M., Lindeque, P., Halsband, C. and **Galloway, T.S.** (2011) Microplastics as contaminants in the marine environment: A review. *Marine Pollution Bulletin*, **62**, 2588-2597.

Collot, J-Y., Lewis, K., Lamarche, G. and **Lallemand, S.** (2001) The giant Ruatoria debris avalanche on the northern Hikurangi margin, New Zealand: Result of oblique seamount subduction. *Journal of Geophysical Research*, **106**, 19271-19297.

Coppock, R.L., Cole, M., Lindeque, P.K., Queirós, A.M, and **Galloway, T.S.** (2017) A small-scale portable method for extracting microplastics from marine sediments. *Environmental Pollution*, **230**, 829-837.

Courtene-Jones, W., Quinn, B., Ewins, C., Gary, S.F. and **Narayanaswamy, B.E.** (2020) Microplastic accumulation in deep-sea sediments from the Rockall Trough. *Marine Pollution Bulletin*, **154**, 111092.

Covault, J.A. and **Romans, B.W.** (2009) Growth patterns of deep-sea fans revisited: Turbidite-system morphology in confined basins, examples from the California Borderland. *Marine Geology*, **265**, 51-66.

Cullen, T.M., Collier, R.E.L., Gawthorpe, R.L., Hodgson, D.M. and **Barrett, B.J.** (2020) Axial and transverse deep-water sediment supply to syn-rift fault terraces: insights from the west Xylokastro fault block, Gulf of Corinth, Greece. *Basin Research,* **32**, 1115-1149.

Cumberpatch, Z.A., Kane, I.A., Soutter, E.L., Hodgson, D.M., Jackson, C.A.-L., Kilhams, B.A. and **Poprawski, Y.** (2021) Interactions between deep-water gravity flows and active salt tectonics. *Journal of Sedimentary Research.*, **91** (1), 34-65.

Curray, J. and **Moore, D.G.** (1971) Growth of the Bengal Deep-Sea Fan and Denudation in the Himalayas. *Geological Society of America Bulletin*, **87**, 563-572.

Daly, E., Johnson, M.P., Wilson, A.M., Gerritsen, H.D., Kirakoulakis, K., Allcock, A.L., and **White, M.,** (2018) Bottom trawling at Whittard Canyon: Evidence for seabed modification, trawl plumes and food source heterogeneity. *Progress in Oceanography*, **169**, 227-240.

Daly, R.A. (1936) Origin of Submarine Canyons. *American Journal of Science*, **31**, 401-420.

De Leo, F.C., Smith, C.R., Rowden, A.A., Bowden, D.A and **Clark, M.R.** (2010) Submarine canyons: hotspots of benthic biomass and productivity in the deep sea. *Proceedings of the Royal Society B*, **277**, 2783-2792.

De Ruig, M.J. and **Hubbard, S.M.** (2006) Seismic facies and reservoir characteristics of a deep-marine channel belt in the Molasse foreland basin, Puchkirchen Formation, Austria. *American Association of Petroleum Geologists Bulletin*, **90**, 735-752.

de Witte, B., Devriese, L., Bekaert, K., Hoffman, S., Vandermeersch, G., Cooreman, K. and **Robbens, J.** (2014) Quality assessment of the blue mussel (Mytilus edulis): comparison between commercial and wild types. *Marine Pollution Bulletin*, **85**, 145-155.

Dennielou, B., Droz, L., Babonneau, N., Jacq, C., Bonnel, C., Picot, M., Le Saout, M., Saout, Y., Bez, M., Savoye, B., Olu, K. and **Rabouille, C.** (2017) Morphology, structure, composition and build-up processes of the active channel-mouth lobe complex of the Congo deep-sea fan with inputs from remotely operated underwater vehicle (ROV) multibeam and video surveys. *Deep Sea Research Part 2: Topical Studies in Oceanography*, **142**, 25-49.

Deptuck, M.E., Piper, D.J., Savoye, B. and **Gervais, A.** (2008) Dimensions and architecture of late Pleistocene submarine lobes off the northern margin of East Corsica. *Sedimentology*, **55**, 869-898.

Deptuck, M.E., Steffens, G.S., Barton, M. and **Pirmez, C.** (2003) Architecture and evolution of upper fan channel-belts on the Niger Delta slope and in the Arabian Sea. *Marine Petroleum Geology*, **20**, 649-676.

Deptuck, M.E., Sylvester, Z., Pirmez, C. and **O'Byrne, C.** (2007) Migration-aggradation history and 3-D seismic geomorphology of submarine channels in the Pleistocene Benin-major Canyon, western Niger Delta slope. *Marine and Petroleum Geology*, **24**, 406-433.

Di Celma, C. (2011) Sedimentology, architecture, and depositional evolution of a coarse-grained submarine canyon fill from the Gelasian (early Pleistocene) of the Peri-Adriatic basin, Offida, central Italy. *Sedimentary Geology*, **238**, 233-253.

Dimante-Deimantovica. I., Saarni, S., Barone, M., Buhhalko, N., Stivrins, N., Suhareva. N., Tylmann, W., Vianello. A. and **Vollertson, J.** (2024) Downward migrating microplastics in lake sediments are a tricky indicator for the onset of the Anthropocene. *Science Advances*, **10**, eadi8136.

Dodd, T.J., McCarthy, D.J. and **Richards, P.C.** (2018) A depositional model for deep- lacustrine, partially confined, turbidite fans: Early Cretaceous, North Falkland Basin. *Sedimentology*, **66**, 53 - 80.

Dorrell, R.M., Darby, S.E., Peakall, J., Sumner, E.S., Parsons, D.R. and **Wynn, R.B.** (2014) The critical role of stratification in submarine channels: implications for channelization and long run-out flows. *Journal of Geophysical Research: Oceans*, **119**, 2620-2641.

Dorrell, R.M., Patacci, M. and **McCaffrey, W.D.** (2018a) Inflation of ponded, particulate laden density currents. *Journal of Sedimentary Res*earch, **88**, 1276-1282.

Dorrell, R.M., Peakall, J., Burns, C. and **Keevil, G.M.** (2018b) A novel mixing mechanism in sinuous seafloor channels: Implications for submarine channel evolution. *Geomorphology*, **303**, 1-12.

Dorrell, R.M., Peakall, J., Darby, S.E., Parsons, D.R., Johnson, J., Sumner, E.J., Wynn, R.B., Özsoy, E. and **Tezcan, D.** (2019) Self-sharpening induces jet-like structures in seafloor gravity currents. *Nature Communications*, **10**, 1381.

Duis, K. and **Coors, A.** (2016) Microplastics in the aquatic and terrestrial environment: sources (with a specific focus on care products), fate and effects. *Environmental Sciences Europe*, **28**, 2.

Duke, W.L., Arnott, R.W.C. and **Cheer, R.J.** (1991) Shelf sandstones and hummocky cross-stratification: New insights on a stormy debate. *Geology*, **19**, 625-628.

Dumas, S. and **Arnott, R.W.C.** (2006) Origin of hummocky and swaley cross-stratification – The controlling influence of unidirectional current strength and aggradation rate. *Geology*, **34**, 1073-1076.

Dykstra, M. and **Kneller, B.** (2007) Canyon San Fernando, Mexico: a deep-water, channel-levee complex exhibiting evolution from submarine canyon – confined to unconfined. In: *Atlas of Deepwater Outcrops* (Eds T. Nilsen, R. Shew, G. Steffens and J. Studlick) *American Association of Petroleum Geologists Studies in Geology,* **56**, 226-230.

Dzulynski, S. and **Sanders, J.E.** (1962) Current marks on firm mud bottoms. *Connecticut Academy of Arts and Science*, **42**, 57-96.

Edwards, D.A., Leeder, M.R., Best, J.L. and **Pantin, H.M.** (1994) On experimental reflected density currents and the interpretation of certain turbidites. *Sedimentology*, **41**, 437–461.

Eggenhuisen, J.T. and **McCaffrey, W.D.** (2012) Dynamic deviation of fluid pressure from hydrostatic pressure in turbidity currents. *Geology*, **40**, 295-298.

Eggenhuisen, J.T., Cartigny, M.J. and **de Leeuw, J.** (2017) Physical theory for near-bed turbulent particle suspension capacity. *Earth Science Dynamics*, **5**, 269-281.

Ellison, T.H. and **Turner, J.S.** (1959) Turbulent entrainment in stratified flows. *Journal of Fluid Mech*anics, **6,** 423-448.

Emmel, F.J. and **Curray, J.R.** (1983) The Bengal Submarine Fan, Northeastern Indian Ocean. *Geo-Marine Letters*, **3**, 119-124.

Engebretson, D.C., Cox, A. and **Gordon, R.G.** (1985) Relative Motions Between Oceanic and Continental Plates in the Pacific Basin. *Journal of Geophysical Research Solid Earth*, **89**, 10291-10310.

Englert, R.G., Hubbard, S.M., Matthews, W.A., Coutts, D.S. and **Covault, J.A.** (2020) The evolution of submarine slope-channel systems: Timings of incision, bypass, and aggradation in Late Cretaceous Nanaimo Group channel-system strata, British Columbia, Canada, *Geosphere*, **16**, 281-296.

Eriksen, M., Lebreton, L.C.M., Carson, H.S., Thiel, M. and **Moore, C.J.** (2014) Plastic pollution in the world's oceans: More than 5 trillion plastic pieces weighing over 250,000 tons afloat at sea. *PLOS one*. **1**, 1-15.

Fagherazzi, S. (2004) Modeling fluvial erosion and deposition on continental shelves during sea level cycles. *Journal of Geophysical Research*, **109**, 1–16.

Farre, J.A., McGregor, B.A., Ryan, W.B. and **Robb, J.M.** (1983) Breaching the shelfbreak: passage from youthful to mature phase in submarine canyon evolution. In: *The shelfbreak: Critical Interface on Continental Margins* (Eds D.J. Stanley and G.T. Moore) *SEPM Special Publication,* **33**, 25–39.

Ferguson, R.A., Kane, I.A., Eggenhuisen, J.T., Pohl, F., Tilston, M., Spychala, Y.T. and **Brunt, R.L.** (2020) Entangled external and internal controls on submarine fan evolution: an experimental perspective. *The Depositional Record*, **6**, 605-624.

Fernandez-Arcaya, U., Ramirez-Llodra, E., Aguzzi, J., Allcock, A.L., Davies, J.S., Dissanayake, A., Harris, P., Howell, K., Huvenee, V.A.I., Macmillan-Lawler, M., Martin, J., Menot, L., Nizinski. M., Puig, P., Rowden, A.A., Sanchez, F. and **Van Den Beld, I.M.J.** (2017) Ecological role of submarine canyons and need for canyon conservation: A review. *Frontiers in Marine Science*, **4**, 5.

Fildani, A. (2017) Submarine Canyons: A brief review looking forward. *Geology*, **45**, 383-384.

Fildani, A. and **Normark, W.R.** (2004) Late Quaternary evolution of channel and lobe complexes of Monterey Fan. *Marine Geology*, **206**, 199-223.

Fildani, A., Normark, W.R., Kostic, S. and **Parker, G.** (2006) Channel formation by flow stripping: large-scale scour features along the Monterey East Channel and their relation to sediment waves. *Sedimentology*, **53**, 1265-1287.

Finnegan, M.D., Süsserott, R., Gabbott, S.E. and **Gouramanis, C.** (2022) Man-made natural and regenerated cellulosic fibres greatly outnumber microplastic fibres in the atmosphere. *Environmental Pollution*, **310**, 119808.

Fisher, W.L., Galloway. W.E., Steel, R.J., Oraliu, C., Kerans, C. and **Mohrig, D.** (2021) Deep-water depositional systems supplied by shelf-incising submarine canyons: Recognition and significance of the geologic record. *Earth-Science Reviews*, **214**, 103531.

Fonnesu, M., Felletti, F., Haughton, P.D., Patacci, M. and **McCaffrey, W.D.** (2018) Hybrid event bed character and distribution linked to turbidite system sub-environments: the North Apennine Gottero Sandstone (north-west Italy). *Sedimentology*, **65**, 151-190.

Frei, S., Piehl, S., Gilfedder, B.S., Löder, M.G.L., Krutzke, J., Wilhelm, L. and **Laforsch, C.** (2019) Occurrence of microplastics in the hyporheic zone of rivers. *Scientific Reports*, **9**, 15256.

Gales, J.A., Forwick, M., Laberg, J.S., Vorren, T.O., Larter, R.D., Graham, A.G.C., Baeten, N.J. and **Amundsen, H.B.** (2013) Arctic and Antarctic submarine gullies – A comparison of high-latitude continental margins. *Geomorphology*, **201**, 449-461.

Galy, V., France-Lanord, C., Beyssac, O., Faure, P., Kudrass, H. and **Palhol, F.** (2007) Efficient organic carbon burial in the Bengal Fan sustained by the Himalayan erosional system. *Nature*, **450**, 407.

Gamberi, F., Rovere, M., Dykstra, M., Kane, I. and **Kneller, B.** (2013) Integrating modern seafloor and outcrop data in the analysis of slope channel architecture and fill. *Marine Petroleum Geology*, **41**, 83-103.

García, M.H. (1994) Depositional turbidity currents laden with poorly sorted sediment. *Journal of Hydraulic Engineering*, **120**, 1240-1263.

Gardiner, A.R. (2006) The variability of turbidite sandbody pinchout and its impact on hydrocarbon recovery in stratigraphically trapped fields. In: *The Deliberate Search for the Stratigraphic Trap* (Eds M.R. Allen, G.P. Goffrey, R.K. Morgan and I.M. Walker), *Geological Society London Special Publication*, **254**, 267–287.

Gastil, R.G., Phillips, R.C. and **Allison, E.C.** (1975) Reconnaissance geology of the state of Baja California. *Geological Society of America Mem*oirs, **140,** 170 p.

Geyer, R., Jambeck, J. and **Law, K.L.** (2017). Production use and fate of all plastic ever made. *Science Advances*. **3**, 1-5.

Gladstone, C., McClelland, H.L.O., Woodcock, N.H., Pritchard, D. and **Hunt, J.E.** (2018) The formation of convolute lamination in mud-rich turbidites. *Sedimentology*, **65**, 1800-1825.

Gladstone, C., Ritchie, L.J., Sparks, S.J. and **Woods, A.W.** (2004) An experimental investigation of density-stratified inertial gravity currents. *Sedimentology*, **51**, 767-789.

Glazner, A.F. (1991) Plutonism, oblique subduction, and continental growth: An example from the Mesozoic of California. *Geology*, **19**, 784-786.

Global Fishing Watch (2024) *Accessed April 25th 2024, https://globalfishingwatch.org/map/index?start=2024-07-25T00%3A00%3A00.000Z&end=2024-10-25T00%3A00%3A00.000Z&longitude=26&latitude=19&zoom=1.49.*

Gorsline, D.S. and **Emery, K.O.** (1959) Turbidity-Current Deposits in San Pedro and Santa Monica Basins off Southern California. *Geological Society of America Bulletin*, **70**, 279-290.

Graf, W.H. (1971) *Hydraulics of Sediment Transport.* New York, NY: McGraw Hill, **513 pp**.

Groenenberg, R.M., Hodgson, D.M., Prélat, A., Luthi, S.M. and **Flint, S.S.** (2010) Flow–deposit interaction in submarine lobes: Insights from outcrop observations and realizations of a process-based numerical model. *Journal of Sedimentary Res*earch, **80**, 252-267.

Hage, S., Baker, M.L., Babonneau, N., Soulet, G., Dennielou, B., Silva Jacinto, R., Hilton, R.G., Galy, V., Baudin, F., Rabouille, C., Vic, C., Sahin, S., Açikalin, S. and **Talling, P.J.** (2024) How is particulate organic carbon transported through the river-fed Congo Submarine Canyon to the deep-sea?, *EGUsphere*, preprint, doi.org/10.5194/eguspehere-2024-900.

Hage, S., Cartigny, M.J., Clare, M.A., Sumner, E.J., Vendettouli, D., Clarke, J.E.H., Hubbard, S.M., Talling, P.J., Lintern, D.G., Stacey, C.D. and **Englert, R.G.** (2018) How to recognize crescentic bedforms formed by supercritical turbidity currents in the geologic record: Insights from active submarine channels. *Geology*, **46**, 563-566.

Hage. S., Galy, V.V., Cartigny, M.J.B., Heerma, C., Heijnen, M.S., Açikalin, S., Clare, M.A., Giesbricht, I., Gröcke, D.R., Hendry, A., Hilton, R.G., Hubbard, S.M., Hunt, J.E., Lintern, D.G., McGhee, C., Parson, D.R., Pope, E.L., Stacey, C.D., Sumner, E.J., Tank, S. and **Talling, P.J.** (2022) Turbidity currents can dictate organic carbon fluxes across river-fed fjords: An example from Bute Inlet (BC, Canada). *Journal of Geophysical Research: Biogeosciences*, **127**, e2022JG006824.

Hajek, E.A. and **Straub, K.M.** (2017) Autogenic sedimentation in clastic stratigraphy. *Annual Review of Earth and Planetary Sciences*, **45**, 681-709.

Hall, R.A., Aslam, T. and **Huvenne, V.A.I.** (2017) Partly standing internal tides in a dendritic submarine canyon observed by an ocean glider. *Deep Sea Research Part 1: Oceanographic Research Papers*, **126**, 73-84.

Hampton, M.A. (1972) The role of subaqueous debris flow in generating turbidity currents. *Journal of Sedimentary Research*, **42**, 775-793

Hampton, M.A., Lee, H.J. and **Locat, J.** (1996) Submarine landslides. *Reviews of Geophysics*, **34**, 33-59.

Hansen, L., Callow, R., Kane, I. and **Kneller, B.** (2017a) Differentiating submarine channel-related thin-bedded turbidite facies: Outcrop examples from the Rosario Formation, Mexico. *Sedimentary Geology,* **358**, 19-34.

Hansen, L., Janocko, M., Kane, I. and **Kneller, B.** (2017b) Submarine channel evolution, terrace development, and preservation of intra-channel thin-bedded turbidites: Mahin and Avon channels, offshore Nigeria. *Marine Geology*, **383**, 146-167.

Hansen, L.A.S., Janocko, M., Kane, I. and **Kneller, B.** (2016) Submarine channel evolution, terrace development, and preservation of intra-channel thin-bedded turbidites: Mahin and Avon channels, offshore Nigeria. *Marine Geology*, **383**, 146-167.

Hansen, L.A.S., Callow, R.H.T., Kane, I.A., Gamberi, F., Rovere, M., Cronin, B.T. and **Kneller, B.C.** (2015) Genesis and character of thin-bedded turbidites associated with submarine channels. *Marine and Petroleum Geology*, **67**, 552-879.

Hansen, L.A.S., Hodgson, D.M., Pontén, A., Bell, D. and **Flint, S.** (2019) Quantification of basin-floor fan pinch-outs: Examples form the Karoo Basin, South Africa. *Frontiers in Earth Science*, **7**, 12.

Harms, J.C. (1969) Hydraulic significance of some sand ripples. *GSA Bulletin*, **80,** 363-396.

Harris, P.T. and **Whiteway, T.** (2011) Global distribution of large submarine canyons: Geomorphic differences between active and passive continental margins. *Marine Geology*, **285**, 69-86.

Harris, P.T., Macmillan-Lawler, M. Rupp, J. and **Baker, E.K.** (2014) Geomorphology of the oceans. *Marine Geology*, **352**, 4-24.

Haughton, P.D.W. (1994) Deposits of deflected and ponded turbidity currents, Sorbas Basin, Southeast Spain. *Journal of Sedimentary Research*, **64**, 233-246.

Haughton, P.D.W. (2000) Evolving turbidite systems on a deforming basin floor, Tabernas, SE Spain. *Sedimentology*, **47**, 497-518.

Haughton, P.D., Barker, S.P. and **McCaffrey, W.D.** (2003) 'Linked' debrites in sand-rich turbidite systems – origin and significance. *Sedimentology*, **50**, 459-482.

Heerema, C.J., Talling, P.J., Cartigny, M.J.B., Paull, C.K., Bailey, L., Simmons, S.M., Parsons, R.R., Clare, M.A., Gwiazda, R., Lundsten, E., Anderson, K., Maier, K.L., Xi, J.P., Sumner, E.J., Rosenberger, K., Gales, J., McGann, M., Carter, L., Pope, E. and **Monterey Coordinated Canyon Experiment (CCE) Team** (2020) What determines the downstream evolution of turbidity currents? *Earth and Planetary Science Letters*, **352**, 116023.

Heezen, B.C., Ewing, M. and **Menzies, R.J.** (1955) The influence of submarine turbidity currents on abyssal productivity. *Oikos*, **6**, 170-182.

Heijnen, M.S., Mienis, F., Gates, A.R., Bett, B.J., Hall, R.A., Hunt, J., Kane, I.A., Pebody, C., Huvenne, V.A.I., Soutter, E.L. and **Clare, M.A** (2022) Challenging the highstand-dormant paradigm for land-detached submarine canyons. *Nature Communications*, **13**, 3448.

Heerema, C.J., Talling, P.J., Cartigny, M.J., Paull, C.K., Bailey, L., Simmons, S.M., Parsons, D.R., Clare, M.A., Gwiazda, R., Lundsten, E. and **Anderson, K.** (2020) What determines the downstream evolution of turbidity currents? *Earth and Planetary Science Letters*, **532**, 116023.

Hernandez-Moreira, R., Jafarinik, S., Sanders, S., Kendall, C.G.S.C., Parker, G. and **Viparelli, E.** (2019) Emplacement of massive deposits by sheet flow. *Sedimentology*, **67**, 1951-1972.

Hill, P.R. and **Lintern, D.G.** (2022) Turbidity currents on the open slope of the Fraser Delta. *Marine Geology*, **445**, 106738.

Hiscott, R.N. (1994) Loss of capacity, not competence, as the fundamental process governing deposition from turbidity currents. *Journal of Sedimentary Res*earch, **64**, 209-214.

Hiscott, R.N. and **Middleton, G.V.** (1980) Fabric of coarse deep-water sandstones, Tourelle Formation, Quebec, Canada. *Journal of Sedimentary Research*, **50**, 703-721.

Hodgson, D.M. (2009) Distribution and origin of hybrid beds in sand-rich submarine fans of the Tanqua depocentre, Karoo Basin, South Africa. *Marine Petroleum Geology*, **26**, 1940-1956.

Hodgson, D.M. and **Haughton, P.D.W.** (2004) Impact of syndepositional faulting on gravity current behaviour and deep-water stratigraphy: Tabernas-Sorbas Basin, SE Spain. In: *Confined Turbidite Systems* (Eds S.A. Lomas and P. Joseph), *Geological Society of London Special Publ*ication, **222**, 135-158.

Hodgson, D.M., Flint, S.S., Hodgetts, D., Drinkwater, N.J., Johannessen, E.P. and **Luthi, S.M.** (2006) Stratigraphic evolution of fine-grained submarine fan systems, Tanqua depocenter, Karoo Basin, South Africa. *Journal of Sedimentary Research*, **76**, 20-40.

Hodgson, D.M., Brooks, H.L., Ortiz-Kampf, A., Spychala, Y., Lee, D.R. and **Jackson, C.L.** (2019) Entrainment and abrasion of megaclasts during submarine landsliding and their impact on flow behaviour. *Geological Society London, Special Publication*, **477**, 223-240.

Hodgson, D.M., Di Celma, C.N., Brunt, R.L. and **Flint, S.S.** (2011) Submarine slope degradation and aggradation and the stratigraphic evolution of channel-levee systems, *Journal of the Geological Society*, **168**, 625-628.

Hodgson, D.M., Peakall, J. and **Maier, K.L.** (2022) Submarine channel mouth settings: Processes, geomorphology, and deposits. *Frontiers in Earth Science, **10**, 790320.*

Hofstra, M., Peakall, J., Hodgson, D.M. and **Stevenson, C.J.** (2018) Architecture and morphodynamics of subcritical sediment waves in ancient channel-lobe transition zone. *Sedimentology*, **65**, 2339-2367.

Horton, A.A. and **Dixon, S.J.** (2017) Microplastics: an introduction to environmental transport processes. *WIREs Water*, **5**, 1268.

Howlett, D.M., Gawthorpe, R.L., Ge, Z., Rotevatn, A. and **Jackson, C.A.-L.** (2021) Turbidites, topography and tectonics: Evolution of submarine channel-lobe systems in the salt-influenced Kwanza Basin, offshore Angola. *Basin Research,* **33**, 1076-1110.

Howlett, D.M., Ge, Z., Nemec, W., Gawthorpe, R.L., Rotevatn, A. and **Jackson, C.A-L.** (2019) Response of unconfined turbidity currents to deep-water fold and thrust belt topography: Orthogonal incidence on solitary and segmented folds. *Sedimentology*, **66**, 2425-2454.

Hubbard, S.M., de Ruig, M.J. and **Graham, S.A.** (2009) Confined channel-levee complex development in an elongate depo-center: Deep-water Tertiary strata of the Austrian Molasse basin. *Marine Petroleum Geology*, **26**, 85-112.

Hughes Clark, J. (1990) Late stage slope failure in the wake of the 1929 Grand Banks earthquake. *Geo-Marine Letters*, **10**, 69-79.

Hurley, R., Woodward, J. and **Rothwell, J.** (2018). Microplastic contamination of river beds significantly reduced by catchment-wide flooding. *Nature Geoscience*. **11**, 251-257.

Hurst, A., **Verstralen, I.**, **Cronin, B.** and **Hartley, A.** (1999) Sand-Rich Fairways in Deep-Water Clastic Reservoirs: Genetic Units, Capturing Uncertainty, and a New Approach to Reservoir Modeling. *American Association Petroleum Geology Bulletin*, **83**, 1096–1118.

Jackson, C.A-L. (2011) Three-dimensional seismic analysis of megaclasts deformation within a mass transport deposit; implications for debris flow kinematics. *Geology*, **39**, 203-206.

Jambeck, J.R., Geyer, R., Wilcox, C., Siegler, T.R., Perryman, M., Andrady, A., Narayan, R. and **Law, K.L.** (2015) Plastic waste inputs from land into the ocean. *Marine Pollution*, **347**, 768-771.

Janocko, J. and **Basilici, G.** (2021) Architecture of coarse-grained gravity flow deposits in a structurally confined submarine canyon (late Eocene Tokaren Conglomerate, Slovakia). *Sedimentary Geology*, **417**, 105880.

Janocko, M., Nemec, W., Henriksen, S. and **Warchoł, M.** (2013) The diversity of deep-water sinuous channel belts and slope valley-fill complexes. *Marine Petroleum Geology*, **41**, 7-34.

Jiang, N., Chang, X., Huang, W., Khan, F.U., Fang, J.K-H., Hu, M., Xu, *E.G.* and **Wang, Y**. (2024) Physiological response of mussel to rayon microfibers and PCB's exposure: Overlooked semi-synthetic micropollutant. *Journal of Hazardous Materials*, **470**, 134107.

Jiang, X., Conner, N., Lu, K., Tunnel, J.W. and **Liu, Z.** (2022) Occurrence, distribution, and associated pollutants of plastic pellets (nurdles) in coastal areas of South Texas. *Science of the Total Environment*, **842**, 156826.

Jobe, Z.R., Howes, N., Romans, B.W. and **Covault, J.A.** (2018) Volume and recurrence of submarine-fan-building turbidity currents. *The Depositional Record*, **4**, 160-172.

Jobe, Z.R., **Sylvester, Z.**, **Howes, N.**, **Pirmez, C.**, **Parker, A.**, **Cantelli, A.**, **Smith, R.**, **Wolinsky, M.A.**, **O'Byrne, C.**, **Slowey, N.** and **Prather, B.** (2017) High- resolution, millennial-scale patterns of bed compensation on a sand-rich intraslope submarine fan, western Niger Delta slope. *Geological Society of America Bulletin*, **129**, 23–37.

Johnson, M.P., **White, M.**, **Wilson, A.**, **Würzberg, L.**, **Schwabe, E.**, **Folch, H.** and **Allcock, A.L.** (2013) A vertical wall dominated by Acesta excavate and Neopycnodonte zibrowii, part of an undersampled group of deep-sea habitats. *PLoS ONE*, **8**, 79917.

Jones, E.S., **Ross, S.W.**, **Robertson, C.M.** and **Young, C.M.** (2022) Distributions of microplastics and larger anthropogenic debris in Norfolk Canyon, Baltimore Canyon, and the adjacent continental slope (Western North Atlantic Margin, U.S.A.) *Marine Pollution Bulletin*, **174**, 113047.

Joseph, P., **Babonneau, N.**, **Bourgeois, A.**, **Cotteret, G.**, **Eschard, R.**, **Garin, B.**, **Granjeon, D.**, **Lerat, O.**, **Ravenee, C.**, **Domes de Souza, O.**, **Guillocheau, F.** and **Qemener, J.M.** (2000) The Annot Sandstone Outcrops (Franch Alps): Architecture Description as Input for Quantification and 3D Reservoir Modeling. In: *Deep-Water Reservoirs of the World* (Eds Weimer. P, Slatt, R.M., Coleman, J., Rosen, N.C., Nelson, H., Bouma, A.H., Styzen, M.J. and Lawrence, D.T.) *SEPM Society for Sedimentary Geology*, **28**, 422-449.

Kane, I.A. and **Clare, M.A.** (2019) Dispersion, accumulation, and the ultimate fate of microplastics in deep-marine environments: A review and future direction. *Frontiers of Earth Science,* **7**, 80.

Kane, I.A. and **Hodgson, D.M.** (2011) Sedimentological criteria to differentiate submarine channel levee subenvironments: exhumed examples from the Rosario Fm. (Upper Cretaceous) of Baja California, Mexico, and the Fort Brown Fm. (Permian), Karoo basin, S. Africa. *Marine Petroleum Geology,* **28**, 807-823.

Kane, I.A. and **Pontén, A.S.M.** (2012) Submarine transitional flow deposits in the Paleogene Gulf of Mexico. *Geology*, **40**, 1119-1122.

Kane, I.A., Clare, M.A., Miramontes, E., Wogelius, R., Rothwell, J.R., Garreau, and **Pohl, F.** (2020) Seafloor microplastic hotspots controlled by deep-sea circulation. *Science*, **368**, 1140-1145.

Kane, I.A., Dykstra, M.L., Kneller, B.C., Tremblay, S. and **McCaffrey, W.D.** (2009) Architecture of a coarse-grained channel-levée system: the Rosario Formation, Baja California, Mexico. *Sedimentology*, **56**, 2207-2234.

Kane, I.A., Hodgson, D.M., Hubbard, S.M., McArthur, A.D., Poyatos-Moré, M., Soutter, E.L., Flint, S.S. and **Matthews, W.** (2022) Deep-water Tectono-Stratigraphy at a Plate Boundary Constrained by Large N-Detrital Zircon and Micropaleontological Approaches: Peninsular Ranges Forearc, Baja California, Mexico. *The Sedimentary Record*, **20**, 37652.

Kane, I.A., Kneller, B.C., Dykstra, M., Khassem, A. and **McCaffrey, W.D.** (2007) Anatomy of a submarine channel-levee: An example from Upper Cretaceous slope sediments, Rosario Formation, Baja California, Mexico. *Marine Petroleum Geol*ogy, **24**, 540-563.

Kane, I.A., Pontén, A.S., Vangdal, B., Eggenhuisen, J.T., Hodgson, D.M. and **Spychala, Y.T.** (2017) The stratigraphic record and processes of turbidity current transformation across deep-marine lobes. *Sedimentology*, **64**, 1236-1273.

Keavney, E., Peakall, J., Wang, R., Hodgson, D.M, Kane, I.A, Keevil, G.M., Brown, H.C., Clare, M.A. and **Hughes, M.J.** (2024) Unconfined gravity current interactions with orthogonal topography: Implications for combined-flow processes and the depositional record. *Sedimentology, https://doi.org/10.1111/sed.13227.*

Keevil, G.M., Peakall, J., Best, J.L. and **Amos, K.J.** (2006) Flow structure in sinuous submarine channels: Velocity and turbulence structure of an experimental submarine channel. *Marine Geology*, **229**, 241-257.

Kilmer, F.H. (1963) Cretaceous and Cenozoic stratigraphy and palaeontology, El Rosario area., Berkely, University of California, 149 p.

Kimbrough, D.L., Smith, D.P., Mahoney, J.B., Moore, T.E., Grove, M., Gastil, R.G., Ortega-Rivera, A. and **Fanning, C.M.** (2001) Forearc-basin sedimentary response to rapid Late-Cretaceous batholith emplacement in the Peninsular Ranges of southern and Baja California. *Geology*, **29**, 491-494.

Kneller, B. (1995) Beyond the turbidite paradigm: Physical models for deposition of turbidites and their implications for reservoir prediction. In: *Characterization of Deep Marine Clastic Systems* (Eds A.J. Hartley and D.J. Prosser), *Geological Society Special Publication*, **94**, 31–49.

Kneller, B. and **Buckee, C.** (2000) The structure and fluid mechanics of turbidity currents: a review of some recent studies and their geological implications. *Sedimentology*, **47**, 62-94.

Kneller, B. and **McCaffrey, W.** (1999) Depositional effects of flow nonuniformity and stratification within turbidity currents approaching a bounding slope; deflection, reflection, and facies variation. *Journal of Sedimentary Research*, **69**, 980-991.

Kneller, B., Bozetti, G., Callow, R., Dykstra, M., Hansen, L., Kane, I., Li, P., McArthur, A., Santa Catarina, A., dos Santos, T. and **Thompson, P.** (2020) Architecture, process, and environmental diversity in a late Cretaceous slope channel system. *Journal of Sedimentary Research*, **90**, 1-26.

Kneller, B., Dykstra, M., Fairweather, L. and **Milana, J.P.** (2016) Mass-transport and slope accommodation: Implications for turbidite sandstone reservoirs. *American Association of Petroleum Geologists Bulletin*, **100**, 213-235.

Kneller, B., Edwards, D., McCaffrey, W. and **Moore, R.** (1991) Oblique reflection of turbidity currents. *Geology*, **19**, 250–252.

Kneller, B.C. and **Branney, M.J.** (1995) Sustained high-density turbidity currents and the deposition of thick massive sands. *Sedimentolog*y, **42**, 607-616.

Kneller, B.C. and **McCaffrey, W.D.** (1995) Modelling the effects of salt-induced topography on deposition from turbidity currents. In: *Salt, Sediment and Hydrocarbons* (Eds C.J. Travis, B.C Vendeville, H. Harrison, F.J. Peel, M.R. Hudec and B.E. Perkins), *Gulf Coast Society Of Economic Paleontologists And Mineralogists Foundation Sixteenth Annual Research Conference 1995*, 137-145 SEPM Society of Sedimentary Geology, Tulsa, OK.

Kneller, B.C., Bennett, S.J. and **McCaffrey, W.D.** (1997) Velocity and turbulence structure of density currents and internal solitary waves: Potential sediment transport and the formation of wave ripples in deep water. *Sedimentary Geology*, **112**, 235–250.

Koelmans, A., Kooi, M., Law, K.L. and **van Sebille, E.** (2017) All is not lost: Deriving a top-down mass budget of plastic at sea. *Environmental Research Letters*, **12**, 114028.

Komar, P.D. (1971) Hydraulic jumps in turbidity currents. *Geological Society of America Bulletin*, **82**, 1477-1488.

Krishnaswamy, S., Lal, D., Martin, J.M. and **Meybeck, M.** (1971) Geochronology of lake sediments. *Earth and Planetary Science Letters*, **11**, 407-414.

Kuenen, P.H. (1938) Density currents in connection with the problem of Submarine Canyons. *Geology Magazine*, **75**, 241-249.

Kuenen, P.H. and **Migliorini, C.I.** (1950) Turbidity currents as a cause of graded bedding. *The Journal of Geology*, **58**, 91-127.

Lamb, M.L., Hickson, T., Marr, J.G., Sheets, B., Paola, C. and **Parker, G.** (2004) Surging versus continuous turbidity currents: Flow dynamics and deposits in an experimental intraslope basin. Turbidity currents as a cause of graded bedding, **74**, 148-155.

LaRowe, D.E., Arndt, S., Bradley, J.A., Estes, E.R., Hoarfrost, A., Land, S.Q., Lloyd, K.G., Mahmoudi, N., Orsi, W.D., Shah Walter, S.R., Steen, A.D. and **Zhao, R.** (2020) The fate of organic carbon in marine sediments – New insights from recent data and analysis. *Earth-Science Reviews*, **204**, 103146.

Lebreton, L.C.M., van der Zwet, J., Damsteeg, J-W., Slat, B., Andrady, A. and **Reisser, J.** (2017) River plastic emissions to the world's oceans. *Nature Communications*, **8**, 15611.

Lee, S.E., Amy, L.A. and **Talling, P.J**. (2004) The character and origin of thick base-of-slope sandstone units of the Peïra Cava outlier, SE France. In: *Deep-water Sedimentation in the Alpine Foreland Basin of SE France: New Perspectives on the Grès d'Annot and Related Systems* (Eds P. Joseph and S.A. Lomas), *The Geological Society of London Special Publication,* **221**, 331-3347.

Li, W., Li, X., Mei, X., Zhang, F., Xu, J., Liu, C., Wei, C. and **Liu, Q.** (2021) A review of current and emerging approaches for Quaternary marine sediment dating. *Science of the Total Environment*, **780**, 146522.

Lintern, D.G., Hill, P.R. and **Stacey, C.** (2016) Powerful unconfined turbidity current captured by cabled observatory on the Fraser River delta slope, British Columbia, Canada. *Sedimentology*, **63**, 1041-1064.

Lo Iacono, C., Guillén, J., Guerrero, Q., Durán, R., Wardell, C., Hall, R.A., Aslam, T., Carter, G.D.O., Gales, J.A. and **Huvenne, V.A.I.** (2020) Bidirectional bedform fields at the head of a submarine canyon (NE Atlantic). *Earth and Planetary Science Letters*, **542**, 116321.

Lowe, D. (1982) Sediment gravity flows; II, depositional models with spatial reference to the deposits of high-density turbidity currents. *Journal of Sedimentary Petrology*, **52**, 279-297.

Luchi, R., Balachandar, S., Seminara, G. and **Parker, G.** (2018) Turbidity currents with equilibrium basal driving layers: A mechanism for long run-out. *Geophysical Research Letters*, **45**, 1518-1526.

Maier, K.L., Fildani, A., McHargue, T.R., Paull, C.K., Graham, S.A. and **Caress, D.W.** (2012) Punctuated Deep-Water Channel Migration: High-Resolution Subsurface Data from the Lucia Chica Channel System, Offshore California, U.S.A. *Journal of Sedimentary Research*, **82**, 1-8.

Maier, K.L., Johnson, S.Y. and **Hart, P.** (2018) Controls on submarine canyon head evolution: Monterey Canyon, offshore central California. *Marine Geology*, **404**, 24-40.

Maier, K.L., Nodder, S.D., Deppeler, S., Gerring, P., Frontin-Rollet, G., Hale, R., Twigge, O. and **Bury, S.J.** (2024) Dynamic near-seafloor sediment transport in Kaikōura Canyon following a large canyon-flushing event. *Journal of Sedimentary Research*, **94**, 283-301.

Maier, K.L., Paull, C.K., Caress, D.W., Anderson, K, Nieminski, N.M., Lundsten, E., Erwin, B.E., Gwiazda, R. and **Fildani, A.** (2020) Submarine-fan development revealed by integrated high-resolution datasets from La Jolla Fan, offshore California, U.S.A. *Journal of Sedimentary Research*, **90**, 468-479.

Maier, K.L., Rosenberger, K.J., Paull, C.K., Gwiazda, R., Gales, J., Lorenson, T., Barry, J.P., Talling, P.J., McGann, M., Xu, J., Lundsten, E., Anderson, K., Litvin, S.Y., Parsons, D.R., Clare, M.A., Simmons, S.M., Sumner, E.J. and **Cartigny, M.J.B.** (2019) Sediment and organic carbon transport and deposition driven by internal tides along Monterey Canyon, offshore California. *Deep Sea Research Part 1: Oceanographic Research Papers*, **153**, 103108.

Marini, M., Milli, S., Ravnås, R. and **Moscatelli, M.** (2015) A comparative study of confined vs. semi-confined turbidite lobes from the Lower Messinian Laga Basin (Central Apennines, Italy): Implications for assessment of reservoir architecture. *Marine Petroleum Geology*, **63**, 142–165.

Marshall, C.R., Dorrell, R.M., Keevil, G.M., Peakall, J. and **Tobias, S.M.** (2021) Observations of large-scale coherent structures in gravity currents: implications for flow dynamics. *Experiments in Fluids*, **62**, 120.

Marshall, C.R., Dorrell, R.M., Keevil, G.M., Peakall, J. and **Tobias, S.M.** (2023) On the role of transverse motion in pseudo-steady gravity currents. *Experiments in Fluids*, **64**, 63.

Marr, J.G., Harff, P.A., Shanmugan, G. and **Parker, G.** (2001) Experiments on subaqueous sandy gravity flows: The role of clay and water content in flow dynamics and depositional structures. *Geological Society of America Bulletin*, **113**, 1377-1386.

Martínez-Doñate, A., Kane, I.A., Hodgson, D.M., Privat, A.M-L., Jackson, C.A-L., Schwarz, E. and **Flint, S.S.** (2023) Stratigraphic change in flow transformation processes recorded in early post-rift deep-marine intraslope lobe complexes. *Sedimentology*, **70**, 1379-1412.

Martínez-Doñate, A., Privat, A.M-L. J., Hodgson, D.M., Jackson, C.A-L., Kane, I.A., Spychala, Y.T., Duller, R.A., Stevenson, C., Keavney, E., Schwarz, E. and **Flint, S.S.** (2021) Substrate entrainment, depositional relief, and sediment capture: Impact of a submarine landslide on flow process and sediment supply. *Frontiers in Earth Science*, **9**, 757617.

Masson, D.G., Huvenne, V.A.I., de Stigter, H.C., Wolff, G.A., Kiriakoulakis, K., Arzola, R.G. and **Blackbird, S.** (2010) Efficient burial of carbon in a submarine canyon. *Geology*, **38**, 831-834.

May, J.A. and **Warme, J.E.** (2007) An Ancient Submarine Canyon, Black's Beach, La Jolla, California, USA. In: *Atlas of Deep-Water Outcrops: AAPG Studies in Geology 56* (Eds T.H. Nilsen, R.D. Shew, G.S. Steffens and J.R.J. Studlick), *The American Association of Petroleum Geologists*.

McArthur, A., Kane, I.A., Bozetti, G., Hansen, L. and **Kneller, B.C.** (2020) Supercritical flows overspilling from bypass-dominated submarine channels and the development of overbank bedforms. *The Depositional Rec*ord, **6**, 21-40.

McArthur, A.D. and **McCaffrey, W.D.** (2019) Sedimentary architecture of detached deep-marine canyons: Examples from the East Coast Basin of New Zealand. *Sedimentology*, **66**, 1067-1101.

McArthur, A.D., Tek, D.E., Poyatos-Moré, M., Colombera, L. and **McCaffrey, W.D.** (2024) Deep-ocean channel-wall collapse order of magnitude larger than any other documented. *Nature Communications Earth and Environment*, **5**, 143.

McCaffrey, W. and **Kneller, B.** (2001) Process controls on the development of stratigraphic trap potential on the margins of confined turbidite systems and aids to reservoir evaluation. *Amercian Association of Petroleum Geologists Bulletin*, **85**, 971-988.

McGee, D.C. (1965) Upper Cretaceous (Campanian) Foraminiferida from Punta Baja, Baja California. *American Association of Petroleum Geologists Bulletin*, **49**, 1087-1087.

McGowan, D., Salian, A., Baas, J.H., Peakall, J. and **Best, J.** (2024) On the origin of chevron marks and striated grooves, and their use in predicting mud bed rheology. *Sedimentology*, **71**, 687-708.

Méjean, S., François, G., Faug, T. and **Einav, I.** (2022) X-ray study of fast and slow granular flows with transition jumps in between. *Granular Matter*, **24**, 26.

Menard, H.W. (1955) Deep-Sea Channels, Topography, and Sedimentation. *The American Association of Petroleum Geologists Bulletin*, **39**, 236–255.

Menard, H.W. and **Ludwick, J.C.** (1951) Applications of hydraulics to the study of marine turbidity currents. In: *Turbidity Currents and the Transportation of Coarse Sediments to Deep Water* (Ed J.L. Hough), *Society of Economic Paleontologists and Mineralogists Special Publication* 2, pp. 2-13. SEPM Society for Sedimentary Geology, Tulsa, OK.

Micallef, A., Mountjoy, J.J., Barnes, P.M., Canals, M. and **Lastras, G.** (2014) Geomorphic response of submarine canyons to tectonic activity: Insights from the Cook Strait canyon system, New Zealand. *Geosphere*, **10**, 905-929.

Middleton, G.V. (1967) Experiments on density and turbidity currents: III. Deposition of sediment. *Canadian Journal of Earth Sciences*, **4**, 475-505.

Middleton, G.V. (1993) Sediment deposition from turbidity currents. *Annual Review of Earth and Planetary Sciences*, **21**, 89-114.

Middleton, G.V. and **Hampton, M.A.** (1973) Subaqueous sediment transport and deposition by sediment gravity flows. In: *Marine Sediment Transport and Environment Management* (Eds D.J. Stanley and D.J.P. Swift), New York, Wiley, 197-218.

Missiaen, L., Wacker, L., Lougheed, B.C., Skinner, L., Hajdas, I., Nouet, J., Pichat, S. and **Waelbroeck, C.** (2020) Radiocarbon dating of small-sized foraminifer samples: Insights into marine sediments. *Radiocarbon*, **62**, 313-333.

Mitchum Jr, R.M. (1977) Seismic stratigraphy and global changes to sea level. Part 11: glossary of terms used in seismic stratigraphy. In: Seismic stratigraphy – Applications to Hydrocarbon exploration (Ed. C.E. Payton), *The American Association of Petroleum Geologists memoir*, **26**, 205-212.

Morris, W.R. and **Busby-Spera, C.J.** (1988) Sedimentologic Evolution of a Submarine Canyon in a Forearc Basin, Upper Cretaceous Rosario Formation, San Carlos, Mexico. *American Association of Petroleum Geologists Bulletin*, **72**, 717-737.

Morris, W.R. and **Busby-Spera, C.J.** (1990) A submarine-fan valley-levee complex in the Upper Cretaceous Rosario Formation: implications for turbidite facies models. *Bulletin of the Geological Society of America.*, **102**, 900-914.

Morris, W.R., Busby, C.J., Abbott, P.L. and **Cooper, J.D.** (1996) The effects of tectonism on the high resolution sequence stratigraphic framework of non-marine to deep-marine deposits in the Peninsular Ranges forearc basin complex. In: *Field Conference Guide*, AAPG National Convention, San Diego, California (Eds P.L. Abbott and J.D. Cooper), *The Pacific Section American Association of Petroleum Geologists,* **73.**

Moscardelli, L. and **Wood, L.** (2008) New classification system for mass transport mechanisms in offshore Trinidad. *Basin Research*, **20**, 73-98.

Mountjoy, J., Howarth, J., Orpin, A., Barnes, P., Bowden, D., Rowden, A., Schimel, A., Holden, C., Horgan, H., Nodder, S., Patton, J., Lamarche, G., Gerstenberger, M., Micallef, A., Pallentin, A. and **Kane, T.** (2018) Earthquakes drive large-scale submarine canyon development and sediment supply to deep-ocean basins. *Science Advances*, **4**, eaar3748.

Muck, M.T. and **Underwood, M.B.** (1990) Upslope flow of turbidity currents: A comparison among field observations, theory, and laboratory models. *Geology*, **18**, 54-57.

Mulder, T. and **Alexander, J.** (2001) The physical character of subaqueous sedimentary density flow and their deposits. *Sedimentology*, **48**, 269-299.

Mulder, T., Razin, P. and **Faugeres, J-C.** (2009) Hummocky cross-stratification-like structures in deep-sea turbidites: Upper Cretaceous Basque basins (Western Pyrenees, France). *Sedimentology*, **56**, 997–1015.

Mutti, E. (1977) Distinctive thin-bedded turbidite facies and related depostional environments in the Eocene Hecho Group (South-central Pyrenees, Spain). *Sedimentology*, **24**, 107-131.

Mutti, E. (1992) Turbidite sandstones, Milan, San Donato, 275 pp.

Mutti, E. and **Normark, W.R.** (1987) Comparing Examples of Modern and Ancient Turbidite Systems: Problems and Concepts. In: *Marine Clastic Sedimentology: Concepts and Case Studies* (Eds J.K. Leggett and G.G. Zuffa), pp1-38. Springer Netherlands, Dordrecht.

Mutti, E. and **Normark, W.R.** (1991) An Integrated Approach to the Study of Turbidite Systems. In: *Seismic Facies and Sedimentary Processes of Submarine Fans and Turbidite Systems* (Eds P. Weimer and M.H. Link), pp75-106. Springer New York, New York, NY.

Muzzi Magalhaes, P. and **Tinterri, R.** (2010) Stratigraphy and depositional setting of slurry and contained (reflected) beds in the Marnoso arenacea Formation (Langhian Serravallian) Northern Apennines, Italy. *Sedimentology*, **57**, 1685–1720.

Näkki, P., Setälä, O. and **Lehtiniemi, M.** (2017) Bioturbation transports secondary microplastics to deeper layers in soft marine sediment in the northern Baltic Sea. *Marine Pollution Bulletin*, **119**, 255-261.

Nardin, T.R., Hein, F.J., Gorsline, D.S. and **Edwards, B.D.** (1979) A review of mass movement processes, sediment and acoustic characteristics, and contrasts in slope and base-of-sope systems versus canyon-fan-basin floor systems. *SEPM Special Publication*, **27**, 61-73.

Nel, H., Krause, S., Sambrook Smith, G.H. and **Lynch, I.** (2019) Simple yet effective modification to the operation of the Sediment Isolation Microplastic unit to avoid polyvinyl chloride (PVC) contamination. *MethodsX*, **6**, 2656-2661.

Nomura, S., Hitomi, J., De Cesare, G., Takeda, Y., Yamamoto, Y. and **Sakaguchi, H.** (2019) Sediment mass movement of a particle-laden turbidity current based on ultrasound velocity profiling and the distribution of sediment concentration. In: Subaqueous Mass Movements and

their Consequences: Assessing Geohazards, Environmental Implications and Economic Signiicance of Subaqueous Landslides (Eds D.G. Lintern, D.C. Mosher, L.G. Moscardelli, P.T. Bobrowsky, C. Campbell, J. Chaytor, J. Clague, A. Georgiopoulou, P. Lajeunesse, A. Normandeau, D. Piper, M. Scherwath, C. Stacey and D. Turmel) *Geological Society of London, Special Publication*, **477**, 427-437.

Normandeau, A., Dafoe, L.T., Li, M.Z., Campbell, D.C. and **Jenner, K.A.** (2024) Sedimentary record of bottom currents and internal tides in a modern highstand submarine canyon head. *Sedimentology*, **71**, 1061-1083.

Normark, W. (1970) Growth patterns of deep-sea fans. *The American Association of Petroleum Geologists Bulletin*, **54**, 2170-2195.

Normark, W.R. (1978) Fan valleys, channels, and depositional lobes on modern submarine fans: characters for recognition of sandy turbidite environments. *American Association of Petroleum Geologists Bulletin*, **62**, 912-931.

Normark, W.R., Piper, D.J.W. and **Stow, D.A.V.** (1983) Quaternary development of channels, levees, and lobes on middle Laurentian Fan. *American Association of Petroleum Geologists Bulletin*, **67**, 1400-1409.

Normark, W.R., and **Piper, D.J.W.** (1991). "Initiation Processes and Flow Evolution of Turbidity Currents: Implications for the Depositional Record", In: *From Shoreline to Abyss*, (Ed R. H. Osborne), *Tulsa: SEPM Special Publication*, **46**, 207–230.

Nwoko, J., Kane, I. and **Huuse, M.** (2020) Mass transport deposit (MTD) relief as a control on post-MTD sedimentation: Insights from the Taranaki Basin, New Zealand. *Marine and Petroleum Geology*, **120**, 104489.

Nyberg, B., Helland-Hansen, W., Gawthorpe, R.L., Sandbakken, P., Eide, C.H., Sømme, T., Hadler-Jacobsen, F. and **Leiknes, S.** (2018) Revisiting morphological relationships of modern source-to-sink segments as a first-order approach to scale ancient sedimentary systems. *Sedimentary Geology*, **373**, 111-133.

Palanques, A., Puig, P., Martín, J., Durán, R., Cabrera, C. and **Paradis, S.** (2024) Direct and deferred sediment-transport events and seafloor disturbance induced by trawling in submarine canyons, *Science of The Total Environment*, **947**, 174470.

Pantin, H.M. and **Leeder, M.R.** (1987) Reverse flow in turbidity currents: the role of internal solitons. *Sedimentology*, **34**, 1143-1155.

Paradis, S., Puig, P., Masqué, P., Juan-Dezia, X., Martin, J. and **Palanques, A.** (2017) Bottom-trawling along submarine canyons impacts deep sedimentary regimes. *Scientific Reports*, **7**, 43332.

Parolini, M., Stucchi, M., Ambrosini, R., and **Romano, A.,** (2023) A global perspective on microplastic bioaccumulation in marine organisms. *Ecological Indicators*, **149**, e110179.

Patacci, M. (2010) Termination of turbidites against confining slopes: Flow behaviour and facies trends*. Doctoral dissertation, University College Dublin.*

Patacci, M., Haughton, P.D.W. and **McCaffrey, W.D.** (2014) Rheological complexity in sediment gravity flows forced to decelerate against a confining slope, Braux, SE France. *Journal of Sedimentary Research*, **84**, 270-277.

Patacci, M., Haughton, P.D.W. and **McCaffrey, W.D.** (2015) Flow Behavior of Ponded Turbidity Currents. *Journal of Sedimentary Research*, **85**, 885-902.

Paull, C., Caress, D., Lundsten, E., Gwiazda, R., Anderson, K., McGann, M., Conrad, J., Edwards, B. and **Sumner, E.** (2013) Anatomy of the La Jolla submarine canyon system; offshore southern California. *Marine Geology*. **335**, 16-34.

Paull, C.K., Green, H.G., Ussler, W. and **Mitts, P.J.** (2002) Pesticides as tracers of sediment transport through Monterey Canyon. *Geo-Marine Letters*, **22,** 121-126.

Paull, C.K., Talling, P.J., Maier, K.L., Parsons, D., Xu, J., Caress, D.W., Gwiazda, R., Lundsten, E.M., Anderson, K., Barry, J.P., Chaffey, M., O'Reill, T., Rosenberger, K.J., Gales, J.A., Kieft, B., McGann, M., Simmons, S.M., McCann, M., Sumner, E.J., Clare, M.A. and **Cartigny, M.J.** (2018) Powerful turbidity currents driven by dense basal layers. *Nature Communications*, **9**, 4114.

Paull, C.K., Ussler III, W., Caress, D.W., Lundsten, E., Covault, J.A., Maier, K.L., Xu, J. and **Augenstein, S.** (2010) Origins of large crescent-shaped bedforms within the axial channel of Monterey Canyon, offshore California. *Geosphere,* **6**, 755-774.

Parker, G., Fukushima, Y. and **Pantin, H.M.** (1986) Self-accelerating turbidity currents. *Journal of Fluid Mechanics*, **171**, 145-181.

Peakall, J. and **Sumner, E.J.** (2015) Submarine channel flow processes and deposits: A process-product perspective. *Geomorphology*, **244**, 95-120.

Peakall, J., Amos, K.J., Keevil, G.M. and **Bradbury, P.W.** (2007) Flow processes and sedimentation in submarine channel bends. *Marine and Petroleum Geology*, **24**, 470-486.

Peakall, J., Ashworth, P. and **Best, J.** (1996) Physical modelling in fluvial geomorphology: principles, applications and unresolved issues. In: *The Scientific Nature of Geomorphology: proceedings of the 27th Binghamton symposium, September 27-29, 1996.* (Eds B. Rhoads and C. Thorn), Hoboken, NJ, Wiley and Sons Ltd, 221-253.

Peakall, J., Best, J.L., Baas, J., Hodgson, D.M., Clare, M.A., Talling, P.J., Dorrell, R.M. and **Lee, D.R**. (2020) An integrated process-based model of flutes and tool marks in deep-water environments: implications for palaeohydraulics, the Bouma sequence, and hybrid event beds. *Sedimentology*, **67**, 1601–1666.

Peakall, J., McCaffrey, B. and **Kneller, B.** (2000) A process model for the evolution, morphology, and architecture of sinuous submarine channels. *Journal of Sedimentary Research*, **70**, 434-448.

Peng, L., Fu, D., Qi, H., Lan, C.Q., Yu, H. and **Ge, C.** (2020) Micro- and nano-plastics in marine environments: Source, distribution and threats – a review. *Science of The Total Environment*, **698**, 134254.

Pham, C.K., Ramirez-Llodra, E., Alt, C.H.S., Amaro, T., Bergmann, M., Canals, M., Company, J.B., Davies, J., Duinevald, G., Galgani, F., Howell, K.L., Huvenne, V.A.I., Isidro, E., Jones, D.O.B., Lastras, G., Morato, T., Gomes-Pereira, J.N., Purser, A., Stewart, H., Tojeira, I., Tubau, X., Van Rooij, D. and **Tyler, P.A.** (2014). Marine litter density and distribution in European seas, from shelves to deep basins. *PLoS One,* 9, 95839.

Pickering, K.T. and **Hilton, V.** (1998) Turbidite Systems of Southeast France. London, Vallis Press, 229.

Pickering, K.T. and **Hiscott, R.H.** (1985) Contained (reflected) turbidity currents from the Middle Ordovician Cloridorme Formation, Quebec, Canada: an alternative to the antidune hypothesis. *Sedimentology*, **32**, 373-394.

Pickering, K.T. and **Corregidor, J.** (2005) Mass-transport complexes (MTCs) and tectonic control on basin-floor submarine fans, middle Eocene, south Spanish Pyrenees. *Journal of Sedimentary Research*, **75**, 761-783.

Pierce, C.S., Haughton, P.D.W., Shannon, P.M., Pulham, A.J., Barker, S.P. and **Martinsen, O.J.** (2018) Variable character and diverse origin of hybrid event beds in a sandy submarine fan system, Pennsylvanian Ross Sandstone Formation, western Ireland. *Sedimentology*, **65**, 952-992.

Pierdomenico, M., Berhardt, A., Eggenhuisen, J.T., Clare, M.A., Lo Iacono, C., Casalbore, D., Davies, J.S., Kane, I., Huvenne, V.A.I., and **Harris, P.T.,** (2023) Transport and accumulation of litter in submarine canyons: a geoscience perspective. *Frontiers in Marine Science*, 101224859.

Piper, D.J.W. and **Normark, W.R.** (1983) Turbidite depositional patterns and flow characteristics, Navy Submarine Fan, California Borderland. *Sedimentology*, **30**, 681-694.

Piper, D.J.W. and **Normark, W.R.** (2009) Processes that initiate turbidity currents and their influence on turbidites: A marine geology perspective. *Journal of Sedimentary Research*, **79**, 347-362.

Pirmez, C. and **Imran, J.** (2003) Reconstruction of turbidity currents in Amazon Channel. *Marine and Petroleum Geology*, **20**, 823-849.

PlasticsEurope (2023) Plastics – the fast Facts 2023. Accessed 24th June 2024. https://plasticseurope.org/.

Pohl, F., Eggenhuisen, J.T., Tilston, M. and **Cartigny, M.J.B.** (2019) New flow relaxation mechanism explains scour fields at the end of submarine channels. *Nature Communications*, **10**, 1-8.

Pohl, F., Eggenhuisen, J.T., Kane, I.A. and **Clare, M.A.** (2020) Transport and burial of microplastics in deep-marine sediments by turbidity currents. *Environmental Science and Technology*, **54**, 4180-4189.

Pope, E.L., Heijnen, M.S., Talling, P.J., Jacinto, R.S., Gaillot, A., Baker, M.L., Hage, S., Hasenhündl, M., Heerema, C.J., McGhee, C., Ruffell, S.C., Simmons, S.M., Cartigny, M.J.B., Clare, M.A., Dennielou, B., Parsons, D.R., Peirce, C. and **Urlaub, M.** (2022) Carbon and sediment fluxes inhibited in the submarine Congo Canyon by landslide-damming. *Nature Geoscience*, **15**, 845-853.

Posamentier, H. (2003) Depositional elements associated with basin floor channel-levee system: case study from the Gulf of Mexico. *Marine Petroleum Geology*, **20**, 677-690.

Posamentier, H.W. and **Kolla, V.** (2003) Seismic geomorphology and stratigraphy of depositional elements in deep-water settings. *Journal of Sedimentary Research*, **73**, 367-388.

Postma, G. (1986) Classification of sediment gravity-flow deposits based on flow conditions during sedimentation. *Geology*, **14**, 291-294.

Pratson, L.F. and **Coakley, B.J.** (1996) A model for the headward erosion of submarine canyons induced by downslope-eroding sediment flows. *Geological Society of America Bulletin*, ***108***, 225-234.

Pratson, L.F., **Ryan, W.B.F.**, **Mountain, G.S.** and **Twichell, D.C.** (1994) Submarine canyon initiation by downslope-eroding sediment flows: evidence in late Cenozoic strata on the New Jersey continental slope. *Geological Society of America Bulletin*, **106**, 395–412.

Prave, A.R. and **Duke, W.L.** (1990) Small-scale hummocky-cross stratification in turbidites; a form of antidune stratification? *Sedimentology*, **37**, 531-539.

Privat, A.M-L. J., Peakall, J., Hodgson, D.M., Schwarz, E., Jackson, C.A-L. and **Arnol, J.A.** (2024) Evolving fill-and-spill patterns across linked early post-rift depocentres control lobe characteristics: Los Molles Formation, Argentina. *Sedimentology*, **71,** 1639-1685.

Privat, A.M-L.J., Hodgson, D.M., Jackson, C.A-L., Schwarz, E. and **Peakall, J.** (2021) Evolution from syn-rift carbonates to early post-rift deep-marine intraslope lobes: The role of rift basin physiography on sedimentation patterns. *Sedimentology*, **68**, 2563-2605.

Puig, P., Palanques, A. and **Martín, J.** (2014) Contemporary Sediment-Transport Processes in Submarine Canyons. *Annual Review of Marine Science*, **6**, 53-77.

Puigdefàbregas, C., Gjelberg, J.M. and **Vaksdal, M.** (2004) The Grès d'Annot in the Annot syncline: outer basin-margin onlap and associated soft-sediment deformation. In: *Deep-water Sedimentation in the Alpine Foreland Basin of SE France: New Perspectives on the Grès d'Annot and Related Systems* (Eds P. Joseph and S.A. Lomas), *Geological Society London Special Publication*, **221**, 367-388.

Rabouille, C., Baudin, F., Dennielous, B. and **Olu, K.** (2017) Organic carbon transfer and ecosystem functioning in the terminal lobes of the Congo deep-sea fan: outcomes of the Congolobe project. *Deep Sea Research Part 2: Topical Studies in Oceanography*, **142**, 1-6.

Reece, J.K., Dorell, R.M. and **Straub, K.M.** (2024) Circulation of hydraulically ponded turbidity currents and the filling of continental slope minibasins. *Nature Communications*, **15**, 2075.

Renne, P.R., Fulford, M.M. and **Busby-Spera, C.** (1991) High resolution 40AR/39AR chronostratigraphy of the Late Cretaceous El Gallo Formation, Baja California del Norte, Mexico. *Geophysical Research Letters*, **18**, 459-462.

Rex, M.A., Etter, R.J., Morris, J.S., Crouse, J., McClain, C.R., Johnson, N.A., Stuart, C.T., Deming, J.W., Thies, R. and **Avery, R.** (2006). Global bathymetric patterns of standing stock diversity and body size in the deep-sea benthos. *Marine Ecology Progress Series,* **317**, 1–8.

Ribó, M. Mountjoy, J.J., Mitchell, N., Watson, S., Hoffmann, J. and **Woelz, S.** (2024) New insights on gravity flow dynamics during submarine canyon flushing events. *Geology*, DOI: 10.1130/G52424.1.

Ricci Lucchi, F. and **Valmori, E.** (1980) Basin-wide turbidites in a Miocene, over-supplied deep-sea plain: a geometrical analysis. *Sedimentology*, **27**, 241-270.

Rist, S., Assidqi, K., Zamani, N.P., Appel, D., Perschke, M.J., Huhn, M. and **Lenz, M.** (2016) Suspended micro-sized PVC particles impair the performance and decrease survival in the Asian green mussel Perna viridis. *Marine Pollution Bulletin*, **111**, 213-220.

Rohais, S., Armitage, J.J., Romero-Sarmiento, M-F., Pierson, J-L., Teles, V., Bauer, D., Cassar, C., Sebag, D., Klopffer, H-M. and **Pelerin, M.** (2024) A source-to-sink perspective of an

anthropogenic marker: A first assessment of microplastics concentration, pathways, and accumulation across the environment. *Earth-Science Reviews*, **254**, 104822.

Romans, B.W., Castelltort, S., Covault, J.A., Fildani, A. and **Walsh, J.P.** (2016) Environmental signal propagation in sedimentary systems across timescales. *Earth-Science Reviews*, **153**, 7-29.

Ruffell, S.C., Talling, P.J., Baker, M.L., Pope, E.L., Heijnen, M.S., Silva Jacinto, R., Cartigny, M.J.B., Simmons, S.M., Clare, M.A., Heerema, C.J., McGhee, C., Hage, S., Hassenhündl, M., Parsons, D.R., JC209 research cruises, and **Shipboard Science Parties on JC187** (2024) Time-lapse surveys reveal patterns and processes of erosion by exceptionally powerful turbidity currents that flush submarine canyons: A case study of the Congo Canyon. *Geomorphology*, **463**, 109350.

Schofield, K. and **Serbeck, J.** (2000) The 'Above Magenta' reservoir at Ursa Field: a process-response model to explain a classic wire-line signature. In: *Deep-Water Reservoirs of the World: Gulf Coast Section Society of Economic Paleontologists and Mineralogists Foundation 20th Annual Bob F. Perkins Research Conference.* (Eds. P. Weimer, R.M. Slatt, J. Coleman, N.C. Rosen, H. Nelson, A.H. Bouma, M.J. Styzen, and D.T. Lawrence), 894-910. SEPM Society for Sedimentary Geology, Tulsa, OK.

Seabrook, S., Mackay, K., Watson, S.J., Clare, M.A., Hunt, J.E., Yeo, I.A., Lane, E.M., Clark, M.R., Wysoczanski, R., Rowden, A.A., Kula, T., Hoffmann, L.J., Armstrong, E. and **Williams, M.J.M.** (2023) Volcaniclastic density currents explain widespread and diverse seafloor impacts of the 2022 Hunga Volcano eruption. *Nature Communications,* **14**, 7881.

Shanmugam, G. (1996) High-density turbidity currents: are they sandy debris flows?: Perspectives. *Journal of Sedimentary Research*, **66**, 2-10.

Shanmugam, G. (2003) Deep-marine tidal bottom currents and their reworked sands in modern and ancient submarine canyons. *Marine and Petroleum Geology*, **20**, 471-491.

Simmons, S.M., Azpiroz-Zabala, M., Cartigny, M.J.B., Clare, M.A., Cooper, C.C., Parsons, D.R., Pope, E.L., Sumner, E.J. and **Talling, P.J.** (2020) Novel acoustic method provides first detailed measurements of sediment concentrations within submarine turbidity currents. *Journal of Geophysical Research: Oceans*. **125**, e2019JC015904.

Simpson, J.E. (1997) Gravity Currents in the Environment and in the Laboratory, 2nd edition. Cambridge University Press, Cambridge, 244 pp.

Sinclair, H.D. (1994) The influence of lateral basin slopes on turbidite sedimentation in the Annot sandstones of SE France. *Journal of Sedimentary Research*, **64**, 42-54.

Siwek, P., Waśkowska, A. and **Wendorff, M.** (2023) Mud-rich low-density turbidites in structurally-controlled intraslope mini-basin: The influence of flow containment on depositional processes and sedimentation patterns (Szczawa, Oligocene, Polish Outer Carpathians). *Sedimentology*, **70**, 1741-1784.

Smith, R., and **Joseph, P.,** (2004) Onlap stratal architectures in the Grès d'Annot: Geometric models and controlling factors. In: *Deep-water Sedimentation in the Alpine Foreland Basin of SE France: New Perspectives on the Grès d'Annot and Related Systems* (Eds P. Joseph and S.A. Lomas), *Geological Society London Special Publication*, **221**, 389-399.

Sømme, T.O., Helland-hansen, W., Martinsen, J. and **Thurmond, J.B.** (2009) Relationships between morphological and sedimentological parameters in source- to-sink systems: a basis for predicting semi-quantitative characteristics in subsurface systems. *Basin Research*, **21**, 361–387.

Sobiesiak, M.S., Kneller, B., Alsop, G.I. and **Milana, J.P.** (2016) Internal deformation and kinematic indicators within a tripartite mass transport deposit, NW Argentina. *Sedimentary Geology*, **344**, 364-381.

Sohn, Y.K. (2000) Depositional processes of submarine debris flows in the Miocene fan deltas, Pohang Basin, SE Korea with special reference to flow transformation. *Journal of Sedimentary Research*, **70**, 491-503.

Southern, S.J., Kane, I.A., Warchoł, M.J., Porten, K.W. and **McCaffrey, W.D.** (2017) Hybrid event beds dominated by transitional-flow facies: character, distribution and significance in the Maastrichtian Springar Formation, north-west Vøring Basin, Norweigan Sea. *Sedimentology*, **64**, 747-776.

Southern, S.J., Patacci, M., Felletti, F. and **McCaffrey, W.D.** (2015) Influence of flow containment and substrate entrainment upon sandy hybrid event beds containing a co-genetic mud-clast-rich division. *Sedimentary Geology*, **321**, 105–122.

Soutter, E., Kane, I., Fuhrmann, A., Cumberpatch, Z. and **Huuse, M.** (2019) The stratigraphic evolution of onlap in siliciclastic deep-water systems: Autogenic modulation of allogenic signals. *Journal of Sedimentary Research*, **89**, 890.

Soutter, E., Kane, I., Hunt, J.E., Huvenne, V.A.I., Charidemou, M., Garnett, R., Edwards, M., Bett, B., Mienis, F., Hall, R., Gates, A., Wolfe, M. and **Clare, M.A.** (2024) Interactions between internal tides and turbidity currents: an under-recognized process in deep-marine stratigraphy? ESE Open Archive, doi.org/10.22541/essoar.171078101.18643908/v1.

Soutter, E.L., Bell, D., Cumberpatch, Z.A., Ferguson, R.A., Spychala, Y.T., Kane, I.A. and **Eggenhuisen, J.T.** (2021a) The influence of confining topography orientation on experimental turbidity currents and geological implications. *Frontiers in Earth Science*, **8**. 540633.

Soutter, E.L., Kane, I.A., Hodgson, D.M. and **Flint, S.S.** (2021b) The concavity of submarine canyon longitudinal profiles. *Journal of Geophysical Research: Earth Surface*, **126**, 2021JF006185.

Sprague, A.R.G., Sullivan, M.D., Campion, K.M., Jensen, G.N., Goulding, F.J., Garfield, T.R., Sickafoose, D.K., Rossen, C., Jennette, D.C., Beaubouef, R.T., Abreu, V., Ardill, J., Porter, M.L. and **Zelt, F.B.** (2002) The physical stratigraphy of deep-water strata: a hierarchical approach to the analysis of genetically related stratigraphic elements for improved reservoir prediction. *National AAPG/SEPM Meeting Abstracts*, Houston, TX, 10-13.

Spychala, Y.T., Hodgson, D.M., Prélat, A., Kane, I.A., Flint, S.S. and **Mountney, N.P.** (2017a) Frontal and lateral submarine lobe fringes: comparing sedimentary facies, architecture and flow processes. *Journal of Sedimentary Research*, **87**, 75-96.

Spychala, Y.T., Hodgson, D.M., Stevenson, C.J. and **Flint, S.S.** (2017b) Aggradational lobe fringes: The influence of subtle intrabasinal seabed topography on sediment gravity flow processes and lobe stacking patterns. *Sedimentology*, **64**, 582-608.

Stevenson, C.J., Talling, P.J., Wynn, R.B., Masson, D.G., Hunt, J.E., Frenz, M., Akhmetzhanhov, A. and **Cronin, B.T.** (2013) The flows that left no trace: Very large-volume turbidity currents that bypassed sediment through submarine channels without eroding the sea floor. *Marine and Petroleum Geology*, **41**, 186-205.

Stevenson, C.J., Jackson, C.A.-L., Hodgson, D.M., Hubbard, S.M. and **Eggenhuisen, J.T.** (2015) Deep-Water Sediment Bypass. *Journal of Sedimentary Research*, **85**, 1058-1081.

Stevenson, C.J., Peakall, J., Hodgson, D.M., Bell, D. and **Privat, A.** (2020) TB or not TB: banding in turbidite sandstones. *Journal of Sedimentary Research*, **90**, 821-842.

Strokal, M., Vriend, P., Bak, M.P., Kroeze, C. van Wijnen, J. and **van Emmerik, T.** (2023) River export of macro- and microplastics to seas by sources worldwide. *Nature Communications*, **14**, 4842.

Sumner, E.J., Peakall, J., Parsons, D.R., Wynn, R.B., Darby, S.E., Dorrell, R.M., McPhail, S.D., Perrett, J., Webb, A. and **White, D.** (2013) First direct measurements of hydraulic jumps in an active submarine density current. *Geophysical Research Letters*, **40**, 5904-5908.

Sumner, E.J., Talling, P.J. and **Amy, L.A.** (2009) Deposits of flows transitional between turbidity current and debris flow. *Geology*, **34**, 991-994.

Sumner, E.J. and **Paull, C.K.** (2014) Swept away by a turbidity current in the Mendocino submarine canyon, California. *Geophysical Research Letters*, **41**, 7611-7618.

Talling, P.J. (2001) On the frequency distribution of turbidite thickness. *Sedimentology*, **48**, 1297-1329.

Talling, P.J., Allin, J., Armitage, D.A., Arnott, R.W., Cartigny, M.J., Clare, M.A., Felletti, F., Covault, J.A., Girardclos, S., Hansen, E., **Hill, P.R., Hiscott, R.N., Hogg, A.J., Hughes Clarke, J., Jobe, Z.R., Malgesini, G., Mozzato, A., Nauruse, H., Parkinson, S., Peel, F.J., Piper, D.J.W., Pope, E., Postma, G., Powley, P., Sguazzini, A., Stevenson, C.J., Sumner, E.J., Sylvester, Z., Watts, C.** and **Xu, J.** (2015) Key future directions for research on turbidity currents and their deposits. *Journal of Sedimentary Research*, **85**, 153-169.

Talling, P.J., Amy, L.A., Wynn, R.B., Peakall, J. and **Robinson, M.** (2004) Beds comprising debrite sandwiched within co-genetic turbidite: origin and widespread occurrence in distal depositional environments. *Sedimentology*, **51**, 163-194.

Talling, P.J., Baker, M.L., Pope, E.L., Ruffell, S.C., Silva Jacinto, R., Meijnen, M.S., Hage, S., Simmons, S.M., Hasenhündle, M., Heerema, C.J., McGhee, C., Apprioual, R., Ferrant, A., Cartigny, M.J.B., Parsons, D.R., Clare, M.A., Tshimanga, R.M., Trigg, M.A., Cula, C.A., Faria, R., Gaillot, A., Bola, G., Wallace, D., Griffiths, A., Nunny, R., Urlaub, M., Peirce, C., Burnett, R., Neasham, J. and **Hilton, R.J.** (2022) Longest sediment flows yet measured show how major rivers connect efficiently to the deep sea. *Nature Communications*, **13**, 4193.

Talling, P.J., Cartigny, M.J.B., Pope, E., Baker, M., Clare, M.A., Heijnen, M., Hage, S., Parsons, D.R., Simmons, S.M., Paull, C.K., Gwiazda, R., Lintern, G., Hughes Clarke, J.E., Xu, J., Silva Jacinto, R. and **Maier, K.L.** (2023) Detailed monitoring reveals the nature of submarine turbidity currents. *Nature Reviews Earth and Environment*, **4**, 642-658.

Talling, P.J., Masson, D.G., Sumner, E.J. and **Malgesini, G.** (2012) Subaqueous sediment density flows: Depositional processes and deposit types. *Sedimentology*, **59**, 1937-2003.

Tarhan, L.G., Droser, M.L., Planavsky, N.J. and **Johnson, D.T.** (2015) Protracted development of bioturbation through the early Paleozoic Era. *Nature Geoscience*, **8**, 865-869.

Taylor, M.L., Gwinnett, C., Robinson, L.F. and **Woodall, L.C.** (2016) Plastic microfibre ingestion by deep-sea organisms. *Nature*, **6**, 33997.

Taylor, W.J., Hodgson, D.M., Peakall, J., Kane, I.A., Flint, S.S., Bouwmeester, M.J., Marsh, J.R., Soutter, E.L., Keavney, E., Poyatos-Moré, M., McArthur, A.D., Brunt, R.L. and **Valdez-Buso, V.** (2024b) Evolution of an overbank in an ocean-facing canyon-fill. EarthArXiv, doi.org/10.31223/X5CQ5Z**.**

Taylor, W.J., Hodgson, D.M., Peakall, J., Kane, I.A., Morris, E.A. and **Flint, S.S.** (2024a) Unidirectional and combined transitional flow bedforms: Controls on process and distribution in submarine slope settings. *Sedimentology*, **71**, 1329-1362.

Tek, D.E., McArthur, A.D., Poyatos-Moré, M., Colombera, L., Patacci, M., Craven, B. and **McCaffrey, W.D.** (2021) Relating seafloor geomorphology to subsurface architecture: How mass-transport deposits and knickpoint-zones build the stratigraphy of the deep-water Hikurangi Channel. *Sedimentology*, **68**, 3141-3190.

Tek, D.E., Poyatos-Moré, M., Patacci, M., McArthur, A.D., Colombera, L., Cullen, T.M. and **McCaffrey, W.D.** (2020) Syndepositional tectonics and mass-transport deposits control channelized, bathymetrically-complex deep-water systems (Ainsa depocenter, Spain). *Journal of Sedimentary Research*, **90**, 729-762.

Thompson, P. (2010) The spatial and temporal variation in stratigraphic elements within the San Fernando Channel System. *Doctoral Dissertation*, University of Aberdeen, UK.

Thompson, R.C., Olsen, Y., Mitchell, R.P., Davis, A. and **Rowland, S.J.** (2004) Lost at Sea: Where is All the Plastic? *Science*, **304**, 838.

Thornburg, T.M., Kulm, L.D. and **Hussong, D.M.** (1990) Submarine-fan development in the southern Chile Trench: a dynamic interplay of tectonics and sedimentation. *Geological Society of America Bulletin*, **102**, 1658-1680.

Tilston, M., Arnott, R.W.C., Rennie, C.D. and **Long, B.** (2015) The influence of grain size on the velocity and sediment concentration profiles and depositional record of turbidity currents, *Geology*, **43**, 839-824.

Tinterri, R. (2006) Proposal for a classification scheme for combined flow sedimentary structures and the meaning of sigmoidal- and hummocky-cross stratification in facies analysis. *Proceedings Annual Meeting, Italian Sedimentology Group GEOSED, Modena 26-27 September 2006,* **111**.

Tinterri, R. (2007) The lower Eocene Roda Sandstone (south-central Pyrenees): an example of a flood-dominated river delta system in a tectonically controlled basin. *Rivista Italiana di Paleontologia e Stratigrafia*, **113**, 223-255.

Tinterri, R. (2011) Combined flow sedimentary structures and the genetic link between sigmoidal- and hummocky-cross stratification. *GeoActa*, **10**, 43-85.

Tinterri, R. and **Muzzi Magalhaes, P.** (2011) Synsedimentary structural control on foredeep turbidites related to basin segmentation: facies response to the increase in tectonic confinement (Marnoso-arenacea Formation, Miocene, Northern Apennines, Italy). *Marine Petroleum Geology,* **67**, 81-110.

Tinterri, R., Mazza, T. and **Magalhaes, P.M.** (2022) Contained-Reflected Megaturbidites of the Marnoso-arenacea Formation (Contessa Key Bed) and Helminthoid Flysches (Northern Apennines, Italy) and Hecho Group (South-Western Pyrenees). *Frontiers in Earth Science*, **10**, 817012.

Tinterri, R., Muzzi Magalhaes, P., Tagliaferri, A. and **Cunha, R.S.** (2016) Convolute laminations and load structures in turbidites as indicators of flow reflections and decelerations against bounding slopes. Examples from the Marnoso-arenacea Formation (northern Italy) and Annot Sandstones (south eastern France). *Sedimentary Geology*, **344**, 382-407.

Tőkés, L. and **Patacci, M.** (2018) Quantifying tabularity of turbidite beds and its relationship to the inferred degree of basin confinement. *Marine and Petroleum Geology*, **97**, 659-671.

Tomasso, M. and **Sinclair, H.D.** (2004) Deep-water sedimentation of an evolving fault-block: the Braux and St Benoit outcrops of the Grès d'Annot. In: *Deep-water Sedimentation in the Alpine Foreland Basin of SE France: New Perspectives on the Grès d'Annot and Related Systems* (Eds P. Joseph and S.A. Lomas), *Geological Society London Special Publication*, **221**, 267-283.

Toniolo, H., Lamb, M. and **Parker, G.** (2006) Depositional turbidity currents in diapiric minibasins on the continental slope: formation and theory. *Journal of Sedimentary Research,* **76**, 783-797.

Treignier, C., Derenne, S. and **Saliot, A**, (2006) Terrestrial and marine n-alcohol inputs and degradation processes relating to a sudden turbidity current in the Zaire canyon. *Organic Geochemistry*, **37**,1170–1184.

Uddin, S., Fowler, S.W., Uddin, M.F., Behbehani, M. and **Naji, A.** (2021) A review of microplastic distribution in sediment profiles. *Marine Pollution Bulletin*, **163**, 111973.

Valdez Buso, V., Kneller, B., da Silva Reis Assis, V., Vesely, F.V. and **Milana, J.P.** (2024) Incorporation of substrate blocks into mass transport deposits: Insights from subsurface and outcrop studies. *The Depositional Record*, doi.org/10.1002/dep2.283.

van Andel, T.H. and **Komar, P.D. (**1969) Ponded sediments of the Mid-Atlantic Ridge between 22 and 23 North latitude. *Geological Society of America Bulletin*, **80**, 1163-1190.

Van Cauwenberghe, L., Vanreusel, A., Mees, J. and **Janssen, C.R.** (2013) Microplastic pollution in deep-sea sediments. *Environmental Pollution*. **182**, 495-499.

van Sebille, E., Wilcox, C., Lebreton, L., Maximenko, M. and **Hardesty, B.D.** (2015) A global inventory of small floating plastic debris. *Environmental Research Letters*. **10**, 124006.

Vetter, E. W. and **Dayton, P. K.** (1998). Macrofaunal communities within and adjacent to a detritus-rich submarine canyon system. *Deep Sea Research Part 2: Topical Studies in Oceanography,* **45**, 25–54.

Von der Borch, C.C., **Grady, A.E.**, **Aldam, R.**, **Miller, D.**, **Neumann, R.**, **Rovira, A.** And **Eickhoff, K.** (1985) A large-scale meandering submarine canyon: outcrop example from the late Proterozoic Adelaide Geosyncline, South Australia. *Sedimentology*, **32**, 507–518.

Waldschläger, K. and **Schüttrumpf, H.** (2020) Infiltration behavior of microplastic particles with different densities, sizes, and shapes – from glass spheres to natural sediments. *Environmental Science and Technology*, **54**, 9366-9373.

Waldschläger, K., Brückner, M.Z.M., Carney Almroth, C., Hackney, C.R., Mehedi Adyel, T., Alimi, O.S., Lynn Belontz, S., Cowger, W., Doyle, D., Gray, A., Kane, I., Kooi, M., Kramer, M., Lechthaler, S., Michie, L., Nordam, T., Pohl, F., Russell, C., Thit, A., Umar, W. and **Wu, N.** (2022) Learning from natural sediments to tackle microplastic challenges: A multidisciplinary perspective. *Earth-Science Reviews*, **228**, 104021.

Walker, R.G. (1967) Turbidite sedimentary structures and their relationship to proximal and distal depositional environments. *Journal of Sedimentary Research*, **37**, 25-43.

Wang, R., Peakall, J., Hodgson, D.M., Keavney, E., Brown, H.C. and **Keevil, G.M**. (2024) Unconfined turbidity current interactions with oblique slopes: deflection, reflection and combined-flow behaviours. *EarthArXiv*, doi.org/10.31223/X5569F.

Wang, Z. and **Larsen, P.** (1994) Turbulence structure of flows of water and clay suspensions with bedload. *Journal of Hydraulic Engineering*, **120**, 577-600.

Wang, Z. and **Plate, E.J.** (1996) A preliminary study on the turbulence structure of flows on non_Newtonian fluid. *Journal of Hydraulic Research*, **34**, 345-361.

White, J.D.L. and **Busby-Spera, C.J.** (1987) Deep marine arc apron deposits and syndepositional magmatism in the Alisitos Group at Punta Cono, Baja California, Mexico. *Sedimentology*, **34**, 911-927.

Wilson, A.M., Raine, R., Mohn, C. and **White, M.** (2015) Nepheloid layer distribution in the Whittard Canyon, NE Atlantic Margin. *Marine Geology*, **367**, 130-142.

Wolfson-Schwehr, M., Paull, C.K., Caress, D.W., Gwiazada, R., Nieminski, N.M., Talling, P.J., Carvajal, C., Simmons, S. and **Troni, G.** (2023) Time-lapse seafloor surveys reveal how turbidity currents and internal tides in Monterey Canyon interact with the seabed at centimeter-scale. *Journal of Geophysical Research: Earth Surface*, **128**, e2022JF006705.

Woodall, L.C., Sanchez-Vidal, A., Canals, M., Patterson, G.L.J., Coppock, R., Sleight, V., Calafat, A., Rogers, A.D., Narayanaswamy. B.E., and **Thompson, R.C.** (2014) The deep sea is a major sink for microplastic debris. *Royal Society Open Science*, **1**, 140317.

Wright, S.L., Thompson, R.C. and **Galloway, T.S.** (2013) The physical impacts of microplastics on marine organisms: A review. *Environmental Pollution*, **178**, 483-492.

Wu, X., Carling, P.A. and **Parsons, D.** (2024) Hummocky sedimentary structures within rippled beds due to combined orbital waves and transverse currents. *Sedimentology*, **71**, 573-589.

Wynn, R.B., Cronin, B.T. and **Peakall, J.** (2007) Sinuous deep-water channels: Genesis, geometry and architecture. *Marine Petroleum Geology*, **24**, 341-387.

Wynn, R.B., Kenyon, N.H., Masson, D.G., Stow, D.A.V. and **Weaver, P.P.E.** (2002b) Characterization and Recognition of Deep-Water Channel-Lobe Transition Zones. *America Association of Petroleum Geologists Bulletin*, **86**, 1441-1462.

Wynn, R.B., Piper, D.J.W. and **Gee, M.J.R.** (2002a) Generation and migration of coarse-grained sediment waves in turbidity current channels and channel–lobe transition zones. *Marine Geology*, **192**, 59-78.

Xu, J. and **Noble, M.A.** (2009) Currents in Monterey Submarine Canyon. *Journal of Geophysical Research: Oceans*. **114**, 03004.

Xue, B., Zhang, L., Li, R., Wang, Y., Guo, J., Yu, K. and **Wang, S.** (2020) Underestimated microplastic pollution derived from fishery activities and "hidden" in deep sediment. *Environmental Science and Technology*, **54**, 2210-2217.

Yalin, M.S. (1971) *Theory of Hydraulic Models*. London, United Kingdom: Macmillan, 266 pp.

Yokokawa, M. (1995) Combined flow ripples: genetic experiments and applications for geologic records. *Kyushu University, Faculty of Science, Memoirs, Series D, Earth and Planetary Sciences,* **29**, 1-38.

Zarfl, C. and **Mattheis, M.** (2010) Are marine plastic particles transport vectors for organic pollutants to the Arctic? *Marine Pollution Bulletin*, **60**, 1810-1814.

Zhang, X., Liu, Z., Li, D., Zhao, Y. and **Zhang, Y.** (2024) Turbidity currents regulate the transport and settling of microplastics in a deep-sea submarine canyon. *Geology,* **52**, 646-65.

Zhang, X., Liu, Z., Zhao, Y., Ma, P., Colin, C. and **Lin, A.T-S.** (2022) Distribution and controlling factors of microplastics in surface sediments of typical deep-sea geomorphological units in the northern South China Sea. *Frontiers in Marine Science*, **9**, 1047078.

Zhengzong, G. and **Eriksson, K.A.** (1991) Internal-tide deposits in an Ordovician submarine channel: Previously unrecognized facies? *Geology*, **19**, 734-737.

Zhong, G. and **Peng, X.** (2021) Transport and accumulation of plastic litter in submarine canyons—The role of gravity flows. *Geology*, **49**, 581-586.

Zitko, V. and **Hanlon, M.** (1991) Another source of pollution by plastics: Skin cleaners with plastic scrubbers. *Marine Pollution Bulletin*, **22**, 41-42.

Appendices
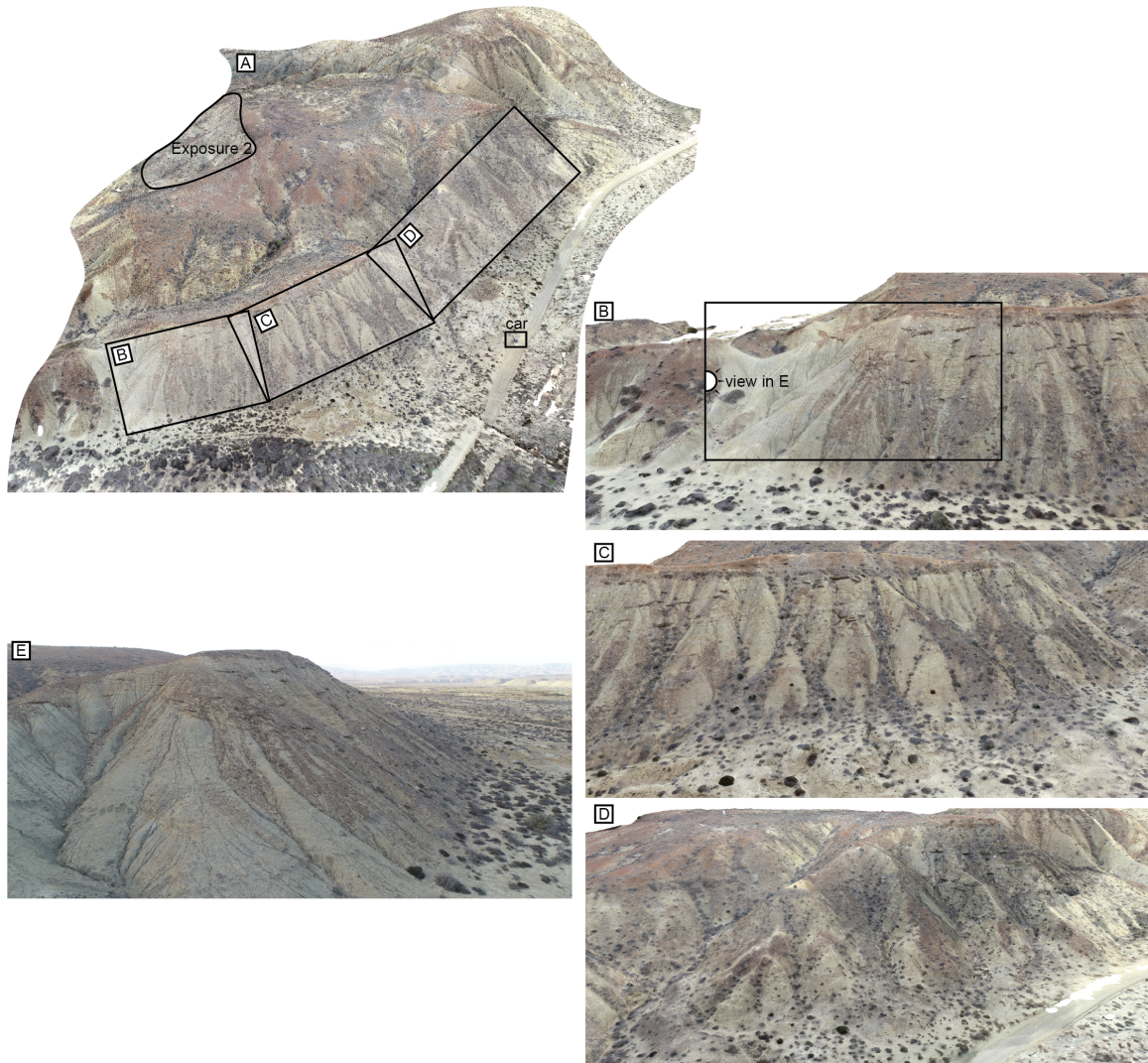
Figure 7.1: Images of Exposure 1 from the UAV photogrammetric model. (A) Overview of the principal outcrop. (B-D) Exposure 1. (E) Photograph of the contact between the slope mudstones and the canyon-confined overbank deposits.
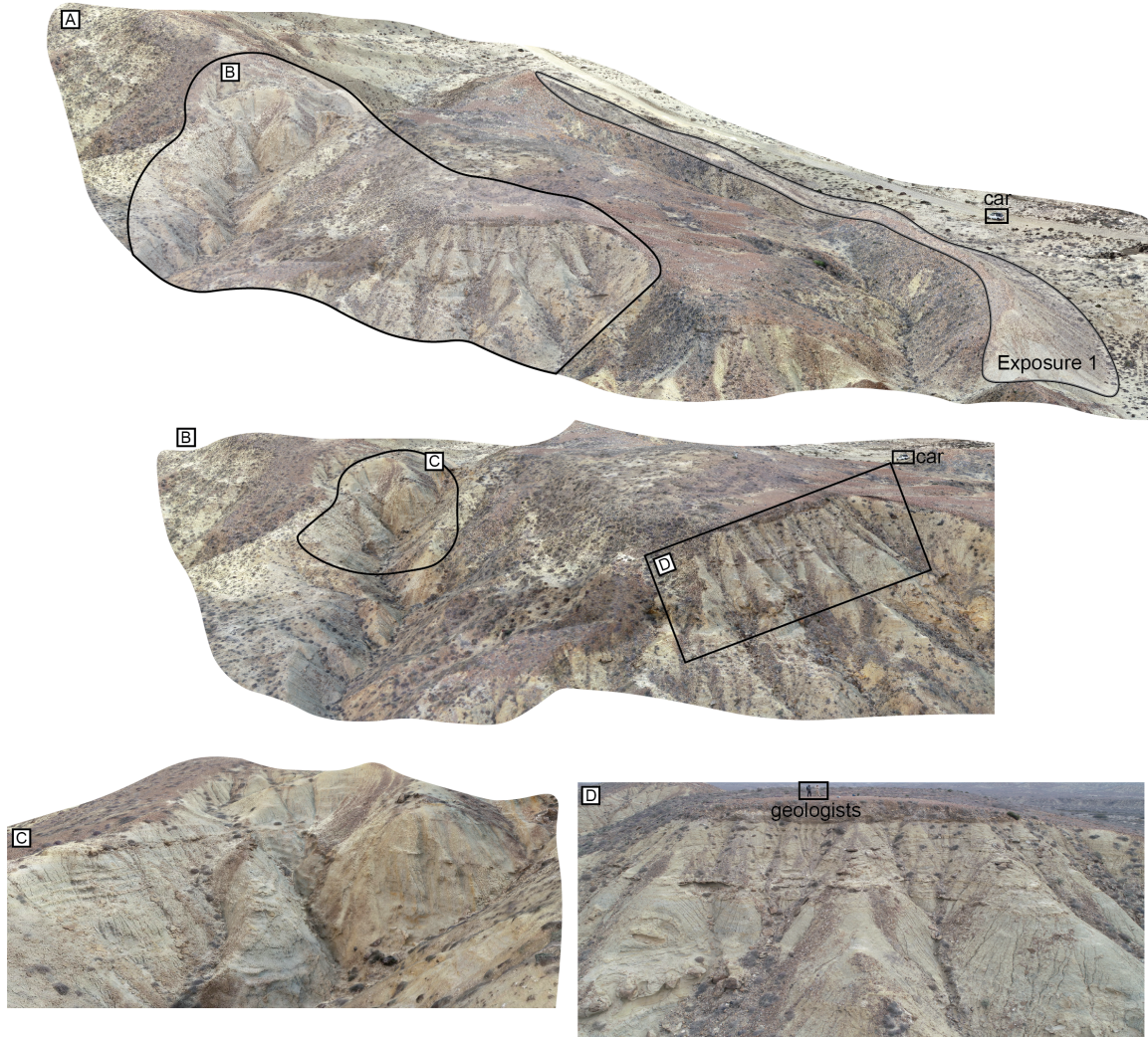
Figure 7.2: Images of Exposure 2 from the UAV photogrammetric model. (A) Overview of the principal outcrop. (B) Exposure 2, (C) Slumped region to the West of Exposure 2, and (D) Photograph of Exposure 2.

Appendix Table A1: Contamination control procedural blank data for the "sample preparation" stage and the "microplastic identification" stage.

Sample number	Sample preparation exposure time (s)	Microfibre count	Microplastic identification exposure time (s)	Microfibre count
PSH_60_A	429	3	1150	0
PSH_60_B	540	0	920	0
PSH_60_C	515	0	879	0
PSH_60_D	457	0	681	0
PSH_60_E	500	0	534	0
PSH_62_A	492	1	689	0
PSH_62_B	525	0	748	0
PSH_62_C	483	0	503	0
PSH_62_D	471	0	597	0
PSH_62_E	531	0	834	0
PSH_62_F	436	0	412	0
PSH_62_G	388	0	456	0
PSH_62_H	540	0	478	0
PSH_62_I	433	0	502	0
PSH_62_J	420	0	330	0
PSH_64_A	408	0	1347	1
PSH_64_B	403	0	810	0
PSH_64_C	414	1	712	0
PSH_64_D	451	0	629	0
PSH_64_E	439	0	1422	0
PSH_64_H	381	0	878	0
PSH_64_I	430	0	720	0
PSH_64_J	490	0	934	0
PSH_66_A	470	0	701	0
PSH_66_B	467	0	645	0
PSH_66_C	483	0	522	1
PSH_66_D	1962	0	326	0
PSH_66_E	580	0	400	0
PSH_66_F	449	0	354	0
PSH_66_G	552	0	570	0
PSH_66_H	442	0	385	1
PSH_66_I	458	0	380	0
PSH_66_J	415	0	321	0
PSH_69_A	N/A	0	N/A	0
PSH_69_B	N/A	2	N/A	0
PSH_69_C	N/A	0	N/A	0
PSH_69_D	N/A	1	N/A	0
PSH_69_E	N/A	0	N/A	0
PSH_69_F	N/A	2	N/A	1
PSH_69_G	N/A	2	N/A	0
PSH_69_H	N/A	3	N/A	0
PSH_69_I	N/A	3	N/A	1
PSH_69_J	N/A	6	N/A	0
PSH_108_A	421	0	410	0
PSH_108_B	410	0	329	0
PSH_108_C	407	0	717	0
PSH_108_D	467	0	682	0
PSH_108_E	403	0	724	0
PSH_108_F	367	0	520	0
PSH_108_G	366	0	489	0
PSH_108_H	406	0	226	0
PSH_108_I	354	0	460	0
PSH_108_J	362	0	357	0
PSH_113_A	410	0	837	0
PSH_113_B	435	0	869	0
PSH_113_C	391	0	708	0
PSH_113_D	399	0	725	0
PSH_113_E	530	0	713	1
PSH_113_F	406	0	442	1
PSH_113_G	448	4	772	0
PSH_113_H	429	0	729	0

PSH_114_A	954	0	1208	0
PSH_114_B	1065	1	1408	1
PSH_114_C	716	0	528	0
PSH_114_D	883	0	482	0
PSH_114_E	839	0	467	0
PSH_114_F	600	0	816	0
PSH_114_G	865	0	962	0
PSH_114_H	595	0	548	0
PSH_114_I	543	0	651	0
PSH_114_J	565	0	605	0
PSH_116_A	412	0	456	0
PSH_116_B	424	1	566	0
PSH_116_C	465	0	493	0
PSH_116_D	515	1	635	0
PSH_116_E	451	0	607	0
PSH_116_F	516	0	469	0
PSH_116_G	520	0	556	0
PSH_116_H	443	0	433	0
PSH_116_I	434	0	396	0
PSH_116_J	493	0	370	0

Appendix Table A2: Sample information, gravel%, sand%, silt%, and clay%, and scaled-up microplastic counts/50 g dry sediment.

Sample number	Latitude	Longitude	Water depth (m)	Height above thalweg (m)	Core depth horizon (cm)	Gravel (%)	Sand (%)	Silt (%)	Clay (%)	Microfibre count / 50 g dry sediment	Microplastic fragment count / 50 g dry sediment	Microbead count / 50 g dry sediment
PSH_060_A	48.61365	-10.01576667	1546	34	0-1	0	99.62	0.38	0	4	0	0
PSH_060_B	48.61365	-10.01576667	1546	34	1-2	1.1	98.90	0	0	10	8	0
PSH_060_C	48.61365	-10.01576667	1546	34	2-3	14.07	85.93	0	0	17	3	0
PSH_060_D	48.61365	-10.01576667	1546	34	3-4	10.16	89.84	0	0	21	0	0
PSH_060_E	48.61365	-10.01576667	1546	34	4-5	22.90	77.09	0	0	30	0	0
PSH_062_A	48.63688333	-10.02356667	1360	220	0-1	0	64.34	35.66	0	14	0	0
PSH_062_B	48.63688333	-10.02356667	1360	220	1-2	0	56.27	42.21	1.53	18	0	0
PSH_062_C	48.63688333	-10.02356667	1360	220	2-3	0	52.14	44.91	2.95	11	0	0
PSH_062_D	48.63688333	-10.02356667	1360	220	3-4	0	53.48	43.45	3.08	3	0	0
PSH_062_E	48.63688333	-10.02356667	1360	220	4-5	0	56.03	40.29	3.68	10	0	0
PSH_062_F	48.63688333	-10.02356667	1360	220	5-6	0	54.46	42.13	3.43	0	0	0
PSH_062_G	48.63688333	-10.02356667	1360	220	6-7	0	45.98	48.79	5.23	11	4	0
PSH_062_H	48.63688333	-10.02356667	1360	220	7-8	0	N/A	N/A	N/A	6	0	0
PSH_062_I	48.63688333	-10.02356667	1360	220	8-9	0	53.06	43.62	3.32	9	0	0
PSH_062_J	48.63688333	-10.02356667	1360	220	9-10	0	64.34	37.09	4.17	0	0	0
PSH_064_A	48.63600667	-10.0248	1303	277	0-1	0	52.65	44.92	2.43	5	0	0
PSH_064_B	48.63600667	-10.0248	1303	277	1-2	0	43.78	50.71	5.51	8	0	0
PSH_064_C	48.63600667	-10.0248	1303	277	2-3	0	40.28	53.72	6	8	0	0
PSH_064_D	48.63600667	-10.0248	1303	277	3-4	0	40.65	54.73	4.62	9	0	0
PSH_064_E	48.63600667	-10.0248	1303	277	4-5	0	34.08	57.59	8.33	3	0	0
PSH_064_H	48.63600667	-10.0248	1303	277	7-8	0	41.3	52.79	5.91	19	0	0
PSH_064_I	48.63600667	-10.0248	1303	277	8-9	0	41.78	52.56	5.66	5	0	0
PSH_064_J	48.63600667	-10.0248	1303	277	9-10	0	45.21	49.46	5.33	14	0	0
PSH_066_A	48.63545167	-10.00317333	1259	321	0-1	0	38.7	53.82	7.48	9	0	0
PSH_066_B	48.63545167	-10.00317333	1259	321	1-2	0	55.43	41.67	2.9	10	0	0
PSH_066_C	48.63545167	-10.00317333	1259	321	2-3	0	48.02	45.68	6.3	7	0	0
PSH_066_D	48.63545167	-10.00317333	1259	321	3-4	0	40.51	50.72	8.77	7	0	0
PSH_066_E	48.63545167	-10.00317333	1259	321	4-5	0	35.87	59.06	5.07	3	0	0
PSH_066_F	48.63545167	-10.00317333	1259	321	5-6	0	31.22	61.79	6.99	0	0	0
PSH_066_G	48.63545167	-10.00317333	1259	321	6-7	0	30.18	62.82	7	3	0	0
PSH_066_H	48.63545167	-10.00317333	1259	321	7-8	0	40.33	54.23	5.44	0	0	0
PSH_066_I	48.63545167	-10.00317333	1259	321	8-9	0	38.4	55.57	6.03	0	0	0
PSH_066_J	48.63545167	-10.00317333	1259	321	9-10	0	40.72	53.65	5.63	0	0	0
PSH_069_A	48.64316667	-9.99879	1062	518	0-1	0	43.45	49.5	7.05	50	8	0
PSH_069_B	48.64316667	-9.99879	1062	518	1-2	0	41.99	51.74	6.27	43	0	0
PSH_069_C	48.64316667	-9.99879	1062	518	2-3	0	42.68	49.87	7.45	14	9	0
PSH_069_D	48.64316667	-9.99879	1062	518	3-4	0	42.25	50.59	7.16	8	0	8
PSH_069_E	48.64316667	-9.99879	1062	518	4-5	0	46.82	47.26	5.92	16	0	8
PSH_069_F	48.64316667	-9.99879	1062	518	5-6	0	44.59	51.57	3.84	3	0	0
PSH_069_G	48.64316667	-9.99879	1062	518	6-7	0	41.23	55.05	3.72	14	0	22
PSH_069_H	48.64316667	-9.99879	1062	518	7-8	0	51.5	45.41	3.09	6	0	0
PSH_069_I	48.64316667	-9.99879	1062	518	8-9	0	66.49	31.89	1.62	5	0	0
PSH_069_J	48.64316667	-9.99879	1062	518	9-10	0	55.31	42.55	2.14	22	3	0
PSH_108_A	48.375593	-10.0446445	3152	52	0-1	0	32.59	61.27	6.14	0	0	0
PSH_108_B	48.375593	-10.0446445	3152	52	1-2	0	25.37	67.79	6.84	9	0	0
PSH_108_C	48.375593	-10.0446445	3152	52	2-3	0	35.47	59.21	5.32	13	0	0
PSH_108_D	48.375593	-10.0446445	3152	52	3-4	0	66.15	31.8	2.05	15	4	0
PSH_108_E	48.375593	-10.0446445	3152	52	4-5	0	71.59	27.57	0.84	10	0	0
PSH_108_F	48.375593	-10.0446445	3152	52	5-6	0	65.16	33.22	1.62	4	0	0
PSH_108_G	48.375593	-10.0446445	3152	52	6-7	0	71.01	27.91	1.08	3	0	0
PSH_108_H	48.375593	-10.0446445	3152	52	7-8	0	82.14	17.86	0	0	0	0
PSH_108_I	48.375593	-10.0446445	3152	52	8-9	0	97.33	2.67	0	11	0	0
PSH_108_J	48.375593	-10.0446445	3152	52	9-10	0	67.89	30.26	1.85	3	0	0
PSH_113_A	48.371195	-10.03929667	3204	0	0-1	0	85.73	14.27	0	32	0	0
PSH_113_B	48.371195	-10.03929667	3204	0	1-2	0	95.27	4.73	0	25	0	0
PSH_113_C	48.371195	-10.03929667	3204	0	2-3	0	97.85	2.15	0	6	6	0
PSH_113_D	48.371195	-10.03929667	3204	0	3-4	0	96.8	3.2	0	10	0	0
PSH_113_E	48.371195	-10.03929667	3204	0	4-5	0	93.65	6.35	0	15	0	0
PSH_113_F	48.371195	-10.03929667	3204	0	5-6	0	88.07	11.93	0	17	0	0
PSH_113_G	48.371195	-10.03929667	3204	0	6-7	0	88.85	11.15	0	5	0	0
PSH_113_H	48.371195	-10.03929667	3204	0	7-8	0	92.87	7.13	0	12	2	0
PSH_114_A	48.36871667	-10.03463333	2995	209	0-1	0	12.3	78.35	9.35	31	0	0
PSH_114_B	48.36871667	-10.03463333	2995	209	1-2	0	12.43	74.21	13.36	18	12	0
PSH_114_C	48.36871667	-10.03463333	2995	209	2-3	0	28.77	64.56	6.67	9	0	0
PSH_114_D	48.36871667	-10.03463333	2995	209	3-4	0	25.7	65.67	8.63	5	0	0

PSH_114_E	48.36871667	-10.03463333	2995	209	4-5	0	12.95	79.55	7.5	5	0	0
PSH_114_F	48.36871667	-10.03463333	2995	209	5-6	0	19.08	70.48	10.44	13	0	0
PSH_114_G	48.36871667	-10.03463333	2995	209	6-7	0	19.09	71.75	9.16	14	0	0
PSH_114_H	48.36871667	-10.03463333	2995	209	7-8	0	14	73.86	12.14	5	0	0
PSH_114_I	48.36871667	-10.03463333	2995	209	8-9	0	13.85	77.71	8.44	13	0	0
PSH_114_J	48.36871667	-10.03463333	2995	209	9-10	0	14.16	73.39	12.45	11	0	0
PSH_116_A	48.36326	-10.03335333	2773	431	0-1	0	25.05	67.94	7.01	51	0	0
PSH_116_B	48.36326	-10.03335333	2773	431	1-2	0	22.27	69.15	8.58	16	0	0
PSH_116_C	48.36326	-10.03335333	2773	431	2-3	0	18.28	73.86	7.86	11	0	0
PSH_116_D	48.36326	-10.03335333	2773	431	3-4	0	19.04	73.91	7.05	29	6	0
PSH_116_E	48.36326	-10.03335333	2773	431	4-5	0	18.66	72.68	8.66	17	0	0
PSH_116_F	48.36326	-10.03335333	2773	431	5-6	0	14.94	74.67	10.39	10	5	0
PSH_116_G	48.36326	-10.03335333	2773	431	6-7	0	12.04	69.94	18.02	0	0	0
PSH_116_H	48.36326	-10.03335333	2773	431	7-8	0	12.29	71.76	15.95	11	0	0
PSH_116_I	48.36326	-10.03335333	2773	431	8-9	0	10.2	75.46	14.34	0	0	0
PSH_116_J	48.36326	-10.03335333	2773	431	9-10	0	11.76	75.44	12.8	10	0	0

Appendix Table A3: Sample number and corresponding particle types, colour and composition obtained from FTIR analysis.

Sample number	Particle type	Particle color	Particle composition
PSH_060_A	Fibre	Black	Rayon
PSH_060_E	Fibre	Black	Chlorinated Rubber
PSH_062_A	Fibre	Black	Chlorinated Rubber
PSH_062_I	Fibre	Black	Chlorinated Rubber
PSH_064_B	Fibre	Blue	Polyester
PSH_064_C	Fibre	Black	Plastic additive
PSH_069_B	Fibre	Black	Polyvinyl chloride
PSH_108_B	Fibre	Black	Synthetic resin
PSH_113_B	Fibre	Black	Polypropylene
PSH_114_I	Fibre	Black	Acrylic
PSH_114_I	Fibre	Black	Acrylic
PSH_114_J	Fibre	Black	Chlorinated Rubber
PSH_116_B	Fibre	Black	Polyvinyl chloride

Appendix Table A4: [210]Pb values used to calculate sediment accumulation rates for the four box-cores.

Box-core	Core depth horizon (cm)	210Pb total (mBq g-1)	210Pb total 1s error (mBq g-1)
BC64	0-0.5	261.27	12.50
	0.5-1	268.59	11.71
	1-1.5	259.18	11.62
	2-2.5	310.24	12.65
	3-4	224.54	9.82
	5-6	290.17	12.28
	7-8	285.75	12.30
	9-10	154.65	7.77
	11-12	51.92	2.21
	13-14	23.56	1.25
	15-16	19.02	1.10
	17-18	21.86	1.16
BC65	0-0.5	522.64	11.90
	0.5-1	493.74	11.98
	1-1.5	431.94	10.07
	2-2.5	404.47	9.58
	3-4	413.64	9.02
	5-6	312.98	8.02
	9-10	284.93	7.19
	13-14	186.10	5.17
	17-18	110.57	3.21
	24-25	66.14	2.33
	31-32	28.84	1.20
	38-39	26.82	1.22
BC72	0-0.5	153.47	4.03
	0.5-1	157.50	4.14
	1-1.5	146.69	3.81
	1.5-2	126.40	3.57
	2-2.5	110.25	3.05
	3-5	60.72	1.89
	5-6	43.46	1.50
	7-8	17.39	0.81
	9-10	10.38	0.85
	11-12	10.40	0.83
	13-14	11.56	0.91
	15-16	12.93	0.99
BC73	0-0.5	654.01	26.95
	0.5-1	640.97	24.23
	1-1.5	612.71	25.47
	2-2.5	664.32	22.85
	3-4	410.35	16.89
	5-6	547.83	22.24
	7-8	264.64	11.14
	11-12	525.91	20.83
	15-16	231.96	6.95
	21-22	103.19	3.79
	27-28	319.65	9.35
	33-34	278.11	8.56

Supplementary Material

The raw, scanned images of the sedimentary logs for Chapter 4 are free to access at: https://figshare.com/s/97f7fc00dfc592edc64d

Acoustic Doppler Current Profiler hydrodynamic mooring data discussed in Chapter 5: https://www.bodc.ac.uk/resources/inventories/cruise_inventory/report/17695/